FIBRE OPTIC TEMPERATURE SENSORS USING FLUORESCENT PHENOMENA

by

Raman Kumar Selli B.Sc.

Submitted for the degree of Doctor of Philosophy

The City University
School of Applied Physics and Engineering
Northampton Square
London
EC1 OHB

June 1989.

LIST OF CONTENTS

TABLES AND FIGURE CAPTIONS

CHAPTER 1

CHAPTER 2

R_{sh} - Shunt resistance
R_s - Series resistance
R_L - Load resistance
C_j - Junction capacitance
V_d - Voltage across the diode
i_L - Output current
V_L - Output voltage

Figure 2.11 - V-I characteristics
V_{op}: Open-circuit voltage
I_{sh}: Short-circuit current

Figure 2.12 - (a) Open-circuit voltage against incident light

Figure 2.12 - (b) Short-circuit current against incident light

Figure 2.13 - Shows the reverse bias connection of a photodiode

Figure 2.14 - Transimpedance mode op-amp circuit diagram

Figure 2.15 - A graph of rise time against reverse voltage (this graph shows a plot for Hamamatsu photodiode S1336BQ with R_L = 1KΩ at λ=655nm)

Figure 2.16 - A graph showing the extension of the linear range of a photodiode as a function of reverse bias and illumination.(Hamamatsu 1333.5BQ; R_L=100KΩ)

Figure 2.17 - Temperature coefficient against wavelength
A: Schottky type GaAsP
B: Hamamatsu 1226 series designed for visible region - Peak response at ~700 nm C:Hamamatsu 1336 series designed for optimal response in the infra red - peak response at ~900nm

Figure 2.18 - Signal at various stages
1: Output of detector
2a: Control pulses for electronic switch
2b: Sample pulses to remove dc offset (S/H)
3: Output of first analogue switch (S/W_1)
4: Output of second analogue switch (S/W_2)
5: Output of difference amplifier
6a: Detected signal with dc bias removed
6b: Pulses for sample and hold device (S/H_2)
7a: 'Probe' dc signal

CHAPTER 3

numbers refer to outputs at various stages shown in figure 3.2

Figure 3.4 - Complete analogue circuit diagram
O/P_1: 'Probe' signal feeding to A/D
O/P_2: 'Reference' signal feeding to A/D, S/H_1, S/H_2 and S/W2 are inputs from digital circuit shown in figures 2.9.

Figure 3.5 - Spectral responsivity characteristics of RCA C30812 photodiode

Figure 3.6 - Schematic of detector signal output showing typical voltage levels.

Figure 3.7 - Test circuit of ICL7135 analogue-to-digital converter

Figure 3.8 - Microprocessor system

Z-80: Microprocessor
ROM: Electrically programmable read only memory
RAM: Random access memory (CMOS 6116)
I/P Lt: Input latch (74LS373)
O/P Lt: Output latch (74LS373)
DECODER: LCD decoder/drive chip (CMOS 4-digit, 7211Hex)
A/D: Analogue-to-digital converter (ICL7135)
LCD: Liquid crystal display
Int: Maskable interrupt
A_0-A_{15}: Address bus
D_0-D_7: Data bus
IROQ: Input/output request
M1: Machine cycle 1
RD: Read
MREQ: Memory request signal
OE: Output enable
CS: Chip select
WE: Write enable
E: Enable
Φ: Clock

Figure 3.9 - Ratio of 'probe' signal x, to 'reference' signal y, as a function of temperature

CHAPTER 4

OG glass temperature sensor

Figure 4.8 - Transmittance (at room temperature) of three absorption glasses (solid lines) OG 515,(A), OG 550,(B), RG-630, (C),(Schott glass). Spectral profile of the green LED is shown as dotted lines (L)

Figure 4.9 - Normalised transmission as a function of temperature of three absorption glasses (20° - $130^{\circ}C$)

Figure 4.10 - Normalised ratio of the measurand and reference signals as a function of temperature.
A - System 1 (ruby crystal housed with the sensing element)
B - System 2 (ruby crystal in the same housing as the LED)

CHAPTER 5

Figure 5.1 - Absorbance (arbitrary units) of ~1mm sample of ruby crystal as a function of wavelength

Figure 5.2 - Schematic of the probe showing ruby crystal and fibre connections

Figure 5.3 - Spectral emission of the green LED as a function of drive current.1: 30mA, 2: 25mA, 3: 20mA, 4: 15mA, 5: 10mA, 6: 5mA.

Figure 5.4 - Block diagram of the electronic circuit. A,B,C,D are the output signals.

Figure 5.5 - Voltage waveforms (Numbers refer to Figure 5.4)
(1) : Signal at point'1' - after amplifier stage
(2) : Signal to analogue switch (at point'2')
(3) A(dashed) : Signal to S/H_3 and S/H_4
.(3) B(solid) : Signal to S/H 1 and S/H_2.
(4) : Outputs at A, B, C, D.

Figure 5.6 - Complete digital circuit diagram (all logic gates used were CMOS)

CHAPTER 6

B.P: Electronic band-pass filter
Amp: Amplifier
Z.C.D: Zero-crossing detector
XOR: Exclusive-OR gate
AND: And gate
L.P + bias: Low-pass filter with dc bias
µP: Microprocessor
LCD: Liquid crystal display

Figure 6.11 - Complete diagram of the sine wave generator and LED drive circuitry.(All op-amps are 071 series) (oscillator feeds into circuit in figure 6.14)

Figure 6.12 - Block diagram of the phase-locked-loop.

Figure 6.13 - Circuit diagram of the phase-locked-loop.

Figure 6.14 - Complete diagram of the analogue phase detection circuit. (All op-amps used were low noise OP-37 series with CMP-01E type).

Figure 6.15 - Input and output waveforms of the zero-crossing detector

Figure 6.16 - Illustration showing the generation of a series of pulses representing the phase difference between two square waves of the same frequency. The output signal pulses are shown in C.

Figure 6.17 - Circuit diagram of the microprocessor system
Z80: Microprocessor
ROM: Electrically programmable read only memory (CMOS 28016 2K)
RAM: Random access memory (CMOS 6116; 2K)
Lt: Input latch (74LS373)
O/P Lt: Output latch (74LS373)
÷ 8 counter: 8 bit counter (74LS393)
÷ 4 counter: 4 bit counter (74LS393)
Monostable 1: (74LS123)
Monostable 2: (74LS123)
Decoder: LCD decoder/drive circuit(CMOS 4 digit 7211Hex)
A_0 - A_{15}: Address bus
D_0-D_7: Data bus
WR: Write signal

RD: Read signal
IORQ: Input/output request
M1: Machine cycle
MREQ: Memory request
OE: Output enable
CS: Chip select
WE: Write enable
OE: Output enable
Int: Maskable interrupt
Φ: Clock

Figure 6.18 - Control logic for circuit in figure 6.17.

Figure 6.19 - Diagram showing division of signal A into smaller pulses B.(A represents signal 'input' in figure 6.17).

Figure 6.20 - Photograph of fluorescence sine wave at the detector stage in figure 6.14.

Figure 6.21 - Photograph of sine wave after band-pass filter APB-6 (figure 6.14).

Figure 6.22 - Photograph of sine wave transformed to a square wave by zero-crossing detector (output of comparator C in figure 6.14).

Figure 6.23 - Photograph of pulse duration representing pulse difference (output of XOR gate in figure 6.14).

Figure 6.24 - Calibration graph of phase change as a function of temperature taken with the Ealing short-pass filter.

Figure 6.25 - Calibration graph of a phase change as a function of temperature. (Calibration A represents readings taken with Glen Creston filter and calibration B represents readings taken with Ealing short-pass filter).

Figure 6.26 - A graph showing the variation in phase as a function of the detected signal amplitude (peak value) A: readings taken by removing SMA connector at emitter end; B: readings taken by removing SMA connector at detector end) Vertical lines show the standard deviation at each point.

CHAPTER 7

APPENDICES

Figure A12.4 - Fluorescence emission spectrum of ruby in the region 620-760nm. The ordinate is calibrated in the same arbitrary intensity units for each of the three temperatures shown. In region 'R' the ordinate is reduced to ~12% (after Burns and Nathan (79))

ACKNOWLEDGEMENTS

Over the course of this work I have sought help from a number of people all of whom have been very kind in offering their time and expertise. Foremost, I wish to express my sincere appreciation to Dr. K.T.V. Grattan for his excellent supervision of this work and for his ability to motivate and encourage at all times. I am very grateful for his encouragement and for making it possible for me to participate and attend conferences, abroad and at home, to gain wider understanding and experience in the field of fibre optic sensors.

I am grateful for the financial support provided by the Science and Engineering Research Council in collaboration with the Central Electricity Research Laboratories, and in particular would like to thank [redacted], at CERL, for his very useful discussions

A debt of gratitude is also owed to [redacted] for his patience and time in reviewing this manuscript thoroughly. In addition, I would like to thank him for his invaluable discussions and comments during the course of this work. I also like to express my thanks to [redacted] for his useful comments and guidance. Finally, I am grateful to all the technical staff, especially [redacted], for their assistance throughout.

ABSTRACT

A number of fibre optic sensors based on fluorescent phenomena using low cost electronic and optical filtering techniques, for temperature sensing applications are described and discussed.

The initial device developed uses the absorption edge change of an optical glass to monitor changes in temperature with a second wavelength reference channel being generated from a fluorescent material, neodymium doped in glass. This device demonstrates the working of the self-referencing principle in a practical device tested over the temperature range of -60°C to 200°C. This initial device was improved by incorporating a microprocessor and by modifying the processing electronic circuitry. An alternative probe was constructed which used a second fibre placed along-side the addressing fibre in contrast to the original device where the fibre is placed at the opposite end of the addressing fibre.

A device based on the same principle but with different absorption glasses and a different fluorescent medium, crystalline ruby, was also examined. This device operated at a lower wavelength region compared to the infra-red working region of the first device. This work illustrated the need to make an appropriate choice of sensor absorption glass so that the cheaper indicator type LEDs, which operated at lower wavelengths, may be used.

Ruby is a fluorescent material which is characterized by each emission wavelength having its own temperature characteristics. The integrated energy output over the complete emission spectrum is independent of temperature. This provided a means of generating a reference from the complete spectrum while a small frequency band gave a temperature dependent output. This characteristic of ruby

was used to develop a temperature measuring device.

A final system which utilises the temperature dependent decay-time emission properties of crystalline ruby was developed. In this case the ruby was excited by sinusoidally modulated light. This system employs a single indicator type green LED to excite the ruby sample and a single very sensitive silicon photodiode detector with an integral amplifier for low optical signal detection. Both of these components were inexpensive. The system yielded very high performance levels in terms of precision and resolution which has the potential for commercial exploitation.

The different devices developed are compared and contrasted in the light of the commercial instruments on the market and other published data.

Current generator

Voltage generator

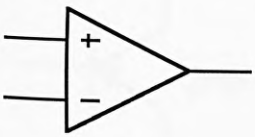

Operational amplifier

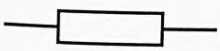

resistor

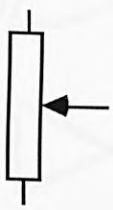

Variable resistor

Electrolytic capacitor

Capacitor

Analogue switch

Diode

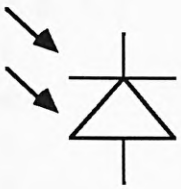

Photodiode

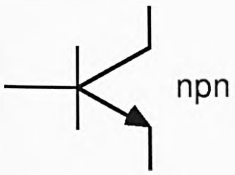

NPN transistor

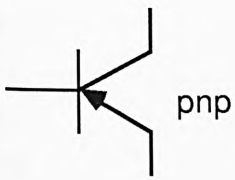

PNP transistor

Exclusive OR-gate

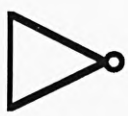

NOT-gate

NOR-gate

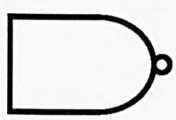

NAND-gate

Battery

Earth

$\alpha, \beta, \delta, \gamma$	Attenuation along the fibre
τ	Time delay or phase delay
ω	Angular frequency
π	3.142
θ, σ, x	Phase angle
λ	Wavelength
λ_a	Antistokes wavelength
λ_s	Stokes wavelength
ϕ	Emissive rate
ΔV	Threshold voltage
Δt	Change in time
A	Amplitude, Area of photodiode
ac	Alternating current
A/D	Analogue-to-digital converter
AND	AND-gate
B	Bandwidth
B.P	Band-pass filter
c	Concentration of absorbing molecule, velocity of light
C	Capacitor
$^{\circ}C$	Degree Celsius
Cr^{3+}	Doped crystalline ruby
C_j	Junction capacitance
dc	Direct current
dB	Decibel
e	Electronic charge, Intensity factor
E	Energy level
f	Frequency
FET	Field effect transistor
h	Planck's constant
H.P	High-pass filter
Hz	Hertz
I	Intensity
i_c	Capacitor current
i_d	Diode current, Dark current
i_j	Thermal or Johnson noise
i_L	Output current
i_n	Noise current

I_o	Input intensity
i_p	Current generated by the incident light
i/p	Input
i_s	Shot noise
i_{SH}	Shunt resistance current
I_{sh}	Short-circuit current
k	Boltzmann's constant
k	Rate of non-radiative decay
K	Kelvin
l	Length of sample
L.C.D	Liquid crystal display
LED	Light emitting diode
L.P	Low-pass filter
Nd^{3+}	Neodymium
NEP	Noise equivalent power
Op-amp	Operational amplifier
o/p	Output
OSC	Oscillator
Pa	Pascal
PCS	Plastic coated Silica
p-i-n	Positive-intrinsic-negative
PLL	Phase locked loop
q	Electronic charge
Q	Quality factor
R	Resistor
RAM	Random access memory
RG	Ruby glass
R_f	Feedback resistor
R_L	Load resistance
Rms	Root-mean-square value
ROM	Read only memory
R_s	Series resistance
R_{sh}	Shunt capacitor
S	Peak radiant sensitivity, Electronic excited state
S/H	Sample and Hold devices
Si	Silicon
S/W	Electronic analogue switch

T	Temperature, Tesla, Triplet state
t	Time
V_{cc}	Supply voltage
V_{ce}	Collector-emitter voltage
VCO	Voltage controlled oscillator
V_d	Voltage across the diode
V_L	Output voltage
V_{op}	Open-circuit voltage
V_p	Peak voltage
W	Watt
XOR	Exclusive OR-gate
YAG	Yttrium Aluminium garnate
Z-80	Microprocessor

T	tera 10^{12}
G	giga 10^{9}
M	mega 10^{6}
k	kilo 10^{3}
m	milli 10^{-3}
μ	micro 10^{-6}
n	nano 10^{-9}
p	pico 10^{-12}

Chapter 1

INTRODUCTION TO FIBRE OPTIC SENSORS

1.0 INTRODUCTION TO FIBRE OPTIC SENSORS

This chapter gives an indication of the market potential of fibre optic sensors and advantages of fibre optic technology. It also provides a general introduction to the various techniques used in fibre optic sensing and, more specifically, describes the techniques used in temperature sensing.

1.1 HISTORICAL DEVELOPMENTS OF OPTICAL FIBRE TECHNOLOGY

The development of optical fibres and optoelectronic components has stimulated considerable interest in fibre optic sensors. Such interest has been reflected by the growing number of international conferences on the subject and investments made by industry. There are a number of commercial devices available for measuring various physical parameters. Many market surveys have been conducted and predict a strong growth in this field. Table 1.1 shows a recently published market forecast (McGeehin) (1) for the

	WORLD	EUROPE
Industrial	50	22
Medical	42	22
Defence/Military/ Aerospace	291	42
1990 Total	383	86
(1986 Total	50	11)

Table 1.1 - Market Projections for Optical Sensors ($M), 1990.

World and Europe for 1990. Table 1.2, shows the European demand for optical sensor technology. Germany, France and the UK being the major users. It was predicted in the reference that the total European demand for 1986 would be $11M, reaching $96M by 1990. This is compared with the

West Germany	24% of total
United Kingdom	20%
France	20%
Italy	13%
Benelux	17%
Others	6%

(Figures for demand for fibre optic sensors).
Table 1.2 - Anticipated European Market, 1990.

Japanese market, shown in table 1.3. The table shows that 0.4% of the market (representing $10M) is taken up by optical fibre sensors, indicating that at present this share in the overall optoelectronics market is very small. Table 1.4 shows that growth in the optoelectronics field has been rapid and will continue to grow. The introduction of commercial devices from Japan in the optical sensor field indicates that this country's World market share ~25% (1986) will not diminish.

The forecasts indicate a considerable level of activity in the field of research and development of fibre optic sensors in Europe, the US and Japan. The growth in this technology is expected to be rapid given the large scale of research being made by the major industrial countries and it would be appropriate at this point to review the early stages of this technology and the general physical principles that have been exploited.

The development of the fibre optic sensors field has stemmed from the rapid growth in optical communications. Optical communications, in turn, developed from the early 1960s with the invention of the laser. This device provided a powerful coherent light source with low beam divergence and made free space optical communication a practical possibility. However, poor light transmission in the atmosphere tended to restrict these systems to short distance applications. This, nevertheless, instigated a tremendous research effort into a suitable form of lightwave carrier medium. The proposals for optical communications through dielectric waveguides or optical fibres fabricated from glass were made almost simultaneously in 1966 by Kao and Hockham (2) and Werts (3).

[redacted]

Table 1.3 - Japanese optical market (1985)

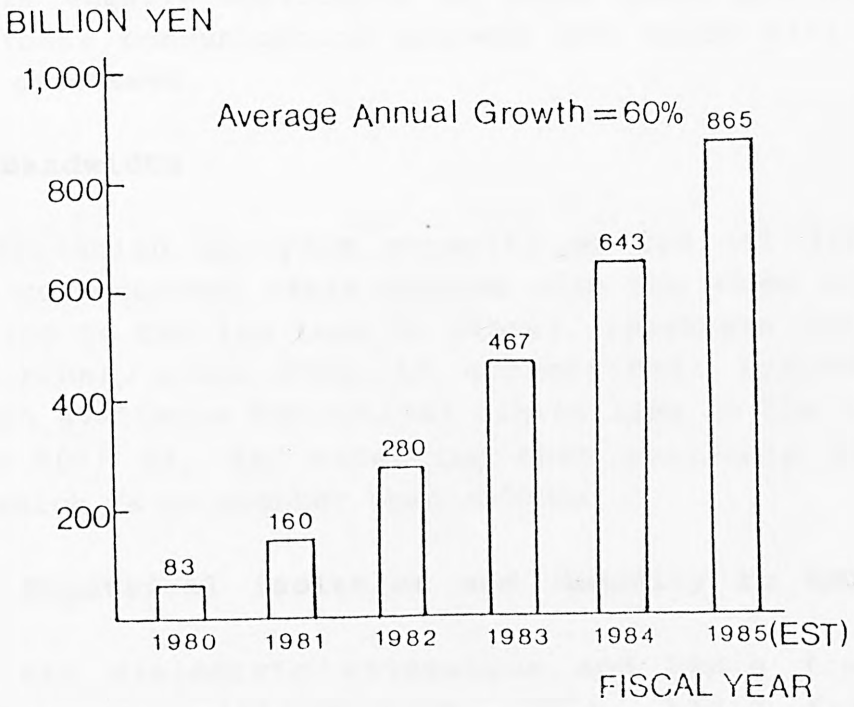

Table 1.4 - Annual production in Japanese optoelectronics industry

Early optical fibres exhibited very high attenuations, typically of the order of $1000dBkm^{-1}$, and loss at interconnections were also unsuitably high. Within the following ten years optical fibre losses were reduced to below $5dBkm^{-1}$ and suitable low loss jointing techniques were perfected.

Considerable efforts were also being directed to the improvement of optical components. Semiconductor optical sources (i.e injection lasers and light emitting diodes) and detectors such as photodiodes compatible in size with optical fibres were designed and fabricated to enable successful implementation of the optical fibre system. The earlier communication light sources emitted wavelengths in the region from 0.8μm to 0.9μm. More recently, this wavelength range has been extended to 1.1μm-1.6μm to utilize the lower attenuation which fibres exhibit at these wavelengths.

Optical means of communication offer a number of advantages which are equally applicable to fibre optic sensors, over conventional communication systems and these will now be briefly discussed.

1.1.1 Bandwidth

The information carrying capacity of optical fibre far exceeds conventional cable systems with the added advantage that owing to the low loss in fibres, repeaters are placed much further apart than in conventional systems. The bandwidth available for optical fibres lies in the range of 10^{13} to 10^{16} Hz, far exceeding that available for coax cables which is no greater than ~500MHz.

1.1.2 Electrical isolation and immunity to EMI

Fibres are dielectric waveguides and hence free from electromagnetic interference (EMI), radio frequency interference (RFI), or switching transients giving electromagnetic pulses (EMP). Hence, the operation of an optical fibre is unaffected by an electrically noisy environment and the fibre cable requires no shielding from EMI. Unlike metallic conductors, fibres do not exhibit

earth loop and interference problems.

Optical fibres are fabricated from glass or plastic polymer and both these materials offer good electrical insulation. These fibres are therefore useful in the electrical supply industry in requirements where this high insulation is paramount. Examples of applications in this industry is the monitoring of faults on lines which carry a few kiloamps at several hundred kilovolts and communications between generating and switching stations in high voltage environments.

1.1.3 Crosstalk

As the light is contained within the boundary of the core and cladding interface, crosstalk between closely held bundles of fibres is negligible. The light from a fibre does not radiate significantly and therefore a high degree of signal security is provided. Sophisticated 'tapping' techniques have to be used to acquire any information from the fibre compared to acquisition of the same information from an ordinary copper cable.

1.1.4 Low loss transmission

The advancement in the fabrication technology of optical fibres has led to the development of low attenuation fibres. Such features are a major advantage in optical communication. However, some of the loss mechanisms in the fibre such as Rayleigh scattering, can be used to detect temperature. Current improvements in fibres have led to attenuation levels being lowered to almost the theoretical limit and further progress is likely to be slow.

There are of course many other advantages such as low cost, small size and weight, flexibility, system reliability and ease of maintenance, which makes fibre optic communication and fibre optic sensing so attractive.

1.2 GENERAL REVIEW OF FIBRE OPTIC SENSOR TECHNIQUES

Optical sensors may be classified into two groups: 'point' or `extrinsic' sensors, in which the optical fibre acts merely as a transmission link and 'distributed' or 'intrinsic' sensors, in which the measurand modulates the light in the fibre itself. Information about a physical or chemical parameter being measured is reflected as modulation of light intensity, phase, polarization, wavelength and associated spectrum.

In this introduction it is only possible to choose a limited number of case studies as a very large number of devices have been reported over the past few years.

1.2.1 Intensity modulation

In all intensity based fibre optic sensors there is an ideal requirement that the detected light should only represent changes caused by the parameter of interest, be it temperature, pressure, strain etc. In practice, however, other effects besides those due to the measurable parameter vary the light signal. For instance, a fibre connector that is unmated and remated may cause a small but significant change in the coupled intensity level, which could be interpreted as a change in the measurand. A number of referencing schemes have been devised to eliminate or at least reduce these adverse effects.

A well established dual wavelength technique relies on using a second light source to provide a reference signal, chosen to lie in a portion of the spectrum where there is little or no sensitivity to the measurand. By taking the ratio of the signal sensitive to the measurand and that which is not, it is possible to derive an output sensitive to the measurand and independent of other optical power variations in the fibre link.

The technique is implemented using two light sources of different wavelength, which can be either time division multiplexed or frequency multiplexed to avoid cross-talk and to allow the use of a single detector. This referencing technique does, however, suffer from differential variations

in the two light sources which may drift with time and vary with temperature. To eliminate such errors, an additional reference signal path may be used with a second detector. However, this does not reduce the possibility of detector sensitivity drifts which may cause further errors, but normally, detector sensitivity variation is a secondary and less severe problem than light source and coupling variations. The addition of a second light source and detector plus fibre optic couplers, which may be two or four port, adds to the cost of this technique. There are many examples where dual wavelength referencing has been used. There are many intensity based sensors which cannot be suitably referenced and an excellent review is given by Medlock (4) which includes a number of examples of intensity modulated sensors with and without dual referencing. There are many forms that an intensity modulator can take and some are now briefly discussed.

1.2.1.1 Displacement sensors

A small linear or angular displacement provides one of the simplest intensity modulated sensors. As an example, a displacement sensor which can be referenced is described by Theocharous (5),(6) based on the optical wedge principle using neodymium doped silicate glass, figure 1.1. He has reported on both the use of absorption and fluorescence for this application. Jones and Spooncer have described a grating displacement sensor (7), which incorporates a shutter modulator consisting of superposed parallel holographic gratings. The reference wavelength passes through the shutter unaffected while the signal wavelength is modulated by the shutter. This displacement sensor, thus, also provides a means of measuring pressure.

The shutter type of mechanism to sense pressure or temperature has led to the development of a simple fibre optic switch manufactured by Delta Controls (UK). Although this sensor does not incorporate a means of referencing the source or connection losses, it has demonstrated that referencing is not essential in cases where the sensing of sudden parameter changes are more important than the absolute measurement.

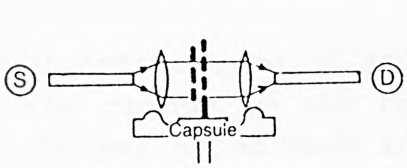

Grating.

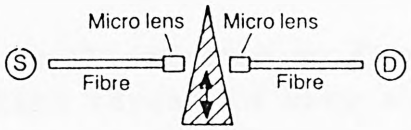

Optical wedge.

Figure 1.1 - Displacement sensors

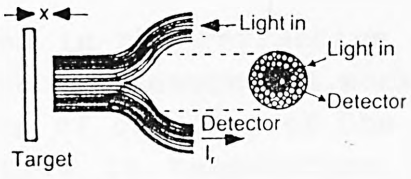

(a) Fibre bundle.

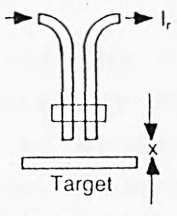

(b) Twin fibre.

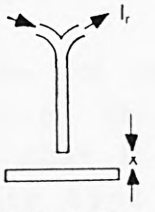

(c) Single fibre.

Figure 1.2 - Reflective sensors

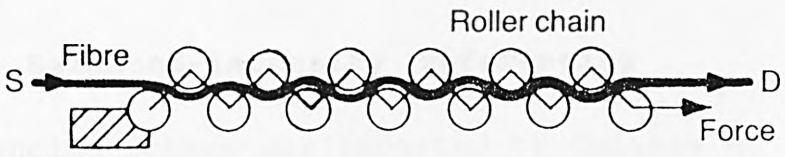

Microbend sensor.

Figure 1.3 - Microbend sensor

1.2.1.2 Reflective sensors

The reflective type of sensor, as illustrated in figure 1.2, uses the change in the reflecting target to vary the level of light reflected back into a single, or a bundle of fibres if greater sensitivity is required. Referencing of such devices is, however, difficult.

1.2.1.3 Fibre loss sensors

These type of intensity modulated sensors rely on the losses from the core or cladding of the fibre. A typical example is the microbend sensor shown in figure 1.3. The bending of the fibre results in losses of the higher order modes through the outer cladding and thus attenuation of the signal.

Changes in the refractive index of the fibre can act as a temperature sensor. In work reported by Kopera et al (8), a section of cladding of the fibre is altered such that it is sensitive to temperature changes. However, this type of sensor is difficult to fabricate and is shown in figure 1.4.

1.2.1.4 Absorption sensors

Intensity variations by colour absorption have been used for both physical and chemical parameter measurements. In work by Grattan et al (9) changes in an indicator dye (Phenol red) were used to monitor pH levels. The sensor uses the absorption of light emitted from a green LED and a second wavelength reference signal generated from crystalline ruby.

1.2.1.5 Balanced-intensity referencing

This referencing scheme was reported by Culshaw et al (10) and is also known as balanced-bridge intensity referencing. It uses two separate fibre paths for the modulated and reference signals. A diagram of this approach is given in figure 1.5. It is necessary to use two transmitters and two receiving channels. Preferably the transmitting wavelengths should be identical so that the detector and fibre variations can be matched. It is necessary for the two transmitted optical signals to be passed through both channels. The value of the detected signals at each receiver

(a)

(b)

Figure 1.4 - Transmission Loss Sensor
(a) Shows a section of fibre with modified cladding,
(b) Shows the refractive index profiles of the normal and the modified cladding.

INTENSITY MODULATOR

Figure 1.5 - Balanced-intensity referencing:
α, β, γ, δ are the fibre attenuations;
R_1, R_2 are reference arms;
M_1, M_2 are the intensity-modulating arms.

are given below and by taking the appropriate ratios, it is possible to eliminate variations due to differential changes in the two light sources, fibre attenuation, sensitivity drifts in the two detectors and also offset voltages and bias current effects in the amplifier circuitry.

Detector signals:

$$D_1 = (\alpha A R_1 + \beta B M_2)$$

$$D_2 = (\alpha A R_2 + \beta B M_1)$$

if $P = \alpha A R_1 \gamma$, $Q = \beta B M_2 \gamma$, $R = \alpha A R_2 \delta$ and $S = \beta B M_1 \delta$ then

$$\frac{PS}{RQ} = \frac{M_1 R_1}{M_2 R_2}$$

Where A and B represent outputs from sources A and B, R_1 and R_2 the reference arm variations, and M_1 and M_2 the changes imposed by the measurand.

Results show that for an imbalance in one of the fibre arms of 20dB there is no more than a 1% change in the final output (Giles et al (11)). The construction of this sensor is complicated (mode selective effects or coupling drifts can be significant) and the system does require four fibres.

1.2.2 Wavelength modulation

There have been a number of devices relying on wavelength modulation and some have been developed for the commercial market. The wavelength modulation scheme offers the major advantage that it is inherently less susceptible to instability of some system components which might cause attenuation in the fibres or connectors; in addition, this method does not require intensity referencing. The demodulation process is, however, more complex than simple intensity modulated devices and requires optical filtering of the various wavelength bands.

1.2.2.1 Optical pyrometer

The optical pyrometer developed by Accufibre Corporation (12), involves the measurement of radiance from a small

black-body cavity, sputtered on the end of a thin (0.25-1.25mm) sapphire fibre, to measure temperature. The diagram of the device is shown in figure 1.6. The broad band radiance from the cavity is transmitted through the fibre and two narrow bands of this radiance are examined. The device is commercially available and the manufacturers claim remarkable performance figures: the temperature range extends from 500 to 2000°C with a resolution of 7.5 x 10^{-6}°C and accuracy of 0.0025%.

1.2.2.2 Photoluminescent and fluorescent temperature sensors

These two modulation techniques have been employed in commercial sensors from ASEA and Luxtron, and shall be discussed in more detail in section 1.4.

1.2.2.3 Displacement measurement

This type of sensor relies on the displacement of a prism, a diffraction grating or simply the displacement of the receiving fibre to modulate the wavelength of the light received. Some typical arrangements are shown in figure 1.7.

1.2.2.4 Thermochromic technique

There are a number of materials, liquids, gaseous and solid, which exhibit a colour change under specific physical conditions. For example, thermochromic substances such as Cobalt Chloride in an isopropyl alcohol/water solution shows a marked colour change between 25°C and 75°C and this can be spectrographically measured and interpreted by a two wavelength detector system, as shown in figure 1.8.

1.2.3 Interferometric techniques

There are a number of forms of interferometers and they were applied to sensor systems before the fibre optic era. However, they are particularly suitable for fabrication and by changing the measurand to an equivalent optical displacement, this device can be used for sensing. There are four main types commonly used and these are the Fabry-Perot, Mach-Zehnder, Michelson and Sagnac interferometers,

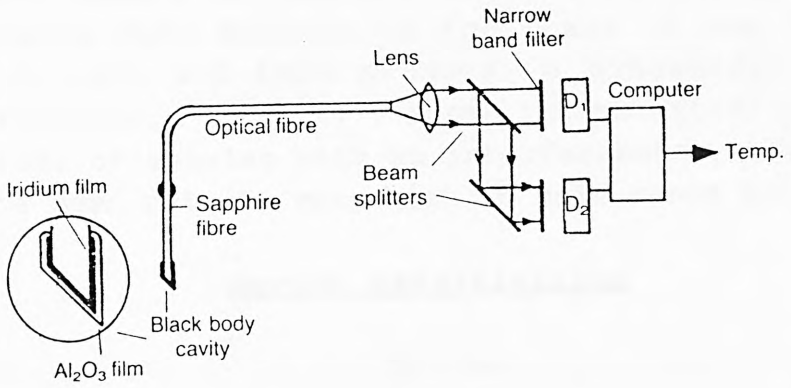

Figure 1.6 - 'Accufibre' optical radiation pyrometer

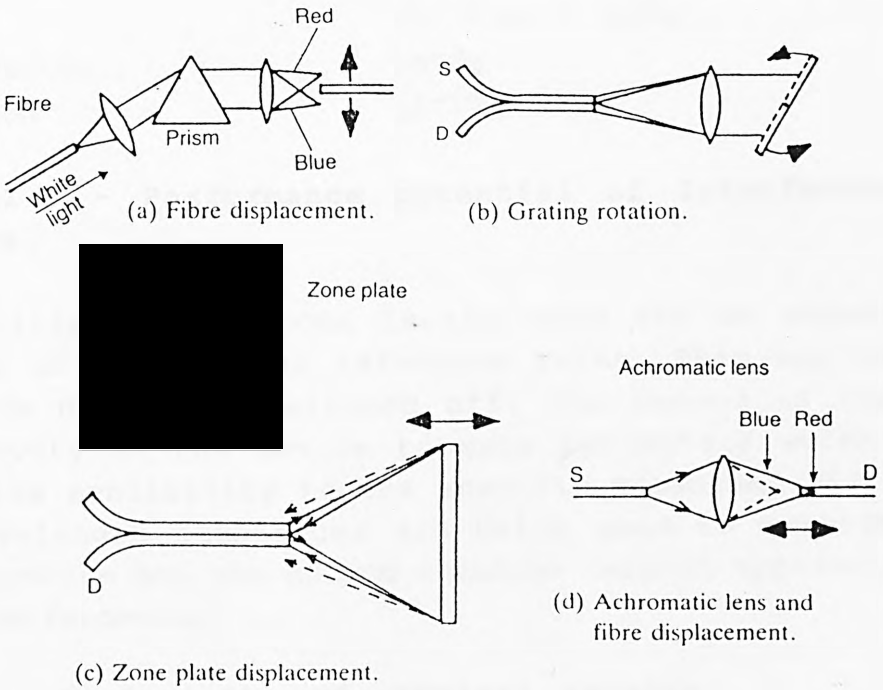

Figure 1.7 - Wavelength displacement sensors

as shown in figure 1.9. The parameter to be measured alters the fibre length or transit time. This alters the phase relationship with respect to the phase of the light in a reference path and this produces a sinusoidal amplitude output function. Table 1.5, shows the potential performance limitations of sensing with an interferometer-based device - as can be seen this is very high in some cases but two major

Device Sensitivities

Acoustic	30 Pa
Pressure	0.15 torr
Rotation	$< 10^{-2}$ deg. hr^{-1}
Magnetic	10^{-7}T (Faraday)
Field	10^{-11}T (magnetostriction)
Temperature	10^{-6}K
Strain	<1 strain
Flow	1 ms^{-1} (Vortex shedding)
	10^{-6} ms^{-1} (LDV)
Acceleration	10^{-9}g
Vibration	10^{-10}m

Table 1.5 - Performance potential of Interferometric sensors.

difficulties remain. One is the need for an unambiguous measure of the initial reference point. This may be lost when the device is switched off. The second is the high sensitivity of the device to many parameters which makes selective sensitivity to the specific measurand difficult. Two wavelength techniques are being used to overcome the first problem but the second requires careful application of the interferometer.

1.2.4 Biological and chemical sensing

This is a field which has developed from initial work to measure pH (13). The medical market was the first to exploit optical fibres commercially for imaging in endoscopy and is currently expanding into other fields. For example, systems for the measurement of oxygen saturation (proportion of blood haemoglobin taking up oxygen) have been in use for

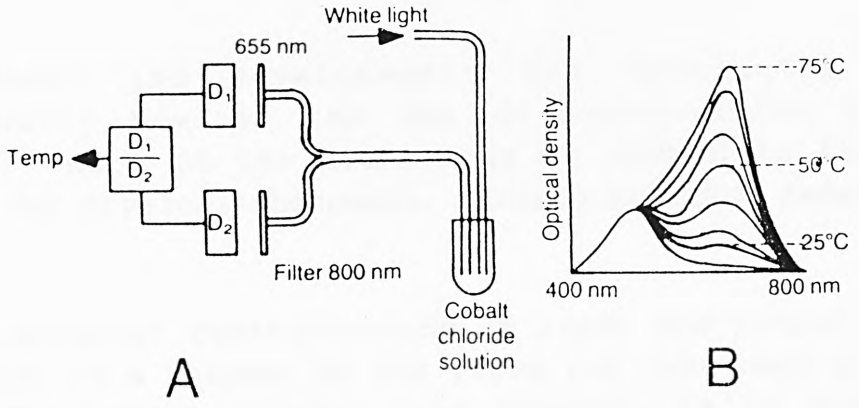

Figure 1.8 - Temperature sensor using colour change
(a) Optoelectronic configuration
(b) Optical density as a function wavelength of sensor material

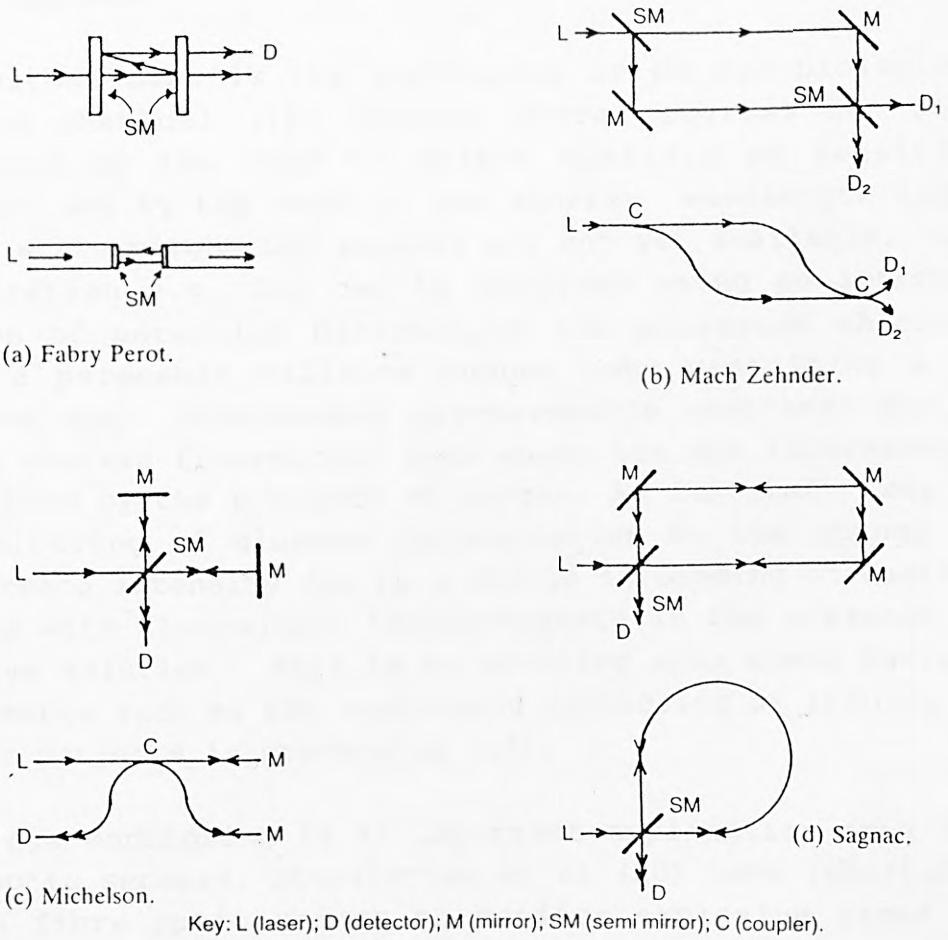

Figure 1.9 - Interferometers with their fibre equivalents

many years and developments are continuing (14), particularly towards the use of non-invasive systems (15,16). Much of the technology is common to that for sensors for physical phenomena, thereby reducing development costs.

Various physical configurations of input and output fibres to connect to a reagent at the fibre tip have been proposed (17). The important part, the reagent, is in general a chemical or combination of chemicals fixed to a surface or contained within some selectively permeable envelope so that the reagent is trapped and not allowed to flow into the system to be measured, particularly if the 'system' is human or biological. The use of dialysis membranes, with the reagent immobilized on relatively large particles within the membrane envelope gives a very flexible sensor format allowing a range of specifications and relatively complex reagent systems.

An important area is the monitoring of pH for biological (13) and chemical (18) systems where progress has been restrained by the need to select specific pH sensitive absorbers and by the need to use shorter wavelength light sources where bright LED sources are not yet available. Gas concentration e.g. CO_2 can be measured using an internal solution of potassium bicarbonate and potassium chloride within a permeable silicone rubber tube containing a pH sensitive dye. Hydrophobic gas-permeable membranes may be used to contain fluorescent dyes where the dye fluorescence is quenched by the presence of oxygen. An important area is the monitoring of glucose concentration by the change in fluorescence intensity due to a change in binding of dextron labelled with fluorescein isothiocyanate in the presence of a glucose solution. This is an exciting area where further developments such as the continuous monitoring of insulin in diabetic patients is proceeding (19).

Remote gas monitoring is an important application area for fibre optic sensors. Stueflotten et al (20) have reported a methane fibre optic sensor to monitor explosive gases on offshore installations. The sensor employs a differential absorption technique near the 1666nm wavelength, a point

where losses in silica fibre are extremely low. Such sensors are of great potential value as the transmitted optical power levels to the sensor head are extremely small and would not cause dangerous local heating effects.

1.2.5 Resonant sensors

One of the important characteristics of recent optical sensor technology has been the departure from "intensity-based" sensing towards a greater reliance upon those where the output and thus the measurand is determined as a frequency variation. Of the many possible materials for such sensor systems, quartz and silicon are particularly outstanding and may readily be coupled to optical systems. Quartz is a stable, inert material which has been well studied as a frequency standard. It is optically polished readily, is inexpensive and very compatible with fused silica (synthetic quartz) fibres. Also being piezoelectric, hybrid optoelectronic devices may be produced. Silicon has the advantage of being open to micromachining, such as is used in the electronics industry and thus very small devices interfaced to fibres may be fabricated. It may be driven into resonance directly by optical means and in both cases, the typical kHz resonant frequencies of the devices which may be constructed are relatively easily measured by conventional electronic means at a remote location.

Early work on such systems included the sensing of the change in the vibration frequency of an optically driven wire as a function of force (21). Further work on the use of quartz has included the development of a force sensor by McGlade et al (22). They used an optically driven, both photovoltaically and photothermally, miniature double-tuning fork structure to sense the force (stress) induced vibration frequency change. Recent work by Grattan et al (23) has enabled such systems to be low-power (~1mW) due to the sensing of the vibration frequency by means of evanescent-wave coupling, taking advantage of the good optical properties of the quartz and the ability to interface directly to a fibre. Ventakesh et al (24) have extensively discussed the properties of miniature (<1mm) Si structures for sensor systems and they look attractive due to the sensitivity of such resonant devices to, for example,

pressure and a comparative insensitivity to temperature. The material can be metal coated to enhance the reflectivity of such a device (to sense its vibration characteristics) or coated with an absorber to enable power to be coupled into the material. As such structures can be of the physical dimensions of the fibres themselves, applications include industrial and biomedical sensing of, for example, pressure and displacement. However Si resonators are inherently low 'Q' devices (c.f. quartz Q>1000, Si Q~several hundred) and this may lead to problems in accurate monitoring.

The fabrication techniques of Silicon are well established and thus, these sensors have the potential of low cost.

1.2.6 Distributed sensors

In addition to the more familiar advantages of optical fibre sensor systems, it should be remembered that optical fibres have the advantage of providing what is essentially a one-dimensional measurement medium, allowing parameter line integrations to obtain high sensitivities (e.g. the Sagnac interferometer based gyroscope and the loop-integration in a fibre of the measurement of electric current). Line differentiation enables the simultaneous understanding of spatial and temporal information about the parameter influencing the optical fibre. As examples, the strain in large engineering structures or the temperature distributions in major plant or equipment may be sensed. Magnetic or electric field variations can similarly be tracked and thus a comprehensive picture of the system under consideration may be built up. Almost uniquely, in the fully distributed system, this information can be obtained without the light leaving the fibre, and a fibre installed for other purposes e.g. data-communications, may be employed for such sensing applications if required. A comprehensive review of this is presented in a recent paper by Rogers (25).

Two such distributed systems may be identified, a quasi-distributed sensor system which consists of a series-distributed array of discrete transducers (26). If a narrow pulse of light is launched, the subsequent measurement of

the differential delay for light returning from various elements can be used to identify the optical interaction and thus the measurand at each element. The spatial resolution of such a system is pre-determined by the size and separation of the element and the number of such elements included in its initial design. This contrasts with the fully distributed system where the spatial resolution is determined by the pulse width and the response time of the detector. This latter system is more flexible and capable of yielding more information. Also an interaction point need not be specified in advance e.g. in security systems and so information can be obtained even when the anticipated likelihood of interrogation of that element is small. In the sensing of temperature, a quasi-distributed and fully distributed sensor devices will be discussed in more detail in section 1.4.3.

1.3 AN INTRODUCTION TO TEMPERATURE MEASUREMENT

Temperature is one of the most important parameters to be measured in an industrial or laboratory environment. A range of instruments, to measure this parameter, are available with a wide range of configurations suitable for a variety of applications; from the simple liquid-in-glass thermometers to the sophisticated Raman effect fibre optic thermometer. It is important to have some understanding of the concepts of temperature measurement, temperature scales and temperature calibration techniques upon which all subsequent calibrations lie.

1.3.1 DEFINITIONS OF TEMPERATURE MEASUREMENT

To understand temperature measurement it is essential to have an appreciation of temperature and heat-related phenomena. It is essential to differentiate between heat and temperature.

1.3.1.1 Temperature

The effect of temperature is on the state of agitation, both oscillation and rotation of molecules in a medium. The higher the temperature of a body, the greater the vibrational energy of its molecules and the greater its potential to transfer this molecular kinetic energy to another body. Temperature is the potential to cause heat to move from a point of higher temperature to one of lower temperature. The rate of heat transfer is a function of that temperature difference.

1.3.1.2 Heat

Heat is basically thermal energy. The quantity of heat in a body is proportional to the temperature of that body i.e., it is the body's heat capacity multiplied by its absolute temperature. Heat is energy and as such is measured in units of energy i.e Joules.

1.3.1.3 Thermal expansion

A solid expands when it is heated and the coefficient of expansion varies from substance to substance. The coefficient of linear expansion of a solid is defined as the increase in length per unit length when the temperature is raised by 1K. Thermal expansion is an important parameter which has to be considered in the design of the optical temperature probes, which will be discussed in this work.

Different materials absorb different amounts of heat to produce the same temperature rise. The specific heat capacity of a substance is the amount of heat which, when absorbed by 1kg of that substance, will raise its temperature by one Kelvin. This parameter affects the speed of response of a material to a sudden change of temperature.

The rate at which heat is conducted through a body depends

upon the material of which the body is composed. The heat conductivity of copper, for example, is much greater than for a piece of plastic. This difference will affect the speed of response of the material to a sudden change in temperature. Thermal conductivity is measured in terms of:

Thermal conductivity = (heat energy x length) / (area x time x temperature difference)

$= J.m^{-1} .s^{-1}.K^{-1}$

1.3.1.4 Radiation

Thermal radiation is the direct transfer of heat across space. Thermal radiation is electromagnetic radiation and lies within the infrared, visible and ultraviolet regions of the electromagnetic spectrum. It travels essentially in straight lines, may be reflected or refracted and the amount of radiant energy falling on a unit area of a detector is inversely proportional to the square of the distance between the detector and the radiating source. This type of thermal heat transfer has very little effect on the calibration process of the optical probes used in these experiments.

1.3.2 TEMPERATURE SCALES

The temperature scales used in instrumentation and metrology are defined in terms of the physical phenomena which occur at constant temperatures. The temperatures of these phenomena are known as 'fixed points'.

1.3.2.1 Celsius temperature scale

The Celsius scale is defined by international agreement in terms of two fixed points, the ice point and the steam point of water. The temperature of the ice point is defined as zero degrees Celsius and the steam point as one hundred degrees Celsius at a pressure of 1.0132×10^5 $N.m^{-2}$.

1.3.2.2 Kelvin and the thermodynamic scale

The theoretical definition of the Kelvin is based on the efficiency of a perfectly reversible heat engine working between two temperatures and which, therefore, does not depend on the properties of a particular substance. The Kelvin scale is divided into 100 units between the ice and steam points, and thus one Kelvin represents the same temperature intervals as one Celsius degree. The definition of the Kelvin is the fraction 1/273.16 of the thermodynamic temperature of the triple point of water (this is the temperature at which water exists in the solid, liquid and gaseous phases in equilibrium).

The thermodynamic temperature scale is based on the gas law PV=nRT, where T is the temperature on the absolute, P is the pressure of the gas, n the molar density, V is the volume occupied and R is the universal gas constant equal to 8.314510 J. $mol.^{-1}$ $.K^{-1}$. Thus, the behaviour of an ideal gas forms the basis of a temperature measurement on the absolute scale. Unfortunately an ideal gas does not exist so gases such as hydrogen, nitrogen, oxygen and helium which obey the law very closely are used. Nitrogen has been found to be most suitable for temperature measurements between 500°C and 1500°C, while at temperatures below 500°C hydrogen is used. For very low temperatures, helium at low pressure is used.

1.3.2.3 International Practical Temperature Scale

The International Practical Scale is based on a number of defined fixed points each of which has been subject to reliable gas thermometer or radiation thermometer observations and these are linked by interpolation using instruments which have the highest degree of reproducibility. In this way the International Practical

Temperature Scale is conveniently and accurately reproducible and provides means for identifying any temperature within much narrower limits than is possible on the thermodynamic scale.

1.3.3 MEASUREMENT TECHNIQUES

There are a wide range of temperature measuring instruments. A list of the temperature range and techniques used are povided in table 1.6. A detailed explanation of these instruments can be found in reference (27).

Range (K)	Technique	Resolution (K)
0.01-1.5	Magnetic susceptance of paramagnetic salt	0.001
0.1-50	Velocity of sound in acoustic cavity	0.0001
0.2-2	Vapour pressure	0.001
1.5-100	Germanium resistance thermometer	0.0001
1.5-100	Carbon resistance thermometer	0.001
1.5-1400	Gas thermometer	0.002
210-430	Silicon P-N junction	0.1
4-500	Thermistor	0.001
11-550	Quartz crystal oscillator	0.001
15-1000	Platinum resistance thermometer	0.00001
20-2700	Thermocouple	1.0
30-3000	Sound velocity in metal rod	1%
130-950	Liquid-in-glass	0.1
130-700	Bimetal	1-2
270-5000	Total radiation thermometer	10
270-5000	Spectrally selective radiation thermometer	2

Table 1.6 - Temperature measurement techniques (27)

1.3.4 TEMPERATURE CALIBRATION TECHNIQUES

In this work on the development of temperature measuring devices, it is necessary to relate the output of the device to a known temperature scale, to enable the user to read the

device in a familiar way.
Thermometer calibration can be carried out by either of two principle techniques (28), i.e using temperature 'fixed points' or by comparison with reference 'standard' thermometers. The former technique is amenable in situations where the temperature dependent characteristics of the device is known and it requires only a few data points. The latter technique involves the realization of a series of temperatures in baths or enclosures and measurement of the thermometric parameter at the temperatures measured by reference thermometers. The comparison is considered to be suitable (28) for all types of thermometers except when the very highest accuracy is sought.

Calibration is a measurement procedure which compares against the 'true' value of the parameter. In the case of temperature, this 'true' value is a value traceable to the international Practical Temperature Scale (IPTS-68). The National Physical Laboratory (NPL) in the UK is responsible for realizing the Scale and disseminating it to users in industry. Under most circumstances a secondary standard traceable to the IPTS is a satisfactory means to calibrate an instrument. A thermocouple is a secondary standard instrument and is a convenient and adequately accurate means of calibrating other instruments, such as those produced during the course of this work. The important feature of secondary standard instruments, whose calibration has to be monitored from time to time, is their departure from the 'true' value. For greater calibration safety, a second similar instrument should be used to monitor the same temperature. This provides a means to check the first instrument and ensures against any errors due to ageing effects. It is also important to be aware that the standards may change together because they are receiving the same treatment.

The environment within which the temperature measurement is

being made should be of uniform temperature through out its enclosure. This, in practice, is achieved by using liquid-baths which are vigorously stirred so that hot and cold spots cannot develop. The type of liquid used to achieve this depends on the temperature of interest. In the range -150°C to 0°C Iso-pentane is normally used. This liquid is cooled by liquid nitrogen. A double walled vessel is normally used with space between the walls which is evacuated when the desired temperature is reached. This arrests rapid cooling which can then be controlled by a bare-wire heater. For a range between 1°C to 100°C water baths are used and beyond this temperature, up to 300°C, a range of oils are used. Oil cannot be used above 300°C, and above this temperature it is necessary to change the medium to a mixture of molten salts. A mixture of approximately equal parts of potassium nitrate and sodium nitrite is used over the range 160°C to 630°C. However, beyond 600°C furnaces or ovens normally give the required temperatures but they may also be used continuously from ambient temperatures. Heat transfer within the oven is predominantly by convection rather than by radiation and the occurance of temperature gradients within the oven is a potential problem. If the oven is large in comparison to the measuring instrument, the flow of air will vary the heat at any particular point inside the oven. To calibrate an instrument inside an oven requires that the calibrating instrument and the instrument under calibration be placed in close contact to one another. The thermocouple is particularly useful since it can be attached physically to the instrument under calibration. The thermocouple is thus heated via conduction of heat from the instrument under calibration, rather than via convected heat which can vary dramatically within the oven. It is important to keep the thermocouple clean as it can be oxidized by the base metals of the oven.

1.3.4.1 Fixed point method of calibration

As mentioned, an alternative or supplementary method of calibrating temperature measuring instruments is by the use of fixed points, that is using the freezing, boiling and triple points of pure substances. The triple point is the temperature of equilibrium between the three phases of pure ice, water and water vapour in the absence of air, as shown figure 1.10.

The IPTS-68 is based on a number of defining fixed points, each of which has been subject to reliable gas thermometer or radiation thermometer observations and these are linked, as mentioned, by interpolation using instruments which have the highest degree of reproducibility. The equilibrium states which define the fixed points are given in table 1.7. Temperatures between and above the fixed points given in this table, can be interpolated if the 'equation of state' of the instrument is accurately known. For example, as

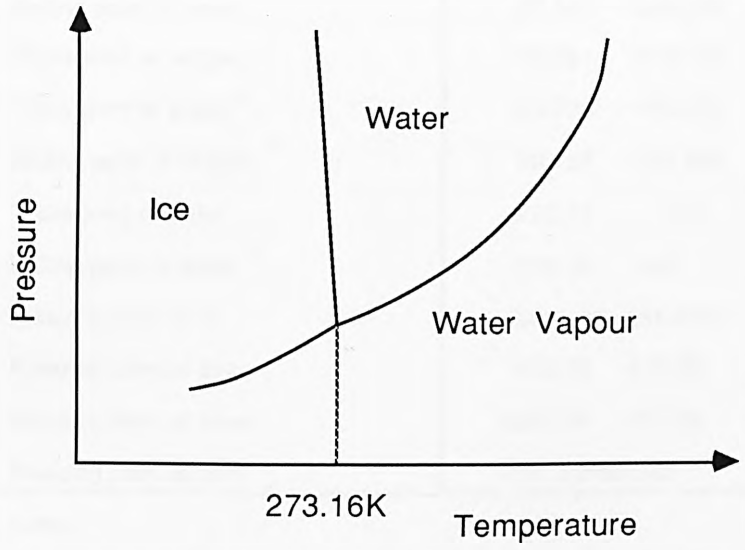

Figure 1.10 - The triple-point in the pressure-temperature phase diagram (29).

already mentioned, the equation of state in an ideal gas thermometer is PV=nRT. The variables of state are the pressure, P, the molar density (i.e the ratio of the number

of moles of gas, n, to the volume, V) and the temperature T. The molar gas constant, R (equal to 8.31451 $J.mol.^{-1}.K^{-1}$), is fixed by reference to the definitions of the SI units involved. In practice there are considerable difficulties associated with pressure measurement, departure of the gas from ideality, dead-space corrections, etc. Other physical laws which have been used in primary thermometry include the Nyquist equation for electrical noise in a resistor, and the laws of cavity. Of these, Planck's Law is the basis of spectral radiation pyrometry which has been a powerful technique for measuring temperatures above 700K.

Equilibrium state	Assigned temperature	
	T/K	$t/^{o}C$
Triple point of equilibrium hydrogen	13.81	-259.34
Boiling point of equilibrium hydrogen at a pressure of 330.6 Pa	17.042	-256.108
Boiling point of equilibrium hydrogen	20.28	-252.87
Boiling point of neon	27.102	-246.048
Triple point of oxygen	54.361	-218.789
Triple point of argon[a]	83.798	-189.352
Boiling point of oxygen[a]	90.188	-182.962
Triple point of water	273.16	0.01
Boiling point of water[b]	373.15	100
Freezing point of tin[b]	505.118	231.9681
Freezing point of zinc	692.73	419.58
Freezing point of silver	1235.08	419.58
Freezing point of gold	1337.58	1064.43

Notes

unless otherwise stated.

Superscripts a and b denote fixed points which are alternatives.

Table 1.7 - The defining fixed points of the IPTS-68 (29).

1.4 GENERAL REVIEW OF FIBRE OPTIC TEMPERATURE SENSORS

1.4.1 Early work and the development of multimode fibre sensors

Early work in the development of optical fibre temperature sensors concentrated upon the conversion to a fibre optic system of techniques which otherwise were known in classical optics. For example, in the work of Dakin et al (30) and Campbell (31) infra-red pyrometry was first extended using fibre optics to transmit the emitted radiation. Inaccuracies can arise from unknown factors such as emissivity and the state of the surface itself. In the work of Dakin et al attempts were made to correct for this and although in the report of Campbell it was claimed that measures could be made from 100°C-1500°C, the technique has been more effective in a high temperature device described later. Detailed specifications and quoted accuracies and resolutions for early work are not reported as a recent paper by Harmer (32) has shown that even commercial devices, under rigorous testing do not meet the optimistic performance figures originally quoted for many of them.

Temperature is a measurand which can readily be converted to a displacement through the well-known phenomena of expansion of materials when heated. As a result a number of devices based on this principle were proposed. In order to be effective, a reference to the actual light input to the sensor head itself is required. For example the early (1967) Fotonic (33) displacement sensor used light reflection where light emitted as a cone from the end of one fibre is reflected from a flat target so that some of the light is incident on a return fibre adjacent to the incident fibre. Although initially demonstrated as a pressure sensor, the technique is equally applicable to temperature measurement. A highly non-linear characteristic emerges. Bergstrom et al (34) proposed a reflective arrangement which would provide measurand and reference reflected signals. The use of submicron displacement for temperature measurement has been proposed by Croft et al (35) through the change in evanescent wave coupling from a critically cut

optical fibre to a second optical element.

Temperature may be measured over a more limited range for example, for biological applications, a 35°-45°C range is useful using scattering by liquid crystals. Problems of accuracy and stability however using liquid crystals were reported in early work (36) which still have to be overcome. The use of thermochromic materials has been explored (37), and developed in a device recently described by Brenci et al (38). These substances, such as cobalt chloride solution in water/alcohol, have created interest due to their properties of colour change with temperature. The particular substance mentioned shows a significant colour change between 25°C and 75°C, as illustrated by figure 1.8. A temperature measuring scheme using this material irradiated with white light has been developed, and again intensity referencing was provided by a two wavelength scheme. The utility of such a system is limited by the hazard of the spillage of the solution used from fracture of the sensor head. Thus its application in biological or biomedical research is severely restricted.

To measure temperatures above room temperature the use of the fact that the refractive index is a sensitive function of temperature in particular materials may be exploited. An early device was developed for 'hot-spot' monitoring (39) (e.g. in electrical transformers) using the differing temperature coefficients of the refractive indices of the fibre core and cladding, which as a result have an effect on the guiding properties of the fibre. Using a liquid-in-core fibre where the liquid refractive index decreases rapidly with temperature, a sensor may be constructed (40) but few suitable liquids are available and liquid-core fibres are not popular for commercial use due to possible spillage and toxicity problems. A recent commercial development is the Pilkington cryogenic liquid leak detector, as shown in figure 1.11, which senses the presence of a cold liquid on the fibre through the fact that at temperatures $\leq 25^{\circ}C$, the cladding of plastic clad silica fibre increases its refractive index to the point where normal guiding of light is interrupted and the presence of the cold liquid is detected (41). By using a liquid of high change of

Figure 1.11 - Cryogenic leak detector.

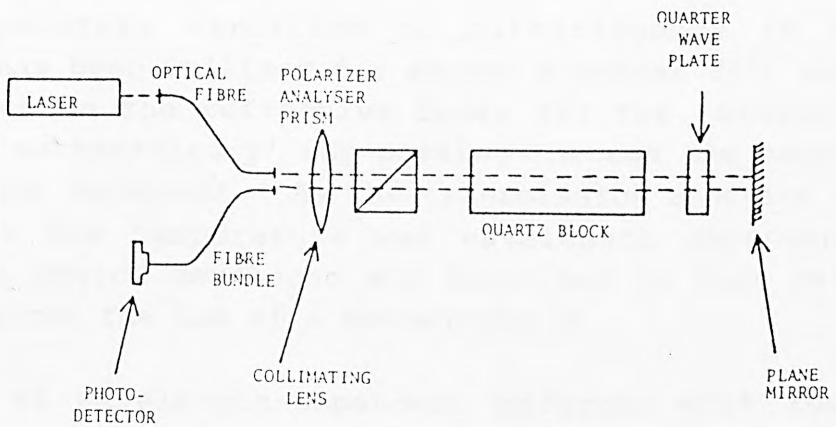

Figure 1.12 - Quartz crystal temperature sensor

refractive index with temperature, into which two fibres with cladding removed are placed, coupling of light from one fibre to another will be a function of temperature and so a sensor scheme is possible (42).

The use of birefringent materials, such as quartz, has been demonstrated for temperature sensing by Rogers (43) as illustrated in figure 1.12. Also, filters which may be birefringent, semiconductor or interference type may be utilized for such a sensor in view of their temperature dependence of transmission. This is, in fact, an irritation in the development of some types of processing optics in optical fibre temperature sensor control systems (e.g. ASEA type 1010 Sensor). This is one reason for the requirement for temperature stabilization of the optical processing and control box. Christiansen (44) has described a sensor using a filter which becomes transmitting at a particular temperature due to refractive index matching conditions within the filter being met. Hence, the temperature is determined by the wavelength of light from a broadband source which is transmitted by it.

The temperature variation of birefringence in lithium niobate has been utilized for sensor purposes (45) where the difference in the refractive index for the 'ordinary' ray and the 'extraordinary' ray passing through the material is temperature dependent. As the transmission function used to determine the temperature was wavelength dependent, the practical device developed and described in this reference (45) required the use of a monochromator.

The use of wavelength-dependent effects, with resulting colour changes, has been attractive for temperature sensing as referencing to the absolute input light intensity is not required, the information being encoded in the wavelength of the light emergent from the sensor. For example, band edge shifts in semiconductors (e.g.GaAs) or doped glasses (which contain semiconductors) have been exploited in sensors since 1979 (46) and early problems with LED wavelength drift may be overcome through the use of high power, infra red LEDs operated well below their maximum power or inexpensive laser diodes.

There have been many proposals for systems which incorporate a referencing technique and an example is described in the work of Kyuma et al (47) using an optical absorption technique where the transmission characteristics of the material change with its temperature. In this work the temperature dependent shift in the absorption edge of a small sample of GaAs is sensed using two widely separated wavelengths (0.88μm and 1.3μm). The shorter wavelength is attenuated by the change in absorption of the semiconductor with temperature while the longer wavelength is transmitted through the sample, unaffected by the temperature. However, errors may arise when two such widely separated wavelengths are passed through long lengths of fibre or through optical couplings and connectors. Schoener et al (48) have reported a similar scheme but the wavelengths were much closer together and Theocharous (49) has developed a system to utilize the change in absorption of a "ruby glass" probed in the visible region of the spectrum by light from a dye laser at 605nm and 622nm. Although these later two schemes use wavelengths of close proximity to minimise differential transmission errors, the maximum range of the device is limited due to the absorption edge affecting the longer wavelength transmission and restricting the wavelength range over which referencing is available.

There are a number of commercial systems available, the Luxtron type 1000/2000 system (50) shown in figure 1.13 and the ASEA type 1010 sensor (51) shown in figure 1.14, which provides referencing against variations of the transmitted light. Both these systems use multimode fibres to transmit the light to the "point" optical sensor.

In the Luxtron arrangement the sensing element is a rare earth phosphor sample. Light from a UV lamp source addresses this material and as a result longer wavelength light is emitted due to the fluorescent properties of the sample. The changing ratio of the emission at two wavelengths is monitored to give a measure of temperature. As this temperature is measured in terms of a ratio, referencing is automatically provided. A second commercial system, the ASEA type 1010 sensor again uses a material with fluorescent properties as the temperature sensing element,

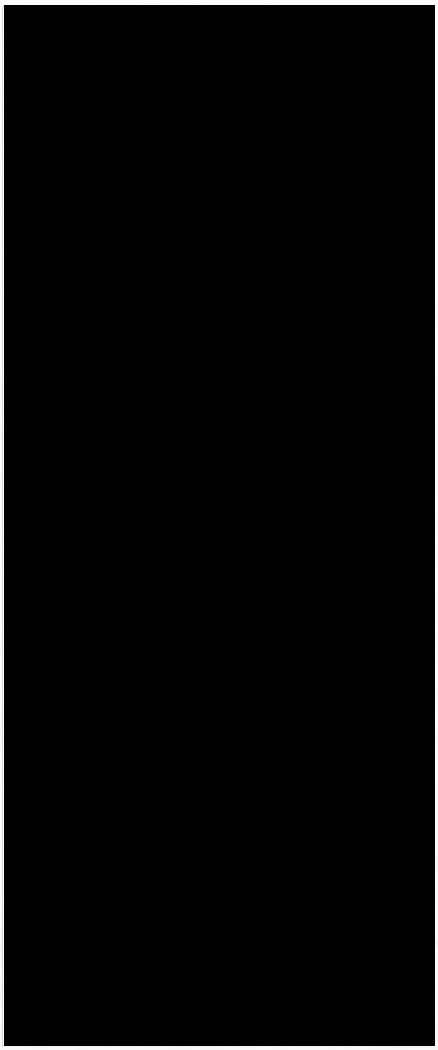

Figure 1.13 - Optical arrangement of Luxtron type 1000 temperature sensor.

namely GaAs. In the ASEA system the GaAs sample is irradiated by directly modulating light from an LED and the temperature dependent quantity is again measured as the wavelength shift of the fluorescence.

It is interesting to note the conclusions made in the independent assessment of a number of commercial optical fibre sensors by Harmer (32). These conclusions are that some of these sensors perform less well in practice than the manufacturers would suggest. This is due to interference from various losses, indicating that although there has been rapid development in this field there is still great scope for improvements in performance or innovations.

Another group of sensors, addressed by multimode fibre optics, depends on the fluorescence decay-time response of the sample to a "chopped" light pulse to measure the temperature. The major advantage of this technique, monitoring the change of "decay-time" as a measure of temperature is that it obviates the need to make an accurate record of the input light intensity as it simply depends on measuring the time between two reference points on the fluorescence decay profile of intensity as a function of time, as shown in figure 1.15.

Refering to that figure, the intensity of the radiation emitted, I(t) at a time t after the termination of the exciting pulse is given by $I(t) = I_o e^{-t/\tau}$ where τ is the temperature dependent decay-time. The time characterizing the temperature dependent decay is measured as the time interval between the intensity I_o and a constant fraction of I_o. I_o is the intensity at any reference time t_o as shown in figure 1.15.

The fluorescent decay-time of phosphors such as ZnCdS and ZnSe excited with a UV lamp was discussed by James et al (52) in 1979 and described <u>in principle</u> in the work of Sholes and Small (53), who illustrated a biological range bulk optical sensor (35°C-40°C range) using fluorescence decay in ruby. McCormack (54) produced a fibre optic sensor based on the decay-time change in $BaClF:Sm^{2+}$, which operated up to ~150°C (due to fibre limitations),using a mechanically

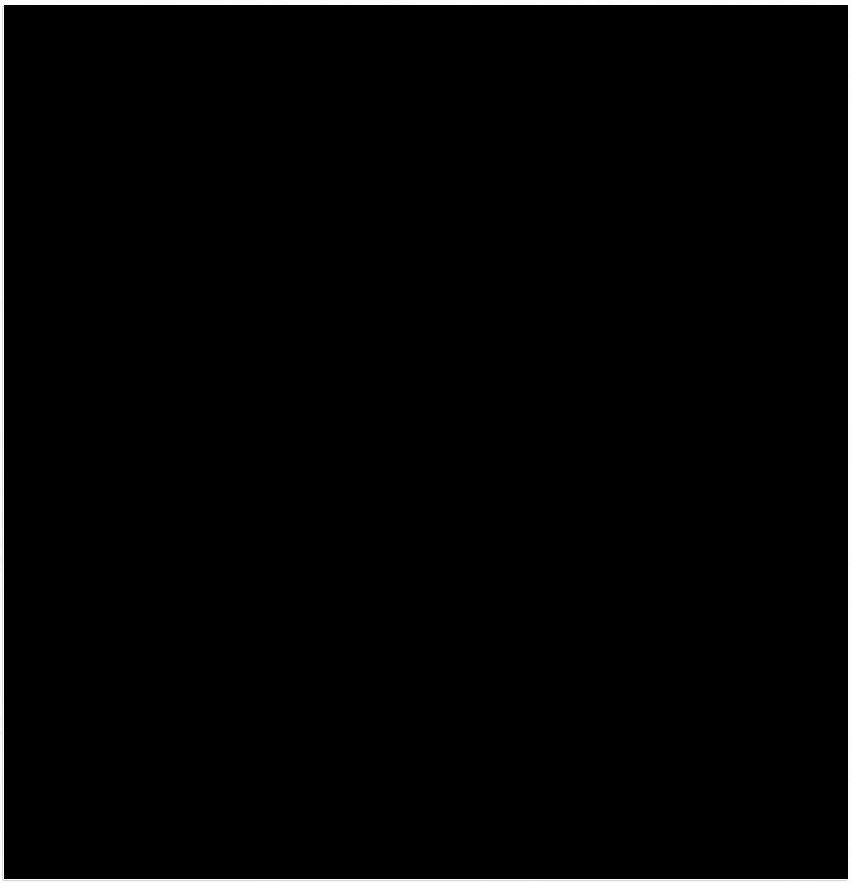

Figure 1.14 - Optoelectronic arrangement of Asea type 1010 temperature sensor.

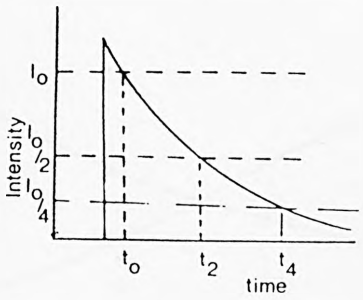

$$I = I_o \exp(-t/\tau)$$

measurement made as

$$I \rightarrow I_{o/2} \quad (t_2 - t_o)$$

or

$$I \rightarrow I_{o/4} \quad (t_4 - t_o)$$

Figure 1.15 - Use of "decay-time" measurement for temperature sensing

Figure 1.16 - Cross-section of the optomechanical configuration of Luxtron temperature sensor, type 750

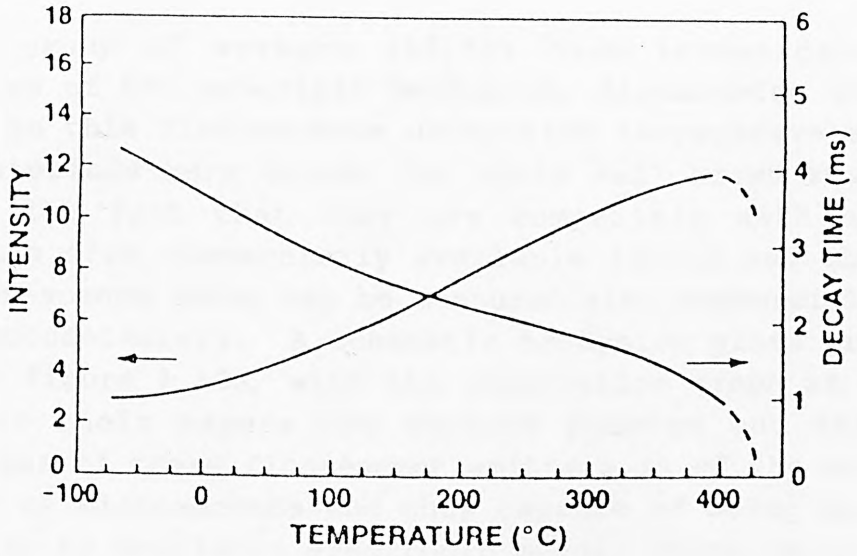

Figure 1.17 - Decay-time and fluorescent intensity changes in Luxtron type 750 sensor with temperature

modulated conventional lamp source similar to that in the earlier quoted work of Sholes and Small (53). Unsatisfactory results, by comparison with laboratory measurements on the transducer material, were obtained which were largely due to imperfect filtering. More recent work by Bosselman et al (55), which measured the decay-time of a chromium doped crystal excited in the red wavelength region, was used to sense temperatures in the range from room temperature to ~200°C.

In 1985 Luxtron announced their model 750 fluoroptic sensor (56) which is illustrated as figure 1.16. This commercial temperature measuring system used the decay-time characteristics of maganesium fluorogermanate as the transducer. This system used a UV lamp excitation which gave a slow data acquisition rate. This instrument's change in decay-time and fluorescent intensity with temperature is shown as figure 1.17. Recently in Japan, Omron (57) announced a new fibre optic temperature sensor which uses this fluorescent decay-time principle to measure in the range -30°C to 200°C. This transducer was made up from a phosphor excited by light from a visible LED.

Another group of workers (58,59) have investigated the properties of the materials Neodymium, Alexandrite and Ruby for use in this fluorescence decay-time temperature sensor. These materials were chosen for their well known stability and for the fact that they are compatible with optical excitation from commercially available lasers and LEDs and the fluorescence decay may be measured with commercial solid state photodetectors. A schematic neodymium glass probe is shown in figure 1.18a, with the calibration graph as figure 1.18b. In their papers the authors pointed out that the decay times of these fluorescent emitters is of the order of hundreds of microseconds and thus capable of being measured accurately by available electronic means. These decay times were measured with high accuracy using a ten megahertz quartz oscillator as illustrated by figure 1.19. These results indicate that inexpensive fibre optic thermometers can be constructed.

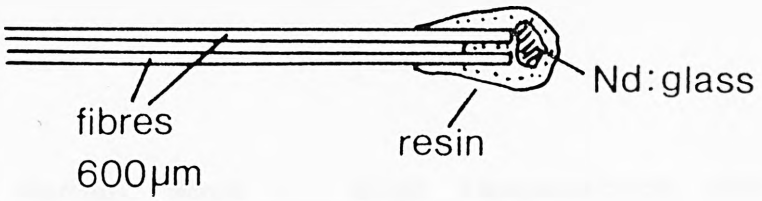

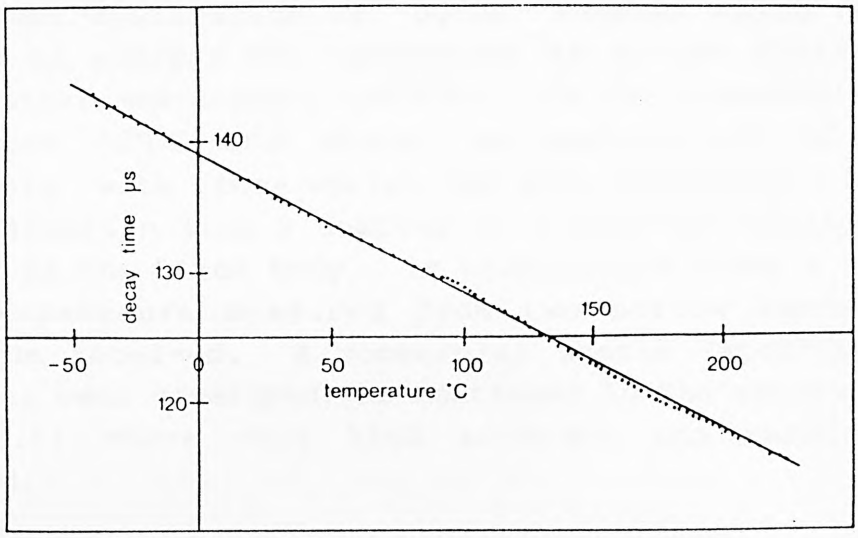

Figure 1.18 - A:Schematic of Nd:glass fluorescent decay time temperature sensor.
B:Calibration curve of above sensor

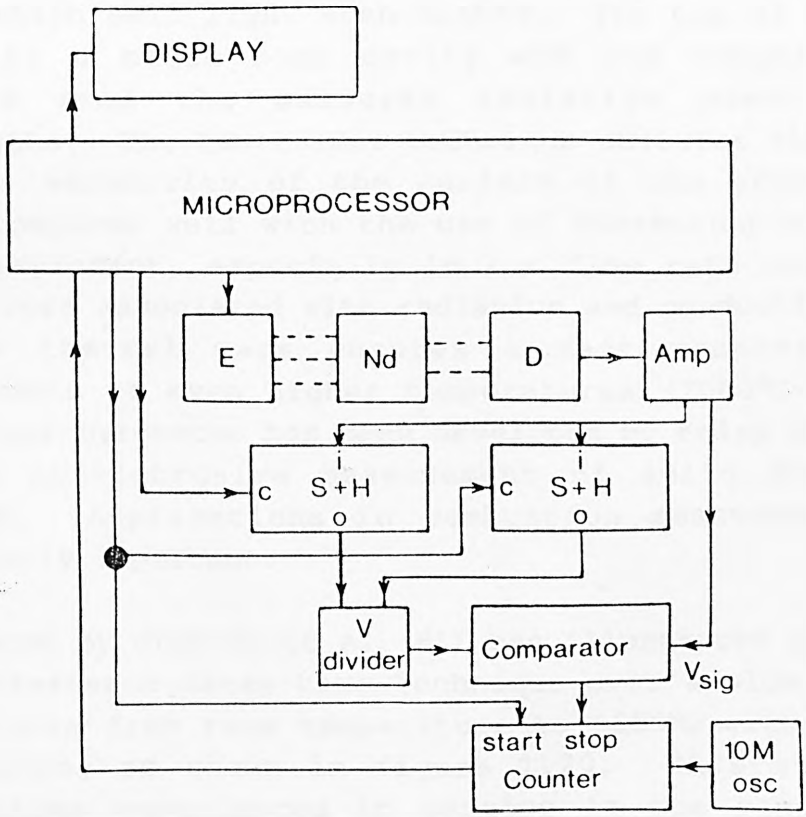

Figure 1.19 - Optoelectronic configuration of sensor in figure 1.18A:
10M: 10MHz quartz timing clock oscillator
E: emitter, Nd: fluorescent material,
D: detector, S+H: sample and hold device,

1.4.2 Recent work - High temperature measurements

A further application of "point" sensors using multimode fibres to address the transducer is in the field of high temperature measurement (>200°C). In the temperature region of about 500°C and above, an application of optical pyrometry with fibre optics has been developed. The black body radiation from a coating on a sapphire optical fibre, acting as the black body, is transmitted along a fibre and the temperature measured from two narrow bands of the spectrum received. A commercial system (Accufibre Corp) (12) has been developed, as mentioned in the earlier section (1.2.2.1) where very high accuracy and resolution is claimed.

This device is used as a temperature standard in the 630°C-1060°C range by the National Bureau of Standards in the USA and it consists of a rigid sapphire rod of length ~0.3-1.0m with a tip coated with thin films of iridium and aluminium oxide, which emit light when heated. The top of the probe acts like a black body cavity and the temperature is computed from the measured radiative power at two wavelengths. The two colour technique obviates the need to know the emissivity of the surface of the sensor. The sensor compares well with the use of thermocouples for the same measurement, especially in low flow rate gas streams where errors associated with radiation and conduction occur. The low thermal mass ensures a fast response. For measurements of even higher temperatures (2000°C-6000°C) a multicolour pyrometer has been developed by Foley et al (60) for the non-intrusive measurement of solid and liquid surfaces. Applications in combustion measurements are particularly important.

Recent work by Grattan et al (61) has illustrated the use of the fluorescence decay-time technique over a wide range of temperatures from room temperature to ~850°C with a single sensor probe as shown in figure 1.20. This avoids any difficulties experienced in sensing in the range around 500°C where the pyrometric devices only begin to operate well, and where sensing over a wide temperature range is needed.

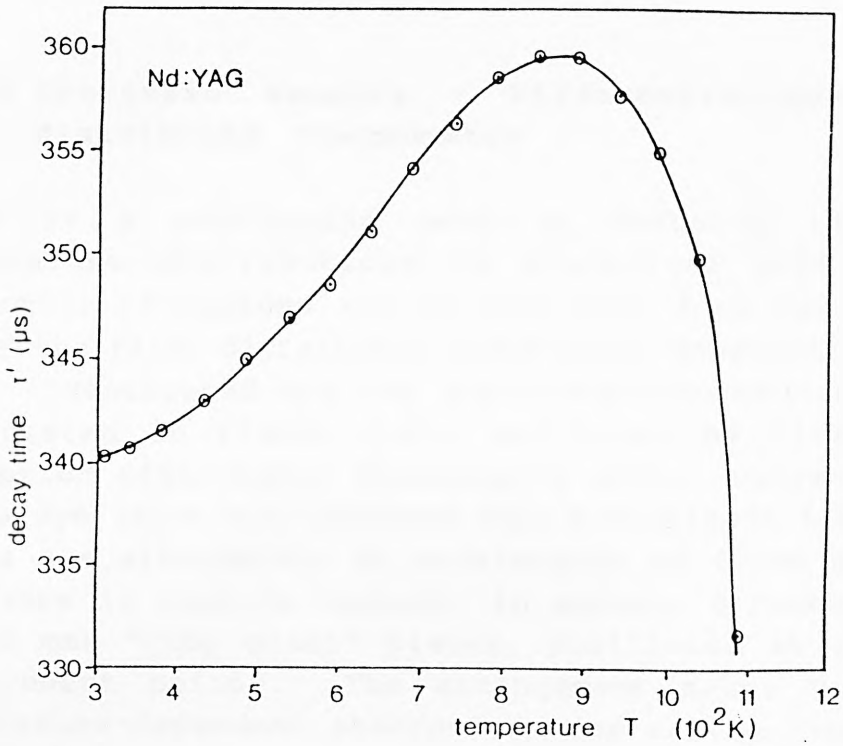

Figure 1.20 - Use of fluorescence in Nd:YAG to measure high temperatures (1100 K)

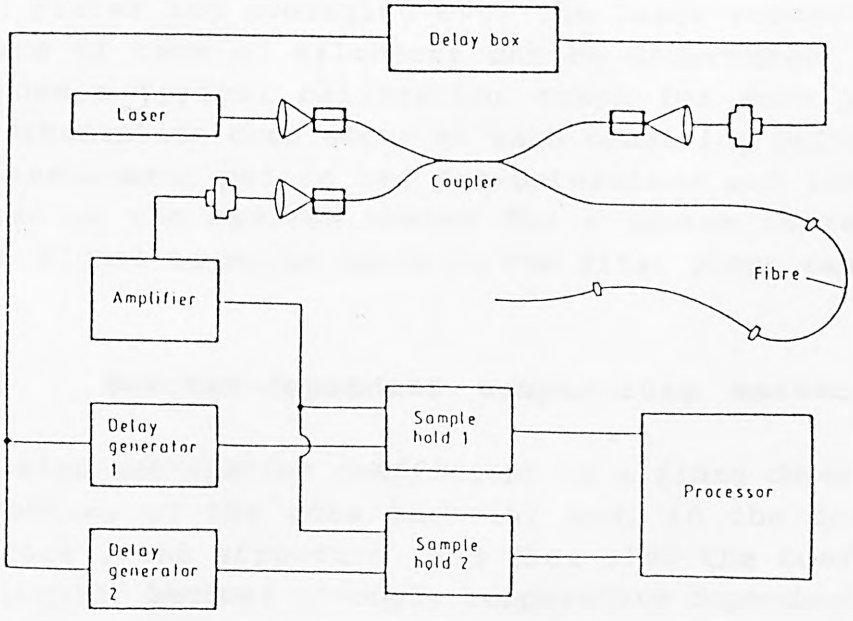

Figure 1.21 - Quasi-distributed thermometry using ruby glass plates

1.4.3 Intrinsic sensors - Differential-absorption distributed thermometry

There is a continuing need in industry to measure temperature distributions in electrical machinery for protection of systems and to make heat flow calculations. One of the first distributed temperature measurement systems to be investigated was the quasi-distributed arrangement, illustrated in figure 1.21, and known as Differential-Absorption Distributed Thermometry (26). Pulses of light from a dye laser are launched into a multimode fibre. These pulses are alternately at wavelengths of 605nm and 625nm. The fibre is used to connect, in series, a number of thin (~0.25 mm) "ruby glass" plates, positioned at convenient measurement points. The arrangement makes use of the temperature-dependent absorption edge of the "ruby glass" and light thus has a temperature-dependent absorption as it passes through the plates. The 625nm wavelength lies in the long-wave transmissive region of the glass, and thus light at this wavelength can act to provide a reference intensity level. The individual ruby glass plates are identified by time resolution of the Rayleigh backscatter signals at the two wavelengths. A fast time response results from the use of thin plates and averaging over the laser pulses emitted at a rate of tens of kilohertz can be undertaken. Figure 1.22 shows a typical calibration graph for such a device (26). Attenuation does occur at each measuring point and so these measurement points are pre-determined and limited to about ten as the maximum number for a system to retain an adequate signal-to-noise ratio in the final plate range.

1.4.3.1 Scatter-dependent temperature measurement

The Rayleigh-backscatter coefficient in a fibre depends upon the structure of the core material and, in the case of a liquid-core , the structure (and thus also the coefficient of the liquid) becomes strongly temperature dependent. This fact has been used to measure the distribution of temperature in a liquid-cored fibre (62), via the arrangement shown in figure 1.23. A light pulse of 10ns duration is launched into a section of multimode fibre joined to a section of liquid-core measurement fibre.

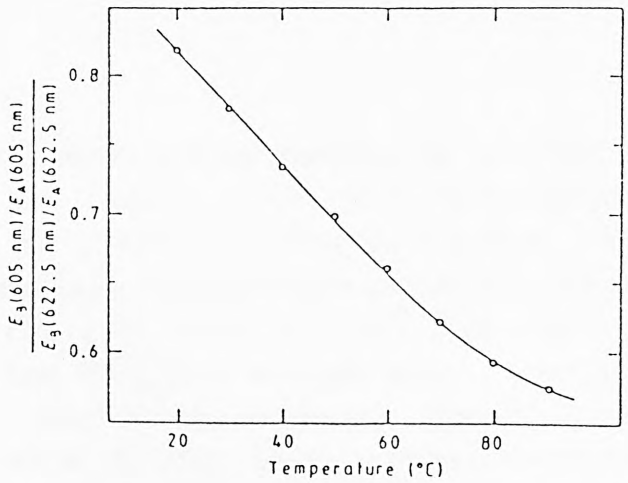

Figure 1.22 - Calibration graph for the device shown in figure 1.21

Figure 1.23 - Temperature sensing in distributed mode using liquid core fibres

Figure 1.24 - Calibration graph for the device shown in figure 1.23

Measurements reported by Hartog et al (62) for this system are shown in figure 1.24 and correspond to a scatter coefficient of $0.42\%^{\circ}C^{-1}$, which is linear up to the value of $80^{\circ}C$. The maximum temperature of operation of this fibre is limited by the fact that at $160^{\circ}C$ the refractive indices of fibre core and cladding become equal, and guiding action is then lost. Higher-temperature operation may be obtained with solid-core fibres (62). Measurements have been made for these, unfortunately showing much lower temperature sensitivities than with liquid-cores. However, solid-cores have the capability of use at elevated temperatures.

The main problem with liquid-core fibres is the danger of spillage of the organic substance contained and the loss of the fibre if this happens, also it would be more costly than regular solid-core fibre. The low scattering characteristics of solid-core fibre are a limiting factor in the use of this more acceptable material.

1.4.3.2 Distributed temperature sensing using doped fibre.

A distributed temperature sensor which combines the ideas involved in the preceding two sections has recently been reported (63). It uses fibre, doped with trivalent neodymium ions (Nd^{3+}), which exhibits a temperature-dependent absorption spectrum. The results reported were based on the use of a dopant concentration of 5ppm, this being the value calculated to optimize performance over ~200m of fibre using optical time domain reflectometry. Since an attenuation measurement is used there is a trade-off in the choice of dopant level, between sensitivity per unit length and the distance over which reasonable measurements can be made. Measurements at an optical wavelength of 904nm showed the dependence of attenuation on temperature to be linear over the range $-50^{\circ}C$ to $100^{\circ}C$, when the fibre used had a temperature coefficient of $\sim 0.18\%^{\circ}C^{-1}$. The performance reported showed a $\sim 2^{\circ}C$ accuracy over the above temperature range, with a spatial resolution of 15m over a fibre length of 140m. Work recently reported by Farries et al (64) indicated that measurements could be extended to a temperature of $\sim 900^{\circ}C$ using neodymium

and erbium doped fibres, specially produced for sensor applications.

A significant difficulty with this technique is the need for special fibres, with the consequent cost of their fabrication, and the problems that exist of non-uniform doping in the fibre yielding variable sensitivity to temperature along the length of the fibre.

1.4.3.3 Distributed anti-Stokes Raman thermometry

Distributed anti-Stokes Raman thermometry differs in several important respects from the preceding three methods for distributed temperature measurement. It was the first method to use a non-linear optical effect, the **Raman effect**, rather than a linear one. It operates independently of the fibre material, providing the important advantage of allowing measurement with optical-fibre systems which are already installed (e.g. communications systems) to become distributed temperature sensors. Also, it measures the absolute temperature and thus (in principle at least) requires no calibration. The technique has been described in detail in the work of Dakin et al (65).

The Raman effect is the effect whereby light propagating in a medium is modulated by the molecular vibrations and rotations within it. A full understanding of this effect must be treated at the quantum level and it can be described in terms of an incident photon being absorbed by a molecule which is then raised to a virtual excited state. The molecule may re-emit a photon of different energy (and thus different wavelength) either greater or smaller than the original. In each case the energy difference will be equal to one of the vibrational/rotational energies of the molecule. However, only if the molecule is already in an excited vibrational state at the time of photon incidence can it emit a photon of greater energy, by decaying from the virtual excited to the ground state. This is called anti-Stokes Raman radiation and its intensity will be temperature dependent, since, for thermal equilibrium, the number of vibrationally or rotationally excited molecules will depend directly on the absolute temperature. For the emitted

photons of smaller energy than the input photons the decay is usually to an excited state from an original ground state, and these are called Stokes photons. The majority of photons will, of course, be re-emitted at the same energy giving the so-called Rayleigh scatter. The Raman spectrum for silica is shown in figure 1.25. The banded nature of the spectrum results from the spread of bond energies characteristic of an amorphous solid. The experimental arrangement which has been devised to make use of this effect is shown in figure 1.26. A high-power optical pulse is launched into a multimode optical fibre at wavelength λ, from an argon ion laser. At chosen values, from the Raman spectrum, Stokes and anti-Stokes backscattered radiation levels at wavelengths λ_s and λ_a respectively, can be detected:

$$1/\lambda s = 1/\lambda - \nu$$

$$1/\lambda a = 1/\lambda + \nu$$

where ν represents a phonon created during the interaction between the incident photon and vibrational modes of the fibre, λ is the wavelength of the incident photon.

The Stokes and anti-Stokes wavelengths are measured with a monochromator and time-resolved. The ratio of anti-Stokes to Stokes measured power levels is given by:

$$R(T) = (\lambda_s/\lambda_a)^4 \exp(-hc\nu/kT)$$

where h is Planck's constant, c is the velocity of light, k is Boltzmann's constant and T is the absolute temperature, as the only unknown which can be deduced directly from a knowledge of R(T). The factor $(\lambda_s/\lambda_a)^4$ is a consequence of the Rayleigh scattering.

The experimental system used 15ns pulses at 514.5nm wavelength and 5W peak power. The Raman wavelengths lay at $\pm$10nm from the 514.5nm line, as shown in the Raman spectrum figure 1.25.

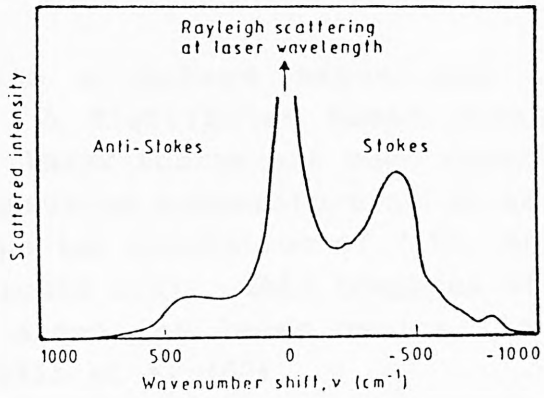

Figure 1.25 - Raman spectrum of Silica

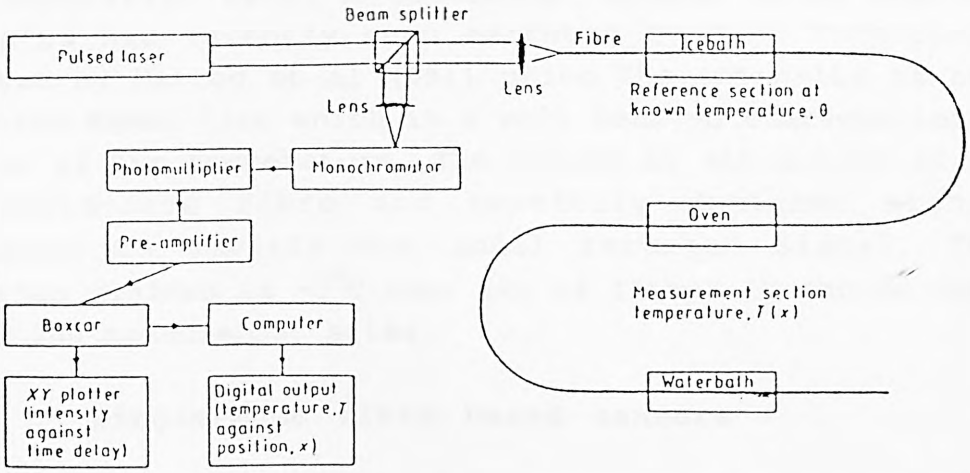

Figure 1.26 - Experimental arrangement for Raman scattering based distributed temperature sensor

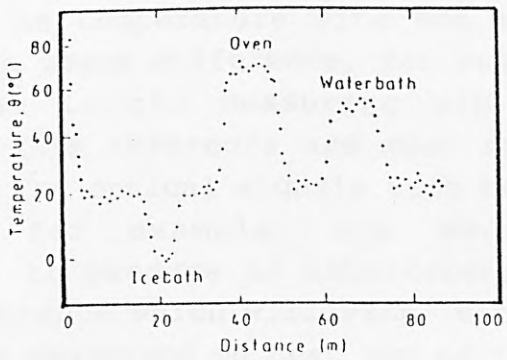

Figure 1.27 - Calibration for the device of figure 1.25 showing different temperatures at different positions from the start of the fibre

For field use a pulsed argon ion laser is largely impractical. A distributed Raman system using an 850nm semiconductor laser source has been reported (66). This is capable of measuring temperature to an accuracy of 1°C over 1km, with a spatial resolution of 7.5m, and a typical result is shown in figure 1.27. This compares with a resolution of 5°C with the argon ion laser device, in the initial work reported by Dakin et al (67).

The primary difficulty with this method lies in the very low levels of Raman backscatter, which are less than the Rayleigh backscatter by a further factor of ~10^3. This necessitates long integration time with a kilohertz laser pulse repetition rate. A commercial system using similar principles has recently been marketed by York Technology (reported by Hartog et al (68)) using the intensity of the Antistokes Raman line which is a well behaved characteristic function of the temperature. The scheme is attractive as it uses solid-core fibre and carefully designed signal processing to amplify the small returned signal. The resolution claimed is ~1°C over 1km of fibre; it can be used to give 200 measurement sites.

1.4.4 Single-mode fibre based sensors

Due to their small core diameter, single mode fibre based temperature sensors are more difficult to handle and align, and the majority of temperature sensor schemes proposed have been those using multi-mode fibres. Sensors based on the change of phase or polarization of light can be configured as fibre optic interferometers and the interaction of a measurand such as temperature with one arm of the device will result in a phase difference, for example, between the modulated light in the measuring arm and light in a reference arm. This reference arm must not be affected by the measurand. The optical signals from the two arms may be combined in, for example, the Mach-Zehnder fibre interferometer, to produce an interference pattern due to this phase difference which will vary with a change in the influence of the measurand on that arm of the device.

These devices are, in principle, very sensitive and would,

at first sight, appear to be very useful for commercial measuring situations. However, two major difficulties exist. Whilst optical phase shifts of ~10^{-6} radians and temperature differences of ~0.005°C may be measured, these devices require reference to an absolute calibration point and are thus more useful for monitoring temperature changes than for absolute measurement. The very high sensitivity available is rarely needed and coherent light sources are required whereas many multimode sensors can use LED or lamp sources. This requirement can make such systems expensive. Additionally, due to their high sensitivity it can be difficult to prevent other physical quantities from interfering with the measurand. This is a difficulty experienced with a number of optical fibre sensors but it is especially a problem in interferometric sensors. Polarization sensors tend to work on the same principle and suffer the same lack of specificity and expense problems. These difficulties could at least partially explain the lack of interferometer based commercial fibre optic sensors. The only exception is the Laser Doppler Velocimeter which offers a unique approach to velocity measurement, and the Sagnac interferometer which is the basis of the fibre optic gyroscope. Extensive development is continuing in these fields but the use of the technique for temperature sensors is limited.

The use of changes in cavity dimensions has long been exploited in temperature sensors. For example, a Fabry-Perot cavity with an air gap the dimensions of which are temperature variant was used by James et al (52) where the first order interference peak is scanned by a broad wavelength source and the shift in peak, corresponding to the temperature change is measured. A recently marketed device by TDI (69) exploits this principle in a temperature sensor operating in the infra red part of the spectrum, addressed by light from an LED.

The use of two wavelengths has been proposed for such a cavity based sensor and interference based sensor schemes to increase the measurement range. The two wavelengths beat together, and the sensitivity to this beat wavelength is much less than to the shorter primary wavelengths of the

sources themselves.

1.5 THIS WORK

A considerable effort has been expended in recent years in the development of fibre optic temperature sensors and many ingenious schemes have been proposed and reported. Sensors which have successfully incorporated two colour referencing or use time-dependent effects have been marketed and a novel distributed temperature sensor scheme is now on sale (70). The optical 'point' temperature sensors have been shown to exhibit, in an independent assessment of their performance by Harmer (32), the capability of making accurate measurements in environments where conventional sensors cannot be used. However, this assessment also indicates that their is considerable scope for improvement and that their is a need to exploit alternative fibre optic temperature measuring schemes, such as those described in this work.

The need to investigate alternative referencing schemes is an important area of research where work is continuing to isolate and hence, compensate for the deleterious long term effects that degrade performance of fibre optic temperature sensors such as fluctuations in the LED light output. This work describes the development of a number of temperature sensors. The work was started, as described in chapter 2, with the development of a novel referencing scheme for intensity based sensors. The sensor uses the temperature dependent properties of a ruby glass absorption edge filter and a reference signal generated from neodymium-in-glass, a fluorescent material. The reference signal compensates for changes in the signal detected, caused by other changes than those due to the measurand. The design of this initial temperature sensor was improved by miniaturizing the optical probe and enhancing the performance of the signal processing electronics; this is described in chapter 3. Chapter 4 describes the extension of this scheme to one using absorption filters at lower wavelength and fluorescent material. This chapter illustrates the effective use of low cost components to develop a commercially viable, 'accurate' fibre optic temperature sensor.

Chapter 5 describes the work carried out on a temperature sensor relying on sensing the fluorescent emission from crystalline ruby. The fluorescent emission spectrum is processed to give two signals; one dependent on temperature and the other independent of temperature to act as a reference in the overall sensor.

The fluorescence emission of crystalline ruby is further exploited in chapter 6. This chapter describes the final piece of work contributing to this thesis. This work was aimed at producing a full working optical fibre temperature sensor relying on the decay-time change of ruby with temperature.

The final chapter summarizes the performance of the various temperature sensors developed and also produces a comparative analysis of these performances.

Chapter 2

SELF-REFERENCED ABSORPTION THERMOMETER

2.0 SELF-REFERENCED ABSORPTION THERMOMETER

Following the scheme of the research programme described in section 1.5, the self-referencing fibre optic thermometer was the first system investigated. This system provided an insight to the problems involved in the development of optical temperature instrumentation. The initial design, as discussed in this chapter, was subsequently improved and chapter 3 describes these improvements. The prime aim of this work was to investigate the optical referencing scheme chosen, develop suitable electronic circuitry to allow the extraction of the required information and investigate the limitations of the optical probe.

Two very similar fibre optic temperature sensors relying on the absorption edge movement of doped filter glass and referencing from a fluorescent material are described. The two transducers differ only in their construction.

The first temperature transducer to be developed was constructed from a piece of doped absorption edge filter glass whose absorption edge movement was monitored as a function of temperature. It was considered important that a cheap and convenient LED source be used rather than a lamp source to sense the absorption edge change. The LED used emitted on a band with a peak wavelength of ~820nm, which overlapped the absorption edge of the filter glass used (RG-830 Schott glass). The absorption spectrum of the glass is shown in figure 2.1, with the emission profile of the LED shown in dotted lines. As the temperature increases, the absorption edge moves to longer wavelengths causing a change in the transmitted intensity through the filter of light from the LED. These filters have been shown to exhibit a fairly linear absorption edge movement with temperature (49) and are commercially available with a wide range of wavelength characteristics, as shown in figure 2.2, and are available in various standard sizes. The absorption effects

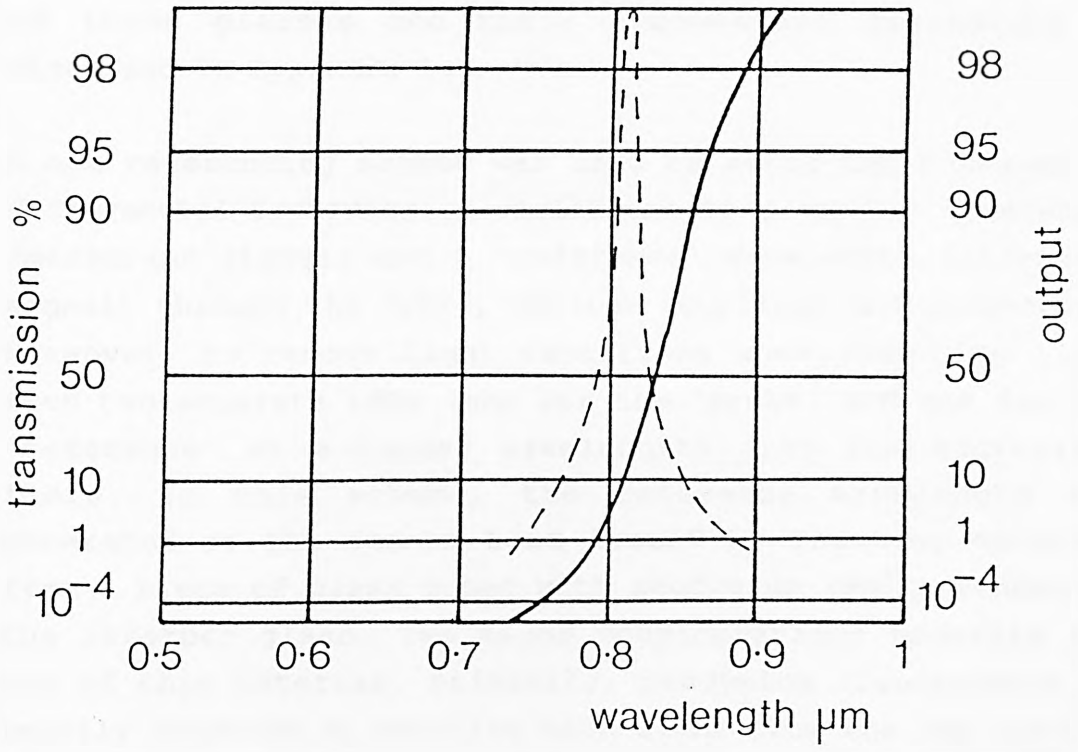

Figure 2.1 - LED spectrum with overlapping absorption edge RG 830 filter

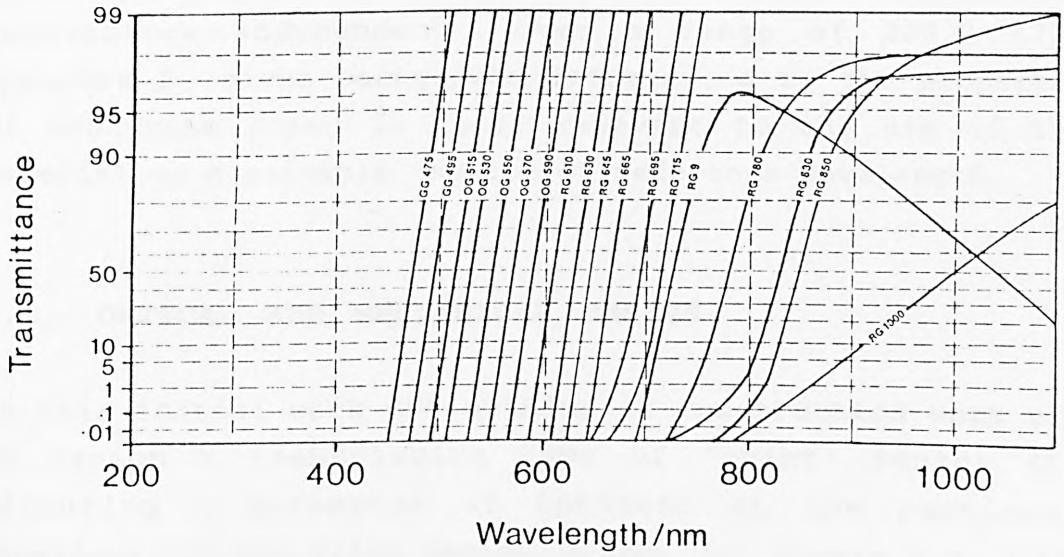

Figure 2.2 - Transmittance characteristics of various temperature sensitive absorption edge filters

of these glasses and their temperature dependence is discussed in Appendix 1.

A new referencing scheme was used to avoid the problems of differential transmission variations of a 'probe' wavelength (measurand signal) and a 'reference' wavelength (reference signal) through the fibre, various couplings and connectors. Moreover, to remove light variations when launching light from two separate LEDs (one for the 'probe' and one for the 'reference' at a longer wavelength) into the addressing fibre. In this scheme, the reference wavelength was generated at the **sensor head itself** by inducing emission from a piece of glass doped with neodymium (Nd^{3+}) bonded to the absorber glass. Two major considerations underlie the use of this material. Primarily, neodymium fluorescence is readily obtained by exciting with light from the LED used in the 820nm region, where the material exhibits strong absorption (71). Secondly, the strongest fluorescence band (emitted at 1.06μm) is essentially unaffected by the absorption changes of the RG material with temperature as this is well beyond the absorption edge. Additionally, the intensity of the fluorescence produced is essentially temperature independent over a range of 200°C (71). Appendix 2 gives background information to the properties of neodymium doped in glass relevant to the use of this material as a suitable source of reference wavelength.

2.1 OPTICAL AND MECHANICAL DESIGN

In this initial work two methods of construction were used to design a transmission type of 'point' sensor (i.e measuring a parameter of interest at one particular location). In the first design, shown in figure 2.3, the

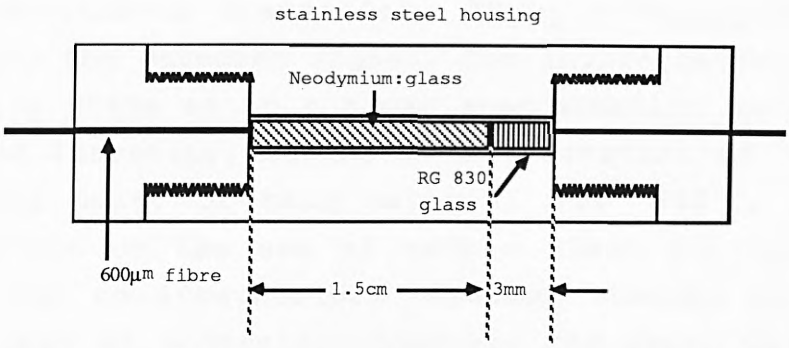

Figure 2.3 - Schematic of probe with optical components housed in stainless steel container.

optical components were housed in a stainless steel cylinder which ensured good optical alignment and low thermal expansion. It is important to minimize such effects since they can produce unwanted changes in the received light intensity. The referencing technique employed eliminates the effects of differential thermal expansion of fibre cladding, resin and the housing material. With some of the commonly used adhesives such as araldite, repeated cycling to elevated temperatures from room temperature can cause a small displacement of the fibre within its housing. Thus, it is important to minimise thermal expansion effects and ensure against long term deterioration of the probe. Ideally, the thermal coefficient of the elements used in the probe construction should be equal or nearly the same. With glass and metal interfaces this is difficult to achieve; it is a problem that has not entirely been solved by commercially marketed probes.

The sample of neodymium glass was cut from a laser-glass (Q-100 Kigre Inc.(72)), to a length of 1.5cm and a cross-section of $6mm^2$. This "super gain" Athermal phosphate glass was the most heavily doped commercially available (9% Nd^{3+}) and its fluorescence spectrum shows three distinct bands with peaks at 0.88μm, 1.06μm and 1.35μm (71). The weaker 0.88μm fluorescence is readily reabsorbed over the length of the glass, and the longer wavelength 1.35μm emission lies

outside the sensitive region of the photodiode used. Hence, the fluorescence transition $^4F_{3/2}$ - $^4I_{11/2}$ near 1.06μm dominates the detected signal. The fluorescence lifetime of the $^4F_{3/2}$ state is to a close approximation an exponential decay of intensity, having a time constant of ~200μs. The softening point of this material was ~420°C, setting an upper limit on the use of such a glass for this kind of sensor due to irreversible chemical changes in the glass which occur at softening. However, the upper working limit of this sensor was set by the absorption edge filter glass whose reversible linearity of transmission against temperature extended up to a temperature of 120°C. This is sufficiently useful, nevertheless, for a wide range of practical applications including the bio-medical temperature sensing region.

The RG glass sample used was also cut to similar cross-sectional dimensions but the length of the glass was used as supplied, at 3mm. Both glasses were polished by hand to give a high optical finish with their end faces parallel and flat. This ensures good optical coupling between the glasses and ensures minimal loss. PCS 600 (600μm diameter core plastic coated silica) fibre was used to guide the addressing light signal to the sensor head and also to receive the transmitted signal at the other end of the sensor, which was then guided to the silicon photodiode detector. The fibre was fixed into the connector of the housing using medical hypodermic needles. The outer protective plastic cladding was stripped back to about 1cm and the hypodermic needle was then glued to the end of the fibre. The outer diameter of this needle was of similar dimensions (~800μm), as the fibre with its outer protective cladding. A further, larger, hypodermic needle was used to encapsulate the smaller needle and extended over the outer cladding by about 1cm, as shown in figure 2.4. This helped to protect the fragile weak point between the smaller hypodermic and outer cladding. The hypodermic needle provided a means of interfacing the fibre to the end

connector which was then polished flat by hand, using various grades of polishing paper and a specially designed polishing jig. Finally, the fluorescent material was coated with a reflective layer of silver-based paint to prevent losses through the sides of the probe.

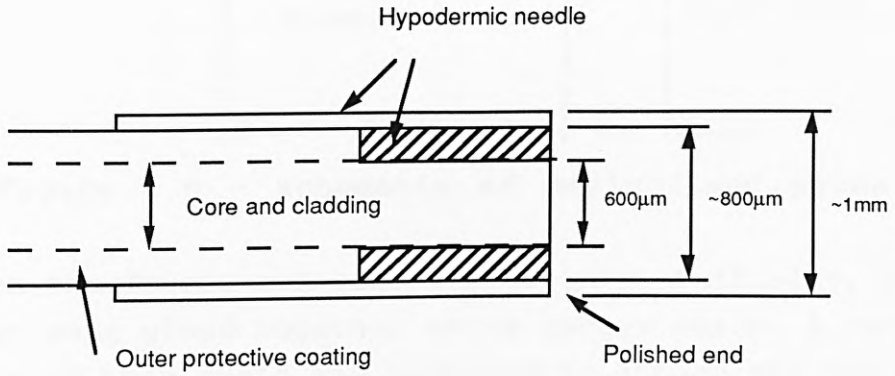

Figure 2.4 - Polished PCS fibre end with protective hypodermic needle interface.

A second construction, shown in figure 2.5, was also used in order to try to eliminate the problems of thermal expansion of the housing. To improve the thermal response, the bulk of the metal of the previous sensor was removed and Epotek epoxy resin was used to bond the fibre and the glasses together. The epoxy resin, type 353ND, is transparent in the infrared region i.e the spectral transmission in the 700-900nm range is quoted as >95% by the manufacturers. The thermal expansion of this resin is small, compared to many other resins. This probe required considerably more care in construction. The dimensions of the fluorescent and absorption material were similar to those used in the first construction, figure 2.3. The end faces were polished flat to maximise coupling of light. A piece of wood with a small V-groove cut into it was used to assemble the optical components, and to ensure good alignment and coupling

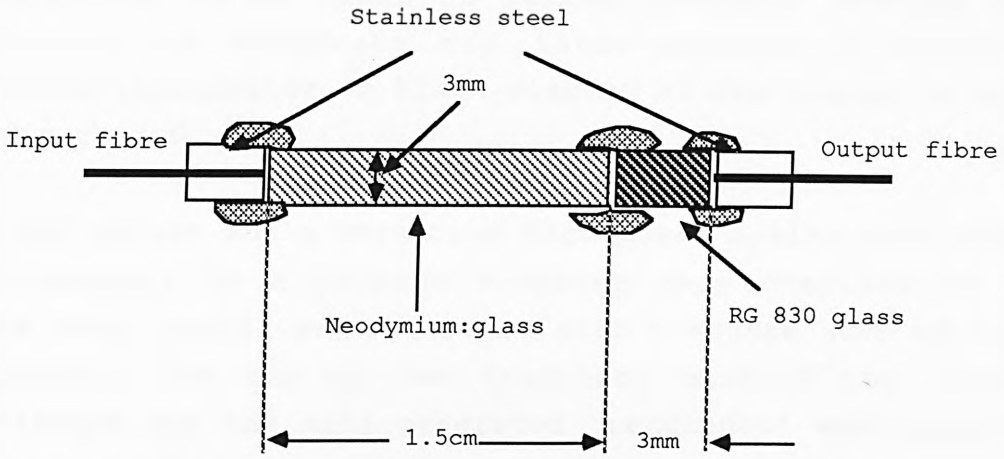

Figure 2.5 - schematic of resin-fixed probe

between the fibres and sensor materials. Initially, the two glasses were glued together using Epotek resin. A very thin coating of this resin was required to attach the two pieces of glass. The curing time of 1 minute at a temperature of 150°C allowed rapid adhesion to take place. Further coatings and curing of resin spread on the outer edge of the joint strengthened the bond between the neodymium and RG materials. The assembly was rotated in the V-groove to allow the four sides to receive equal amounts of resin. Finally, the fibre ends were glued into the hypodermic needles and then the fibre/hypodermic needle ends were polished to a high degree of flatness and finish. The neodymium and RG materials were held in the V-groove with adhesive tape and both ends coated with the resin. The fibre/hypodermic needle ends were placed in positions at either side with adhesive tape. The assembly was then placed in a pre-heated oven. More resin was added subsequently to strengthen the bond between the two glasses and the fibre/hypodermic interface.

2.2 ELECTRICAL DESIGN

The electrical system was designed to separate the temporal variations of the 'probe' intensity from the fluorescence 'reference' signal to enable the ratio of their relative

intensities to be taken to remove unwanted changes and, moreover, to calibrate the ratio against a secondary standard thermometer. A block diagram of the system is shown in figure 2.6.

The LED chosen was a versatile high power GaAlAs type (500μW max. output) in a package enabling easy coupling to the fibre used, and it was modulated with a square wave of 250Hz frequency. The use of low frequency enabled the 'probe' wavelength and the self generated 'reference' wavelength to be separated temporally, rather then optically, as this eliminated the need for a further optical filter whose characteristics could have varied with time, temperature or orientation. The LED and thus the 'probe' signal could be

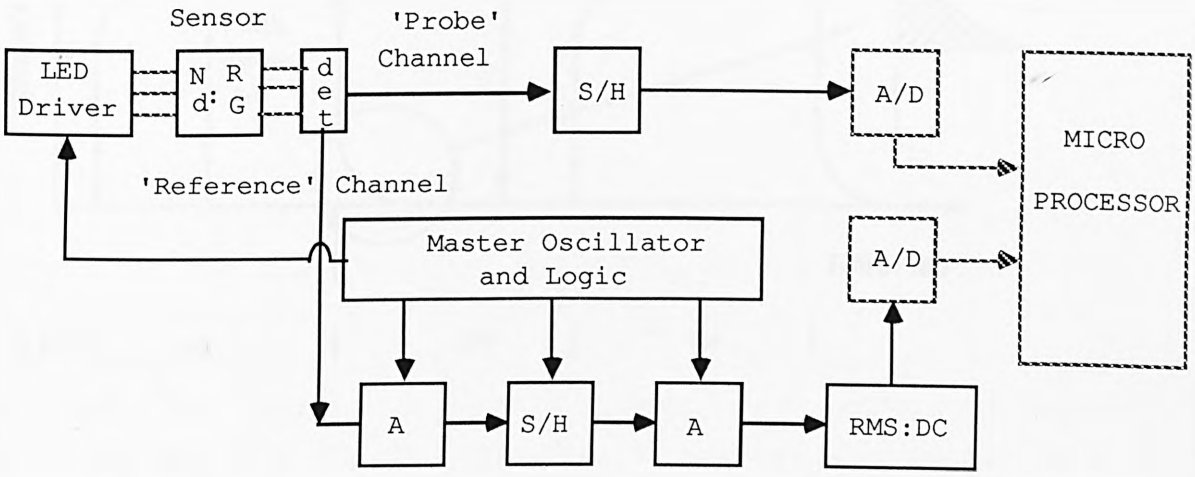

Figure 2.6 - Block diagram of the electrical system of the sensor. (where A: Electronic switch; S/H: Sample and Hold device; A/D: Analogue-to-digital converter; det: P-I-N detector and amplifier).

switched off very rapidly (on a time scale short compared to that of the fluorescence decay (a few microseconds). Light transmitted through the sensor was received by a p-i-n silicon photodiode (RS type 309-521), and connected to a transimpedance amplifier. The signal was then processed in

two separate ways to obtain the 'reference' and 'probe' signals (where detected peak voltage 'A' represents the peak intensity of the light signal at the LED wavelength), as shown schematically in figure 2.7. The 'probe' signal, which suffers increasing attenuation with temperature due to the band edge shift in RG-830 was obtained by sampling the square wave part of the received signal just before the LED was switched off, using a sample and hold (S&H) device. The sampling pulse width ensured that the sample was only taken at the constant intensity portion of the square wave, representing the ON period of the LED.

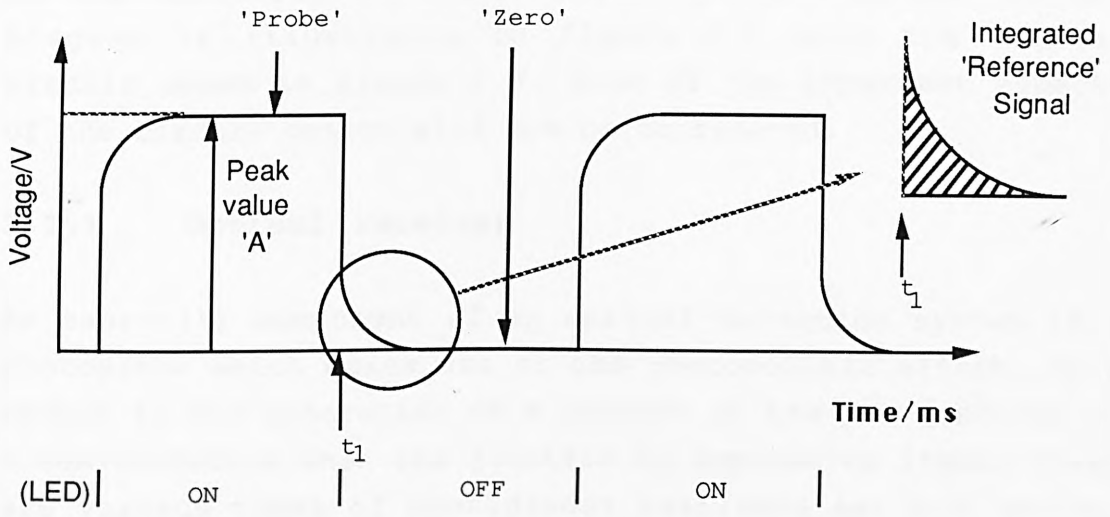

Figure 2.7 - Schematic separation of 'probe' and 'reference' signals

To obtain the 'reference' signal a second oscillator at the same frequency as the LED driver was used to switch out that part of the signal occurring during the interval from 10μs after the LED was switched off (time t_1) until the LED was switched on again in the next cycle. This 10μs delay was to allow time for high frequency 'ringing' to be switched out electronically. The signal was then amplified and

referenced to a dc 'zero' level obtained by sampling the signal just before the LED switched ON. This was set to occur after ~10 lifetimes of the fluorescence had passed (subsequently a time interval of 5 lifetimes was found to be adequate), to refer this signal to a point where the fluorescence light level was effectively zero and eliminating any small effects due to ambient light. Finally, the rms value of this signal, corresponding to the integrated fluorescence emission was converted to a dc signal and the ratio of this to the 'probe' signal level represented the temperature dependent quantity.

A more detailed description of the circuit design is given in the following sections. The complete analogue circuit diagram is illustrated in figure 2.8 with the digital circuit shown in figure 2.9. Some of the important aspects of the circuit design will now be considered.

2.2.1 Optical receiver

An essential component of an optical detection system is a photodiode which makes use of the photovoltaic effect. This effect is the generation of a current at the p-n junction of a semiconductor when the junction is exposed to light. There are various types of photodiodes available eg. p-n, p-i-n, Schottky and Avalanche. Each construction provides different features in respect of linearity, low noise considerations, wide spectral response etc. The p-i-n type, used in this system gives a good response time typically in the nanosecond region into a standard 50Ω load and offers low leakage currents, typically a few microamps, at low cost.

A photodiode can basically be considered as a current generator in parallel with an ideal diode with its associated junction capacitance C_j and resistance R_{sh}, as shown in the photodiode equivalent circuit of figure 2.10.

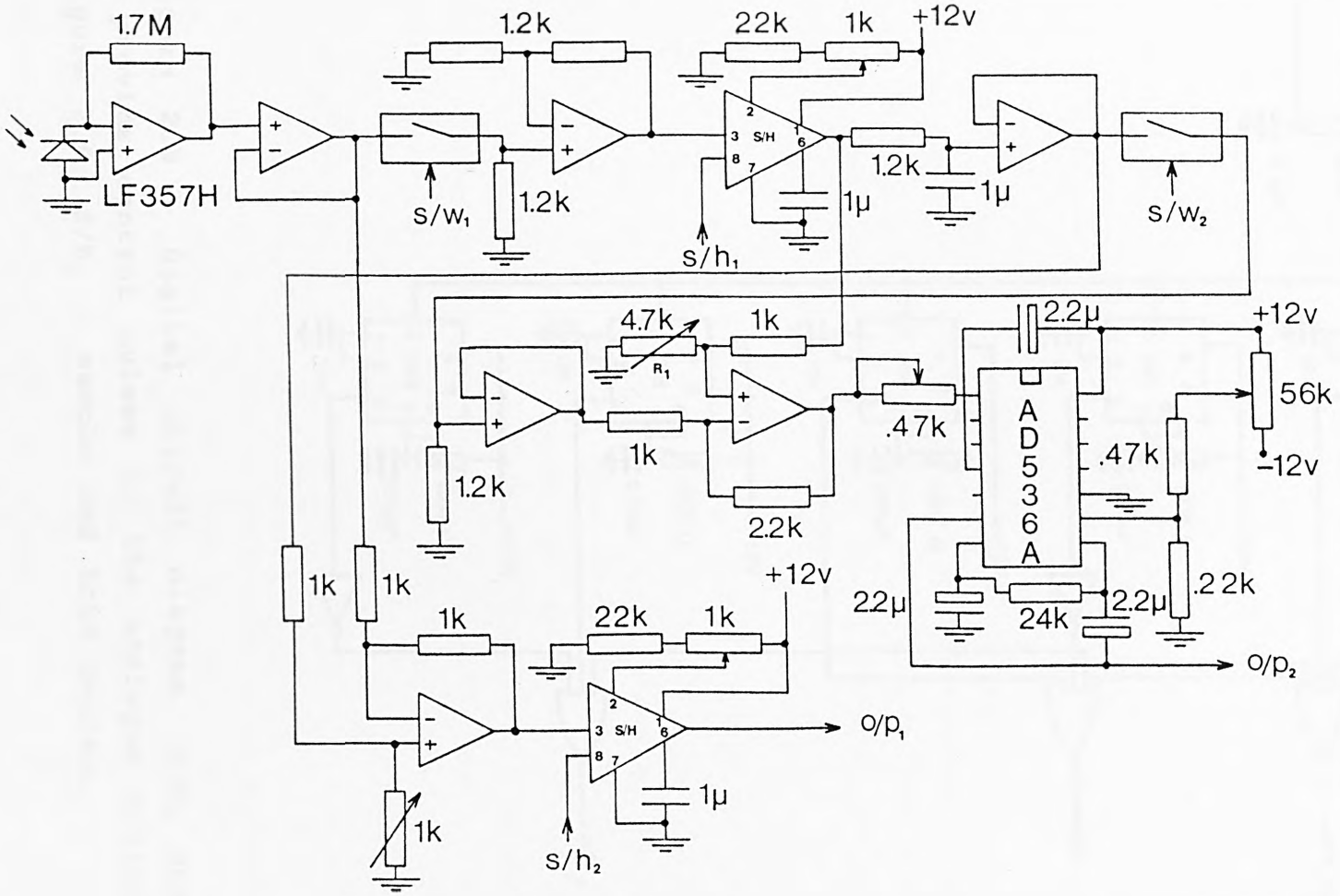

Figure 2.8 - Complete analogue circuit diagram. All op-amps, save for the first stage of the detector, are 071 series.

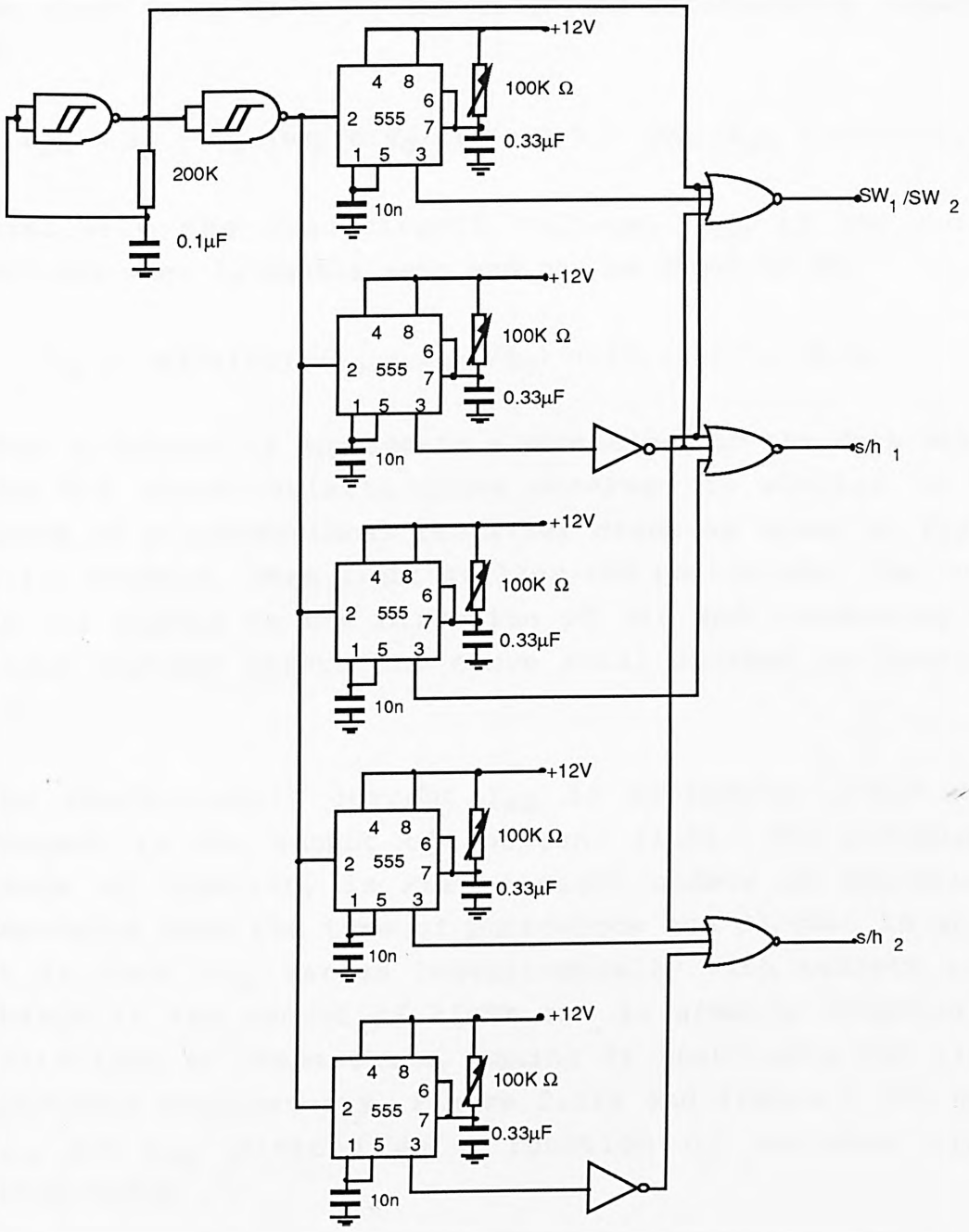

Figure 2.9 - Digital circuit diagram. S/W_1 and S/W_2 - provide control pulses to the analogue switches on figure 2.8. S/h_1 - sample and hold pulses.

The short-circuit current I_{sh} is the output current when the load resistance, R_L equals zero and V_o equals zero and can

be shown to be given by the following relationship (Appendix 3).

$$I_{sh} = i_p - i_o\,(\exp(e.V_d/kT) - 1\,) - (V_d)/R_{sh} \text{ -------(2.1)}$$

Similarly the open-circuit voltage, V_{op} is the output voltage when I_o equals zero and can be shown to be:

$$V_{op} = (kT/e)\ln(((i_p - i_{SH})/i_o) + 1) \text{ --------(2.2)}$$

When a voltage is applied to a photodiode in the dark state, the V-I characteristic curve observed is similar to the curve of a conventional rectifier diode as shown in figure 2.11. However, when light strikes the photodiode, the curve at (1) shifts in the direction of (2) and increasing the light further shifts the curve still further to position (3).

The short-circuit current I_{sh} is extremely linear with respect to the amount of incident light. The achievable range of linearity is six to eight orders of magnitude, depending upon the type of photodiode and circuit in which it is used. V_{op} varies logarithmically with respect to a change in the amount of light and is greatly affected by variations in temperature, making it unsuitable for light intensity measurements. Figure 2.12a and figure 2.12b show I_{sh} and V_{op} plotted as a function of incident light illuminance.

Figures 2.13 and 2.14 show the circuits used for measuring the light intensity by measuring I_{sh}. In figure 2.13, the voltage (I_{sh} x R_L) is amplified by an amplifier and the use of the bias voltage V_R enhances the speed of response to high-speed optical pulses. In the circuit of figure 2.14 the photodiode is connected to an operational amplifier in a transimpedance mode (Appendix 4). The input resistance of this type of feedback circuit is several orders of magnitude smaller than R_f and the output voltage is ($-I_{sh}$ x R_f). The

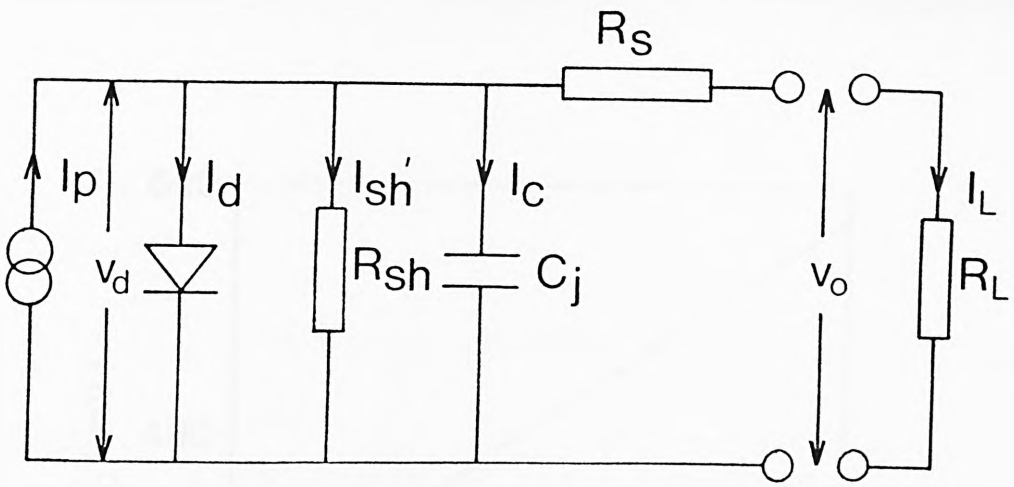

Figure 2.10 -Equivalent circuit diagram of a photodiode.

i_p - Current generated by the incident light

i_d - Diode current

$i_{sh'}$ - Shunt resistance current

i_c - Capacitor current

R_{sh} - Shunt resistance

R_s - Series resistance

R_L - Load resistance

C_j - Junction capacitance

V_d - Voltage across the diode

i_L - Output current

V_L - Output voltage

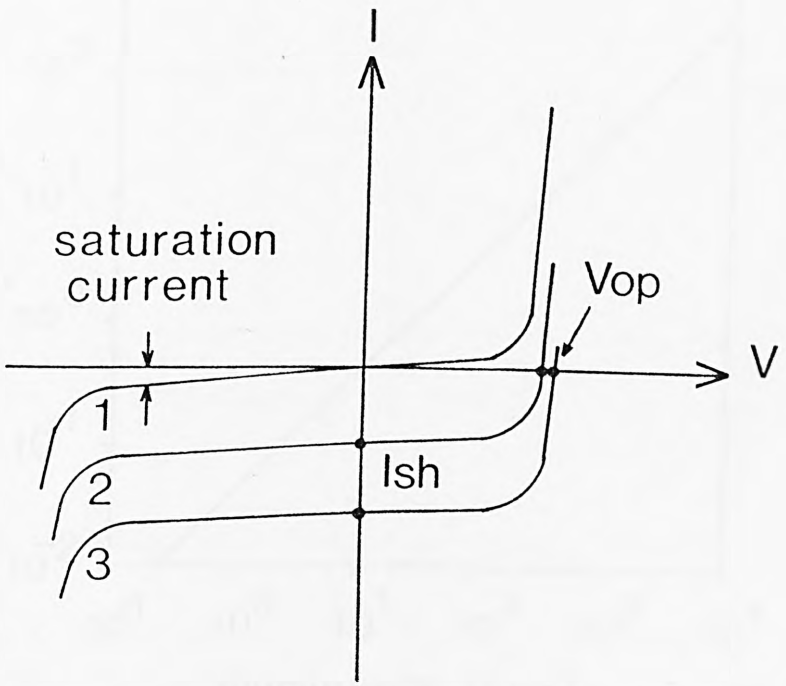

Figure 2.11 - V-I characteristics

Vop: Open-circuit voltage

Ish: Short-circuit current

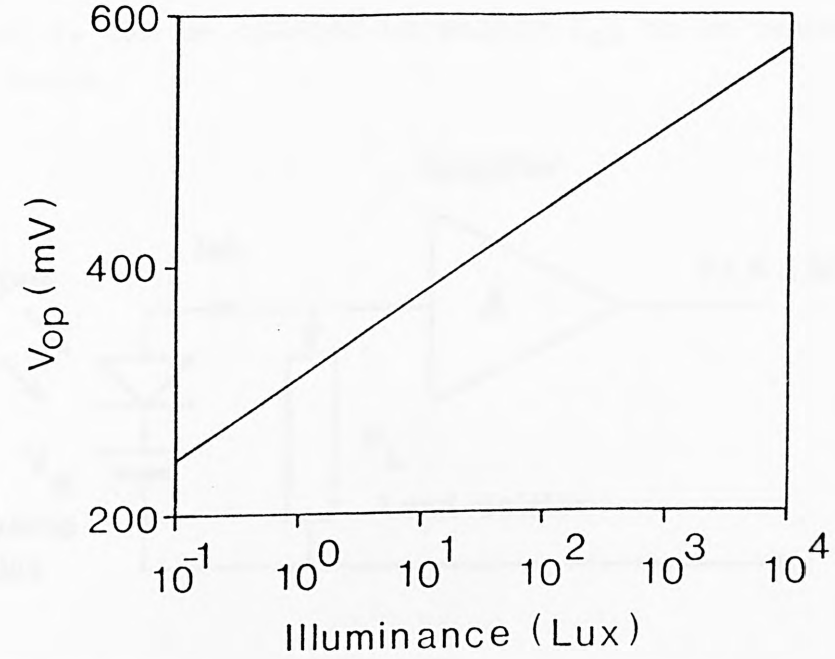

Figure 2.12 - (a) Open-circuit voltage against incident light

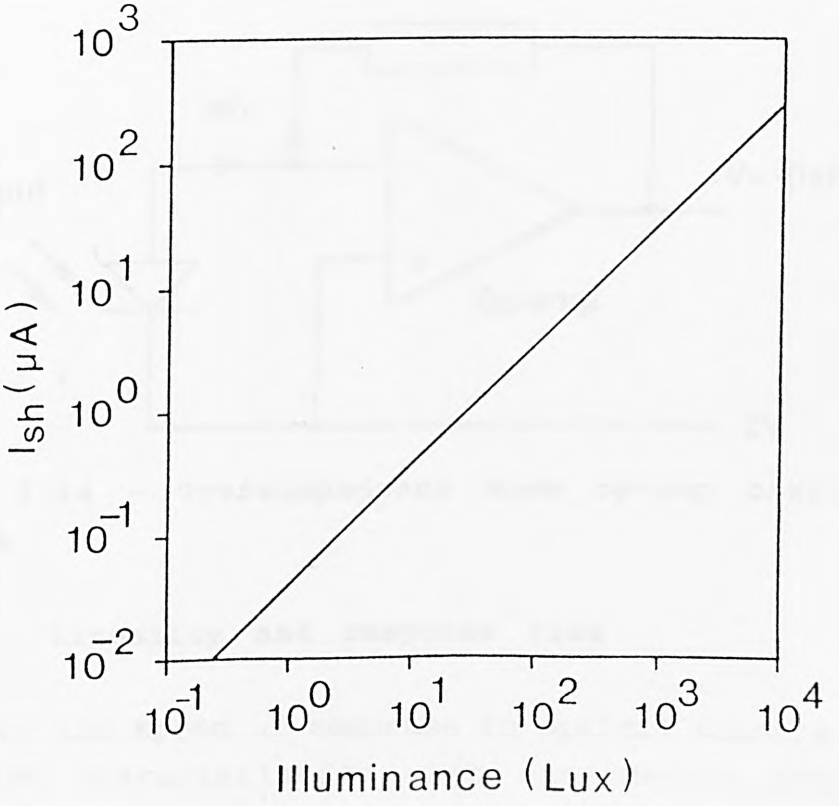

(b) Short-circuit current against incident light

value of R_f can be changed to enable I_{sh} to be measured over a wide range.

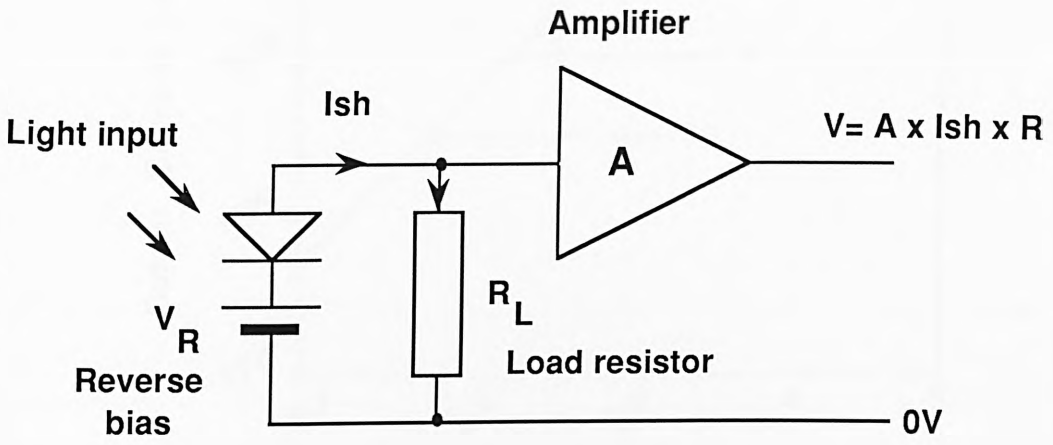

Figure 2.13 - Shows the reverse bias connection of a photodiode.

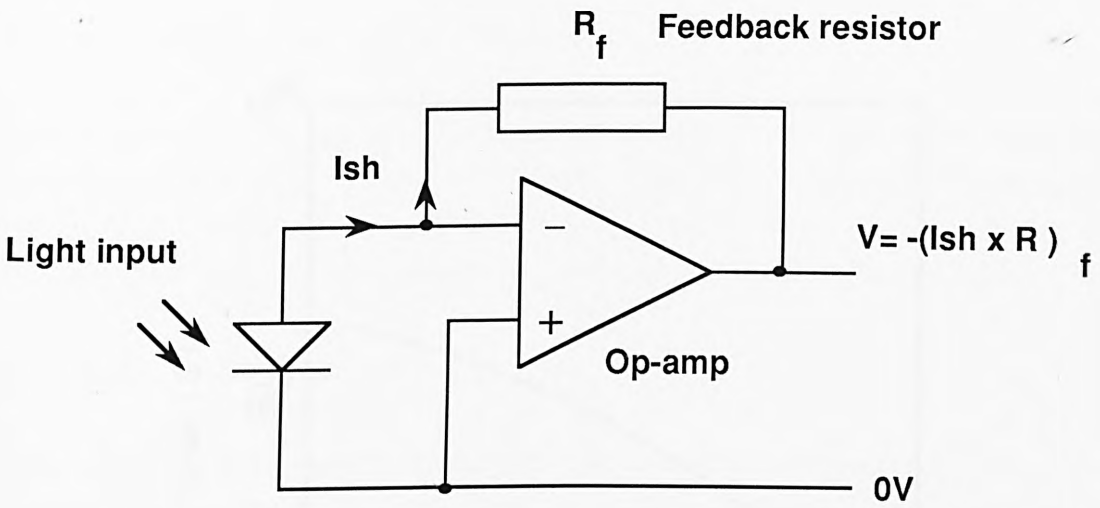

Figure 2.14 - Transimpedance mode op-amp circuit diagram.

2.2.2 Linearity and response time

Linearity and speed of response to optical signals are two important characteristics when considering the choice between transimpedance and reverse bias configuration. Figure 2.15 and 2.16 show the effects of reverse bias

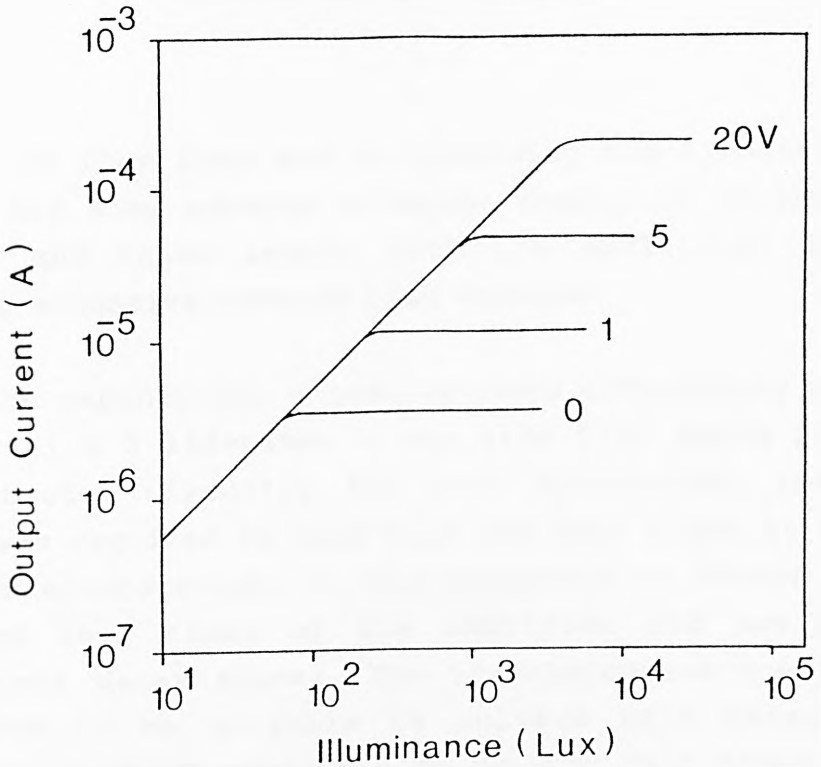

Figure 2.15 - A graph of rise time against reverse voltage (this graph shows a plot for Hamamatsu photodiode S1336BQ with R_L= 1K at λ = 655 m)

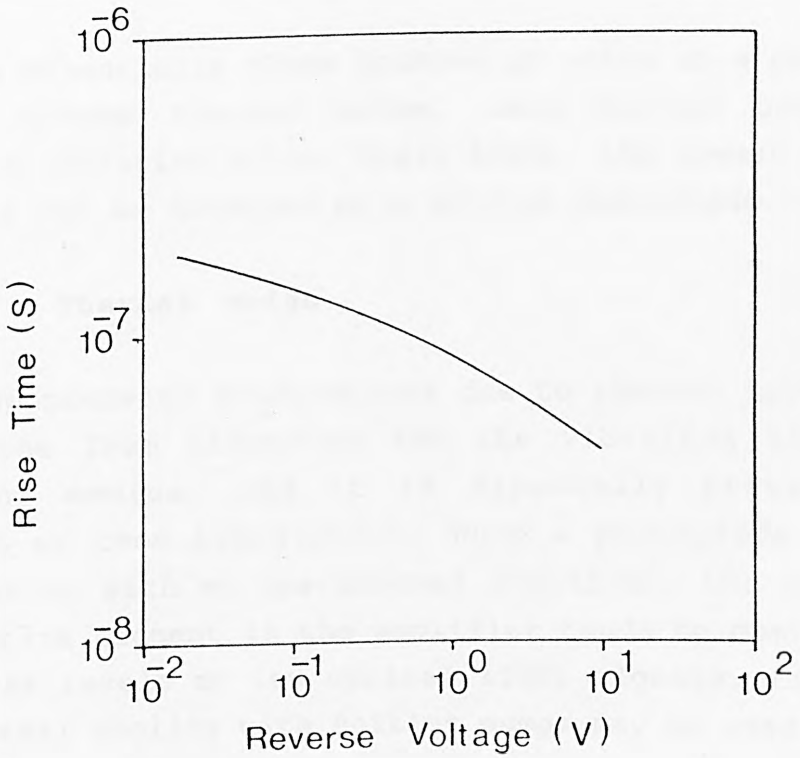

Figure 2.16 - A graph showing the extension of the linear range of a photodiode as a function of reverse bias and illumination. (Hamamatsu 1333.5BQ ; R_L= 100K)

voltage on rise time and in expanding the linearity range, but it has some adverse effects; namely it increases dark current and noise levels with the additional danger of applying excessive reverse bias voltage.

Since the exponential signal decayed effectively to 'zero' in ~1ms (i.e 5 lifetimes - one life time being 200μs) the photodetector circuitry for this fluorescent referencing sensor was required to have rise and fall times of the order of a few microseconds. It was necessary to ensure that the rise and fall times of the amplifier did not mask the fluorescent decay signal. The transimpedance configuration was found to be suitable to achieve this using certain values of feedback resistors to provide fall times of a few microseconds. Also, at the low optical power levels which were available to be detected (tens of microwatts), the linearity available from this configuration was ideal.

2.2.3 Noise in photodiodes

There are essentially three sources of noise in a photodiode receiver system: thermal noise, dark current noise and background radiation noise. These limit the lowest level of light that can be detected by a silicon photodiode.

2.2.3.1 Thermal noise

This is spontaneous fluctuations due to thermal interaction between the free electrons and the vibrating ions in a conducting medium, and it is especially prevalent in resistors at room temperature. When a photodiode is used inconjunction with an operational amplifier, the noise due to the active element in the amplifier tends to dominate the other noise levels at low optical light signals. In extreme cases thermal cooling with Peltier pumps may be used.

The thermal noise current, also known as Johnson noise i_j, in a resistor is normally expressed by its root mean square

value and is given by:

$$i_j = (4kTB/R)^{1/2} \text{ -------(2.3)}$$

where k = Boltzmann's constant
T = Absolute temperature of the photodiode
B = Post-detection (electrical) bandwidth of the system (assuming the resistor is in the optical receiver)
R = Resistor

2.2.3.2 Dark current noise

When there is no optical light signal incident on the photodiode a small reverse leakage current still flows from the device terminals. This dark current contributes to the noise in the photodiode and manifests its as shot noise on the photocurrent. The dark current noise is given by:

$$i_d = (2qi_dB)^{1/2} \text{ -------(2.4)}$$

where q = Electron charge
i_d= Dark current
B = Noise bandwidth

2.2.3.3 Background radiation noise

This is noise generated by leakage of ambient light through the optical fibre and can normally be avoided by using an opaque jacket around the fibre. This precaution is only required in cases of very low light detection or where ambient lighting is particularly bright.

2.2.3.4 Noise equivalent power (NEP)

The lower limit of light detection for a photodiode is usually expressed as the intensity of incident light

required to generate a current equal to the noise current as expressed in equation 2.3 and equation 2.4. Essentially this is the noise equivalent power (NEP), which is defined as the amount of optical power per unit bandwidth required to produce an output power equal to the detector (or detector-amplifier combination) output noise power. The NEP is therefore the value of power which gives an output signal-to-noise ratio of unity. Thus the lower the NEP for a particular detector, the less optical power is needed to obtain a particular signal-to-noise ratio.

$$NEP = i_n/S \qquad (W/Hz^{1/2}) \text{ -------(2.5)}$$

where i_n = Noise
S = Peak radiant sensitivity

2.2.4 Temperature characteristics of photodiodes

Ambient temperature variations greatly affect photodiode sensitivity and dark current levels. This is caused by variations in the light absorption coefficient which is temperature related. For long wavelengths, sensitivity increases with increasing temperature, as shown in figure 2.17, and this increase becomes prominent at wavelengths longer than the peak wavelength.

The variation in dark current with respect to temperature occurs as a result of increasing temperatures causing electrons in the valence band to become excited, pulling them into the conduction band. These temperature effects can only be reduced, in practice, by strict control of the temperature of the photodiode environment. However, in normal use the photodiode control box would not be operated, except under extreme conditions, at an ambient temperature $>35^{\circ}C$. Thus under normal conditions there is no real problem. Morover, thermostatic control could be built in for operation elsewhere.

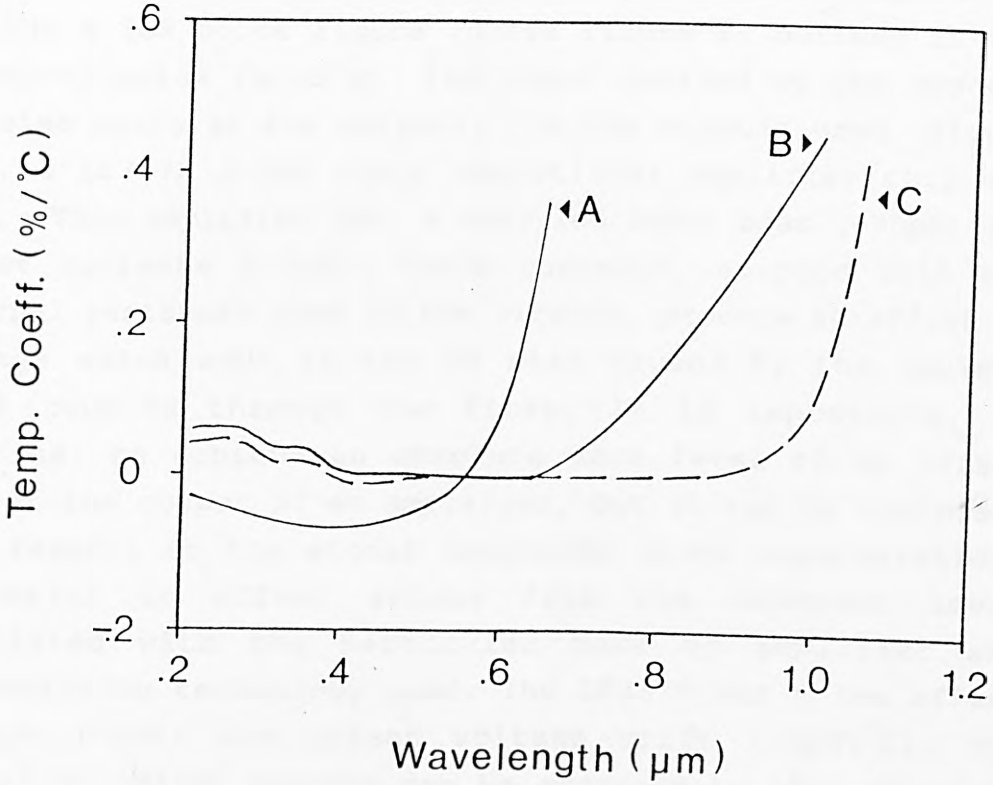

Figure 2.17 - Temperature coefficient against wavelength

A: Schottky type GaAsP

B: Hamamatsu 1226 series designed for visible region - Peak response at ~700 nm

C: Hamamatsu 1336 series designed for optimal response in the infra red - peak response at ~900nm

2.2.5 Noise problems in the transimpedance photodiode detector used

Most of the 'noise' in a photodiode is thermally generated and adds to the noise generated within the amplifier. The first stage of any receiver circuit gives the largest contribution to the overall noise in the system. Hence, it is important to choose the components of this stage which provide a low noise figure (noise figure is defined as the signal-to-noise ratio at the input divided by the signal-to-noise ratio at the output). In the circuit used (figure 2.8), a LF357H J-FET input operational amplifier chip was used. This amplifier has a very low input bias (~30pA) and offset currents (~3pA). These currents, coupled with the external resistors used in the circuit, produce an offset dc voltage which adds to the dc bias caused by the ambient light coupled through the fibre. It is impossible, in practice, to achieve an absolute zero level of dc offset bias at the output of an amplifier, but it can be minimised with respect to the signal amplitude under consideration. The major dc offset arises from the inherent level associated with the particular make of amplifier and manufacturing technology used. The LF357H has a low offset voltage (~1mV) and offset voltage drift (~3$\mu V/^{\circ}C$). The overall dc offset voltage can be adjusted by the use of an offset-null potentiometer. The data for this amplifier can be found in reference (73).

The most important feature of this amplifier which helps to provide low noise is its high input impedance, $10^{12}\Omega$. The thermal noise due to this load resistance is given by equation 2.4, where R in the equation can be replaced by a load resistor R_L of the amplifier . A discussion on thermal noise in detector circuits is given in reference (74), which illustrates its dominating effect in the detector circuit compared to other sources of noise, such as shot noise. From equation 2.4, it can be seen that if the load resistor is made large, then the i_j term decreases. Also the signal-to-

noise ratio for the photodiode receiver may be reduced by using low photodiode and amplifier capacitance; capacitors also have noise sources associated with them. The expression for the signal-to-noise ratio is derived for example by Senior (74) and is as shown in equation 2.6.

$$S/N = \frac{I_p^2}{2eB(I_p + I_d) + \frac{4KTB}{R_L} + I_{amp}^2} \qquad \text{----------(2.6)}$$

where I_p - photodiode current (Appendix 3)

I_d - dark current

i_{amp}^2 - total noise associated with the amplifier given by equation 2.7

$$i_{amp}^2 = \frac{1}{B} \int_0^B (i_a^2 + v_a^2 |Y|^2)\, df \qquad \text{--------(2.7)}$$

where $|Y|$ is the shunt admittance (combination of shunt capacitance and resistance)

and f - frequency

B - Bandwidth

i_a^2 - Shunt current noise

v_a^2 - Shunt voltage noise

As stated above, it is important to select a photodiode and amplifier which results in a combination with low input capacitance. This is not only required for the noise considerations but also to give an acceptably large bandwidth. The input capacitance and resistance form a RC network whose time constant is governed by the values of R_L and C_T. The post detection bandwidth, B, of the detector is given by equation 2.8 (74).

$$B = \frac{1}{2\pi R_L C_T} \qquad \text{--------(2.8)}$$

Assuming the total capacitance, C_T, can be minimized, then the other parameter which affects the value of B is the load resistance R_L. One way to increase B is to reduce R_L. However, this introduces a thermal noise penalty, as seen from equation 2.3. There is therefore a trade-off between the bandwidth which can be achieved and the level of thermal noise which may be tolerated. The bandwidth considerations become very important when accurate reproduction of a square wave signal is required. The Fourier series of a square wave consists of an addition of an infinite number of odd terms of sine waves. If the high order terms are attenuated then the square wave function will distort. In this work, it was important to detect a square wave with minimum distortion. The slope at the transition edges of the square wave was required to have a minimum ($\leq 1\mu s$) rise time otherwise the exponential decay detected would have been distorted by the detector circuit. The 'slew rate' of the amplifier (i.e the change in the output voltage of the amplifier against time) needs to be relatively high in order to respond adequately to the sharp transition edges of the square wave over the range of 'swing' of the amplifier supply voltage, but too high a 'slew rate' can cause ringing effects on the square wave which may cause errors in the measurement. A compromise between all these competing effects was achieved by testing a wide range of different amplifiers; this was the cheapest alternative to varying the range of photodiodes and yet was effective. As was mentioned earlier, ringing occurred on the edges of the square wave, this effect is also known as 'gain peaking' (Appendix 5)(75), and this was attributed to the mismatch of the photodiode and amplifier input capacitances and resistances. This was another factor which had to be reduced by careful matching at the design stage.

The second important contribution to noise results from the external feedback resistor R_f. The value of this resistor controls the level of voltage at the amplifier output and as a result the generated photodiode current. From equation

2.3, the larger this resistor the less noise is contributed to the circuit. But too large a resistor can cause saturation of the output voltage for the light level detected. The choice of this resistor was governed by the light intensity received and the level of noise tolerable on the weaker exponential signal compared to the 'probe' signal intensity. The detector circuit in this earlier design was constructed on a vero-board but, in the improved circuit described in the next chapter it was designed on a printed circuit board with a ground plane on one side; this helped to minimise capacitive coupling effects and hence reduced the noise in the circuit.

2.2.6 Separation of exponential decay and zero referencing circuitry

The received signal from the photodetector, as shown in figure 2.18(1), was passed through a buffer stage with unity gain to an electronic, FET type, analogue switch (HI-200). The switch was controlled (i.e opened or closed) by the pulses shown in figure 2.18(2A), to pass only the fluorescent emission, which was seen on the detected input as an exponential decay just after the LED turned off, shown in figure 2.18(3). There was also slight 'ringing' in addition to the exponential decay at the point when the LED switched off. This can be eliminated by placing a capacitor across the feedback resistor of the first stage, but this introduces a longer fall time which distorts the time profile of the fluorescent emission. The ringing occurred for a period of ~10μs, and to eliminate this the controlling pulse to the FET switch was delayed by this time. The switch had a low ON resistance (100Ω) and a very high OFF resistance (10MΩ). The effect of the OFF position of the switch leaves the non-inverting input of the amplifier of the next stage 'floating' and susceptible to capacitive pickup from the rest of the circuit . To avoid this, a 1.2kΩ

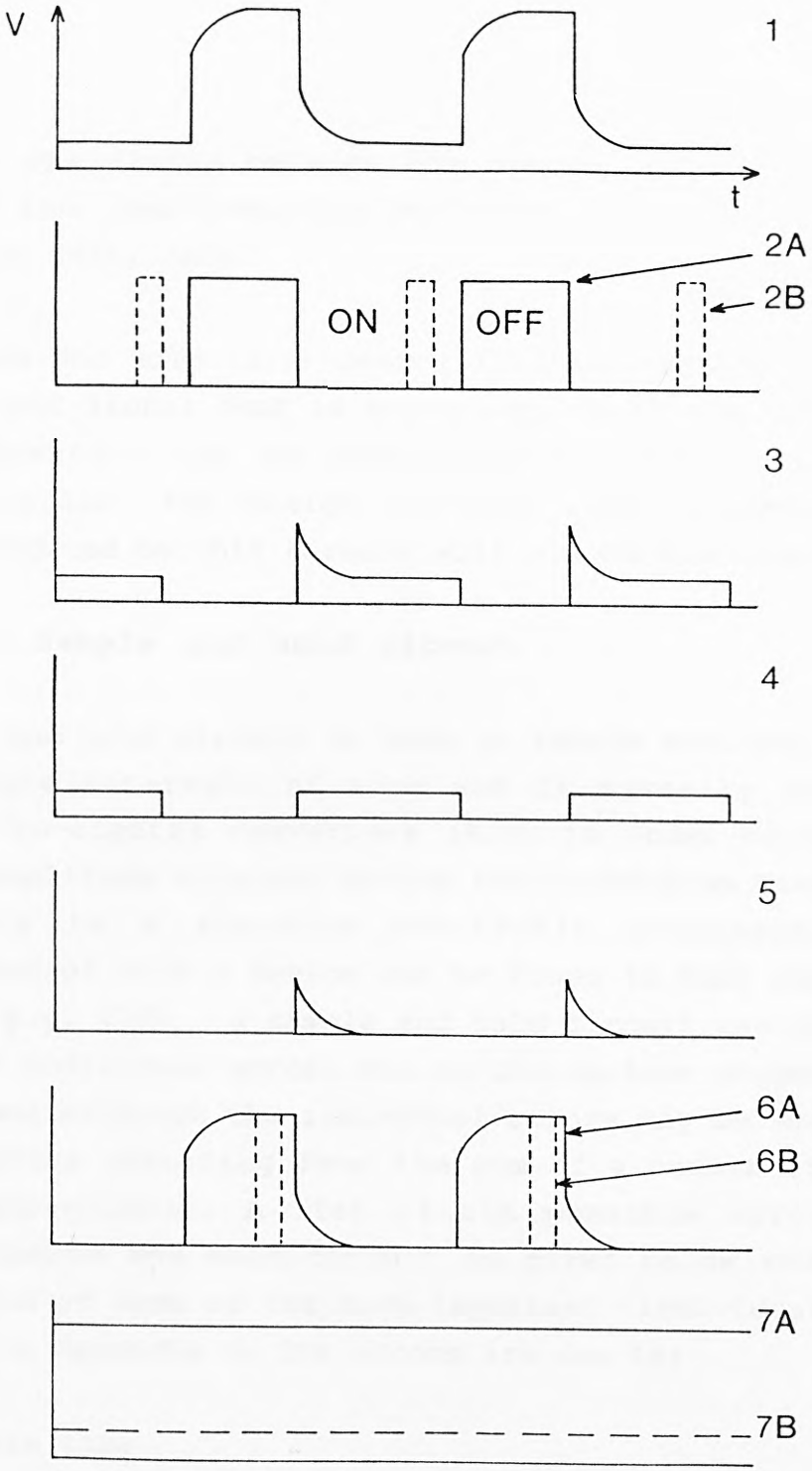

Figure 2.18 - Signal at various stages

1: Output of detector

2a: Control pulses for electronic switch

2b: Sample pulses to remove dc offset (S/H)

3: Output of first analogue switch (S/W_1)

4: Output of second analogue switch (S/W_2)

5: Output of difference amplifier

6a: Detected signal with dc bias removed

6b: Pulses for sample and hold device (S/H_2)

7a: 'Probe' dc signal

7b: 'Reference' dc signal

resistor was placed between the output of the switch and input of the non-inverting amplifier, which in this case, was set at unity gain.

The sample and hold (S/H) device (LF398H) retains the value of the input signal that is being sampled at its output. The sample duration can be controlled by the width of the sampling pulse. The design criteria used to minimise the errors produced by this circuit will now be discussed.

2.2.6.1 Sample and hold circuit

A sample and hold circuit is used to sample analogue signals at discrete intervals of time and is normally used with analogue-to-digital converters (A/D) in order to hold the sampled amplitude constant during the conversion time of the A/D. This is a standard electronic component and a description of such a device can be found in most electronic manuals, e.g. (76). A sample and hold circuit can produce a number of individual errors due to the various stages of the circuit and although the individual errors may be small, the uncertainties resulting from the sum of a number of errors may be appreciable. A list of the possible errors in a typical sample and hold circuit is given below and a full explanation of some of the more important individual errors is given in Appendix 6. The errors are due to:

1) Aperture time
2) Setting time
3) Voltage droop
4) Switching transient
5) Feed-through of a.c signal via the capacitance of the switch
6) Dielectric absorption (exists across capacitor after discharge caused by relaxation time of dipoles).
7) Gain error

The most important feature of a sample and hold circuit

design is the choice of the 'hold' capacitor, which is selected to minimise these errors for the required sampling time. The 'hold step', 'acquisition time' and 'droop rate' are the major considerations in the selection of a hold capacitor value. The selection of a suitable value was done with the aid of graphs given in the manufacturer's data sheets (77). A significant source of error in an accurate sample and hold circuit is dielectric absorption in the hold capacitor. A polyester capacitor, for example, may 'sag back' up to 0.2% after a quick change in voltage. A long 'soak' time is required before the circuit can be put back into the hold mode with this type of capacitor.

The sample and hold circuit used offered less than 10μs acquisition time and when sampling high frequency signals (i.e >10kHz), the circuit layout and the dynamic range of the signals become very important in reducing errors from this circuit.

2.2.6.2 Bias level separation from the input signal

The exponential decay of the fluorescence resulted in a signal which had a small dc level introduced by bias voltages, dark current noise in the photodiode and ambient light variations. To eliminate this, the signal was sampled at the point on time after 10 decay lifetimes had occurred, as shown in figure 2.18(2B). To do this, the signal passed through a simple first order low-pass filter to produce a steady dc value. A second electronic analogue switch and buffer stage were used to provide square pulses whose heights corresponded to the unwanted dc offsets, as shown in figure 2.18(4). This signal was then subtracted in a differential amplifier from the original exponential pulse, shown in figure 2.18(3). Hence the exponential output was referenced to a zero level corresponding to 'zero light' input, shown by figure 2.18(5). The difference amplifier used had to be carefully designed to ensure that resistor

values were exactly the same. The choice was made from a large batch of resistors of the same value. One of the resistors, R_1, was made variable for finer adjustment. The value of R_1 was preset by applying a known voltage level to both inverting and non-inverting inputs. Since the amplifier provided the difference between the inputs, R_1 was adjusted to give a zero output. All the resistors used had 1% tolerance limits. The errors introduced by a difference amplifier are discussed in Appendix 7. The output of the difference amplifier was then fed to an rms-to-dc converter, which is discussed in section 2.7.7.

The 'probe' intensity information from this signal was retrieved by initially removing the dc offsets in a difference amplifier. Figure 2.18(6A) shows the output of this stage. The signal was then sampled at the point shown by the dotted pulses in figure 2.18(6B) by a sample and hold device to give a voltage level (o/p_1), figure 2.18(7A), corresponding to the intensity of the detected light.

2.2.7 Rms-to-dc conversion

The total intensity of fluorescent emission can be analysed by evaluating the area under the exponential decay. Using a simple integrator type of circuit for this has one major disadvantage in that the output tends to drift due to op-amp offset voltage and bias currents (76). This effect can be reduced by using an FET amplifier with low bias currents and discharging the voltage across the integrating capacitor through an FET switch, which is placed in parallel with this capacitor. A more suitable approach is to use an rms-to-dc converter IC which is capable of evaluating accurately the rms value of a wide range of waveforms containing ac and/or dc components. The rms value of the exponential emission signal gives a dc value corresponding to the integrated fluorescent emission, (o/p_2) as shown in figure 2.18(7B), i.e the total light of the fluorescence emission. An

explanation of the principles of operation of the rms-to-dc converter IC is given in the data sheet in Appendix 8. It has a number of standard features to improve the accuracy and linearity, and has to be calibrated against a standard digital voltmeter.

2.2.7.1 Rms-to-dc converter performance considerations

The rms-to-dc converter IC is simple to set up for the majority of 'high' accuracy rms measurements, requiring only an external capacitor to set the averaging time constant. This device will compute the rms values of both ac and dc signals. If the input is a slowly-varying dc, the output of the device will track the input exactly. At higher frequencies, the average output will approach the rms value of the input signal. The actual output will differ from the ideal output by an average or dc error and some small amount of ripple. The dc error is dependent on the input signal frequency and the value of the capacitor setting the time constant. From the data sheets, for frequencies above 5kHz, the input voltage has to be kept within the required limits i.e. as indicated by the graphs in the data sheets, otherwise large errors in measurement can result (see data sheet in Appendix 8).

The dc output may have a certain level of ripple and this can be reduced by adding extra components i.e. a two-pole active filter stage, to give even greater ripple reduction without substantially increasing the settling time of the circuit. Such a circuit offers greater stability and accuracy than a conventional integrator type of circuit which may require an electronic switch to discharge the integrating capacitor at the "switch-on" time of the circuit.

2.2.7.2 Digital means of measuring the Intensity and RMS values

As an alternative, the complete input signal, as shown in figure 2.18(1), could be sampled rapidly via a faster sample and hold circuit than that described previously, following which the sampled analogue signal could be converted into a digital signal via an analogue-to-digital converter (A/D). A microprocessor could be used to interpret the results.

There are several problems with this type of approach but the cost and processing time are the most severe limitations compared to the previous circuit. The square wave to be sampled is at a frequency of 250Hz, which is relatively low, and it can be sampled accurately with the sample and hold device described previously. However, the exponential component is of approximately 1ms duration and the Fourier spectrum of its frequency components must be known. For example, say that a set of samples is required to represent the waveform with an accuracy of 1%. The highest frequency component will need to be considered above which frequency the components of the exponential contribute less than 1% to the total waveform intensity. Once this limit is known, then the exponential needs to be sampled at least twice that frequency (according to the sampling theorem). However, this will not produce a very accurate representation of the exponential in the store of the microprocessor and thus there is a need to sample at least ten or twenty times this frequency. Alternatively, to reduce the number of samples required an exponential decay function could be programmed into the microprocessor so that it can reproduce to an adequate degree of accuracy a representation of the complete exponential signal. The sampling in either case needs to be very fast, which increases the cost of the scheme. Once this signal is sampled it has to be converted into a digital form via an A/D. The cost of A/Ds is proportional to their speed of conversion and for

conversion times of 0.1μs with resolution of 10 to 12bits, such as would be needed, the cost of single A/D can be up to a hundred pounds.

Finally, the processing time of the microprocessor is significantly increased but this can be reduced by using a 16-bit microprocessor instead of a 8-bit processor or by increasing the clock frequency. The major disadvantage of this technique is the higher cost involved compared to the rms-to-dc converter chip, and one objective of this work was to investigate low cost schemes for optical sensors.

2.2.8 Oscillator and combinational logic

The Schmitt nand gate, resistor and capacitor network generates a square wave with a frequency of 250Hz. The waveform produced by this circuit was not a perfect square wave, the ON period (1.5ms) being shorter than the OFF period (2.5ms), caused by the inherent hysteresis of the Schmitt gate. The frequency of operation could be adjusted by changing the values of the resistor or the capacitor in the network. The oscillator provided triggering for the 555 timer circuits, which in conjunction with combinational logic, provided the required pulses for the analogue switches and sample/hold circuitry. The 555 timers operated in the monostable mode, triggering on the negative edge of the pulses arising from the oscillator output. This allowed a great deal of flexibility in varying the pulse durations and were simple to implement.

2.2.9 LED drive circuit

There are a number of LED drive circuits that could be used and some examples are given by Senior (74). The simplest drive circuit is that shown in figure 2.19, using a

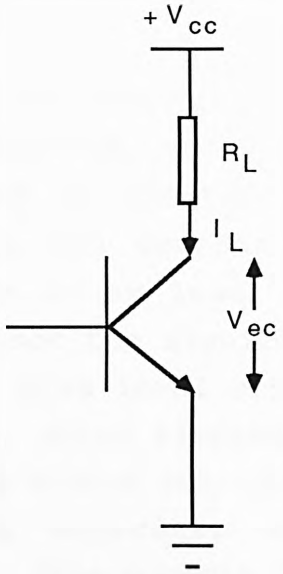

Figure 2.19 - Transistor Switch Circuit (where R_L: Load resistor; I_L: Load current; V_{cc}: Supply voltage; V_{ce}: Collector-emitter current).

transistor as a switch. This type of circuit offers the advantage of very reliable high speed operation. The transistor is allowed to be switched ON or OFF by the voltage applied to its base. The current through the load will very nearly be V_{CC}/R_L and it is essentially independent of the transistor characteristics. The power in the load will thus be very nearly $V_{CC}I_C$, where I_C is the collector current, when the transistor is ON. The collector-emitter voltage is usually about 0.2 Volts. Thus, in the ON condition, the power dissipated in the transistor will be $V_{CE}I_L$, which is about 2% of that dissipated in the load. The value of the switched load current may be determined by either the power dissipation or the current rating for the particular transistor used. Additionally, by using pulses to switch ON a transistor, the peak power delivered to the load can be made several orders of magnitude greater than the average power. This enables greater peak intensity levels to be emitted from LEDs.

2.3 SOURCES OF ERROR RESULTING FROM THE CIRCUIT DESIGN

There are many sources of errors in this initial circuit design and which are improved, to a certain degree, in the latter design discussed in chapter 3. The noise in the detector is unavoidable but certain steps, as have been discussed, can be taken to at least minimise its effect. The offset voltages are not too significant at this stage as they are removed by the bias level separation circuit. The sample and hold circuit, which samples this bias level will obviously introduce some errors but this can be minimized be choosing the sampling capacitor value with care and calibrating its output. This circuit is likely to introduce two forms of errors: systematic and random drift errors.

The systematic error in this circuit is caused by small dc bias levels appearing in addition to the sampled waveform. There is an offset trimmer resistor that should be added to the circuit in order to minimise this effect. To do this, a known precise input voltage is applied and the trimmer resistor, adjusted to give the correct output voltage. The main problem with systematic errors is that they are not constant and will generally vary from one experiment to another. Very often they are constant or at least vary slowly over the time required to make a single measurement.

Random errors and random drift errors can also occur in the sample and hold circuit. Since the signal being sampled contains some noise, the sampled output value will contain a mean value of this noise plus the signal itself. Since any two mean values are unlikely to be the same, the output will contain a small random variation due to this noise. It cannot be totally eliminated but averaging by the sample and hold circuit does reduce the initial, much larger noise variations in the signal. In addition, as all electronic components are affected by temperature, there is also likely to be a small drift in the circuit with time which will add

a dc error voltage to the output. Such a drift can only be minimized to within the required accuracy of the instrument, but never totally eliminated. In the circuit in figure 2.8, the bias voltage variations are eliminated separately for the probe and exponential signals. This introduces extra components in the circuit and also extra sources of error. In the circuit design discussed in chapter 3, the bias voltage variations are eliminated before the signal is separated into its exponential and probe components. This separation can be achieved since the exponential and probe components of the detected signal occur at different time intervals.

The second source of error in the circuit of figure 2.8, is introduced in the difference amplifier. This stage is likely to produce systematic errors in the measurement but these can be minimized by careful selection of the resistor values which were matched to within one ohm. A further improvement to this circuit is recommended in chapter 3, but this was only realized after the work in chapter 3 was completed. However, such a circuit could be used to improve the system for future work.

Finally, the last source of error in this circuit comes from the rms-to-dc converter. This was minimized by calibrating the circuit against a standard digital multimeter with a variable dc and ac voltage source. A comparison of this circuit to give reasonably accurate rms values of the exponential pulse were made against the same digital voltmeter. The voltmeter essentially employs the same type of rms-to-dc converter circuit to calculate the rms value of the signal being measured and so a direct comparison was possible.

2.4 RESULTS OF INITIAL DEVICES

Both systems were tested in the same manner and the referencing scheme used was verified within the temperature region studied.

2.4.1 Test Of Fluorescence Referencing Scheme

The requirement of this scheme was to verify that the reference light level detected at the photodiode represented changes in the optical path due to coupling variations and not those due to the parameter being measured. This means that any mechanical effects at elevated temperatures where the alignment of components actually changes and consequently alters the light levels transmitted, should be automatically taken into account. The close relationship between the fluorescence signal and the incident light actually falling on the RG glass is shown in figure 2.20. To obtain this graph the RG glass was removed from the stainless steel housing thus eliminating the 'probe' intensity variation due to its presence. The signal was thus only affected by the thermal expansion effects of the sensor due to temperature.

The significance of geometrical effects is clearly illustrated by the variation with temperature of the detected probe signal as the LED was driven by a constant current and the 'sensor' heated. Over the temperature range studied, the received 'probe' signal varies by ~6% but it was of great significance for the fidelity of the measurement that the detected 'fluorescence' signal followed it very closely over this range, to $\pm$1% (when normalized to the same peak intensity). Consequently, the fluorescence referencing technique can be seen to be an accurate means of monitoring the actual signal level incident at the sensor element.

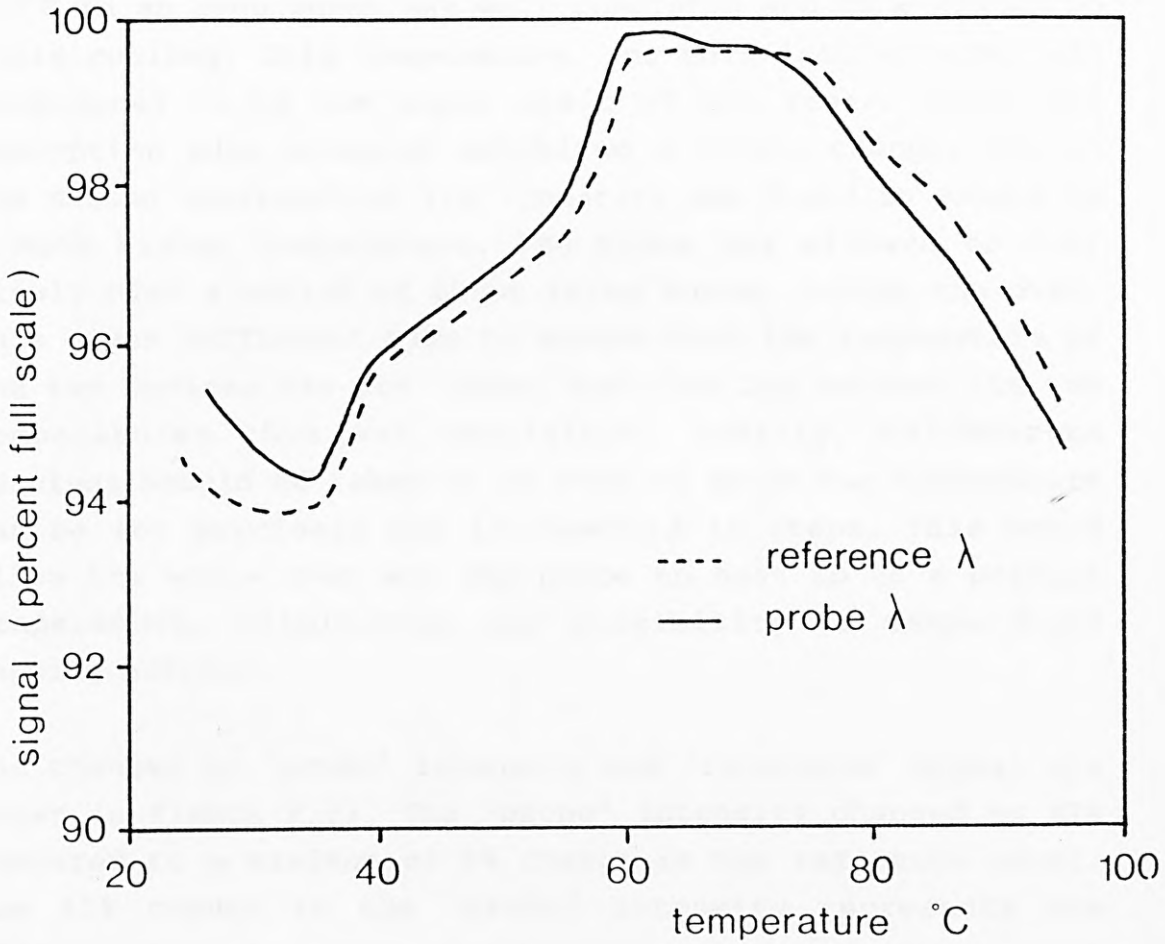

Figure 2.20 - Test of referencing technique - variation of 'probe' and 'reference' signals with RG glass removed

2.4.2 Calibration of the 'housed' sensor

Both devices were calibrated with respect to a thermocouple held in close contact. A thermocouple, as a secondary standard, was used at this stage as it was sufficiently accurate to investigate the performance of the device. The probe enclosed in the housing was heated to a temperature of 120°C in an oven which was well insulated and thus prevented rapid cooling. This temperature, for this initial work, was considered to be the upper limit of the region where the absorption edge movement exhibited a linear change, but in the second construction the linearity was found to extend to a much higher temperature. The probe was allowed to cool slowly over a period of about three hours, inside the oven. This gives sufficient time to ensure that the temperature of the two devices was the same. The time lag between the two temperatures thus was negligible. Ideally, calibration readings should be taken in an oven in which the temperature can be set precisely and incremented in steps. This would allow the whole oven and the probe to heat up to a precise temperature, eliminating any possibility of temperature lagging effects.

The changes in 'probe' intensity and 'reference' signal are shown in figure 2.21. The 'probe' intensity changed by 41% compared to a maximum of 5% change in the reference level. The 41% change in the 'probe' intensity represents the change due to the absorption edge movement over approximately 100°C change in temperature. The maximum of 5% variation in the reference signal represents the variation due to thermally induced geometrical changes in the sensor head. The ratio of the 'probe' to 'reference' signals gave a normalized transmission as a slowly varying function of temperature deviating only slightly from linearity, as shown in figure 2.22. The slope of the line was measured to be $0.48^{\circ}C^{-1}$ and gave a standard deviation of 0.11 for the points relative to the best line fitted through them. This standard deviation gives an equivalent temperature variation

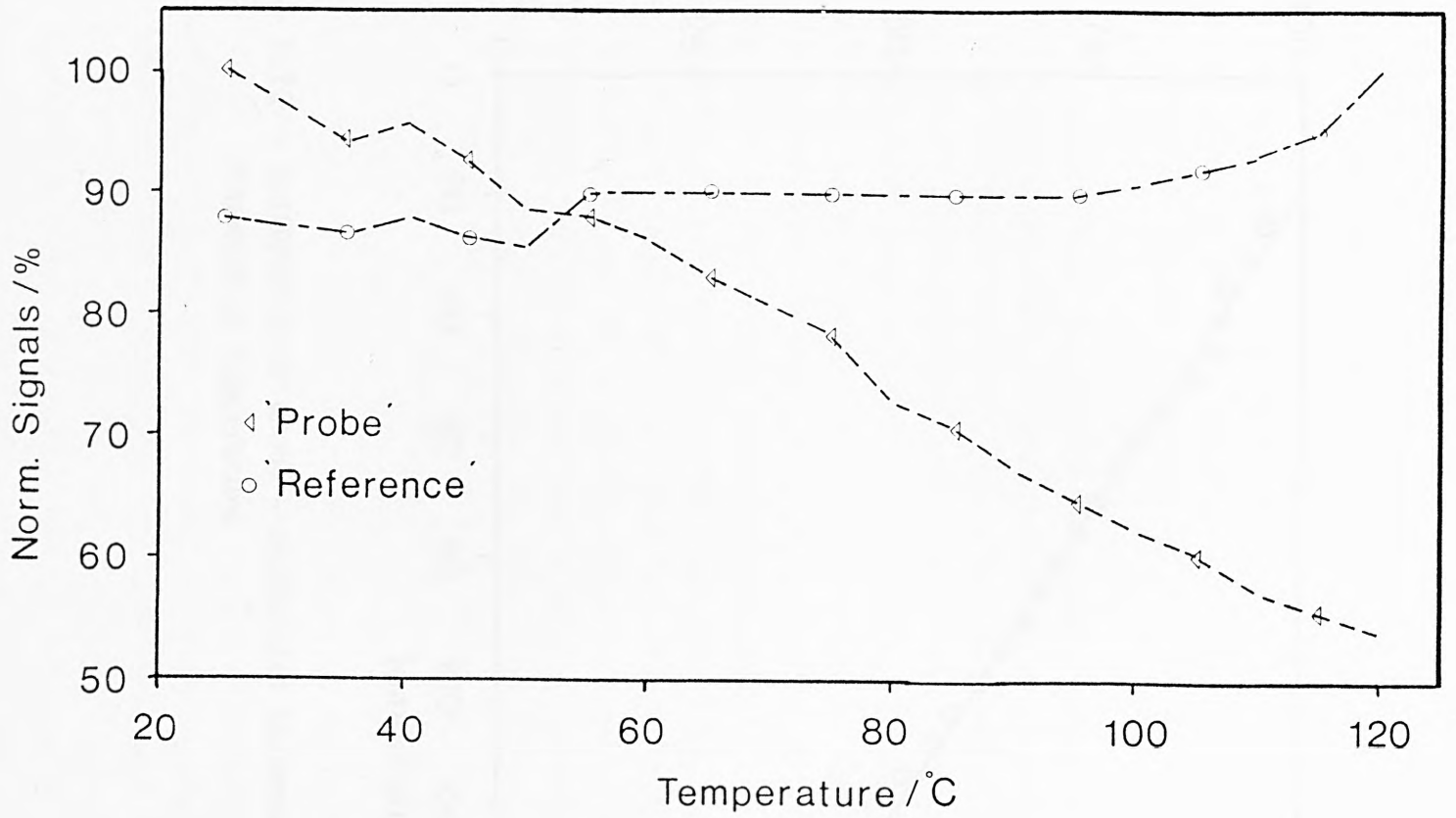

Figure 2.21 - Graph showing the variation in 'probe' and 'reference' signals with temperature

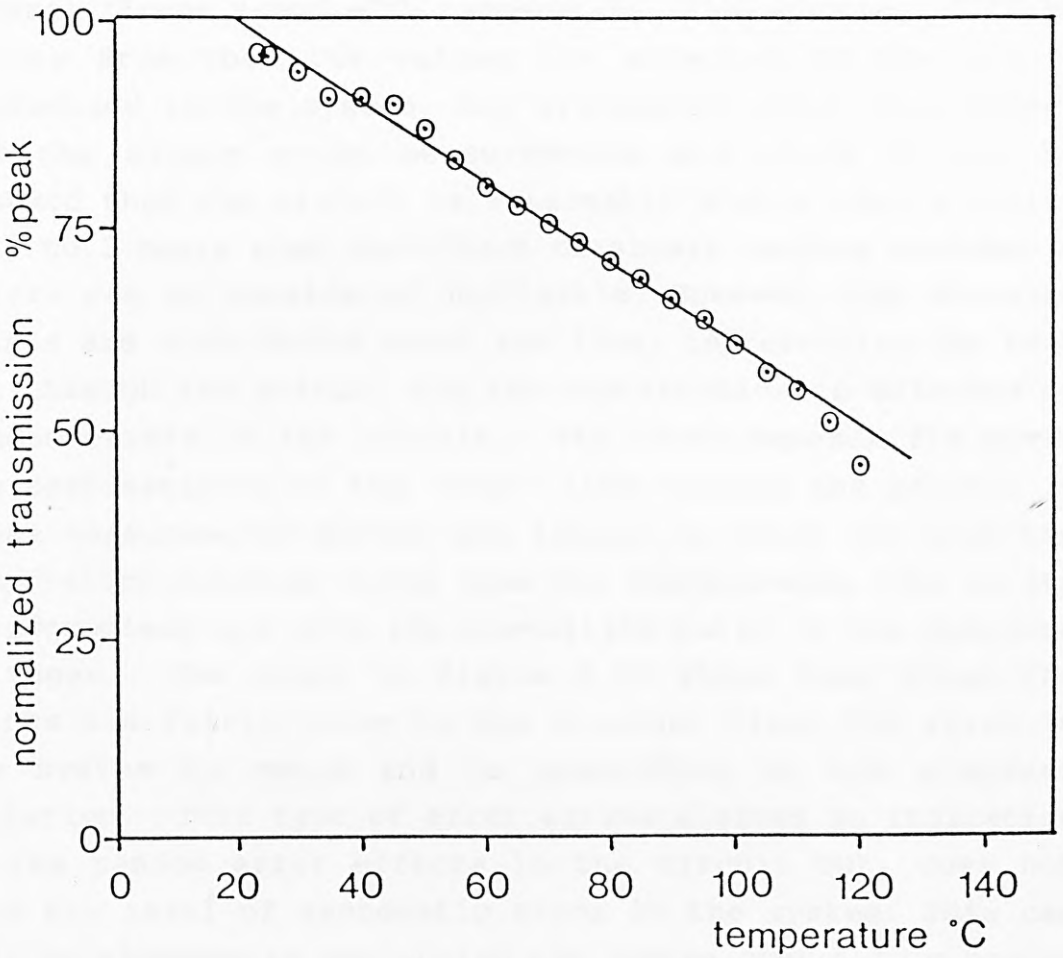

Figure 2.22 - Calibration of probe - normalized transmitted signal as a function of temperature

of 0.3°C. The most extreme point from the line, deviated by 4.6%, an error of 10°C. However, for most of the points lying near or on the line, the inaccuracy was considerably lower.

The quoted accuracy or precision of measurement stated above, are for single point measurements which follow a general linear trend with temperature. The accuracy of these values from the true values are affected by the errors introduced in the system. Any systematic error will affect all the single point measurements and since it can be assumed that the circuit is reasonably stable over a period of 2 to 3 hours then the effect of slowly varying systematic errors can be considered negligible. However, the measured points are distributed about the line, representing the best fit through the points, and the distribution is affected by random errors in the circuit. The least squares fit gives the best estimate of the 'true' line through the points. In these measurements errors are likely to exist for both the temperature readings taken from the thermocouple (due to its inaccuracies) and from the normalized ratio of the measured voltages. The graph in figure 2.22 shows that since the points lie fairly close to the straight line, the error in the system is small and is quantified by the standard deviation. This type of error estimate gives an indication of the random error effects in the circuit but, does not show the level of systematic error in the system. This can only be assessed by monitoring the system over a long period of time for a fixed optical probe temperature and configuration. However, any drifts in the system would be a function of the drifts in the optical referencing scheme and the electronics and hence it would have been impossible to say which of the two contributed to this change.

The response time for the probe is the time required for it to change from one steady light intensity reading to another for a given temperature change. In practice, the probe is heated to a known temperature e.g. 100°C and quickly plunged

into cold water or a much lower temperature environment. The time taken for the light intensity levels to reach a steady value would give an approximate response time of the sensor. The sensing and electronic processing used had estimated response times of tens of milliseconds, but the two multimeters used to give the dc values had, typical, response times of hundreds of milliseconds. Therefore these effects can be ignored by comparison to mechanical effects. The theoretical response time of the stainless steel part of the probe, however, was estimated at ten seconds with the addition of two to three seconds for the glass elements. This is under transient conditions. However, under normal circumstances the cooling rate of the probe is determined by essentially two laws which are discussed in Appendix 9.

The drift in the system was measured as a change in the ratio of the signals with time, which gave an indication of the stability of the electronics and the intensity output of the LED. For a stable temperature, the drift in the received value corresponded to 0.5% over 30 minutes. Normally, electronic devices and especially LEDs, take a certain time to reach steady state values hence all measurements should be recorded after this warm up period. A re-chargeable battery in the control box used as a "keep alive" could keep the electronics at the operating temperature and overcome the warm up period.

2.4.3 Calibration of the resin-fixed sensor

The calibration of the resin-fixed sensor was conducted in the same manner as for the stainless steel housed sensor. The sensor was subjected to much higher temperatures to investigate the linearity properties of the absorber glass. It was also tested at below room temperature in order to examine its usefulness in this region. Figure 2.23 illustrates the 'hot' regime in the temperature range of 20-200^{o}C. The 'reference' and 'probe' signal values are shown to vary in a similar manner. The graph also shows a sudden

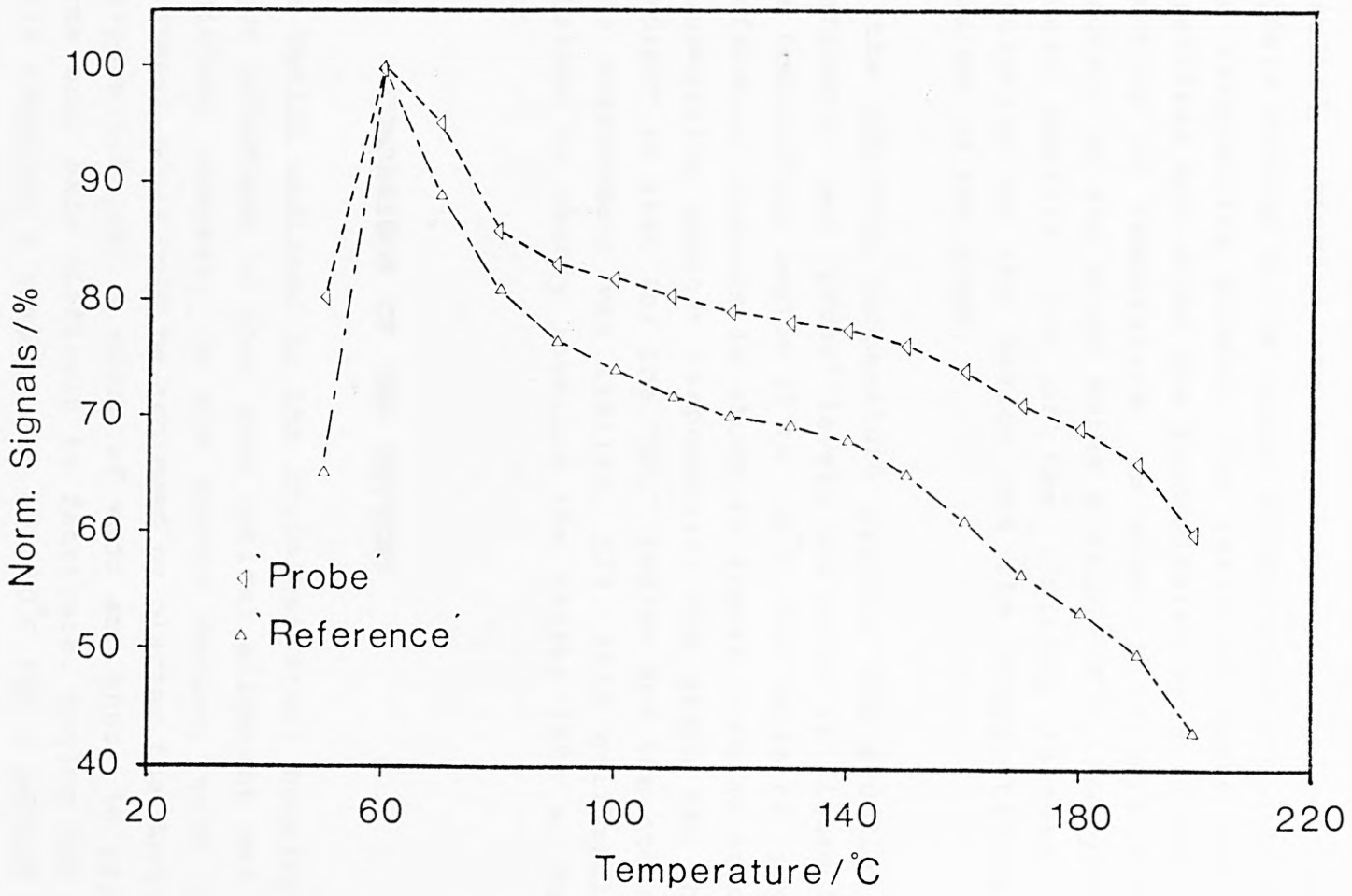

Figure 2.23 - Graph showing the variation in 'probe' and 'reference' signals with temperature

change near 60°C, this is likely to have occurred in the probe head. The resin may have fatigued and moved the fibre relative to the glasses or the glasses may have parted. This would have caused an air-gap to be created between the surfaces and a change in the refractive index would have resulted, altering the coupling. As can be seen, both signals respond to the change illustrating the usefulness of the referencing scheme. The ratio of these values was normalized and shows the transmission as a slowly varying function of temperature, as shown in figure 2.24; the gradient of the graph being 8.2×10^{-3} K^{-1}, and yielding a linear profile. One of the limiting factors of the resolution of the device was the comparatively small gradient of the graph.

In the sub-room temperature region, the profile of the 'reference' and 'probe' levels are shown in figure 2.25 in the temperature region 20 to -60°C. The ratio of 'probe' to 'reference' signals is shown in figure 2.26 as normalized transmission against temperature. The graph had the same gradient as that for the "hot" regime and the accuracy of this measurement was similar, ±2%. This calibration was obtained by gently lowering the sensor into a 'dry ice' bath.

2.5 COMPARISON OF THE DEVICES

The device enclosed in the stainless steel housing had a major advantage in that good optical alignment was easily achieved, whereas, in the second device, good optical alignment could only be achieved by placing the device in a V-groove cut into a piece of wood and thus, in practical terms was, more difficult to fabricate. Curing the Epotek resin required a temperature of 150°C for a period of one minute and for this period the two fibres had to be held in fixed positions by adhesive tape. This made the construction

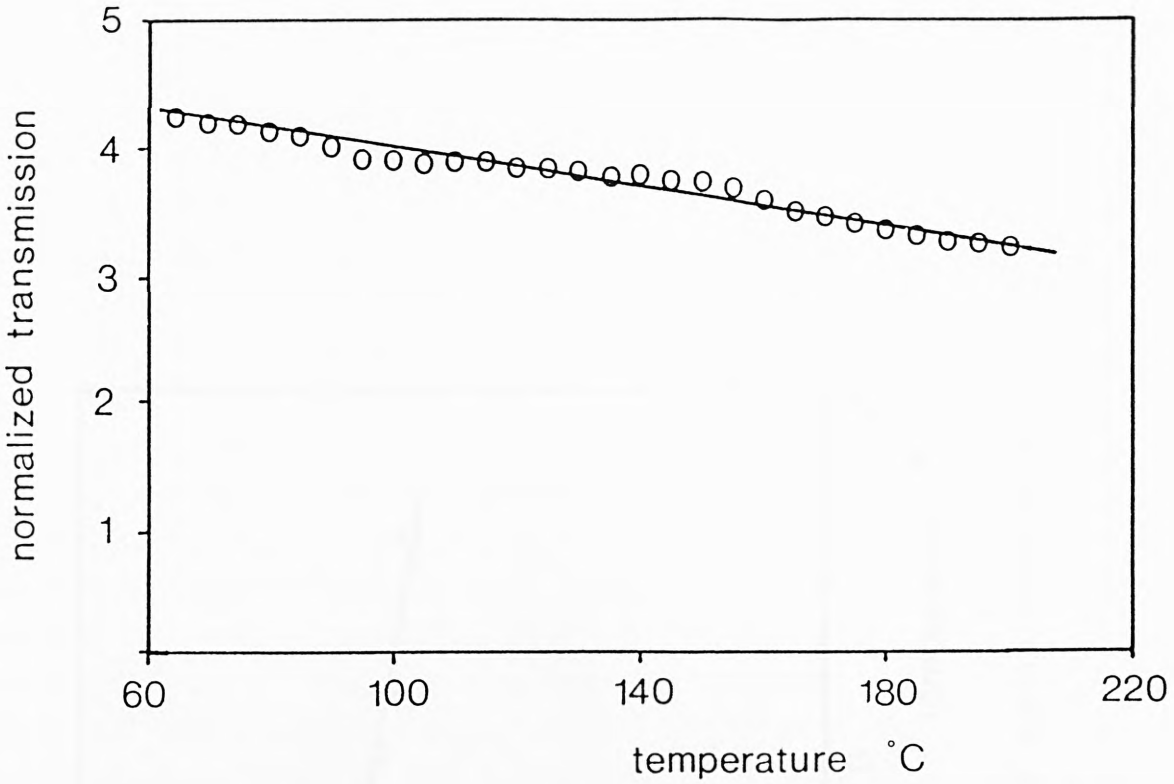

Figure 2.24 - Device calibration - normalized transmission as a function of temperature (hot regime)

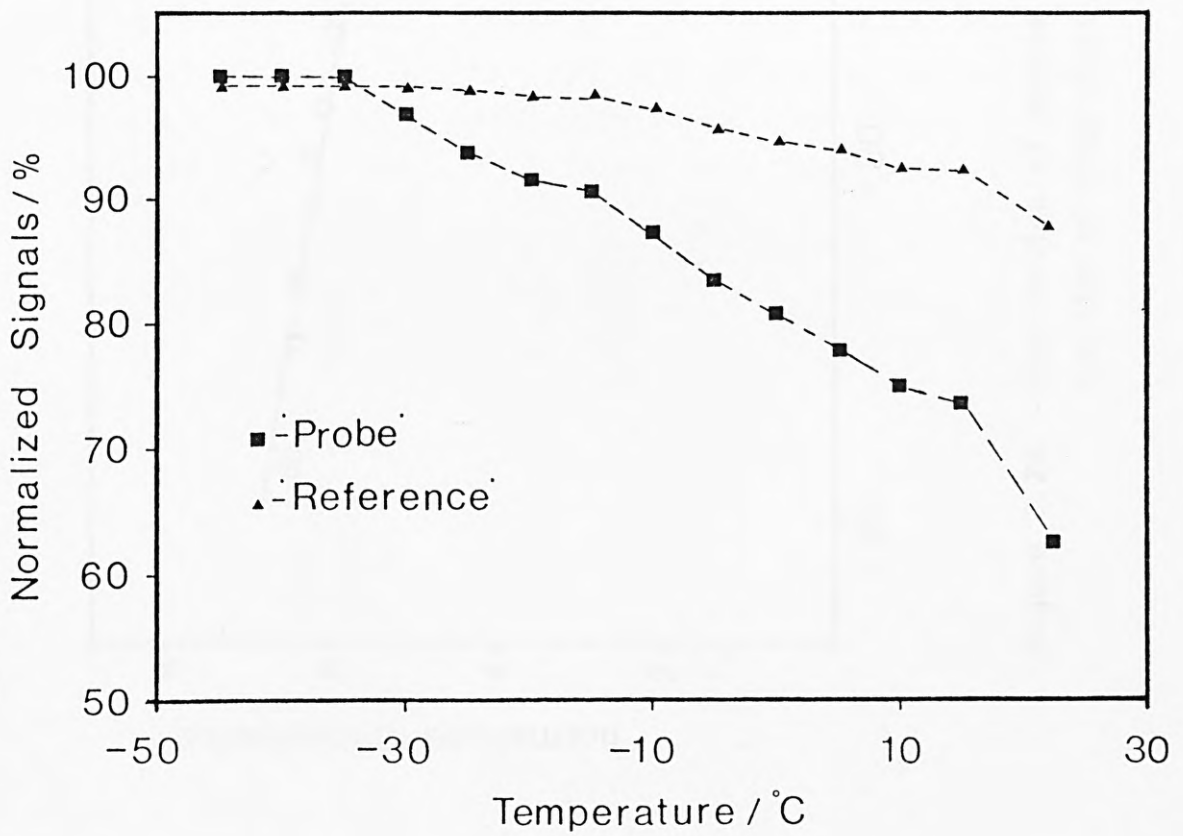

Figure 2.25 - Variation of 'probe' and 'reference' signal with temperature

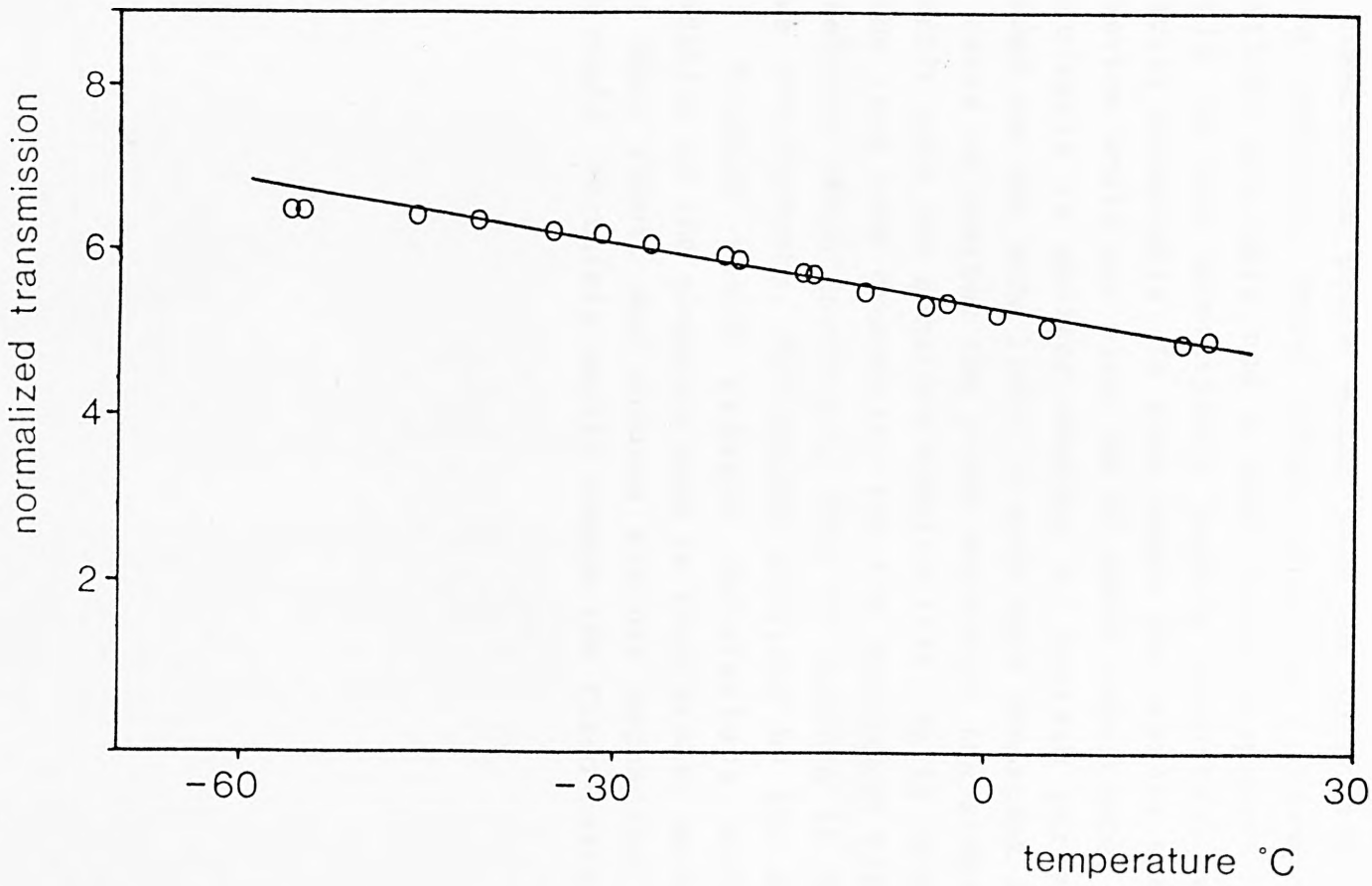

Figure 2.26 - Calibration of device - normalized transmission as a function of temperature (cold regime)

of such a probe that much more difficult since it was important to retain good optical alignment during the curing process. The stainless steel housing, thus, overcomes this alignment problem by its inherent design.

In practice, where fast thermal response may be required, the fixed-resin probe would have an advantage over the housed version. More often than not, however, such situations are rare and a much lower response time, for example in the electricity supply industry, would be perfectly acceptable. In such cases the overall accuracy of the device would not also, be of great importance; since it is desirable to monitor whether a certain parameter has exceeded the set safe limit. A much more important aspect in such cases is whether the probe maintains its stability and low drift over its required working life. It is necessary to provide long term protection for the measurand elements of the sensor, which invariably have to operate in harsh and severe environments. Protection provided by the stainless steel housing would prevent deleterious effects of degradation of the elements used in this probe. Mechanically it is more robust and ensures against mechanical shocks, which could certainly easily damage the fixed-resin probe.

Chapter 3

PRISM-DESIGN SELF-REFERENCED ABSORPTION THERMOMETER

3.0 PRISM-DESIGN SELF-REFERENCED ABSORPTION THERMOMETER

This thermometer is a refinement of the transmission type self-referenced sensor described in chapter 2. It was considered important that such development work should continue - to miniaturize and thereby reduce the volume of the sensor head and make the device more suitable for use in an industrial environment. This could increase the acceptability of such sensors for applications outside the laboratory. The principle of the device is the same as that for described in chapter 2, save for the construction of the probe head and additional refinements to the electronic circuitry, which was housed in a box along with a microprocessor for instant calculation and the output of the ratio on a liquid crystal display (LCD).

3.1 OPTICAL DESIGN

The neodymium-doped glass fluoresces isotropically, i.e emission of radiation is in all directions. The best fluorescence signal is obtained by capturing emitted light from the glass at right angle to the direction of the pump light. This method of light collection optimizes the ratio of fluorescence to the scattered pump light received since it minimizes the amount of scattered light collected. The optical temperature sensor was constructed from a piece of Nd^{3+} doped phosphate glass material (Q-100 Kigre Inc.,) cut into a small rectangle of a few mm^3 volume. This was bonded with Epotek resin (type-353ND) to a piece of RG-830 glass which was cut and polished into a right-angled prism to provide total internal reflection, and thus the return light path was on the same side of the sensor, as is shown in figure 3.1.

The optical temperature sensor was constructed in the

following manner. Firstly, the neodymium doped glass was cut from a standard size of $5mm^2$ by 3cm in length, available

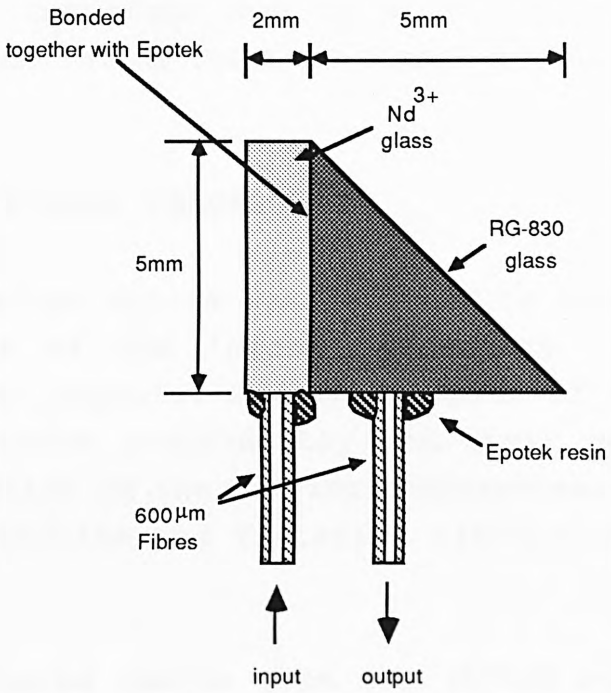

Figure 3.1 - Schematic of the sensor

from Kigre Inc.(USA). A length of 5mm was cut from the end which was then polished flat; all the other sides were available as polished. The absorption edge filter glass was cut ensuring that the sides at right angles were of the same length as the piece of neodymium doped glass. All sides, including the hypotenuse, were polished by hand. A thin layer of Epotek resin was applied to the joining sides and the end faces, which were to receive the fibres, were aligned before curing in a preheated oven. Further resin was deposited subsequently along the length of the joining edges to strengthen the bond.

The addressing and receiving PCS 600 (600µm diameter core) silica fibres were cut, ends polished and glued to the two glasses in positions ensuring maximum optical coupling. For test devices, the optimum positions of the fibres could be adjusted as the resin cured by monitoring the signals received. The whole sensor was coated with a layer of

aluminium, by evaporation, to produce a tough reflective coating to minimise losses through the sides and to prevent refractive index changes at the surface of the prism at the glass:air interface due to moisture, which could cause fluctuations in the received signal intensity.

3.2 SIGNAL PROCESSING

The electrical system was designed to separate in time the variations of the 'probe' intensity and fluorescence 'reference' signals. The intensities of these two signals were monitored individually and their ratio obtained, as representative of the varying temperature. The block diagram of the detection and filtering circuit is shown in figure 3.2.

A high powered GaAlAs type LED (500μW output in a package for easy coupling to the fibres) was modulated at 250Hz with a square wave pulse. The received signals from the Nd:RG sensor were detected by a single RCA p-i-n diode which was anti-reflection coated for optimal response at 1.06μm and was connected to an amplifier in a transimpedance configuration which gives high bandwidth with a good signal-to-noise ratio. This enabled the 'probe' and 'reference' wavelength to be separated in time, rather than optically, the former being more convenient and eliminating the need for a further optical filter. This ensured that only one detector was used. Figure 3.3 shows the signal at various stages of processing. The detected signal was a square wave with an additional exponentially varying component on the rising and falling edges (representing fluorescent absorption and emission respectively) as shown in figure 3.3(1). The signal had a small level of dc bias due to ambient light coupled into the fibres. This was eliminated by sampling the signal when the LED was OFF (figure 3.3(2A)) and subtracting this dc value from the original input, using

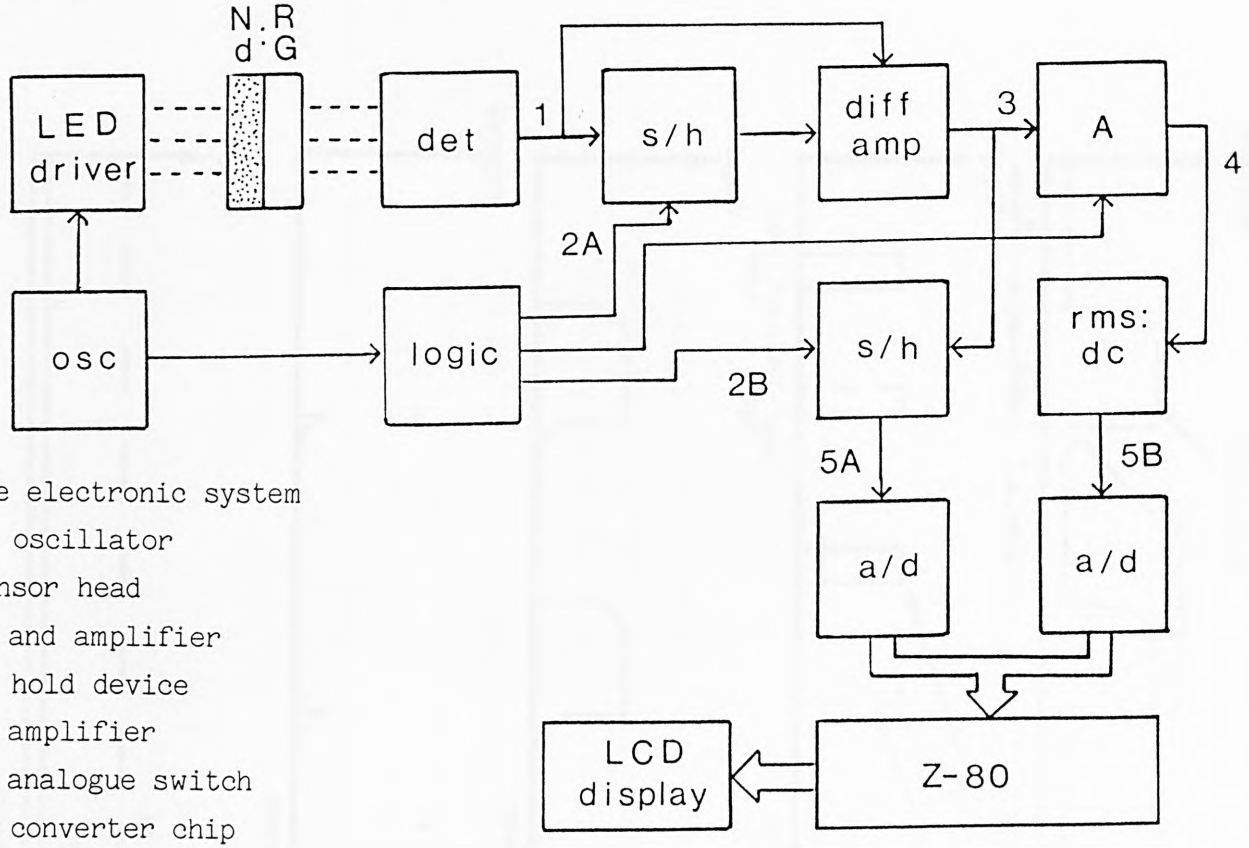

Figure 3.2 - Schematic of the electronic system

OSC: Electronic oscillator

Nd:RG: Optical sensor head

Det: Photodiode and amplifier

S/H: Sample and hold device

Diff amp: Difference amplifier

A: Electronic analogue switch

rms:dc: Electronic converter chip

Logic: Combinational logic circuitry

A/D: Analogue-to-digital converter

Z-80: Microprocessor

(Numbers refer to signal outputs shown in figure 3.3)

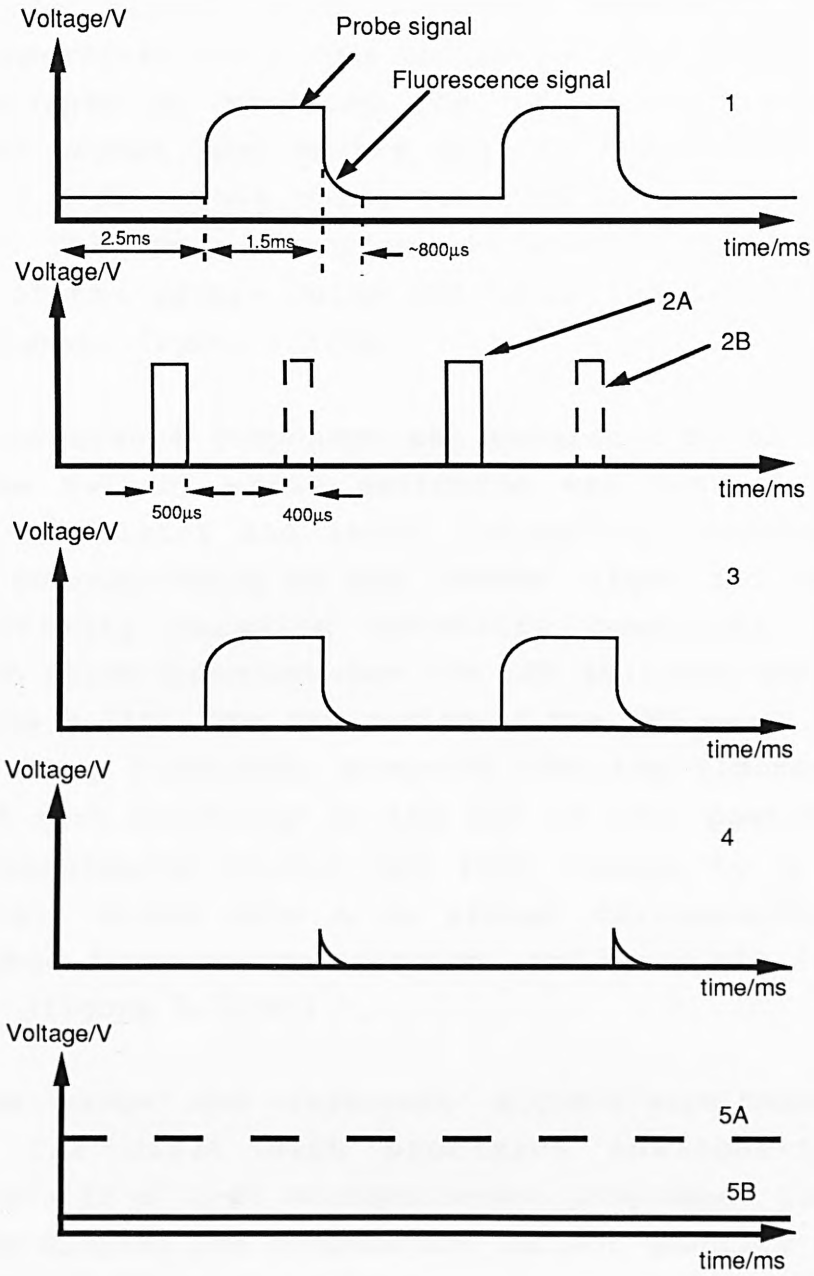

Figure 3.3 - Signals at various stages of processing - numbers refer to outputs at various stages shown in figure 3.2.

a differential amplifier to give the signal shown in figure 3.3(3). Hence, the signal was referenced to a level independent of ambient light under normal usage. The signal was then processed in two different ways to obtain the 'reference' and 'probe' signals.

The 'probe' signal, which underwent increasing attenuation with temperature due to the absorption edge shift in RG-830, was obtained by sampling the square wave part of the received signal just before the LED turned OFF (shown in figure 3.3(2B)) this being achieved by a sample and hold circuit. This gave a constant dc level proportional to the height of the square pulse and hence the intensity of the input signal, figure 3.3(5A).

The fluorescence component was separated by an electronic analogue switch, whose switching was controlled by the master oscillator and logic circuitry, eliminating the signal corresponding to the 'probe' light and leaving the exponentially decaying intensity component i.e. that emission which occurred when the LED switched OFF, as shown in figure 3.3(4). The OFF period of the LED was 2.5ms, which was 10 decay lifetimes, ensuring that the fluorescence has reached zero intensity at the end of this period of time. The fluorescence signal was then passed to a rms-to-dc converter, which gave a dc signal corresponding to the integrated fluorescence emission, and hence the 'reference' signal, (figure 3.3(5B)).

Both the 'probe' and 'reference' signals were passed through two 4 1/2 digit high precision analogue-to-digital converters to a Z-80 microprocessor programmed to calculate and then display the temperature variant quantity which then may be calibrated against an accurate conventional thermocouple.

3.2.1 Details of circuit design

The complete analogue circuit diagram is given in figure 3.4 with the digital circuitry remaining essentially the same as described in chapter 2. This circuit is a modified version of the circuit in chapter 2, but it essentially performed the same function with an additional microprocessor system to evaluate the ratio of the measurand and reference

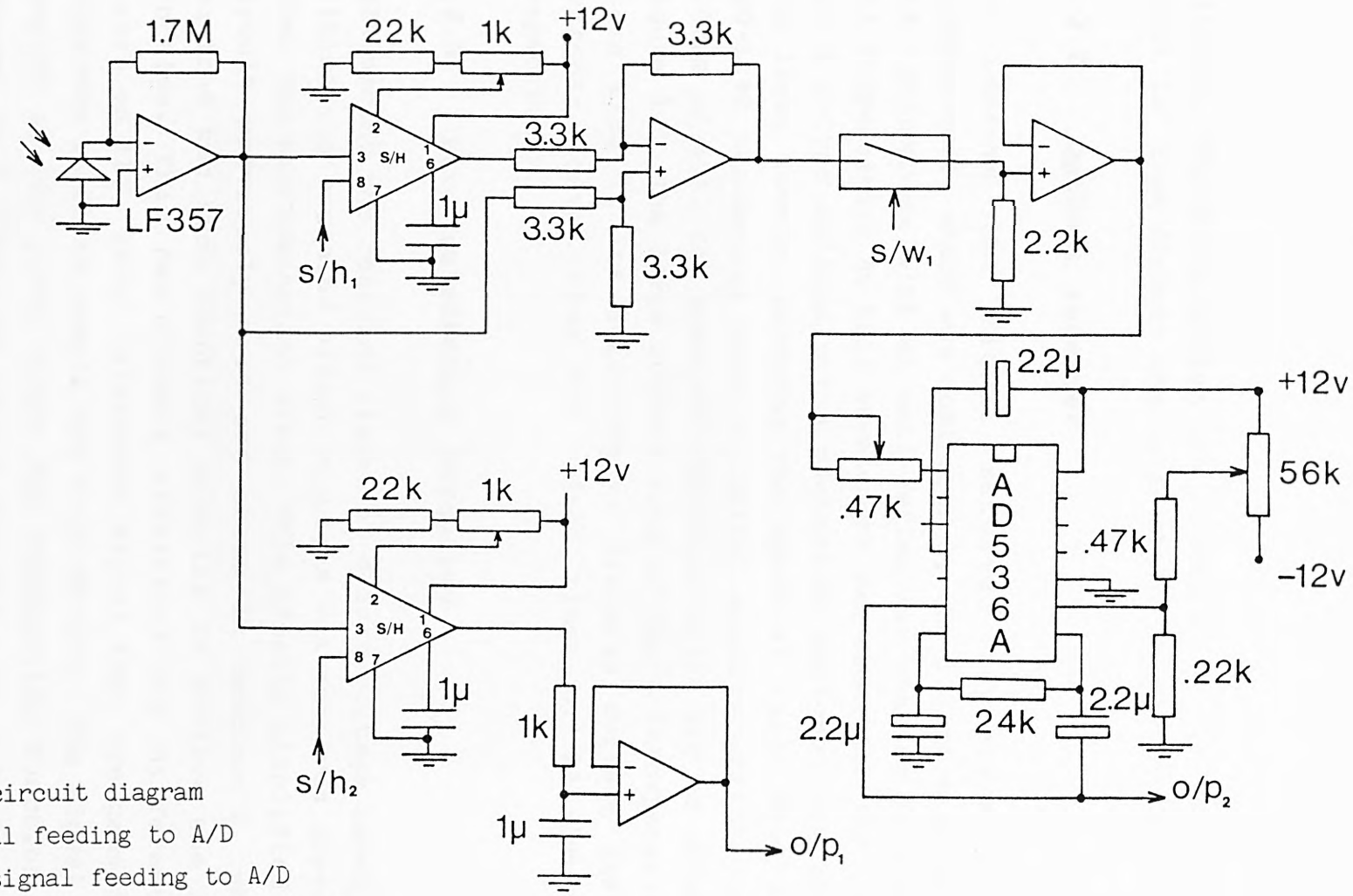

Figure 3.4 - Complete analogue circuit diagram

O/P_1: 'Probe' signal feeding to A/D

O/P_2: 'Reference' signal feeding to A/D

S/H_1, S/H_2 and S/W_2 are inputs from digital circuit shown in figure 2.9.

signals. The whole system was packaged in a small box with 'slot in' type circuit boards as shown in photograph 1.

3.2.2 Optical receiver

To improve the signal received representing the fluorescence, which was dominated by the 1.06μm emission, an RCA photodiode with an anti-reflection coating to enhance its responsivity at this wavelength was used. The RCA C30812 was a p-type silicon p-i-n photodiode designed for use in low light levels, covering the spectral range from about 400-1140 nanometers with a typical quantum efficiency at 1.06μm of 60%. The spectral characteristics are as shown in figure 3.5. The large surface area of $5mm^2$, incorporating a guard ring in its structure to minimize surface leakage currents, gives rise and fall times of 12 and 15ns respectively.

3.2.3 Zero referencing circuitry

Referencing the detected signal to a zero voltage level and eliminating unwanted offset voltages was achieved directly after the photodetection stage. This greatly simplified the circuit previously used and shown in chapter 2, which required two such identical circuits to achieve the same function. This new circuit eliminates any differential errors on the 'zero' referenced signal that are caused by using two separate sample and hold devices. The signal was sampled at the point where the exponential function had decayed to 5 lifetimes, using a sample and hold circuit. This sampled value was subtracted from the original signal to eliminate the unwanted bias voltage level. It was important to eliminate this bias level since it tended to vary with fluctuations in ambient light and offset voltages of the amplifier which can also vary with temperature. The typical signal voltage levels at the detector stage are shown in figure 3.6. As can be seen the ambient light and offset voltage effects represent, typically, a 20mV level

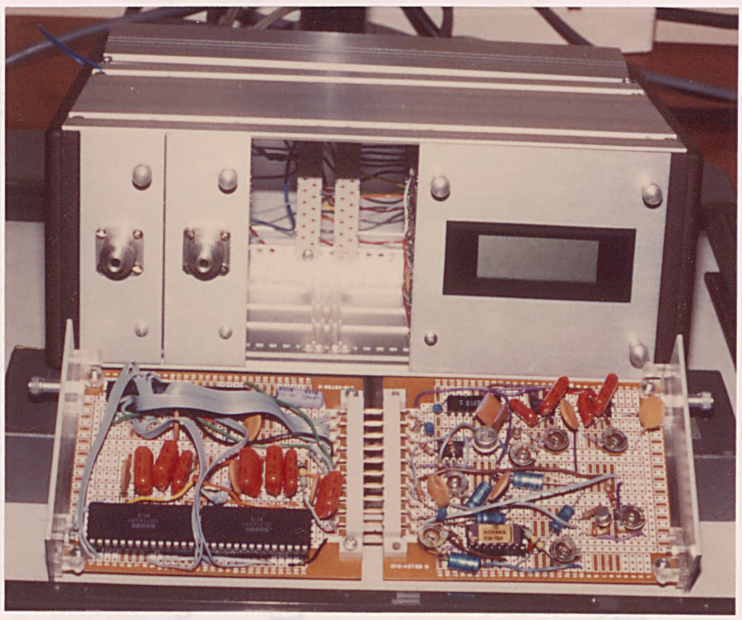

Photograph 1 - Microprocessor unit for the self-referenced absorption sensor.

Figure 3.5 - Spectral responsivity characteristics of RCA C30812 photodiode

Figure 3.7 - Test circuit of ICL7135 analogue-to-digital converter

which is smaller than the fluorescence signal. Hence the subtraction of the comparatively small dc offset from the rest of the signal produces very little error.

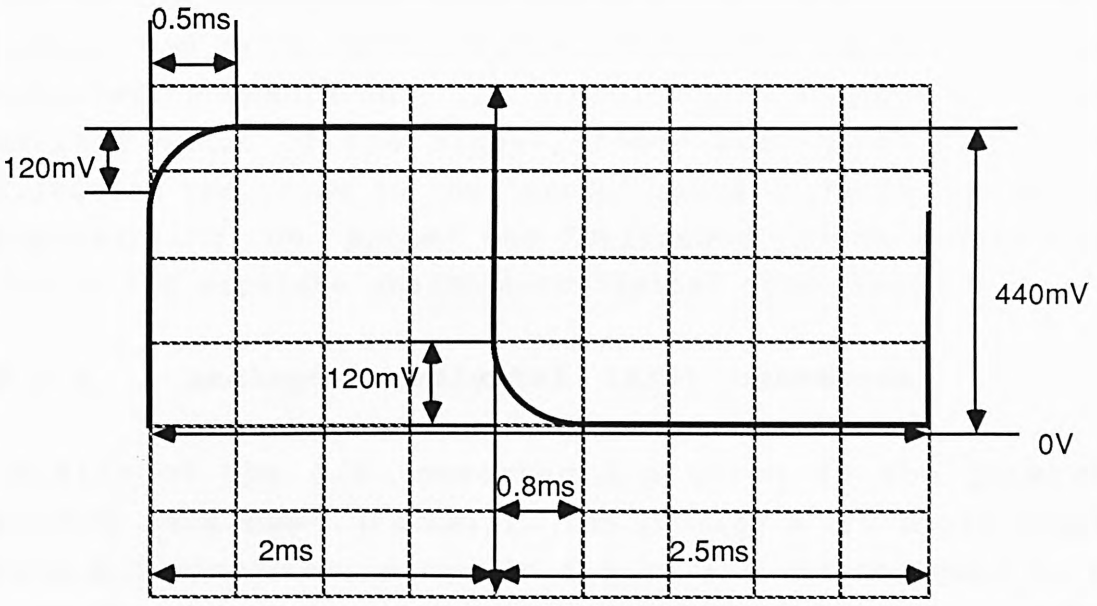

Figure 3.6 - Schematic of detector signal output showing typical voltage levels.

It appears from the output waveform shown in figure 3.6 that the exponential decays within a millisecond, but on closer inspection of the 'tail' of the decay the exponential, in fact, takes a few hundred microseconds longer. This was one of the reasons why the OFF period was made significantly longer than one exponential decay period. Similarly, this was the underlying reason why the ON period of the LED was made quite long, when compared to the absorption period of neodymium. The long ON period of the LED ensured that the sample of neodymium would emit the maximum fluorescence signal as a 'steady-state' condition was reached. The long ON and OFF periods also allow the sampling pulses on the sample and hold devices to be made much longer. Hence the 'probe' and dc offset levels can be sampled more accurately, as a longer sampling period reduces the uncertainty in the sampled value. The noise on the sampled signal decreases as

the sampling time is made longer, because the 'Hold' Capacitor essentially acts as an integrator.

The 'probe' signal, representing the intensity variations due to the absorption edge movement, was extracted using a sample and hold (S/H) device. The sampling duration was selected to ensure that the S/H capacitor charged up to the average value of the signal, hence providing a means of filtering the noise in the 'probe' signal. The two dc values representing the 'probe' and 'reference' signals were then fed to two separate analogue-to-digital converters.

3.2.4 Analogue-to-digital (A/D) conversion

Details of the A/D converter are given in the Intersil ICL7135 data sheet (Farnell). The ICL7135 4 1/2 digit single chip A/D converter, shown in figure 3.7, is designed to be interfaced to a microprocessor and offers accuracies guaranteed to ±1 count over the entire ±20,000 counts (2.0000 volts full scale) at very low cost. This type of A/D converter uses dual-slope integration (73) and is extensively used in precision digital multimeters; its only limitation is the comparatively long conversion time (333ms). This was not a problem in this application since the response time was limited thermally rather than electronically. However, the advantages of the dual-slope integration technique are that the device averages the input over fixed time intervals, it is insensitive to pickup 50Hz and its harmonics, thus reducing the noise on the input.

The ICL7135 needs an accurate voltage reference of 1.0000 volt. This was derived from a band-gap reference IC producing an extremely stable voltage of 1.26V (typical). A variable resistor of 10kΩ was used as potential divider to give 1.0000 volt at pin 2. The clock pulses were generated from a 4MHz quartz crystal oscillator and a divide by five counter which produced a frequency of 125kHz.

The Run/Hold (R/H) (pin 25) allows the A/D to operate continuously with equally spaced measurement cycles every 40,002 clock pulses. If this pin voltage is 'low', the converter will continue the full measurement cycle in progress and then hold this reading as long as R/H is held low. This pin was kept at a 'high' voltage level (or open) since it was unnecessary for the microprocessor to control the period of measurement. Continuous operation was satisfactory and the information from the A/D was taken by the processor sequentially using the strobe pulses at pin 26.

Pin 26 generates 5 negative going strobe pulses that come in the centre of each of the digit drive pulses and occur once and only once for each measurement cycle starting 101 pulses after the end of the full measurement cycle. The strobe pulses allow the BCD outputs at pins 13-16 and 'digit select' pulses to be synchronised with the microprocessor. The strobe pulses were fed to the maskable interrupt pin on the processor to enable it to receive the data from the A/D in the correct order. The LSB was the first output followed by the next most significant digit and so on. There are also over-range, under-range and polarity output facilities available on the A/D which can be fed to the non-maskable interrupt to indicate such conditions. These would be useful features in a commercial device and the microprocessor hardware and software can easily be adapted to allow for these extra functions.

3.2.5 Microprocessor design

The Z-80 microprocessor system used to determine the ratio of the 'probe' and 'reference' signals is given in figure 3.8. The Z-80 used a 4MHz single-phase clock and a 5 volt power supply. A 2K random-access memory (RAM) and a 2K fast (450ns) electrically programmable read only memory (EPROM) provided sufficient memory space for the software which was

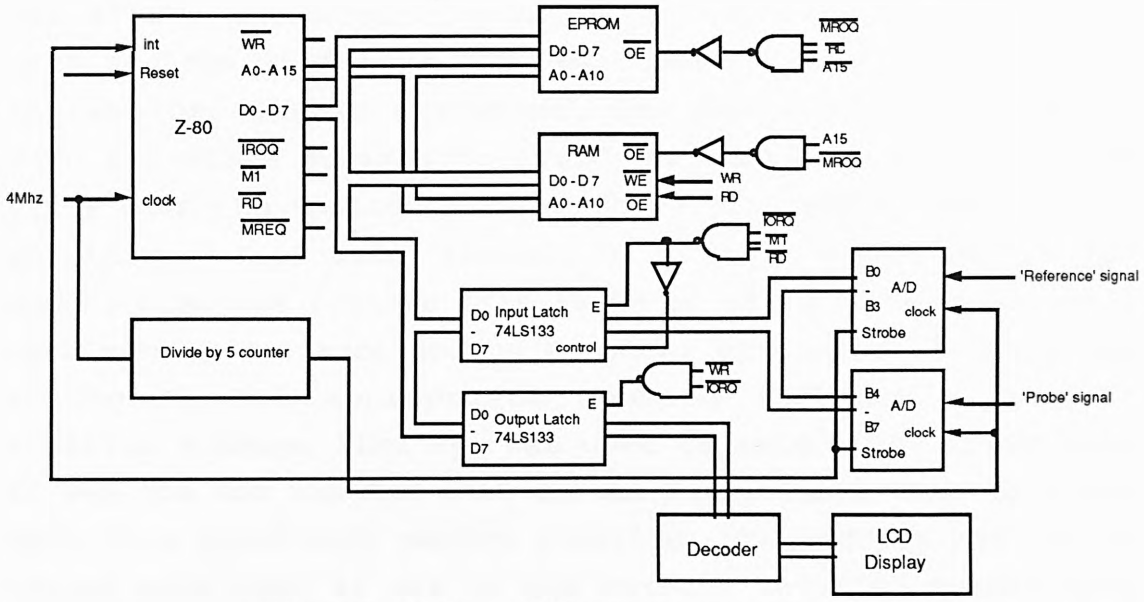

Figure 3.8 - Microprocessor System

Where Z-80:Microprocessor, EPROM:Electrically programmable read only memory, RAM:Random access memory (CMOS 6116), Decoder: LCD decoder/drive (CMOS 4-digit, 7211HEX), A/D:Analogue-to-digital converter (ICL7135), LCD:Liquid crystal display, Int:Maskable interrupt, A0-A15:Address bus, D0-D7:Data bus, IROQ:Input/output request, M1:Machine cycle 1, RD:Read, MREQ:Memory request signal, OE:Output enable, CS:Chip select, WE:Write enable, E: Enable.

written (Appendix 10) and allowed for further additions in this program if, for example, a calibration curve was to be added to give a direct readout in degree units. The choice of this microprocessor was determined to a large degree by the facilities available at the University. However, any comparable eight-bit microprocessor could have been used. The Z-80 is a very versatile processor offering high-speed at very low cost. However, there are processors available which have in-built RAM and ROM memory space, and also better software capabilities. Functions such as division and multiplication are standard single commands, whereas in the Z-80, these have to be programmed-in using continuous subtraction or addition routines.

The EPROM was used to provide the 2048 bytes of program area and the 2048 byte RAM was used to provide read-write storage of dynamic variables. The RAM and output latches were tri-state devices to avoid ambiguity of a low or high state when the devices were inactive. The EPROM memory area was located from 0000H through to location 0340H and the RAM memory area was located from FF00H to FFFFH (256 locations). Each memory was accessed by a number of control lines going active at the appropriate command instruction and in addition address line A_{15} was used to select the EPROM when it was low and the RAM when it was high. Thus, when data was sent to a particular memory location, the address had to be chosen such that it was in the correct required memory area otherwise the data was not stored.

The reset on the micro allowed various registers to be initialised and the execution of the program to begin at 0000H by disabling the interrupts. The maskable interrupt was made active by a software command and once it was active the micro jumped to the location of the interrupt routine (at address 0038H). This was basically a sub-routine which allowed the micro to accept data from external latches. Once the routine was executed, the micro jumped back to the location it originally jumped from, the main program to manipulate this data was then executed, and during its execution the interrupt signals were ignored until they were again enabled by the software.

The liquid crystal display (LCD) was addressed through a decoder/drive chip which latched onto the data from the output latch. This (7211Hex) decoder/driver chip took several microseconds to latch on to the data and the micro had to output the data a number of times for latching to take place, otherwise the display did not respond to the information that it was receiving.

The Z-80, memories and decoder/drive chips were all CMOS integrated circuits and this helped to reduce the current

consumption of the whole system. The cost of these integrated circuits and the metal box was estimated at one hundred pounds.

3.3 REQUIREMENTS OF THE REFERENCING TECHNIQUE

In order to prove the validity of the self-referencing technique it was necessary to show that the integrated fluorescence signal was a direct measure of the 'probe' pulse, was not influenced by temperature and was directly proportional to the pump intensity, as it varied.

To meet the former requirement, a test 'sensor' with the RG glass removed was constructed, thus eliminating the 'probe' intensity variations due to its presence. The probe was then heated from 298-403K (25°C to 130°C) and a close correlation between the 'reference' and 'probe' signals was observed (i.e ±0.5% variation), as shown in figure 3.9, over almost the entire range. This confirmed the observations of Thornton et al (71) that the conversion efficiency of Nd^{3+} doped materials excited at 810nm to 1060nm radiation is constant over the temperature range studied, and shows agreement with previous work in chapter 2. The ratio of the fluorescence emission and the received 'probe' signal thus should remain independent of the input pump light and exhibit a constant relationship. Beyond 400K, the deviation in the constant ratio of these signals becomes significant at >3% of the room temperature value. This may be attributed to a change in the quantum efficiency in the doped glass at higher temperatures. The intensity of the pump was varied by gradually unscrewing the fibre connector from the LED housing, and again a close correlation (±1%) of the 'reference'-integrated fluorescence and 'probe' signals was observed as shown in figure 3.10. This confirmed the observations of DeShazer et al (78) that conversion efficiency is essentially independent of the pumping level,

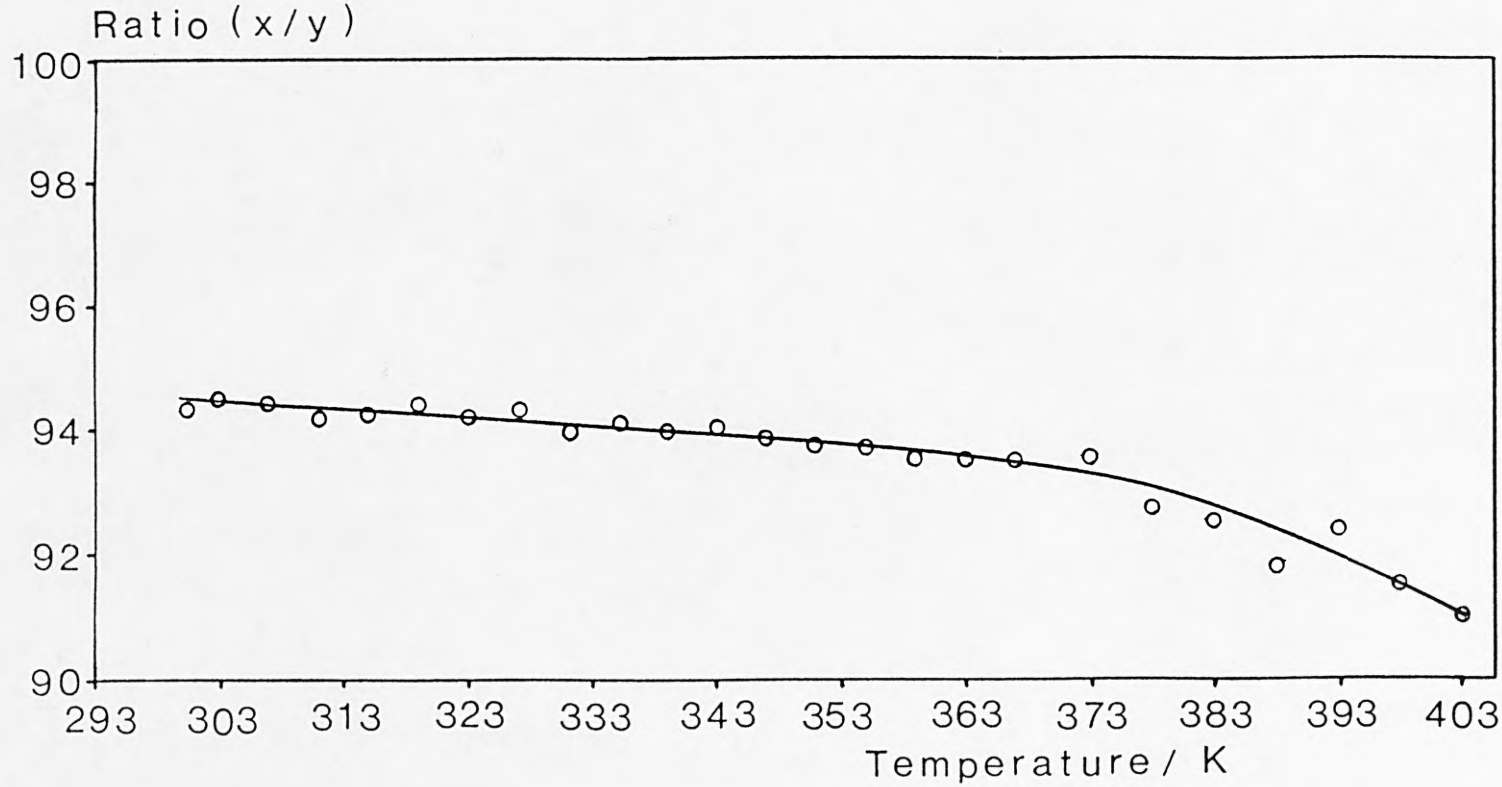

Figure 3.9 - Ratio of 'probe' signal x, to 'reference' signal y, as a function of temperature

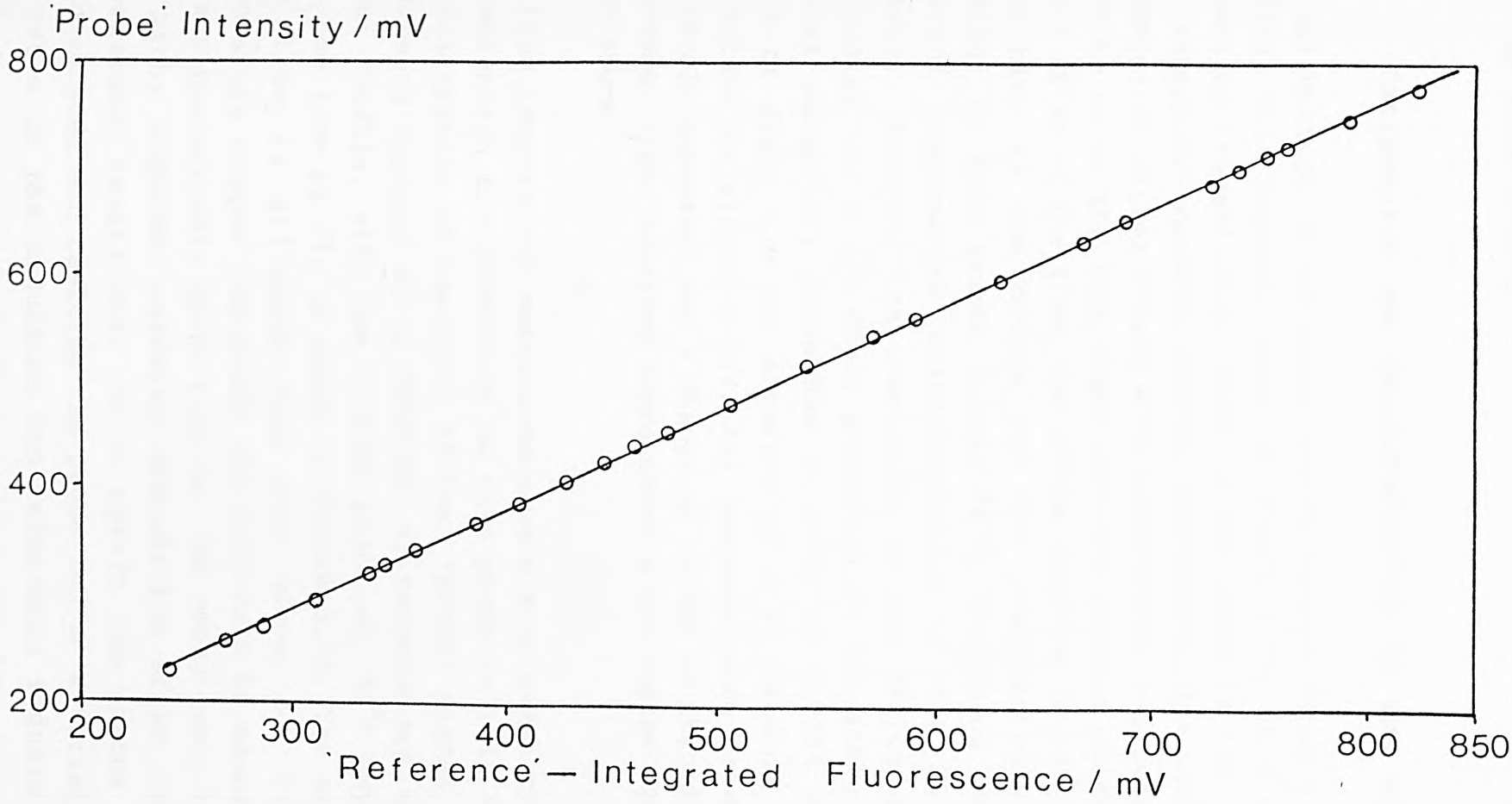

Figure 3.10 - Graph of change in 'probe' signal with corresponding change in the 'reference' signal showing linear relationship

over the range studied.

3.4 CALIBRATION AND CHARACTERISTICS OF THE SENSOR

The calibration of the prism 'point sensor' shows a linear profile. This profile, shown in figure 3.11, is a plot of normalized transmission, which is the ratio of the 'probe' and 'reference' signals, against temperature. The normalized transmission varies slowly with temperature; all points lie close to or on the line drawn with the extreme point lying within +2.0% of the line. One of the limiting factors of the resolution of the device was the comparatively small gradient of this graph, $2.2 \times 10^{-4} K^{-1}$, resulting from the inherent temperature characteristics of the RG glass material. However, the resolution of the device was not limited by the 4 1/2 digit precision of the analogue-to-digital converter, which has an error of 0.005% at full scale of 2Volt i.e the accuracy of a 2V reading can be guaranteed to within 0.1mV. All readings were taken to a 'millivolt accuracy' and a change of ~0.8mV in the intensity of 'probe' light received represented a one degree change in temperature.

Sub-room temperature measurements were also taken to prove the extension and usefulness of this probe in this region. The calibration of the ratio of the 'probe' signal to the 'reference' signal as a function of temperature shows a linear profile, with the extreme point at $-60^{\circ}C$ deviating from the line by 2%, as shown in figure 3.12. The slope of this line is different from that shown for the hot temperature regime. The probe was difficult to manufacture and was mechanically quite fragile. The epoxy resin holding the probe together suffered degradation after repeated temperature excursions. As a result the probe often disintegrated and regluing the probe led to a variation in the ratio of the modulated and referenced signals for a given temperature and thus a loss of the individual

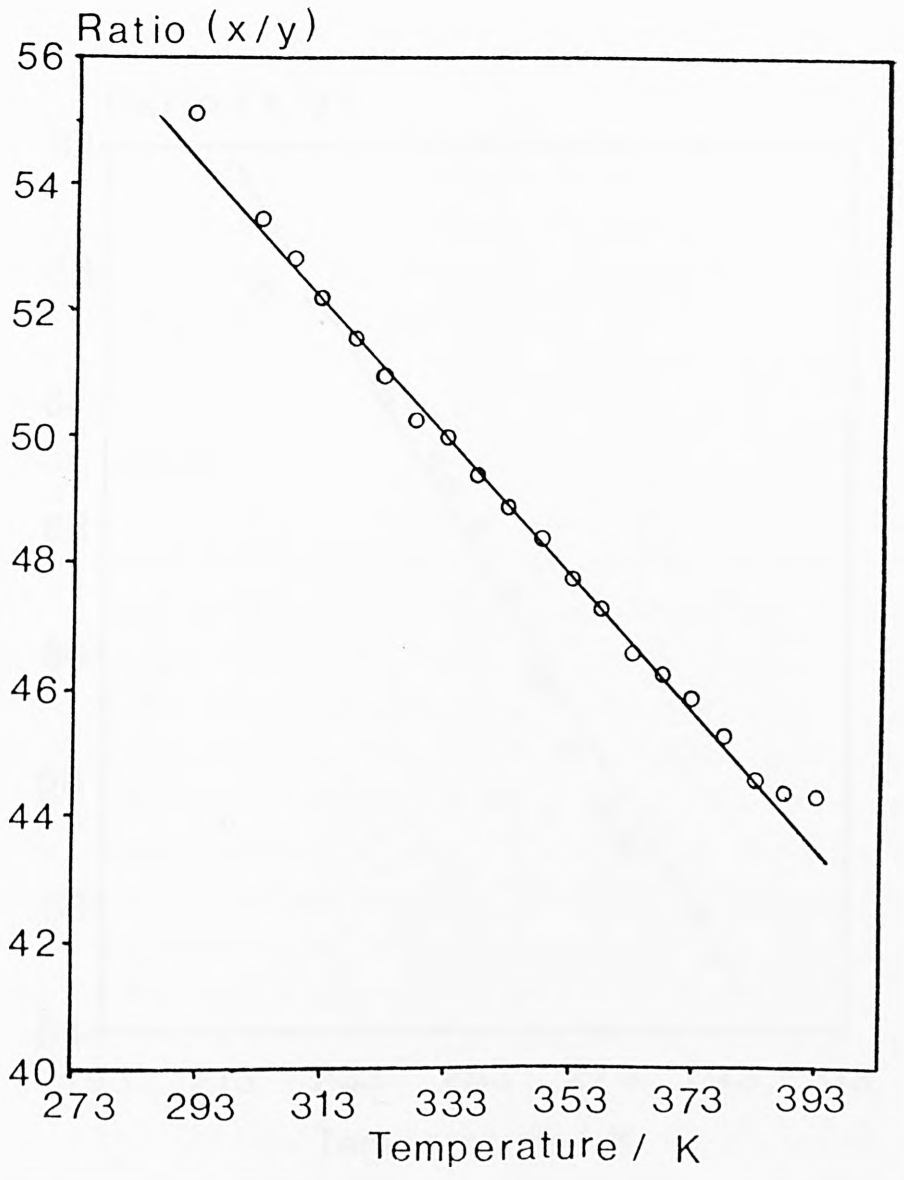

Figure 3.11 - Calibration of the device. Ratio of 'probe' to 'reference' signal (x/y), as a function of temperature, showing a linear relationship (hot regime)

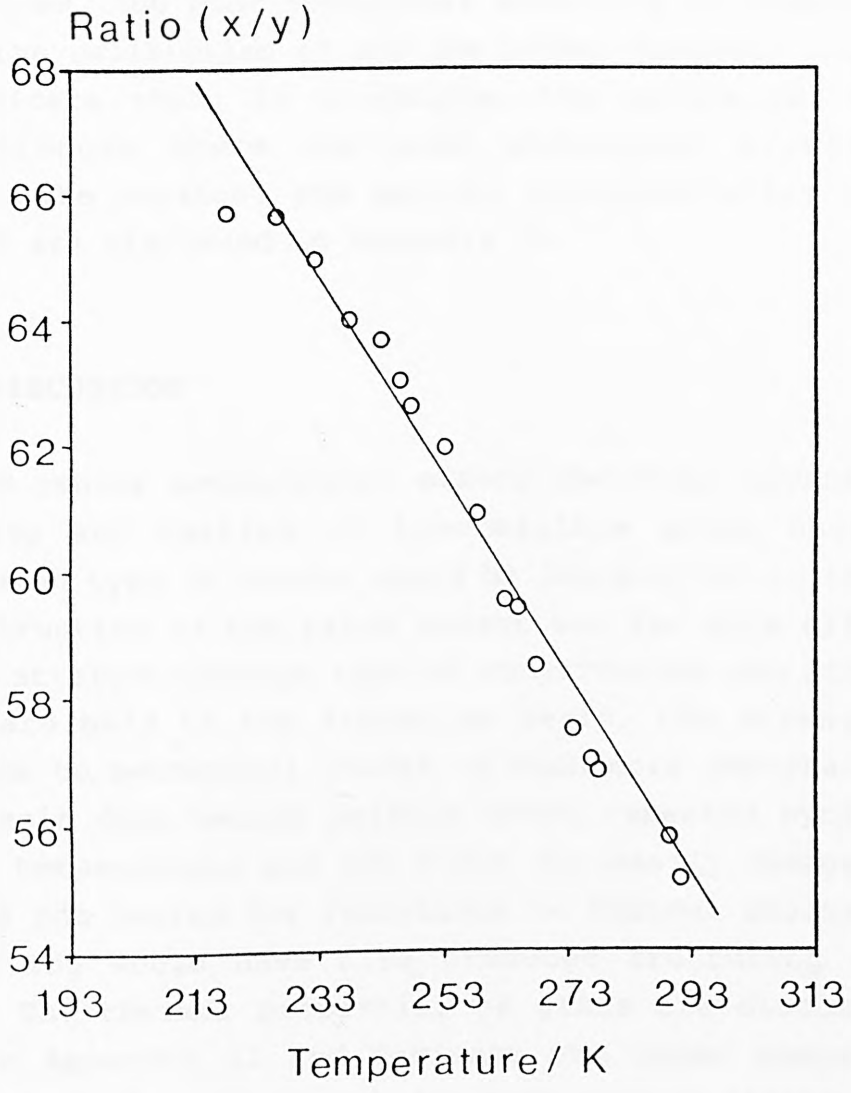

Figure 3.12 - Calibration of the device. Ratio of 'probe' to 'reference' signal (x/y), as a function of temperature (cold regime)

calibration. This is the most significant reason why the slope was different when the probe was subjected to sub-room temperatures. It could also have been some form of drift in the electronics with time; the experiments were carried out several days apart. In addition, it could also have been due to the change in the transparency of the epoxy resin at low temperatures. The poor mechanical stability of these probes limited the calibration of any one probe. However, this work does indicate that, in principle, the device has a wide range although there are some mechanical problems to overcome. The physical and optical characteristics of Epotek 353ND are discussed in Appendix 11.

3.5 DISCUSSION

The prism sensor construction offers the major advantage of monitoring and testing in inaccessible areas where the transmission type of sensor would be impractical to install. The construction of the prism sensor was far more difficult than the straight-through type of construction and since the glasses are held to the fibres by resin, the strength and resistance to mechanical shocks is much more important. The Epotek resin does become brittle after repeated cycling to elevated temperatures and the probe was easily damaged. The resin was not tested for resistance to thermal shocks since such testing would have also produced fracturing of the glasses. The thermal properties of glass are discussed in detail in Appendix 12 and indicate the upper temperature limitations, which are beyond the temperature limits of the fibres.

The prism sensor greatly improved the detected level of fluorescence (~10dB); this was due to the reduction of the 'probe' intensity, which made the signal levels detected more comparable. In the transmission sensor, the level of 'probe' intensity required a reduction in amplification at the first stage of the electronics, which, as a consequence,

also reduced the signal-to-noise ratio of the fluorescence signal. The larger fluorescence signal level with the prism probe increased the S/N ratio of the reference signal, which improved the accuracy of this measurement.

The electronic processing was improved by extracting ambient light variations before the separation of the signal into 'probe' and 'reference' components. This simplified the circuit design and reduced the number of components, which was essential in optimizing costs.

Chapter 4

ABSORPTION GLASS THERMOMETER BASED ON RUBY FLUORESCENT REFERENCING

4.0 ABSORPTION GLASS THERMOMETER BASED ON RUBY FLUORESCENT REFERENCING

This work uses similar principles to that described in chapter 2, save for the wavelength region examined and the fluorescent material used. The need for such an examination arises from the comparatively poor sensitivity of the previous device and a belief in the efficiency of the technique. Also, with the use of visible wavelengths, the extension of the technique to other systems is possible (9); in it is described the generation of a reference signal from a sample of crystalline ruby used to monitor and correct for any changes in terms of intensity in the light source and optical path, with the measurand signal being generated from the 'absorption edge' movement with temperature. Two systems of generating a reference signal are described; in system 1, the crystalline ruby was housed in front of the LED and in system 2, it was housed in the probe head itself. The former approach showed distinct advantages; coupled with an overall simplicity in probe design it obviated the need for the referencing material to be subjected to the same temperature excursions as the transducer material. Hence, any temperature sensitivities of the reference source were irrelevant since it was housed in the same box as the control and processing electronics.

4.1 PRINCIPLES OF OPERATION

The principle of the device is as discussed in chapter 2. The temperature sensor relies on the absorption edge shift of an optical high-pass edge (Schott glass) filter, which exhibits a significant change in its optical properties at elevated temperatures. However, in this case, a cheap indicator green LED was used rather than the more expensive infra red LED to monitor this change, which was detected and processed with simple low cost electronics. Three edge

filters at different wavelengths were examined and a comparison of their performances was made. Figure 4.1 shows a graph of normalized absorption against wavelength for two different temperatures. The figure shows how the absorption edge shifts with temperature to higher wavelength.

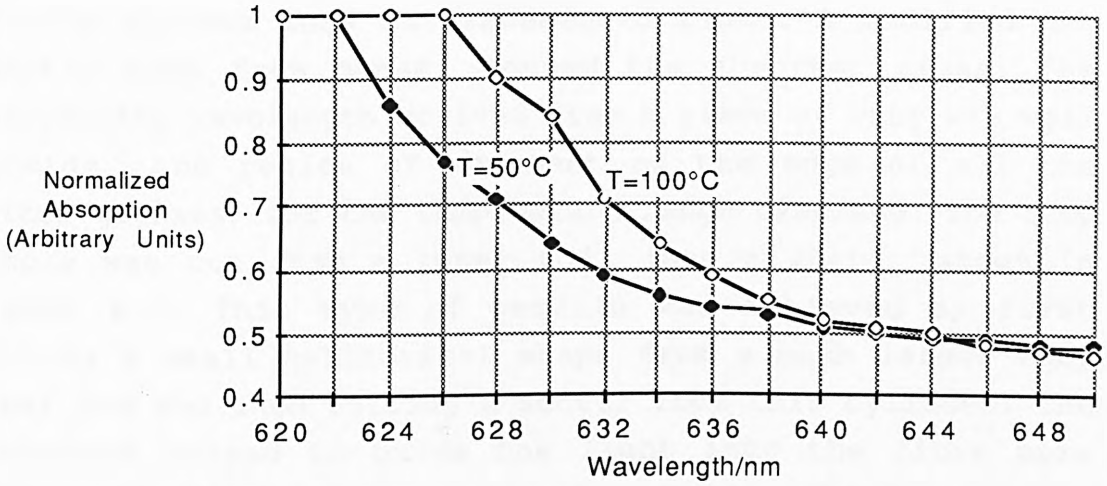

Figure 4.1 - Graph showing absorption edge movement with temperature for RG-630.

Two approaches to the generation of the reference wavelength are discussed. The material from which it was produced is the familiar laser material, pink ruby, which has a strong emission in the deep red, primarily on two bands close to a wavelength of ~694nm. This material has a high quantum efficiency, is readily polished by conventional optical means, and most important, as will be discussed in more detail in the next chapter, the integrated total fluorescence emission is independent of temperature over a wide range (79). It should be noted that although the decay-time changes significantly with temperature (an effect which can be used to sense temperature, described later in chapter 6), this does not affect the quantum efficiency and hence the integrated intensity of the deep red reference wavelength generated by the crystal.

4.2 OPTICAL DESIGN

The probe was designed as a transmission type of 'point sensor'. Three absorption glasses were used (OG515,OG550 and RG-630) to sense temperature. Each glass was cut to approximately 2mm thickness and polished on each side to provide minimum loss in transmitted light. A modified SMA adaptor made from brass housed the absorber glass. The referencing wavelength derived from a piece of ruby was well outside the region of movement of the edge of all the filter glasses, for the temperature range examined. The ruby sample was cut from a laser rod into a shape shown in figure 4.2. This type of profile was achieved by first cutting a small cylindrical shape from a much larger ruby laser rod and then cutting a sector from this cylinder. The curvature helped to guide the light into the fibre more efficiently than a rectangular shaped ruby. The crystal was only partially polished since polishing sapphire of such a shape was extremely difficult. In fact, tests showed that partial polishing produced equally good results in comparison to well polished surfaces. The only consequence was a slight reduction in the amount of green light transmitted beyond the ruby sample.

The ruby was placed in the same Radiall SMA flange housing as the green indicator LED to maximize the reference fluorescence signal generated and also to simplify construction of the probe head. The LED was pulsed and most of the green light passed through the ruby with very little attenuation (with about one percent being absorbed by the ruby and some lost via coupling losses into the fibre). The absorbed light was re-emitted, and was seen as an exponential decay on the falling edge of the pulse in the time domain. The red light, as mentioned, passed through the absorber glass unaffected by temperature, whereas the green light underwent a change in intensity owing to the overlap of the LED output with the glass absorption edge profile.

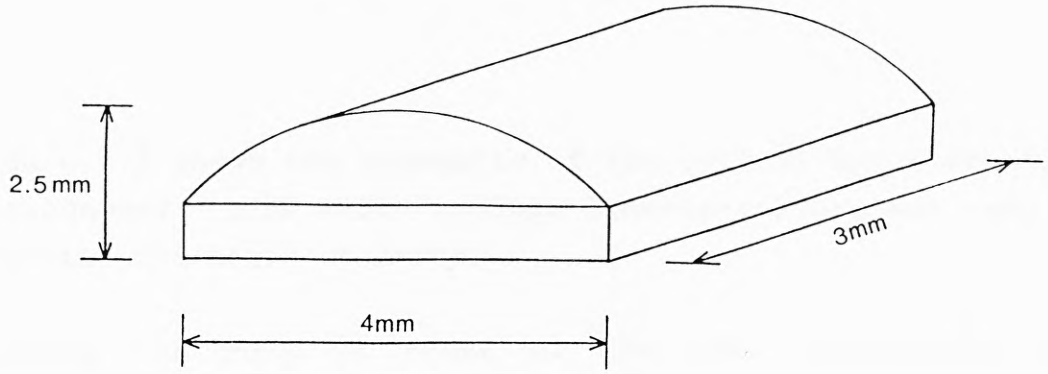

Figure 4.2 - Schematic diagram of ruby sample

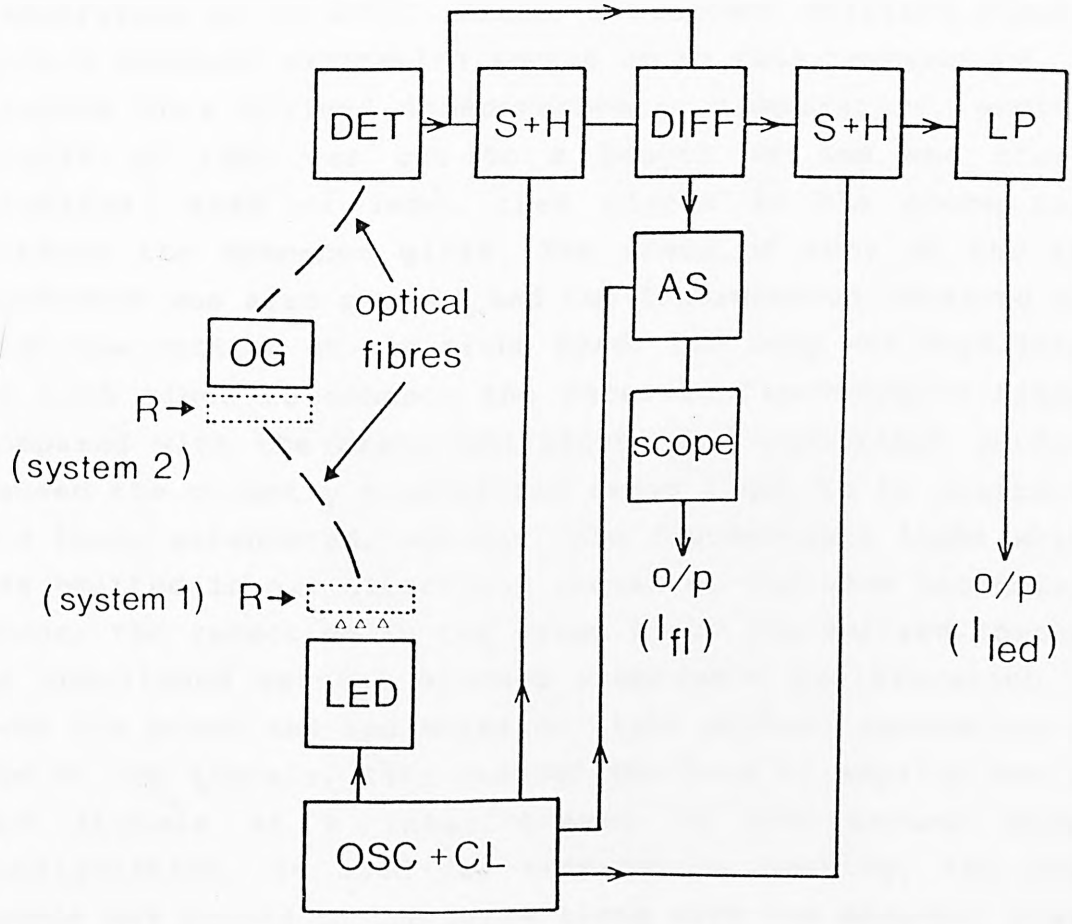

Figure 4.3 - Schematic of optical and electronic system

R: Ruby sample

OG: Absorption edge filter

Det: Detector and amplifier

S/H: Sample and hold device

Diff: Difference amplifier

AS: Electronic analogue switch

LP: Low-pass filter

OSC+CL: Oscillator and combinational logic

LED: Light-emitting diode and drive circuit

Figure 4.3 shows the schematic of the optical and electrical arrangement. PCS 1000 (1000μm diameter) fibre was used to maximize the light collected.

Placing the ruby in front of the LED eliminated the requirement for the fluorescent emission from the ruby sample to be independent of temperature, as was essential in the neodymium sensors. However, the total red emission was found, by Burns and Nathan (79), to be independent of temperature up to 240°C. Hence, a constant emission results from a constant excitation source up to this temperature. To examine this claimed independence of temperature, another sample of ruby was cut to a length of 3mm and cross-sectional area of $1mm^2$, then placed in the probe head without the absorber glass. The piece of ruby at the LED connector was also removed and the fluorescence observed was that now excited at the probe head. The ruby was unpolished at both sides to enhance the received fluorescence signal compared with the green LED light. The unpolished surface caused the directly transmitted green light to be scattered and thus, attenuated, whereas the fluorescence light which was emitted in all directions stayed at the same intensity. Hence, the reduction in the green light transmitted through an unpolished crystal allowed comparable amplification of both the green and red emission light without saturation of one of the signals. This avoided the need to amplify one of the signals at a later stage. In the second probe configuration, as used for temperature sensing, the ruby sample was housed in the probe along with the absorber glass OG550. The emitted light excited from the ruby passed through the absorber essentially unaffected over the temperature range studied. A schematic of the probe is shown in figure 4.4; the housing was the same SMA adaptor used to house the absorber glass. Only OG550 glass was used in this case as it demonstrated a large change in the ratio of the 'probe' and 'reference' signals against temperature, as will be discussed later.

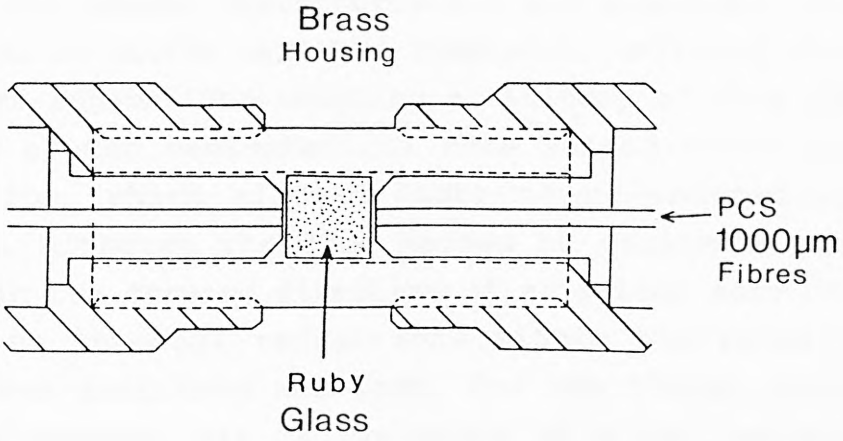

Figure 4.4 - Schematic of probe

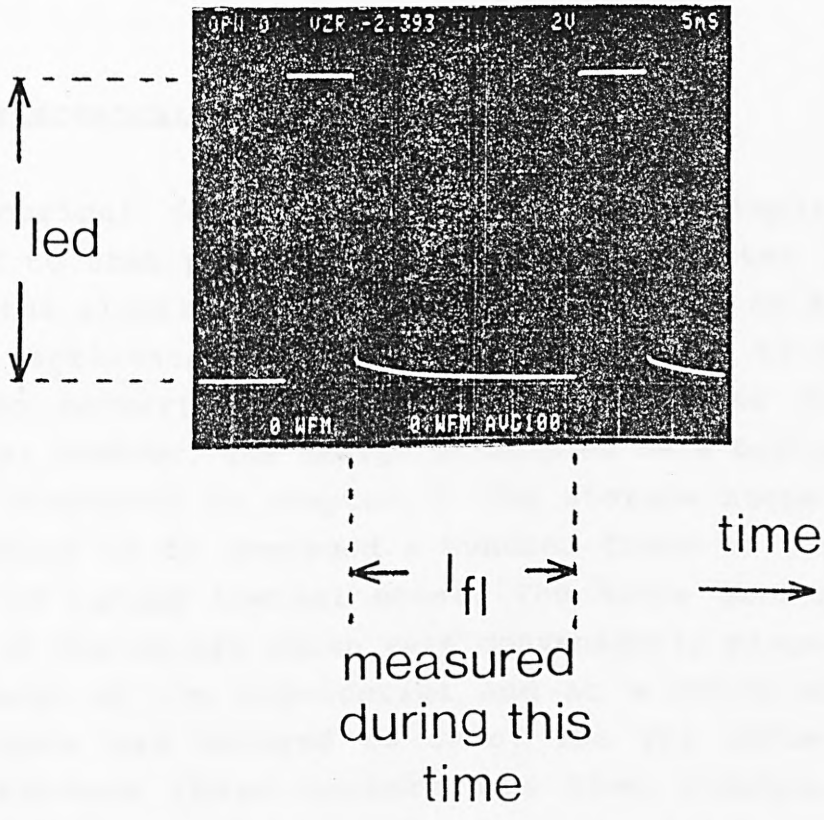

Figure 4.5 - Photograph of detected signal showing 'probe' signal I_{led} and fluorescence emission I_{fl}

The ruby emission was excited by a single broad-band green indicator LED (whose characteristics are examined closely and reported on in the next two chapters), emitting strongly in the 565nm region. The coupling efficiency of this LED was poor owing to the hemispherical dome shaped clear plastic encapsulation, which allowed light to be emitted in all directions. Although the dome helped to collimate most of the light in the forward direction of emission, some of that light due to internal reflections within the plastic/air interface was scattered and lost. For the 1000μm fibre the coupling efficiency was of the order of a few percent and was further reduced at the probe head due to losses. It did, however, couple more light than into three 600μm fibres formed into a bundle. As a consequence, a highly sensitive photodiode detector with an integral amplifier (600mV/μW) was used, costing twelve pounds (unlike the neodymium system where the detection of the fluorescence was carried out by an expensive and specialized detector).

4.3 ELECTRICAL SYSTEM

The electrical design of the device was simplified as compared to that previously discussed in chapter 3, since part of the signal processing was accomplished on a digital storage oscilloscope. This obviated the need to design a rms-to-dc converter with additional low-pass filtering circuitry; however, the design principles were basically the same as discussed in chapter 3. The storage scope allowed the readings to be averaged a hundred times to remove the effects of random thermal noise. The scope generated two cursors on the screen which were conveniently placed on the rising edge of the exponential and at a point where the fluorescence had decayed to zero. The rms value of the signal between these cursors was then computed after averaging the stored signal. It was still necessary, however, to build the other units of the electronic processing to separate temporally the fluorescence, I_{fl},

which occurred on the tail of the light pulse received from the sensor and also to sample the height of the green pulse, I_{led}, which contained the intensity information representing the change in the measurand.

The LED was modulated with a pulse which fell to zero on a time-scale of several microseconds and thus the signal received after this time corresponded to the total ruby fluorescence signal caused by excitation of the sample by the green light. This is shown in figure 4.5. Hence, a single detector was used, in this case a Si p-i-n diode with an integral amplifier, for low signal amplification. This removed the need for two such detectors for each wavelength band, with the consequent difficulty of cross-referencing, as discussed in chapter 5. A similar electrical configuration to that described in the previous chapter, but with the addition of a storage scope, was used to determine the temperature dependent normalized transmission. A block diagram of the electrical system is shown in figure 4.3.

4.3.1 Detailed circuit discussion

The complete diagram of the circuit used to derive the switching and sample/hold pulses, plus the drive circuitry for the LED is shown in figure 4.6. This digital part of the circuit represents the second main difference between the detector circuit described in chapter 3. The photodiode detector, in this case, was a large area ($5mm^2$) integral amplifier type with high sensitivity ($600mV/\mu W$) and a low bandwidth of 5kHz. This relatively low bandwidth was an advantage in terms of discriminating against high frequency noise, but it did have its disadvantages in that it suffered from 'gain peaking' effects. The 'gain peaking' effects are essentially additions of oscillations on the transition edges of the detected square wave intensity pulses. In such fluorescence sensing work, these can distort the received fluorescent emission exponential profiles. Thus the 'gain peaking' effects had to be minimized by either adding a low-

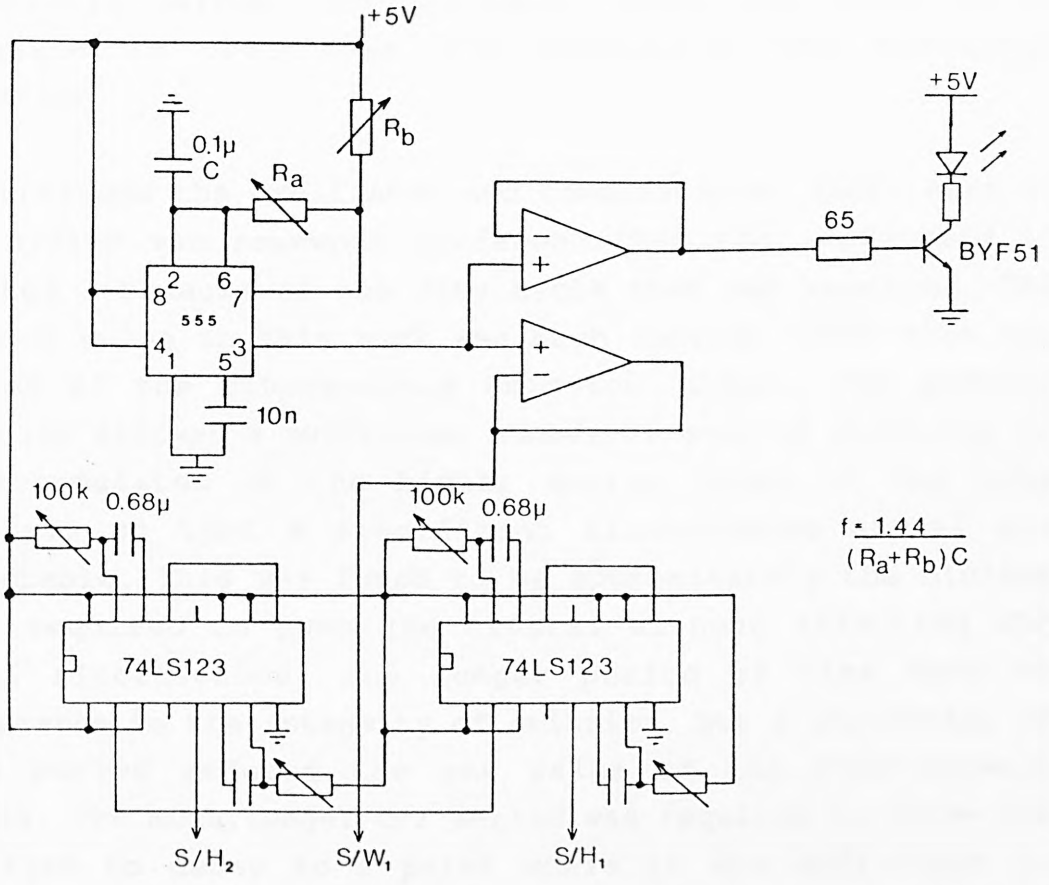

Figure 4.6 - Schematic of digital circuit diagram (S/H_1, S/H_2 and S/W_1 that feeds into a similar analogue circuit as shown in figure 3.4. R_a and R_b are variable 10k resistors, and both op-amps are 082)

pass filter, i.e a RC network, at the first amplification stage or a capacitor across the feedback resistor of the amplifier or as was previously described in section 2.2.6, by switching the transient out altogether, through the electronic switch. The low-pass filter was found to be adequate in this case and eliminated the transient variation.

As mentioned the oscillator and combinational logic half of the system was somewhat different than that described in chapter 3 because of the duty cycle that was required. The pumping pulse in this work was much shorter (7ms) than the period of the fluorescence emission (20ms). The pumping duration allowed a sufficient number of excited electrons to be accumulated in the higher energy level of the ruby crystal, so that a significant fluorescence signal was detectable. This was found to be approximately the minimum time required to pump the crystal without affecting the total fluorescence. Any longer period of time made no difference to the intensity of emission, but a shortening of this period reduced the rms value of the fluorescence signal. The much longer OFF period was required to allow the emission to decay to a point where it was sufficient to conclude that it represented a 'zero' level of emission of light (i.e 5 lifetimes - a lifetime being approximately 3.5ms for the sample of ruby used). An astable multivibrator 555 timer chip generated a square pulse with the required duty cycle and also provided switching pulses for the J-K flip-flops, used to generate the control pulses for the analogue switch and sample/hold circuitry.

The single transistor driver circuit passed a peak current of ~183mA through the LED in the ON period, giving an average current of ~45mA. Although, this exceeded the rated maximum of 30mA for the LED used, it did not exhibit any observable adverse effects on the LED, which worked continuously throughout the experiments. This value of drive

current was not essential and could have been reduced to 30mA, but the signal-to-noise ratio of the detected signals would have decreased slightly. This, however, could have been compensated for by additional filtering. This was considered unnecessary at this stage in the sensor development. For long term operation it would be necessary to operate the LED within the maximum rated current limit to avoid rapid ageing effects and an investment in additional electronic filtering would be justified.

4.4 CALIBRATION OF RUBY FLUORESCENCE REFERENCING

Initially, the ruby was tested to prove the validity of the referencing technique and its independence of temperature effects. Several filter glasses were then tested with the ruby at the probe head and in the LED housing.

4.4.1 Temperature effects on ruby referencing

The integrated fluorescence signal obtained from the ruby sample had to be a direct measure of the intensity of the green LED signal which both induced it and was attenuated, in a temperature-dependent way, by the OG glass sample. Figure 4.7 shows the proof of this principle, where the ratio of the integrated fluorescence to the peak green LED signal obtained under steady pumping is shown as a function of temperature for a 'probe' made up with only the ruby present and the OG glass removed. This simulated the effects of temperature on the probe but allowed for the elimination of the change in the absorption of the glass. Over the range studied 20°C-130°C, the ratio was a constant to $\pm$1% of the peak value, clearly showing the validity of the reference technique, as would be expected from the constant quantum efficiency of the ruby. It was important to carry out such a test as the geometrical changes in the probe itself with temperature can mean significant (<10%) changes in the green signal reaching the OG glass. Beyond 130°C and up to

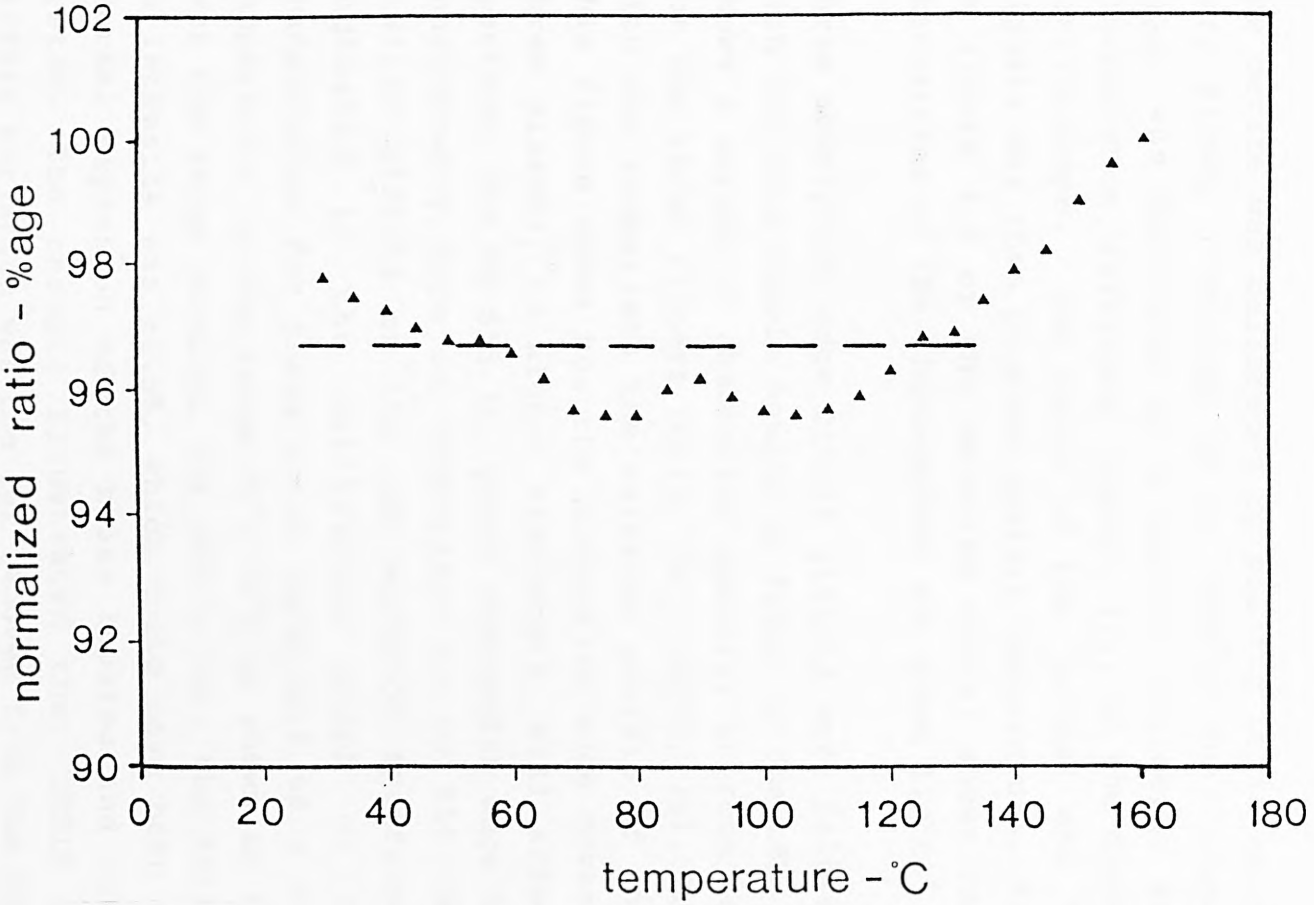

Figure 4.7 - Normalised ratio (100 at 160°C) of the integrated ruby fluorescence, I_{fl} to the peak green LED signal, I_{led}, as a function of temperature for a 'probe' not containing an OG glass temperature sensor

160°C, the graph shows that the fluorescence had an excessive dependence on temperature for referencing purposes, thus dictating the probe design which may be used, described as system 1.

4.4.2 Calibration results

The device was calibrated by placing it in an oven heated very slowly (~4hours) up to ~200°C. The 'probe' signal, I_{led}, was monitored on a digital voltmeter and the red fluorescence 'reference' signal, I_{fl}, on the digital storage oscilloscope. The ratio of the 'probe' and 'reference' signals was then plotted against temperature. A photograph in figure 4.5 of the detected signal shows the relative intensities of the fluorescence and green light.

Three absorption edge filter glasses were initially tested with the ruby sample housed in front of the LED. Figure 4.8 shows a series of absorption spectra, at room temperature, for the three filters OG515, (A), OG550, (B), RG-630, (C), with for comparison the emission profile of the LED (L). This figure shows how the absorption edge movement of the three glasses, to higher wavelength, will affect the LED spectrum. The OG 515 (A) glass absorption edge has to move considerably more in comparison to OG 550 (B) to have similar effects on the LED emission spectrum. This is indicated in the calibration graph of normalized transmission for these three materials as a function of temperature in the range 20°C-30°C as shown in figure 4.9. Over the range studied, for OG515, (A), the maximum change in intensity was ±1.5%, which could have been due to the thermal expansion of the brass housing and noise in the system. The results illustrated that OG515 absorption profile variation was too far removed from the LED emission spectrum to have made any impression on the transmitted intensity. A calibration graph, in the same figure, with RG-630, (C), showed a slightly non-linear profile of normalized transmission with temperature. The change in the

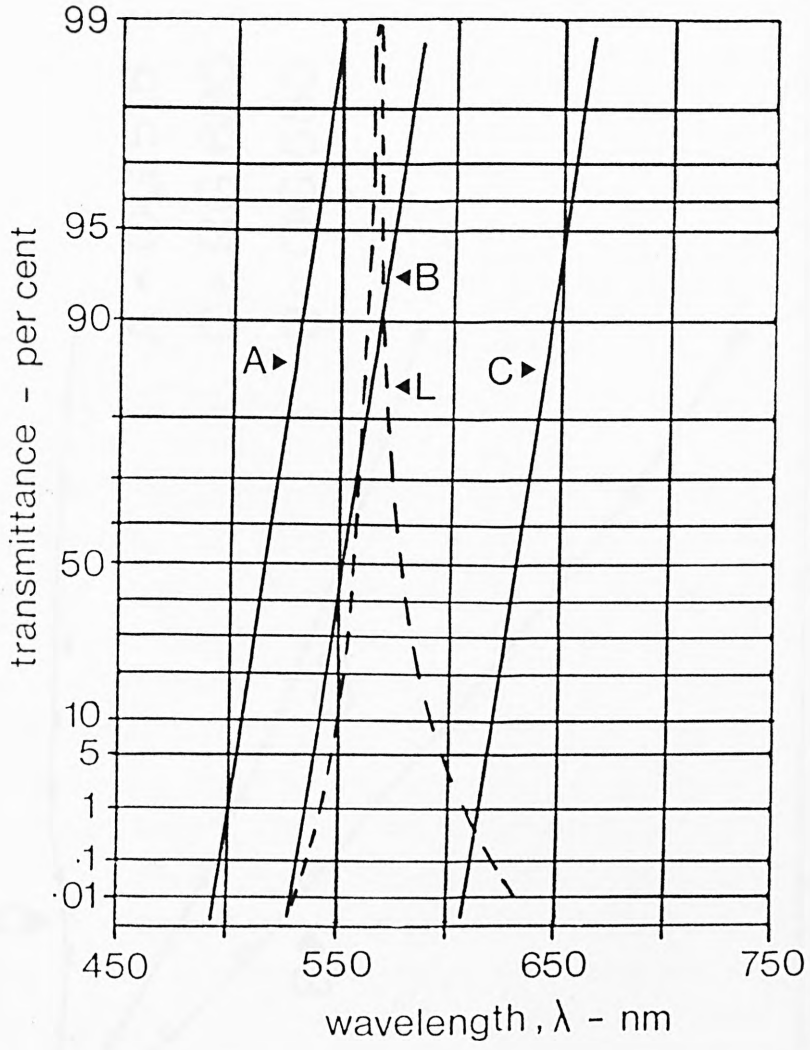

Figure 4.8 - Transmittance (at room temperature) of three absorption glasses (solid lines) OG 515, (A), OG 550, (B), RG 630, (C), (Schott glass). Spectral profile of the green LED is shown as dotted lines (L)

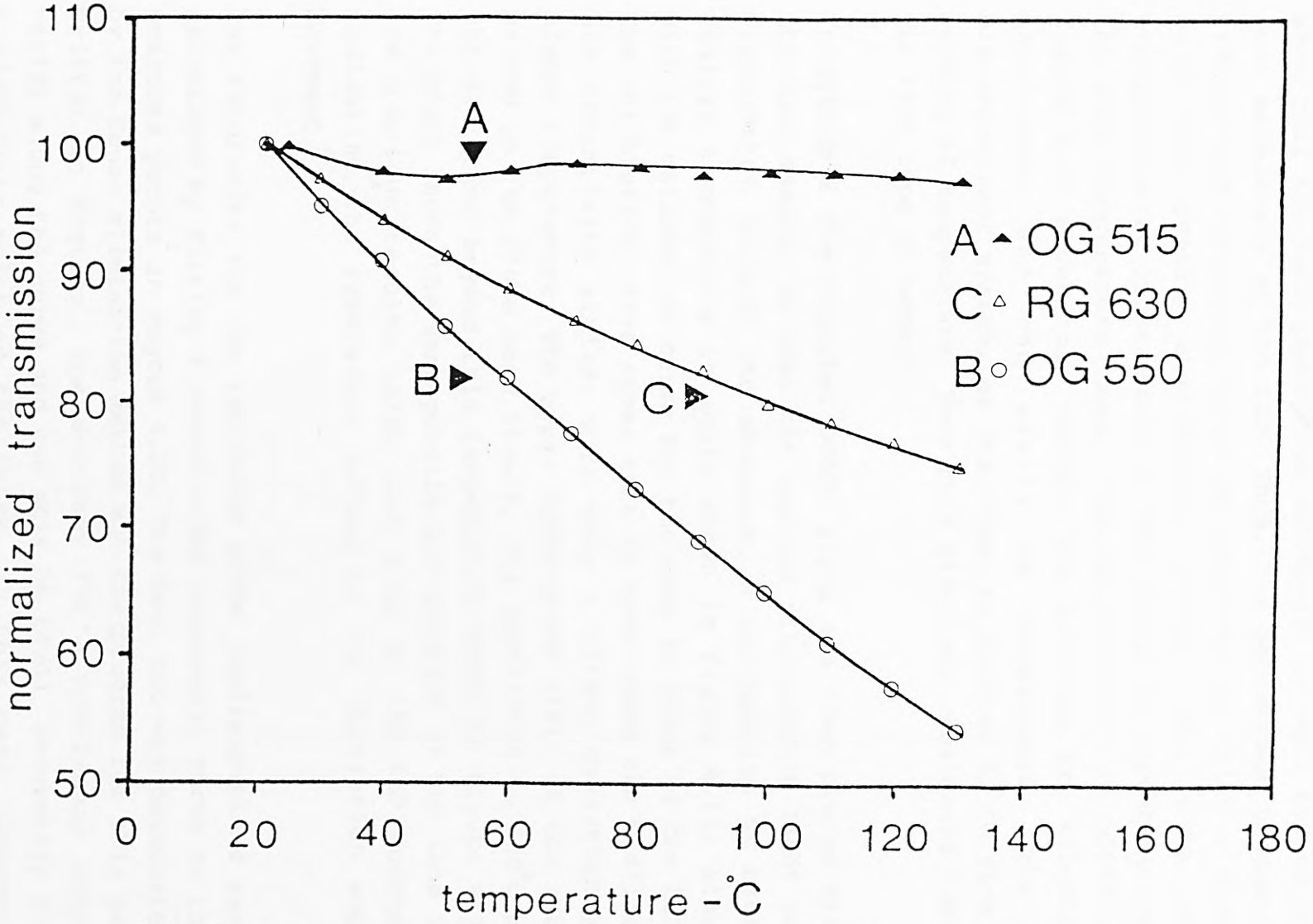

Figure 4.9 - Normalised transmission as a function of temperature of three absorption glasses (20° - 130°C)

ratio recorded on this graph was 25% over the temperature range studied. From the LED profile in figure 4.8 it can be seen that the main absorption of RG-630 is well beyond the peak wavelength of the LED. Thus, the percentage change in transmitted intensity could be improved by using a glass near the centre wavelength. OG550, (B), with 45% transmission at 550nm, shows a ~45% change in intensity over the same temperature range. The calibration of OG550 in figure 4.10 shows this change. The profiles are slightly non-linear and can easily be programmed into a microprocessor system, as described in chapter 2, to give a reading of temperature. Thus this glass was considered ideal for this type of sensor.

In system 2 the absorber OG550 glass was then placed with the ruby sample, so that the excited fluorescence light was transmitted through the absorber. A calibration of ratio against temperature is again shown in figure 4.10, along with the calibration curve for the ruby in front of the LED. The calibration curve shows that in both cases the profiles are essentially similar with only a slight deviation at higher temperature. The upper temperature limit of the ruby housed in the probe head itself, was restricted to 130°C by the deviation beyond this temperature shown in figure 4.7. The graph shows the same profile and gradient of the line as the previous results taken with ruby in the LED housing indicating the reversible nature of the absorption edge movement.

The accuracies for the two OG550 probe configurations were calculated by fitting a second-order polynomial curve to the measured points in figure 4.10. The best fit was calculated by the Gauss elimination method and the program for this was written in Fortran. The accuracy for a non-linear graph varies along the curve and can only be found accurately for a particular point on the curve. In this case, however, since the curve was only slightly deviating from linearity, the accuracy figure did not differ very much from one point

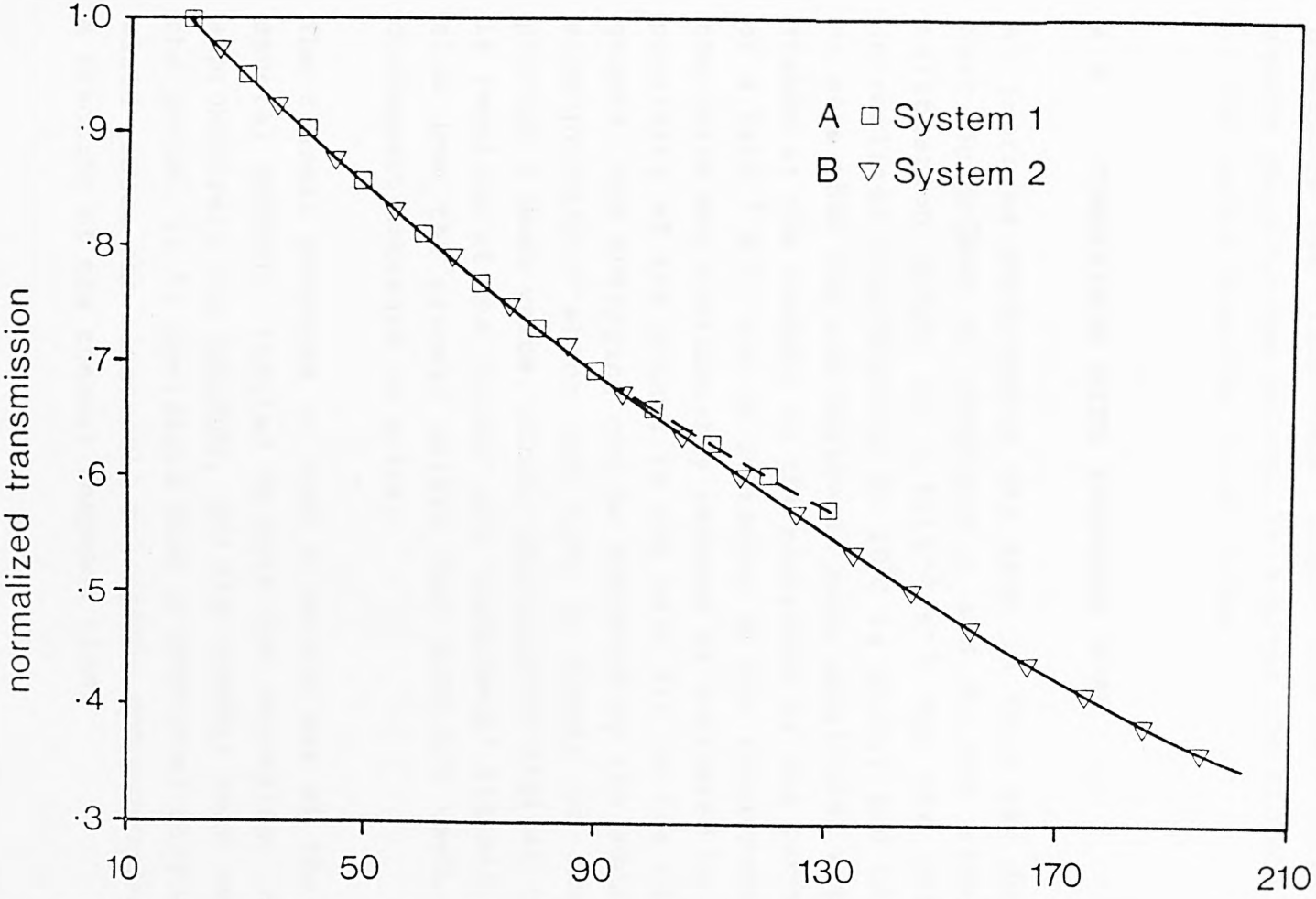

Figure 4.10 - Normalised ratio of the measurand and reference signals as a function of temperature.
A - System 1 (ruby crystal housed with the sensing element)
B - System 2 (ruby crystal in the same housing as the LED)

of the curve to another. For the calibration curve shown in figure 4.10, with the ruby housed in front of the LED, the accuracy at 75°C was calculated to be ±0.6°C for both curves. It is important to note that in both systems, very high accuracies in measurement were achieved through averaging the 'reference' signal and by fitting a least square curve to the points. This gives the minimum deviation of the points from the 'true' value.

4.5 COMPARISON WITH PREVIOUS WORK

An improved performance was seen in this new device over that described in chapters 2 and 3. The slope of the calibration graph is 1.7×10^{-3} K^{-1} for the prism probe (normalized transmission at 20°C is unity) and thus it can be seen that the new device is more sensitive, with a slope (taken as the tangent to the mid-point of the curve (~75°C)) of 4.1×10^{-3} K^{-1}. Due to averaging of the fluorescence signal the noise was considerably reduced as indicated by the close proximity of the points to the best fit on the calibration graphs. The averaging can be achieved by the addition of a microprocessor which can take a number of samples and provide a mean value. Since analogue-to-digital conversion is required of the 'probe' and 'reference' signals, this may slow down the process unless fast A/Ds are used, with the consequent increase in price.

The thermal response of such a device was of the order of several seconds, limited by both the averaging, which took approximately ten seconds, and the thermal heat capacity of the probe. It is envisaged that a dedicated microprocessor would reduce the electronic processing and averaging time to a fraction of the thermal response time.

4.6 DISCUSSION

The fibre optic visible-wavelength-based intensity referencing scheme has demonstrated its usefulness and can be applied to a wide range of intensity based sensors, where optical processing in the visible region is carried out. The first system makes probe design simpler, a prism configuration would allow the return fibre to be bonded to the same side as the addressing fibre. This type of configuration allows greater flexibility in terms of accessibility in confined areas. The scheme is relatively inexpensive as simple electronic components may be used without the need to use expensive filters and optical couplers to branch off to another detector or LED.

Chapter 5

FLUORESCENCE WAVELENGTH DIVISION EMISSION THERMOMETER

5.0 FLUORESCENCE WAVELENGTH DIVISION EMISSION THERMOMETER

This work was initiated from much earlier work carried out by Burns and Nathan (79) on the quantum efficiency of ruby (studied for laser purposes) and it seeks to exploit their findings in the development of a fibre optic temperature sensor.

The principle of the device described here relies on the monitoring of the fluorescence emission from pink (laser) ruby crystal. The fluorescent emission is separated in wavelength terms, with a combination of electronic and optical techniques, into two regions; one to give a temperature variant quantity and the other to provide a self-generated reference to allow for variations in the input 'pump' intensity of the light causing the fluorescent emission.

The fluorescent emission from the ruby (doped with Cr^{3+}), which occurs mainly in the deep red part of the visible spectrum, results from strong absorption of light on wavelength bands at 410nm and 555nm, as shown in figure 5.1. The quantum efficiency of ruby is found to be independent of temperature up to 500K (79), above which temperature it decreases quite rapidly. Thus, a constant light input results in a steady emission in the red region, up to this temperature, but the R-line contribution to that intensity decreases with temperature. The R-lines are two strong emission lines at 692.7nm and 694.3nm, which yield laser action in the untuned ruby laser. This loss of energy in the R-line region is redistributed to higher and lower wavelengths on either side of it, hence maintaining a constant total fluorescent output, to ~500K. The ratio of the two quantities provides a self-referenced temperature measuring system, which enables the elimination of errors due to variations in the optical linkage. The absorption and

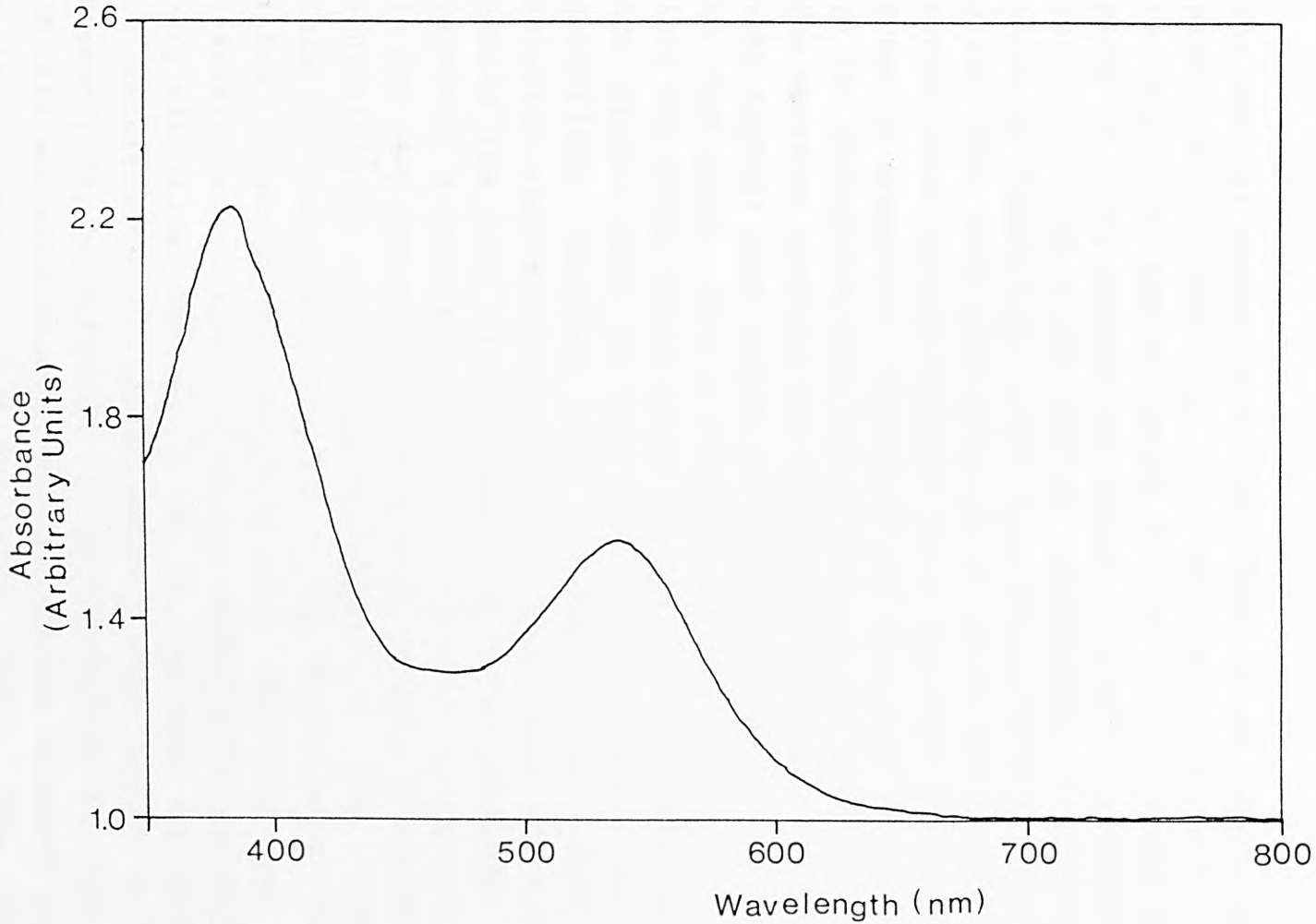

Figure 5.1 - Absorbance (arbitrary units) of ~1mm sample of ruby crystal as a function of wavelength

fluorescence characteristics of ruby are discussed in detail in Appendix 13, along with its temperature characteristics.

5.1 THE OPTICAL AND MECHANICAL SYSTEM

The optical sensor probe was constructed from a piece of pink ruby laser rod, cut and polished into a small rectangle of ~4mm in length by $1mm^2$ in cross-section. The piece of ruby crystal was housed in a small stainless steel container with a low thermal coefficient of expansion, as shown in figure 5.2. Light from two ultra-bright broad-band green LEDs, with peak emission at 565nm, was coupled to the sensor head through PCS 600 fibre (plastic coated silica - 600μm in diameter). These are the same type of LEDs as used in the absorption edge filter work in the previous chapter. The emission spectrum for these LEDs is given in figure 5.3, with typical peak output of 120 millicandela, corresponding to ~1mW power. Only a fraction of the light was launched into the 600μm fibres since the plastic encapsulation of the LED causes most of the light to be scattered in all directions. However, this portion of the output green emission that was launched into the fibre was enough to excite the ruby fluorescence and to be detected at the receiver. A second type of LED, with peak emission at 697nm in the deep red was used to provide a means of balancing the sensitivities of the two photodetectors used, light from this LED also being coupled to the sensor head via 600μm fibre. Although the detectors were identical they would, however, have slightly different responsivities, which may vary with time. The second LED thus allowed any variations in sensitivity to be normalized. The offset voltages, however, may be different for each detector, but the effect of this was eliminated by referencing the detected signal to a level corresponding to 'zero light'. The LED peak wavelength was very close to that of the temperature variant R-lines and was the nearest available from a normal commercial LED source. The red and green light was of

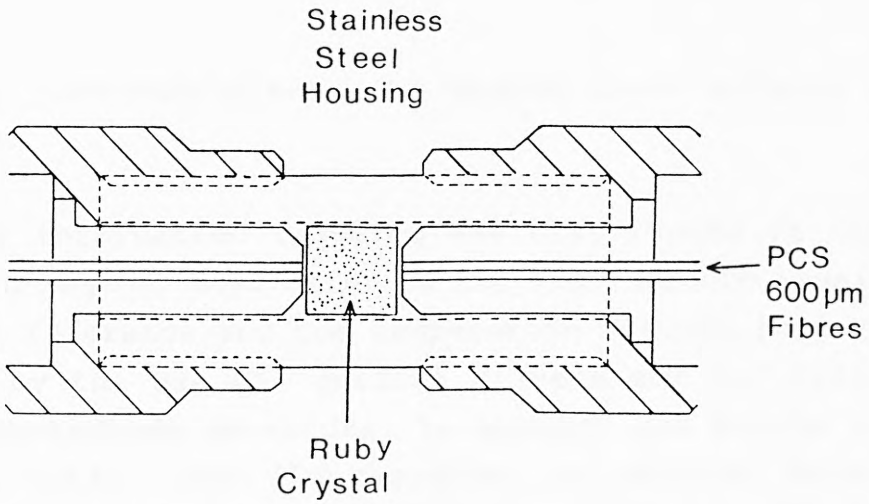

Figure 5.2 - Schematic of the probe showing ruby crystal and fibre connections

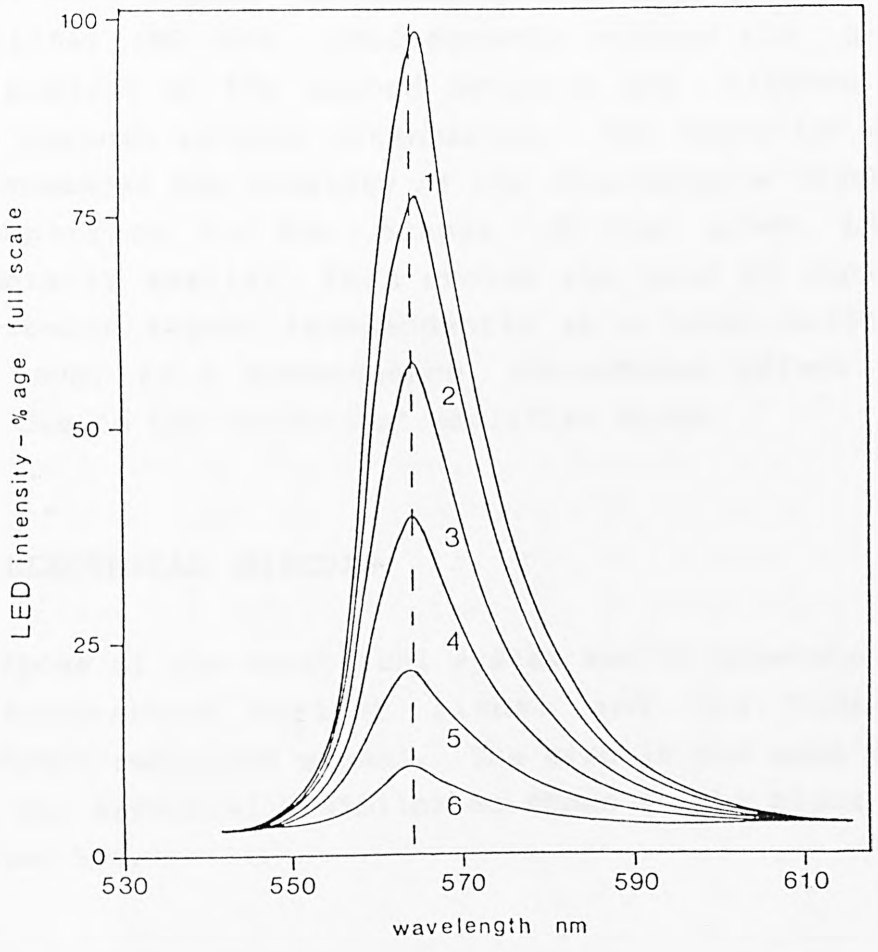

Figure 5.3 - Spectral emission of the green LED as a function of drive current.
1: 30mA, 2: 25mA, 3: 20mA, 4: 15mA, 5: 10mA, 6: 5mA.

necessity time-multiplexed, to enable their effects to be separated.

Since the information required was distributed in the red wavelength region, separation of the fluorescence wavelength into the reference and the temperature varying regions was achieved by the use of optical filters and two sensitive silicon photodiode detectors. To extract the R-line region from the total red fluorescence, an optical band-pass interference filter centered at 695nm with a bandwidth of 5nm was placed in front of one of the detectors. This is a standard filter for laser applications and as such relatively inexpensive. This detector was, thus, highly sensitive to emission from the R-lines and light from the red LED as well as passing a small amount of other fluorescence light. A second optical high-pass absorption edge filter (RG-630) considerably reduces the green LED light present at the second detector but allowed the red light through without attenuation. The reduction of green light enhanced the fidelity of the fluorescence signal which in comparison to the output of the green LEDs was considerably smaller. This avoids the need to amplify the fluorescence signal independently at a later stage, which could have, as a consequence, introduced offset voltage errors due to the additional amplifier stage.

5.2 ELECTRICAL CIRCUIT

The purpose of the electrical system was to separate in time the temperature variant signal and the temperature independent reference signal. The circuit for each detector output was essentially similar as shown in the block diagram of figure 5.4.

A master oscillator coupled with simple combinational logic gates, controlled the switching and sampling pulses required. The oscillator output was fed to three drive

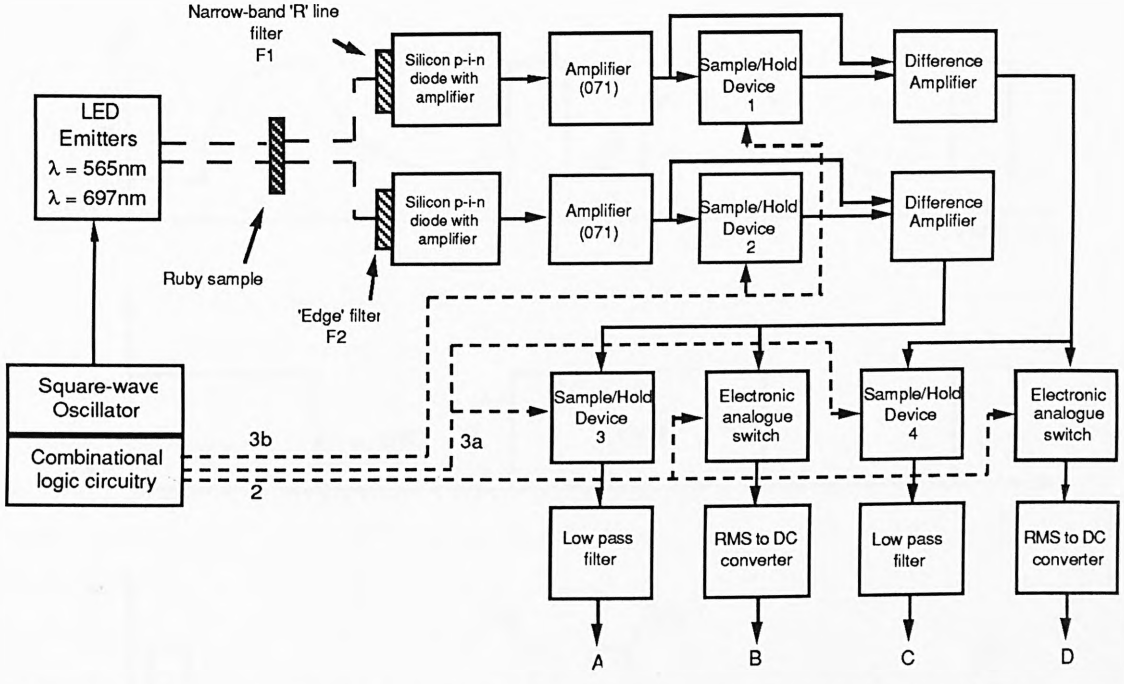

Figure 5.4 - Block diagram of the electronic circuit. A,B,C,D are the output signals.

circuits which controlled the switching and drive current to the two green and one red LEDs. The green LEDs were driven above their rated current limits to increase their output and hence maximize the overall fluorescence detected. The green and red LEDs were time multiplexed so that the two green LEDs were ON together for a period of 10ms and OFF for 30ms. During the OFF period the fluorescence was allowed to decay to nearly zero (i.e 5 decay lifetimes - a lifetime being approximately equal to 3.5ms for the sample used). During the period the exponential decay was essentially at a zero level, the red LED was switched ON for a period of 5ms, as is shown schematically in figure 5.5.

The signals received from the ruby sample were detected by silicon photodiodes (sensitive in the visible region), with integrated amplifiers. These signals were further amplified

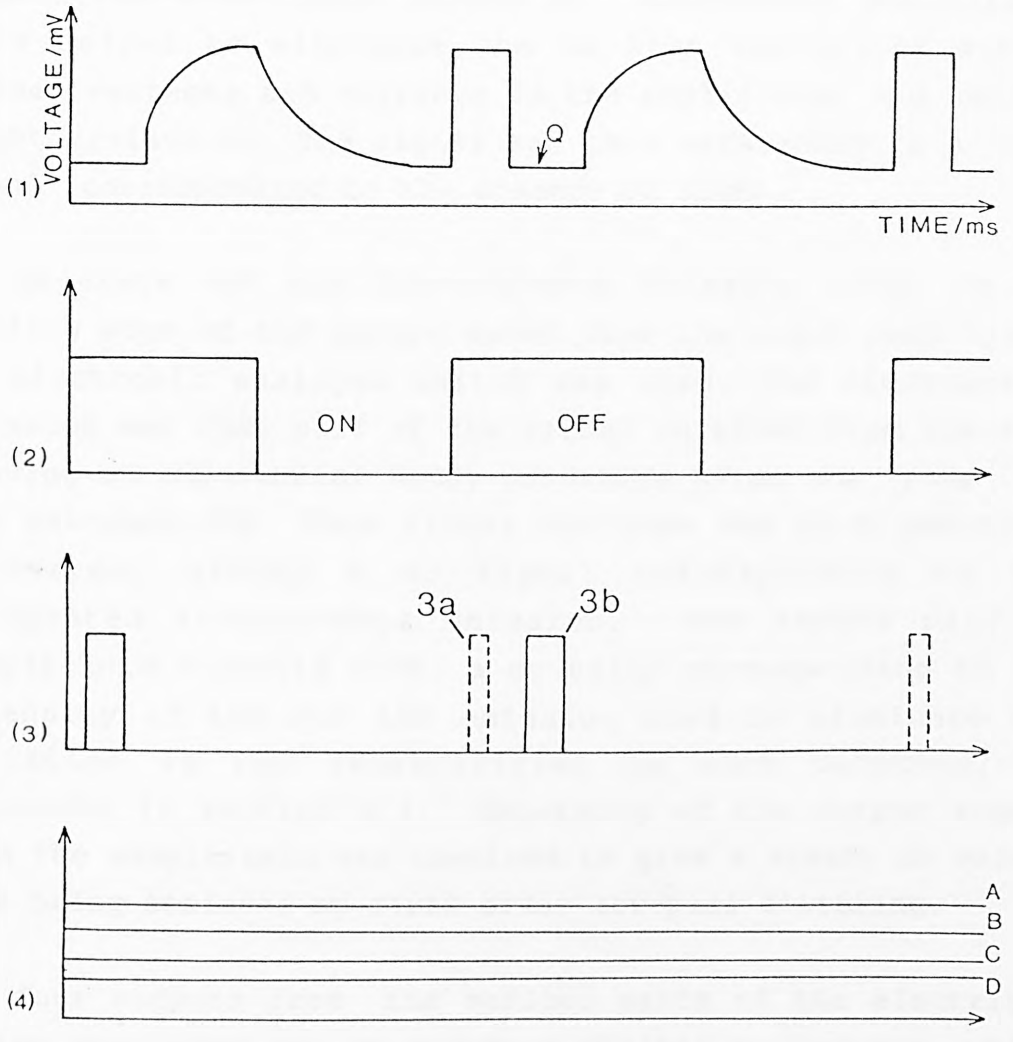

Figure 5.5 - Voltage waveforms (Numbers refer to Figure 5.8)

(1) : Signal at point '1' - after amplifier stage

(2) : Signal to analogue switch (at point '2')

(3) A(dashed) : Signal to S/H 3 and S/H 4.

(3) B(solid) : Signal to S/H 1 and S/H 2.

(4) : Outputs at A, B, C, D.

by external amplifier stages and fed to sample/hold circuitry. The signal was sampled at the point when both LEDs were OFF and when there was no fluorescence (point Q - figure 5.5). The outputs of the sample-hold circuits were subtracted from their inputs by difference amplifiers. This helped to eliminate the dc bias variations due to offset voltages and currents in the amplifiers, and ambient light variations. The signal was thus referenced to a 'zero level' corresponding to the absence of light.

To separate out the fluorescence emission (seen on the falling edge of the square wave) from the input pump light, an electronic analogue switch was used. The fluorescence emission was that part of the signal received from the ruby showing an exponential decay occurring after the 'pump' LED was switched OFF. This signal was then fed to a rms-to-dc converter, giving a dc signal corresponding to the integrated fluorescence emission. The second pair of sample-hold circuits gave a dc value corresponding to the intensity of the red LED emission used to eliminate the variation in the sensitivities in each detector, as discussed in section 5.3. Smoothing of the output signal from the sample/hold was required to give a steady dc value, this being achieved by first-order low-pass filtering.

The four outputs from the various parts of the electrical system were read out on standard digital voltmeters, which provided further smoothing and hence, filtering of noise; alternatively these voltages could provide an input to a simple microprocessor to be related directly to a temperature calibration, as discussed below. These outputs are denoted by intensities A, B, C, D respectively in figure 5.5(4).

5.2.1 Detailed electronic design

The electronic design of the receiver was similar to that used in chapter 3, except that in this case, two photodiode

receiver circuits were used and the signal processing for both receiver channels was exactly the same. Hence, there were four outputs which were monitored on standard digital voltmeters.

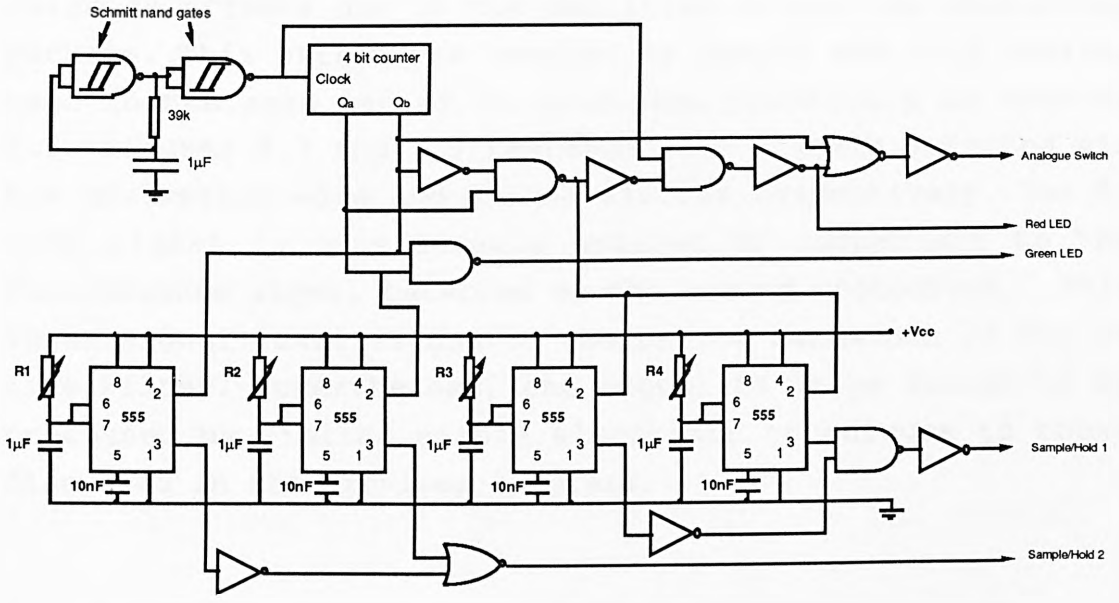

Figure 5.6 - Complete digital circuit diagram (all logic gates used were CMOS).

The combinational logic circuitry was, however, different and shall now be described. The diagram of the combinational logic circuit is given in figure 5.6. A resistor and capacitor were connected across a Schmitt nand gate and generated square pulses. These were fed to a second nand gate acting as a buffer stage and then to a four bit binary counter. The Q_a and Q_b outputs combined with the original clock signal were fed through logic circuitry to provide the switching pulses for the two electronic analogue switches, one in each detector stage, and pulses for the red LED. Four 555 timer chips with a few logic gates generated pulses for the two sample/holds which were used to extract the peak levels of the red LED pulses at each photodiode receiver stage. These pulses were made variable through the use of a 555 timer circuitry and could be adjusted in duration by the

preset resistors R1, R2, R3 and R4 shown in figure 5.6. The red and green LED signals were fed to single transistor stages similar to those described in the earlier work.

Typical voltage levels detected at each photodiode stage are shown in figures 5.7 and 5.8. Both signals experienced large dc offsets due to the amplifier within the photodiode package. This offset was removed by sample and hold devices used in the same manner as discussed previously in section 5.2. Figures 5.7 and 5.8 represent the signals detected via the absorption edge and R-line filters respectively. The R-line signal is considerably smaller by comparison to the fluorescence signal detected on the second photodiode. This lower signal level is due to the narrow bandwidth of the R-line filter. Nevertheless, the signal is large enough to be processed by similar simple electronic techniques to those discussed in the previous chapters.

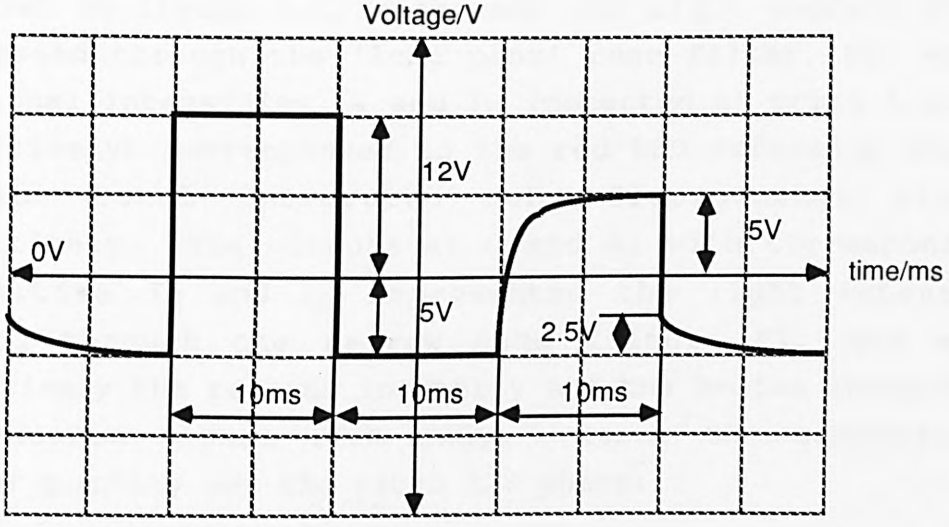

Figure 5.7 - Signal detected via the absorption edge filter.

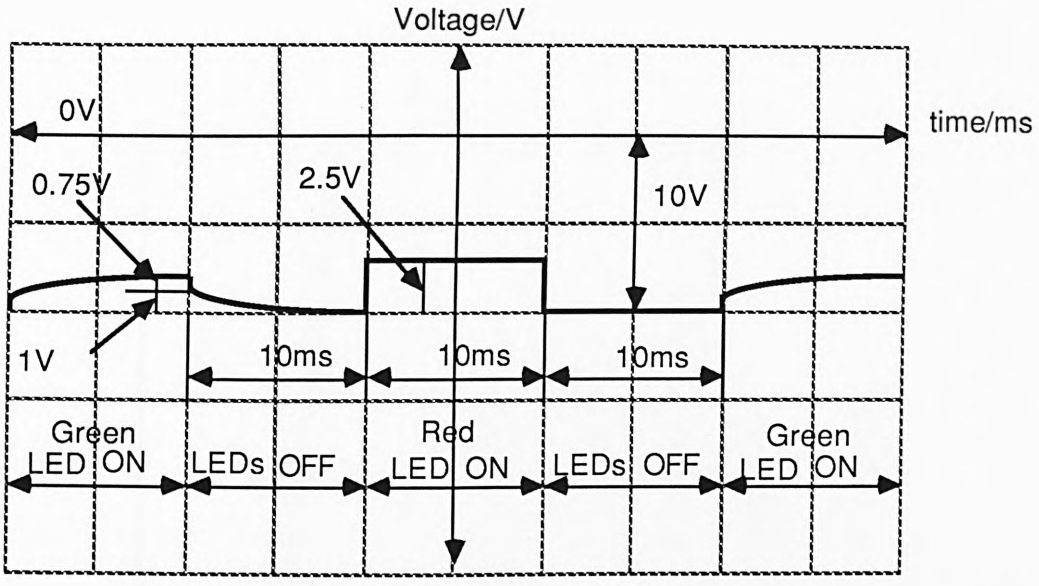

Figure 5.8 - Signal detected via the R-line filter.

5.3 CALIBRATION AND CHARACTERISTICS OF THE SENSOR

The device was calibrated as follows. The outputs at A and B, shown in figure 5.4, represent the light signals which had passed through the 'long pass' edge filter, F2, where the signal intensities I_A and I_B (detected at ports A and B respectively) corresponded to the red LED reference signal and the total integrated ruby fluorescence signal respectively. The outputs at C and D, with corresponding intensities I_C and I_D represented the light intensity passing through the narrow band filter, F1, and were respectively the red LED intensity and the R-line integrated fluorescence signal from ruby. Hence the temperature varying quantity was the ratio X/Y where:

$$X = I_B/I_A \text{ and } Y = I_D/I_C$$

This was plotted as a function of temperature, measured in Kelvin, as shown in Figure 5.9.

The calibration of the ruby crystal transmission type 'point

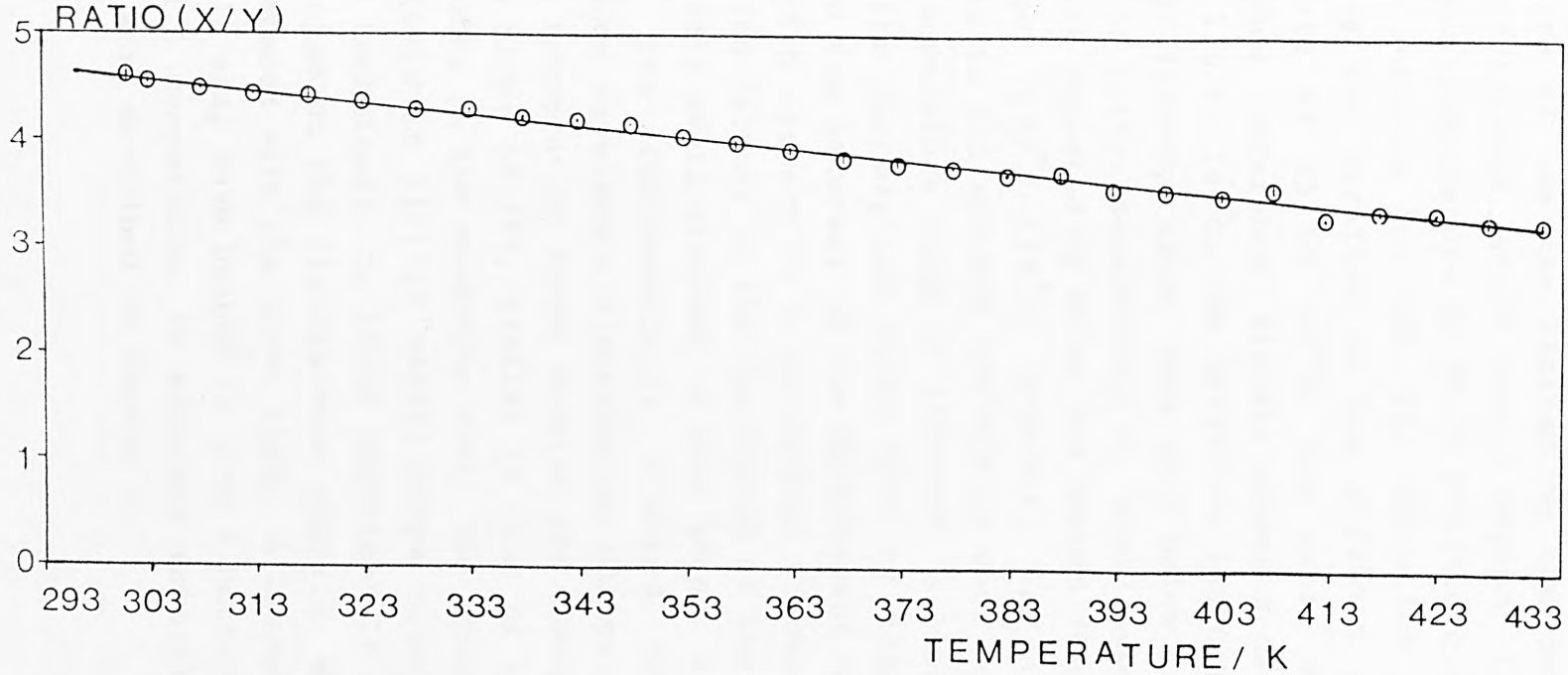

Figure 5.9 - Calibration graph of the probe in the region from 293K to 433K (20°C to 160°C).

sensor' showed a linear profile obtained with the normalized transmission being a slowly varying quantity with temperature over the range illustrated. The upper temperature of use was limited by the deviation in the quantum efficiency, which occurs beyond ~160°C (80), also the maximum temperature at which plastic clad silica (PCS) fibre is suitable for use. The deviation in the quantum efficiency was verified in the previous chapter. For a temperature of up to 130°C, the ratio of 'probe' and fluorescence 'reference' signals showed a deviation of ±1%, but from 130 to 160°C, the deviation increased to ±2%. The quantum efficiency, thus, does vary below 240°C indicating the lack of either sensitivity or 'high' experimental error in the work reported by Burns and Nathan (80) especially in the range ~160°C-240°C. However, for this work the variations in the quantum efficiency were relatively small for the temperature range of interest. A linear profile was seen in the temperature range 293K to 433K (i.e 20°C to 160°C) and the accuracy of the measurement was recorded to be ±3K, with respect to a calibrated thermocouple. One of the limiting factors of the resolution of the device was the comparatively small gradient of this graph, 0.010 K^{-1}, which reflects the fundamentally limited nature of the fluorescence wavelength distribution change. However, over the whole temperature range studied the change in the ratio is of the order of 26%, similar to that of the resin-fixed sensor probes in the neodymium work. The accuracy could have been improved if similar oscilloscope based sampling and averaging techniques, to those described in chapter 4, had been employed on the fluorescence signals, which were much weaker compared with the green light. A larger change in the ratio would also have helped to give a better accuracy, but it is still comparable, in accuracy nevertheless, to the neodymium work described in chapter 2.

5.4 DISCUSSION

A preliminary device illustrating the use of an internally generated reference signal from ruby fluorescence has been constructed and tested. The scheme used can minimize the long term uncertainties seen in other forms of referencing using a second source at a different wavelength, whose spectral characteristics cannot be guaranteed invariant with ageing, as the second LED wavelength is merely used to maintain the relative calibration of two detector photodiodes. Changes in the output as a function of wavelength of the green LED source in the long term will affect the overall intensity of fluorescence produced. This is due to the change in the overlap of the green LED's emission spectrum with the absorption profile of the ruby sample. However, as both the LED emission spectrum and the ruby absorption spectrum are broad, the change in intensity is expected to be small ($\leq$10%) for a shift in the peak LED emission of ~5nm and, of more importance, this change in intensity affects both the emission in the R-line region and the overall fluorescence intensity equally. The only consequence of a drop in fluorescence intensity was on a slight decrease in the signal/noise ratio. Thus the change expected from spectral shifts or an overall intensity drop is small, and this should have a negligible effect on the calibration. Any deviation of the ruby fluorescence decay from being a true exponential is not important as it is the integrated fluorescence intensity which is measured.

A change in the output profile with wavelength of the red LED emission will have some effect upon the calibration. However, to reduce the effect, the red LED is operated well below its maximum current to reduce ageing significantly. The use of a 5nm bandwidth interference filter (F1) in front of one photodetector coupled with an LED emission spectrum which is almost an order of magnitude greater in bandwidth (~40nm) means that even if a shift of several nanometers in

the wavelength corresponding to the peak intensity of the red LED spectrum occurred, the transmitted intensity through the filter would change by only a few percent. By these means it is expected that recalibration, which could easily be performed, is avoided due to the relative insensitivity of the system to LED spectral or intensity variations. The signal with the lowest value of signal/noise ratio, which ultimately limits the accuracy of the ratio X/Y, is the R-line intensity when observed through the narrow band filter (i.e. I_D). The signal/noise ratio in this channel was measured as 35 dB and therefore the optical fibre thermometer is relatively insensitive to small fluctuations in the output of the green LED due to ageing or power supply variations.

Such a thermometer is inexpensive, relying as it does, upon simple optoelectronic and electronic components. The long (~3.5ms) decay time of the ruby crystal enables 'low' bandwidth components to be employed, further reducing cost. Although ruby itself is expensive, the small crystal used is not required to be of high optical quality and 'reject' material from the laser industry is adequate.

The observed accuracy and responsivity of this sensor make it ideally suited to industrial control systems where high accuracy is not paramount and where the need for protection from the electrically hostile nature of the environment is important.

Chapter 6

RUBY FIUORESCENCE DECAY-TIME TEMPERATURE SENSOR

6.0 RUBY FlUORESCENCE DECAY-TIME TEMPERATURE SENSOR

This chapter describes the work on a crystalline ruby temperature sensor relying on the change of fluorescence decay-time with temperature.

6.1 PREVIOUS WORK

The first demonstration of the principle of an optical temperature sensor based on the fluorescent decay of ruby was made by Sholes and Small (53). A sample of ruby was investigated for possible use in an optical probe, but a fibre optic version was not constructed. The optical arrangement employed used light from a tungsten lamp, mechanically chopped with a camera shutter and focused on to the sample of ruby through optical lenses and filters. Electronic signal processing was used to measure the rate at which the fluorescent emission, excited by a short pulse of light, decayed by measuring the area under the decay curve between two accurate timing intervals at various temperatures. From this information the exponential decay time was measured. The dominant fluorescent emission from the ruby sample was centred around the R-line wavelengths. The signal averaging scheme gave a reported resolution for this device of $\pm 0.3^{\circ}C$. This piece of work demonstrated, although with a rather crude optical arrangement, the potential of this material for accurate temperature measurement. Bosselmann et al (55) reported on a different principle of measuring fluorescence decay-time. In their system, using Cr-doped crystal (Lutetium-Aluminium-Chrome-Borate), the received signal is fed back to the modulation stage of the emitter to create a self-oscillating system, whose frequency depends on the decay-time and hence on the temperature to be measured. Both sinusoidal and square wave modulation were investigated, with the square wave modulation giving better results. A standard deviation of 0.04K was achieved in their system for temperature between

0°C and 70°C. Grattan et al (58) have demonstrated an all fibre optic infra-red decay-time measurement system relying on the decay-time properties of neodymium doped in glass. This work has led to a refined system which is only limited by the relatively small change in decay-time with temperature (i.e approximately 0.2μs change per degree). More recent work published by Augousti et al (81), on an intensity independent fibre-optic temperature sensor uses the fluorescence effect of an alexandrite crystal for temperature measurement, in which the exciting light is electro-optically modulated with a He-Ne laser source. The device uses sinusoidal modulation and the resulting phase difference between a reference sine wave and the sine wave returning from the crystal gives an indication of the temperature. This laser-pumped temperature sensor achieved an accuracy of ±1°C with a 3-second response time.

In this work to produce a temperature measurement system a phase sensitive detection scheme was designed using a combination of optical and electronic filtering. The system uses a light emitting diode as the light source which has the advantages of small size, low cost and the ability of being modulated at reasonably high rates compared to incandescent light sources. Laser diodes can couple more than tens times the amount of optical power into fibres than LEDs, but there are no laser diodes on the market that emit at the required wavelength for the ruby phase sensor and, in general, laser diodes are considerably more expensive than LEDs.

6.2 THEORETICAL BACKGROUND TO DECAY-TIME MEASUREMENT

There are two main methods used for the measurement of fluorescence decay-time, namely the "pulse method" and the "phase modulation" method. In the former method the sample is excited by a short pulse of light and the resulting emission at a longer wavelength is an exponentially decaying

function whose rate of decline with time can be measured. In the latter method, the sample is excited with sinusoidally modulated light and this results in a sinusoidally modulated fluorescent emission which lags in phase with the original excitation sinusoid. The phase shift gives an indication of the decay-time. The major advantage of such decay-time measurement techniques is that they obviate the need to make accurate measurements of the input light intensity for reference purposes. This is a very important consideration in fibre optic sensors, as the information is carried by the fluorescence decay-time.

6.2.1 Pulse decay-time measurement

The lifetime of an excited electron in a fluorescent material is on a time scale from tens of nanoseconds to milliseconds. The probability of decay is independent of the lifetime of the excited electron. Thus if a large number of excited electrons are present, the number of such electrons (and their decay rate) will decline exponentially. Hence a material excited by a short duration pulse will exhibit an exponential decay, characterized by a specific decay-time, which may be measured.

If a fluorescent medium is excited by an infinitely short duration pulse of light, the rate of decay of the fluorescence emission can be given by the following differential equation which illustrates the decay of excited species:

$$\frac{dN(t)}{dt} = -(\phi + \kappa)N(t) \quad \text{-------(6.1)}$$

where N(t) is the number of excited species at time t after excitation, ϕ is the emissive rate, and κ is the rate of non-radiative decay. If $N(t)=N_o$ at t=0, the solution of the above equation becomes:

$$N(t) = N_o.e^{-t\ (\phi + \kappa)} \quad \text{-------(6.2)}$$

Hence, under these circumstances, the emission is seen to be an exponentially decaying function of time.

If the fluorescence intensity thus produced is seen to decrease from any level I_a to a level I_e (where for convenience $I_a = 2I_e$) then $(\phi + \kappa)$ is given by

$$(\phi + \kappa) = (t_e - t_a)/\ln 2 \quad \text{-------(6.3)}$$

where t_a and t_e are the times corresponding to I_a and I_e respectively. Hence, Grattan et al (58), have described experimental configurations based on this method using doped Nd:glass bonded to two optical fibres for temperature measurement, and this method of decay-time monitoring uses quartz crystal-based timing circuits.

6.2.2 Phase modulation measurement

In this method the sample of fluorescent material is excited with light whose intensity is sinusoidally modulated. The modulated emission lags in phase the excitation sinusoidal light. The emission of a sinusoidally excited fluorescent material is a sine wave and this can be proved by using the Convolution integral. It has to be assumed that for a unit impulse or a delta function of light, the emission intensity is an exponentially decaying function of time i.e $e^{-t/\tau}$, where τ is the decay constant. Hence, the Convolution integral for sinusoidal modulation becomes

$$= \int_0^t I_o \sin\omega x \, . \, e^{-((t-x)/\tau)} dx \quad \text{-------(6.4)}$$

$$= I_o \, e^{-t/\tau} \int_0^t \sin\omega x \, . \, e^{x/\tau} \, dx \quad \text{-------(6.5)}$$

Using integration by parts gives

$$= \frac{I_o \omega\tau^2}{1 + \omega^2\tau^2} \left(\frac{\sin\omega t}{\omega\tau} - \cos\omega t + e^{-t/\tau} \right) \quad \text{-------(6.6)}$$

The $e^{-t/\tau}$ term decays to nearly zero after effectively 5τ. The phase angle can be found by combining the $\sin\omega t$ and $\cos\omega t$ terms, thus, equation 6.6 can be written in a general form as

$$G(\omega) \sin(\omega t - \sigma) \quad \text{-------(6.7)}$$

where $G(\omega)$ is a function of the angular frequency and σ the phase angle between the incident wave and the output fluorescence wave. From equation 6.6, phase angle is given by

$$\sigma = \tan^{-1} (1/\omega\tau) \quad \text{-------(6.8)}$$

The phase angle is, thus, a function of the frequency of the sine wave and the decay-time constant. It is important to select an appropriate working frequency and to do this the phase angle was plotted as a function of decay-time for the various frequencies, as shown in figure 6.1. This gives the potential to maximize the sensitivity of the device. As can be seen from these curves, at higher frequencies the curve becomes rapidly non-linear, but shows two approximately linear regions, with different gradients. In the first linear region a small change in the decay-time produces a comparatively large change in the phase angle, whereas, in the second linear region a very much larger decay-time corresponds to the same phase change. For the pink ruby sample the decay-time at room temperature is approximately 3.5ms. This is expected to reduce at higher temperatures. Clearly, as frequency is reduced the whole curve tends towards linearity. A frequency near 50Hz seems ideal,

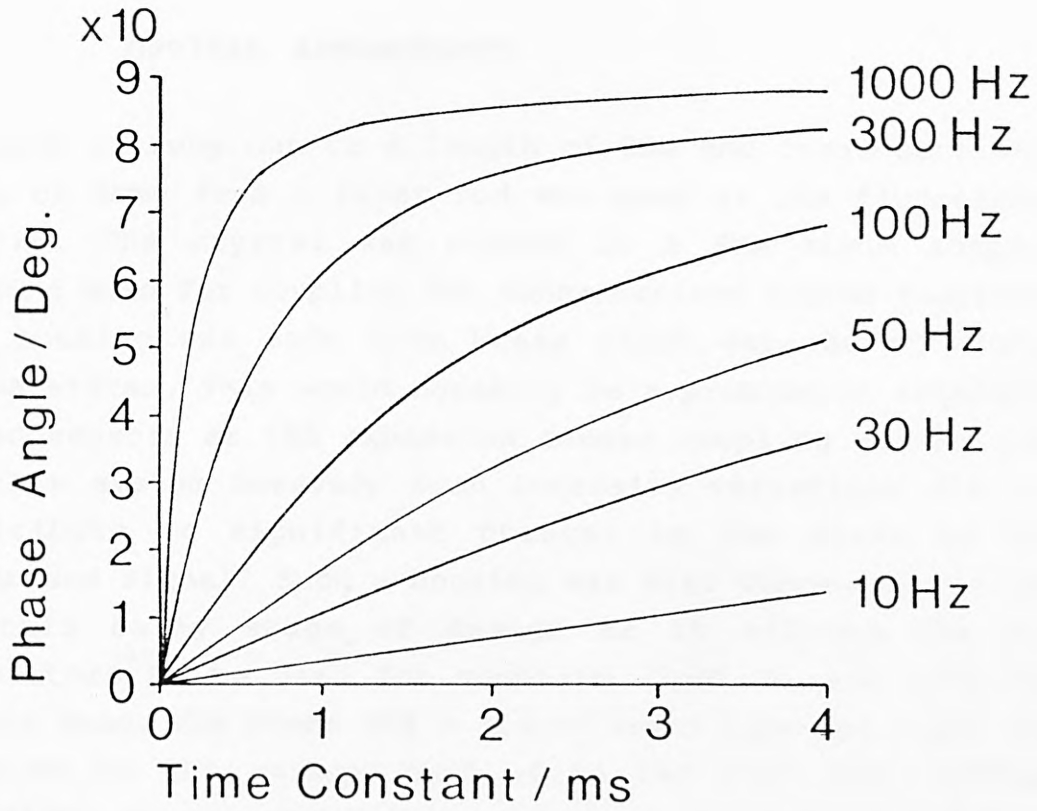

Figure 6.1 - Graph of phase angle against time-constant for various modulating frequencies

exhibiting a large change in the phase angle with decay-time, but using 50Hz presents electrical problems due to pick-up of the mains frequency. Secondly, using a lower frequency means slowing the data accumulation rate and the processing time of the microprocessor system and hence increasing the response time of the whole system. As a compromise between higher resolution and response time, a frequency of 125Hz was selected.

6.3 OPTICAL ARRANGEMENT

A piece of ruby cut to a length of 3mm and cross-sectional area of $1mm^2$ from a laser rod was used as the fluorescent medium. The crystal was placed in a SMA style adaptor housing used for coupling SMA connectorized fibres together. The housing was made from brass which expands at higher temperatures. This would normally be a problem in intensity based sensors as the expansion causes coupling variations. In this system however, such intensity variations did not contribute to significant changes in the phase of the measurand signal. Such a housing was also convenient to use in this early stage of design as it allowed SMA end connectors to be used for coupling light to and from the sensor head. The probe was a transmission type and light was coupled to the sensor head using two 1000 PCS (1000µm diameter) fibres. These provided for a sufficient level of light to be received at the detection stage. The alternative would otherwise have been the use of either a bundle of fibres or a much more powerful light source than the one that was used, to give the equivalent level of coupled light. A single broad band green LED, sinusoidally modulated, with peak emission at a wavelength of 565nm was used instead of bulky, cumbersome and expensive lamp light sources. The emission profile of the LED is as shown in figure 6.2, at various drive currents up to its maximum rated limit. A small shift in peak wavelength to the

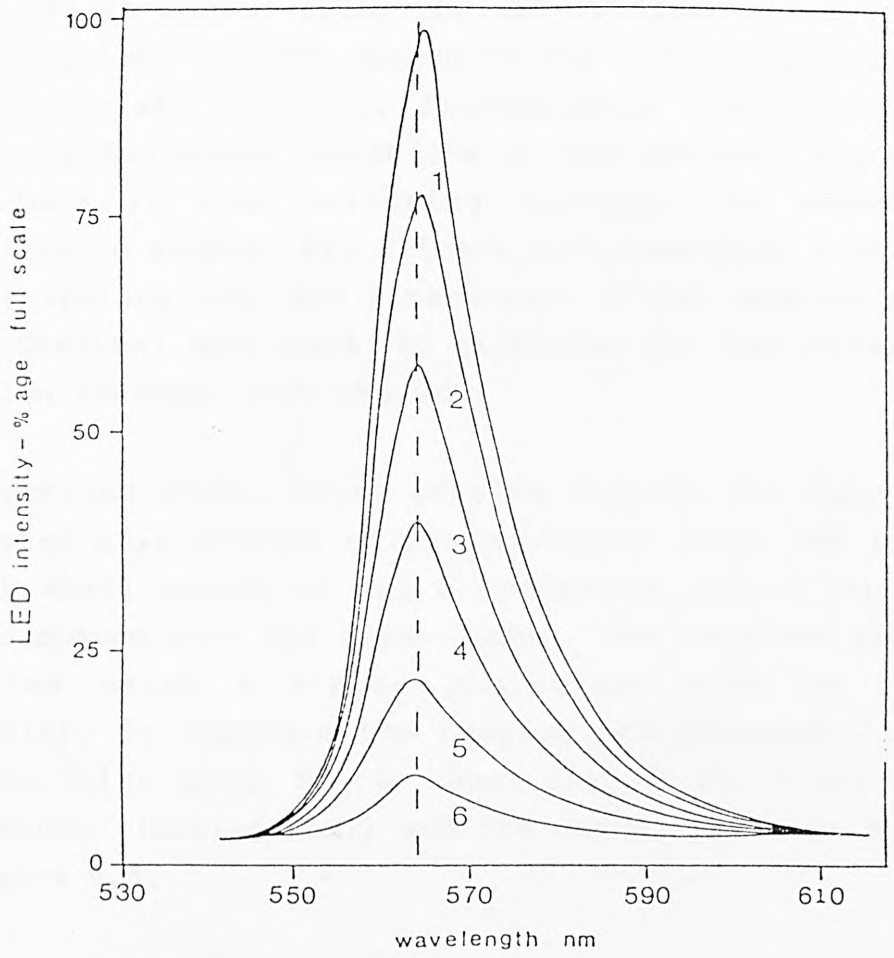

Figure 6.2 - Spectral emission of the green LED used in this work as a function of drive current.
1: 30mA, 2: 25mA, 3: 20mA, 4: 15mA, 5: 10mA, 6: 5mA.

red (2-3nm) is seen over the current range shown in figure 6.2. The LED may be driven much further beyond this current limit, but the output colour and thus, the whole output profile starts to shift towards the longer wavelength region. This causes severe problems which are discussed later. As it can be seen, the LED emission has a long tail extending into the red region of the visible spectrum. This emission mixed with the fluorescence signal and caused amplitude and phase variations in the detected signal as is explained in the following section. To reduce this interference effect, two filters were examined; a short-pass filter (Ealing Ltd) and a band-pass filter centred at 565nm (Glen Creston) were used to eliminate the low intensity red emission (>630nm) from the LED.

The received light, after passing through the ruby sample, consisted of a mixture of predominantly green LED light and a very small amount of red fluorescence signal (about 10^{-4} less compared with the green light). The received signal was detected using a single photodiode with an integral amplifier. To separate the pumping and emission light, an optical high-pass filter was placed in front of the photodiode, (Ealing Ltd)) and its characteristics are shown in figure 6.3.

6.3.1 Optical filtering

It was important to separate the green and red emission at the optical receiver since the mixing of these waves caused amplitude and decay-time variations and thus errors in the final calibration. Hence, the detected phase of the signal became sensitive to the coupling effects of fibre connections. To illustrate the effect, consider the superposition of two waves of constant phase difference and of the same frequency. Using complex vector addition consider the real parts of the two sine waves with phases of θ_1 and θ_2, and amplitude A_1 and A_2.

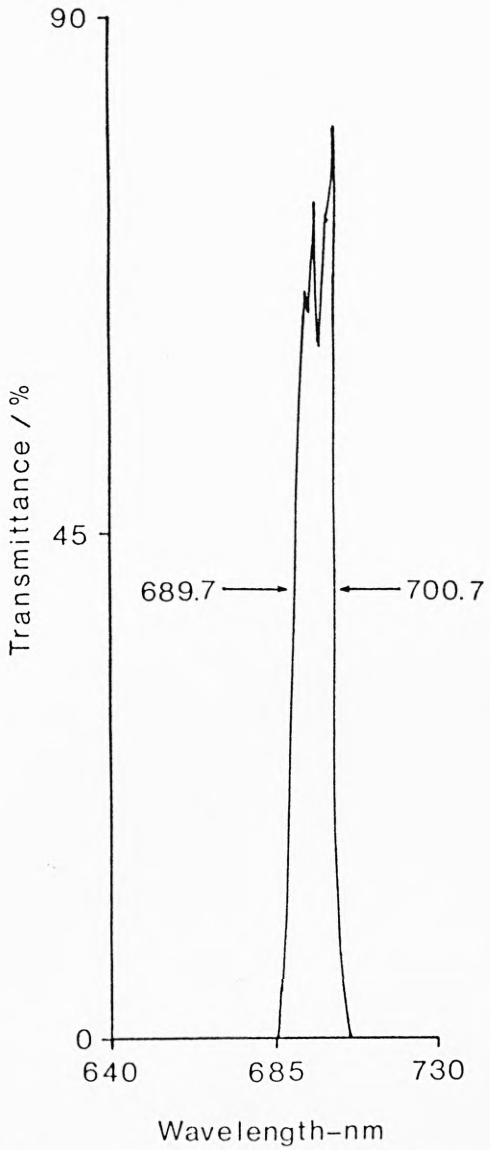

Figure 6.3 - Spectral response of the Ealing interference filter, centred near the R-lines

$$A_1 = A_1 e^{i(\omega t + \theta_1)} \quad \text{-------(6.9)}$$

$$A_2 = A_2 e^{i(\omega t + \theta_2)} \quad \text{-------(6.10)}$$

Adding these two equations gives

$$A = A_1 + A_2 = e^{i\omega t} (A_1 e^{i\theta_1} + A_2 e^{i\theta_2}) \quad \text{-------(6.11)}$$

multiplying both sides by the complex conjugate

$$A^2 = A_1^2 + A_2^2 + A_1 A_2 (e^{i(\theta_1 - \theta_2)} + e^{-i(\theta_1 - \theta_2)}) \quad \text{-------(6.12)}$$

Using Euler's formula

$$A^2 = A_1^2 + A_2^2 + 2A_1 A_2 \cos(\theta_1 - \theta_2) \quad \text{-------(6.13)}$$

Since the intensity of a wave is proportional to the square of the amplitude, $I \alpha A^2$, and as $\theta_1 - \theta_2$ is the phase difference, σ, equation 6.13 becomes:

$$I = I_1 + I_2 + 2(I_1 I_2)^{1/2} \cos\sigma \quad \text{-------(6.14)}$$

When $\sigma = 0$, I becomes a maximum

$$I_{max} = I_1 + I_2 + 2(I_1 I_2)^{1/2} \quad \text{-------(6.15)}$$

When $\sigma = 180^{o}$, I becomes a minimum

$$I_{min} = I_1 + I_2 - 2(I_1 I_2)^{1/2} \quad \text{-------(6.16)}$$

Figure 6.4 shows the two sine waves and their resultant wave, which shows that for maximum phase difference due to ruby emission and insensitivity to any long term variations in the green LED emission intensity, the green light has to be completely eliminated.

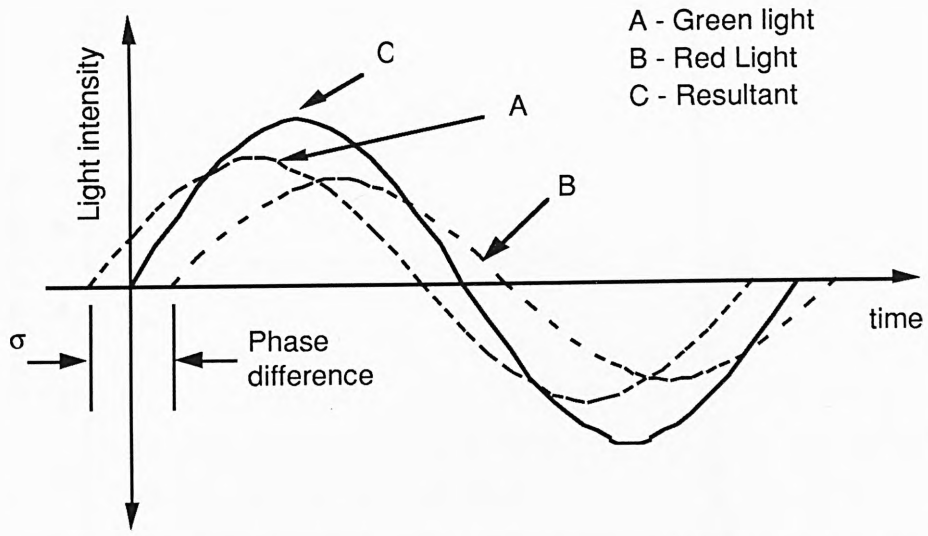

Figure 6.4 - Two sine waves, A, and, B, of constant phase difference, σ, with their resultant sine wave, C, which represents the detected signal.

6.3.1.1 Filter characteristics

An interference-type, low-pass, edge filter was used to remove the red light emanating from the green LED. The filter characteristic spectrum is displayed in figure 6.5 and shows a 'cut-off' region at 629nm (a point where there is 45% transmission of light through the filter). This filter allowed very little red emission from the LED (7% of total signal) compared to the ruby red fluorescence emission (93%) near the emission wavelength of the ruby, to pass through. It was impossible to eliminate all the unwanted LED light, but the sharpness of the cut-off edge of the filter can be improved with higher quality filters. The results of comparing the, above, 'low' quality Ealing filter and a 'high' quality Glen Creston filter, whose transmission characteristics are shown in figure 6.6, are given later in the chapter.

The interference-type edge filters consist of quarter wave and modified quarter wave layers sandwiched together. They are characterized by an 'edge' region where the filter characteristics quickly changes from reflection to

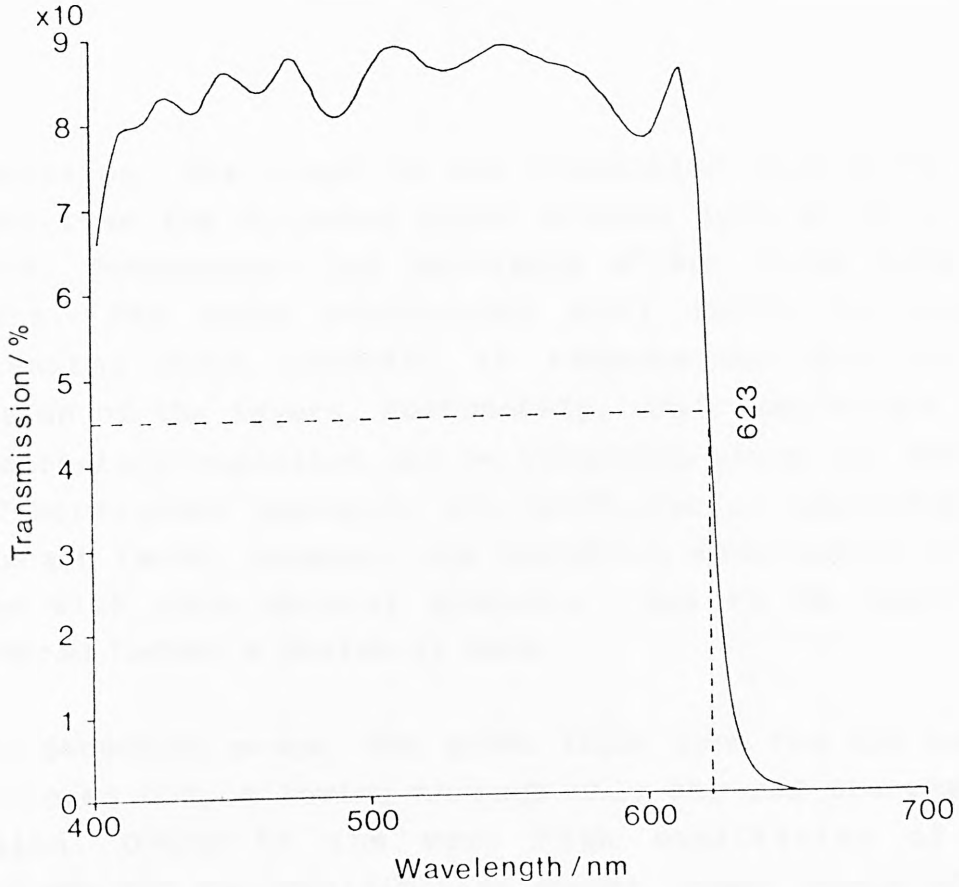

Figure 6.5 - Spectral response of the Ealing interference short-pass filter

Figure 6.6 - Spectral response of the Glen Creston filter with transmission plotted as a function of wavelength

transmission. The slope in the transition region is much sharper than for coloured glass filters such as OG and RG filters. Temperature can adversely affect these types of filters. The edge wavelength will shift to longer wavelengths with increase in temperature due to the expansion of the layers. Fortunately, small variations of a few nanometers expansion can be tolerated since the pumping and fluorescence emission are sufficiently separated in wavelength terms. However, the operating environment of the system with such optical elements has to be carefully considered before a choice is made.

At the detection stage, the green light from the LED had to be filtered out, allowing through only the red fluorescent emission. Owing to the very high sensitivity of the photodiode and the amplification stages, power levels of the order of tens of nanowatts could be detected. Simple RG-glass absorption edge filters (Schott glass) were initially used. An RG-630 high-pass filter reduced the green light by at least an order of magnitude and the RG-695 filter reduced the green even further, but the level of green transmitted by these filters, owing to the long cut-off tail, was enough to completely swamp the ruby fluorescent emission. The diagram in figure 6.7 illustrates the extremely small level of LED light (L) that was able to be transmitted through both the low (B) and high-pass filters (C).

To reduce the green light significantly i.e to a tiny fraction of the red emission (~1%), a band-pass interference filter centred at 695.2nm with a bandwidth of 11nm, was used. A band-pass filter consists of a series of thin films, which make up partially reflecting layers arranged as a single or multiple Fabry-Perot interferometers. The spacing between the layers is chosen so that the beams produced by multiple reflections from the layers are in phase with the transmitted beam for the

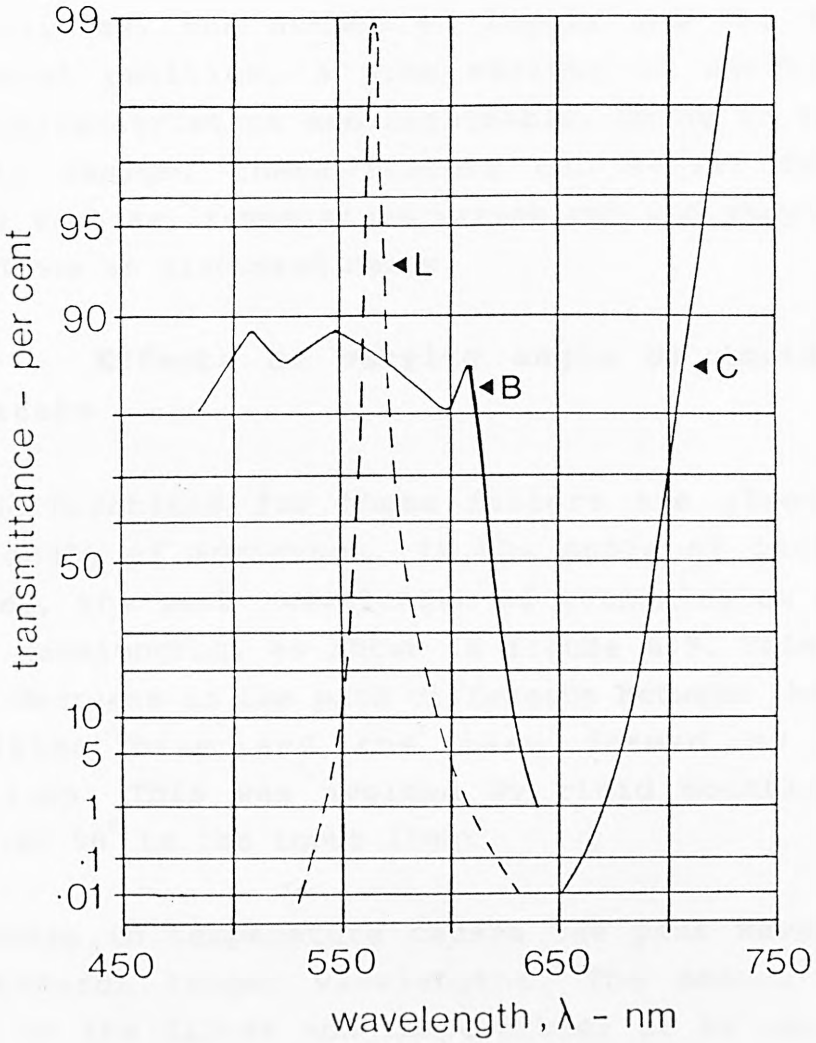

Figure 6.7 - Transmission characteristics.
Ealing shortpass(B) and RG630(C) filters as compared to the LED emission(L)

desired wavelength, (figure 6.8), thus enhancing the transmittance of the filter for that wavelength. Other wavelengths are reflected because these multiple beams destructively interfere with each other. By varying the reflectivities, the number of layers and the number of Fabry-Perot cavities, a wide variety of bandwidths and filter characteristics are obtainable. Owing to the nature of their design, these filters can suffer from major problems such as, temperature variations and varying angles of incidence as discussed below.

6.3.1.2 Effects of varying angle of incidence and temperature

The specifications for these filters are given for the normal angle of incidence. If the angle of incidence is increased, the peak wavelength of transmission shifts to shorter wavelengths, as shown in figure 6.9. This shift is due the decrease in the path difference between the directly transmitted beam and the beam formed by multiple reflections. This was avoided by rigid mounting of the filters at 90° to the input light.

An increase in temperature causes the peak wavelength to shift towards longer wavelengths. The amount of shift depends on the filter and temperature; it is usually only very important at narrow bandwidths where typically shifts of 0.003% per $^{\circ}C$ in the peak wavelength may occur. But a more serious effect at high temperature is the degradation and darkening of optical cement which can cause non-reversible shifts in the centre wavelength. However, in this application the filter will be mounted in the control and detector box and thus will not be subject to major temperature excursions. Additionally, as the effect of a shift in its wavelength characteristics will only be to reduce the intensity of the fluorescence detected, and the measurement of decay-time is non-intensity dependent, the effect described should not be a severe problem.

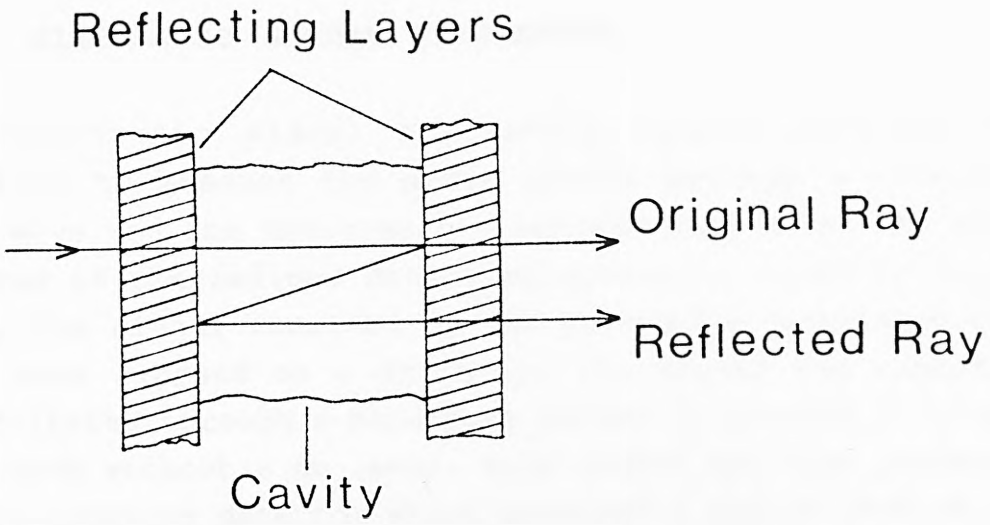

Figure 6.8 - Single wavelength-selecting cavity

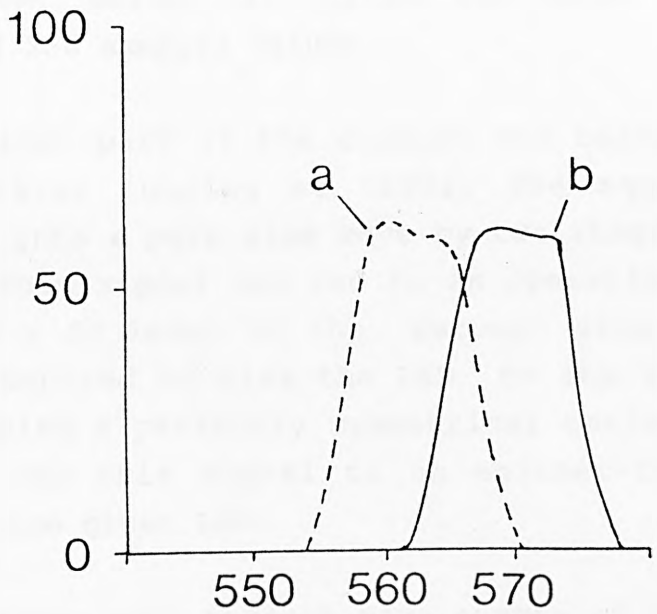

Figure 6.9 - Effect of a change in the angle of the incident light
(a) 20^0 incidence
(b) normal incidence

6.4 ELECTRONIC SIGNAL PROCESSING

The electronic signal processing system produced was required to measure the phase change between a reference sine wave and the detected fluorescent sine wave. The block diagram of the refined detection system is given in figure 6.10. The signal received by the photodiode consisted of a sine wave imposed on a dc level. The signal was amplified and filtered through a band-pass filter to provide a 'clean' sine wave without a dc level. This signal was then passed to a zero-crossing detector which provided a square wave of the same frequency as the sine wave.

This square wave plus a square wave from the oscillator, which drove the LED, was fed through an exclusive-OR gate to produce pulses whose length corresponded to the phase difference between the emitted and detected sine waves. The duration of these pulses was determined by a microprocessor based system, which calculated the mean and standard deviation of 256 sampled values.

The transmitter part of the circuit was based on a square wave oscillator running at 125Hz. The square wave was transformed into a pure sine wave by two stages of low-pass filtering. This signal was fed to an operational amplifier which added a dc level to the output sine wave. The dc level was required to bias the LED to its linear region, hence producing a perfectly symmetrical optical sine wave. The op-amp fed this signal to an emitter-follower stage which drove the green LED.

The final system went through many stages of refinement and redesign to reduce the effects of noise on the very weak detected signal and to produce a system with a very high resolution. The system can, basically, be separated into the analogue and digital stages; the following sections will give an account of the various analogue circuits considered and subsequently refined.

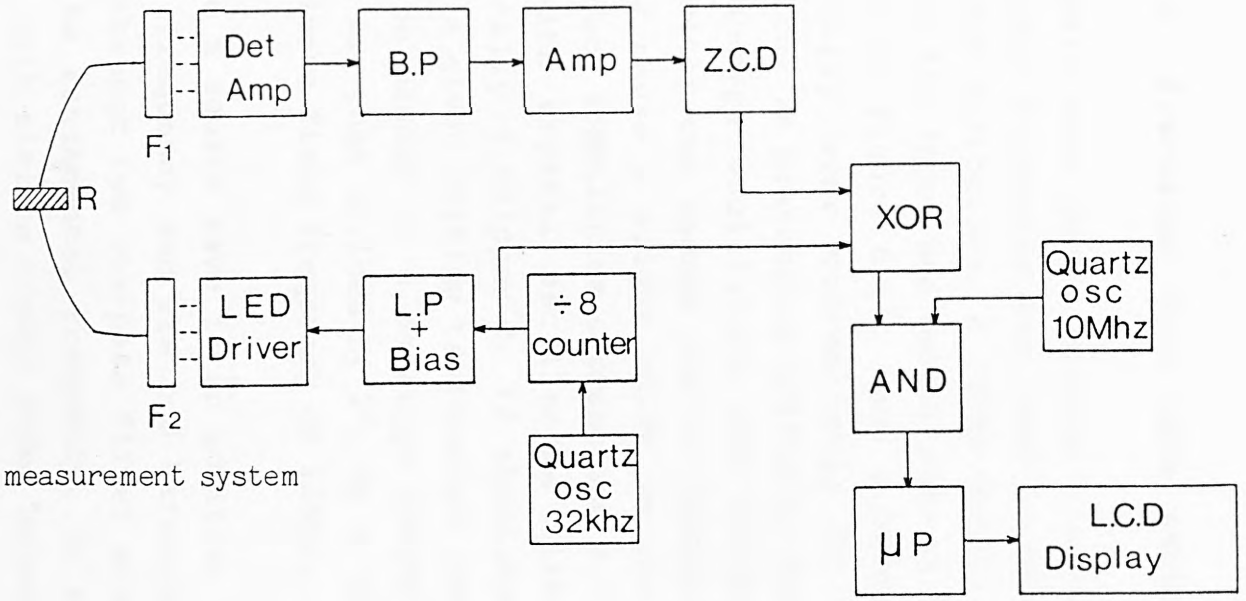

Figure 6.10 - Block diagram of the phase measurement system

F_1: Short-pass filter

F_2: R-line filter

R: Ruby sample

Det amp: Detector with amplifier in transimpedance mode

B.P: Electronic band-pass filter

Amp: Amplifier

Z.C.D: Zerocrossing detector

XOR: ExclusiveOR gate

AND: And gate

L.P + bias: Low-pass filter with dc bias

μP: Microprocessor

LCD: Liquid crystal display

6.4.1 Precision sine wave generation

A square wave quartz crystal oscillator with two stages of low-pass filtering was used to generate a sine wave with minimum distortion. A 32kHz quartz crystal was connected across the input and output pins of a CMOS inverter chip, as shown in figure 6.11. Such a circuit offers much greater stability over conventional RC oscillators, which is critical in preventing drifts in frequency and hence phase. In RC-type oscillators the values of the resistor and capacitor can change due to temperature and these changes would cause a slight shift in the frequency. With this approach stabilities approaching 0.1% can be attained. Where as with crystal oscillators stability of frequency is typically 0.001ppm/$^{\circ}$C. If absolute stability is required over a given working temperature range, then the oscillator can be placed in a constant temperature oven. The square wave was then divided by 2^8, by a 'divide-by-eight' counter, to give a fixed frequency of 125Hz.

Since a square wave is an addition of the fundamental sine wave frequency and its odd harmonics, the square wave was fed through two low-pass filter stages to give a sine wave at the fundamental frequency. In order to produce a sine wave with minimum higher order harmonic distortion, the cut-off frequencies (i.e -3dB frequency point) of the first and second filters were set at 90Hz and 75Hz respectively. These were found to be the best combination of filter cut-off frequencies to produce low distortion on the sine wave. The filters were originally designed with 3dB cut-off point at around 125Hz, but this allowed the higher harmonics of the square wave to filter through to the output. Hence, the cut-off frequencies were chosen to lie well below the 125Hz range. The filters introduced a phase difference between the original square wave and the output sine wave and this produced a constant systematic error in the final phase difference readings. This, however, can be readily taken into account in the calibration programme.

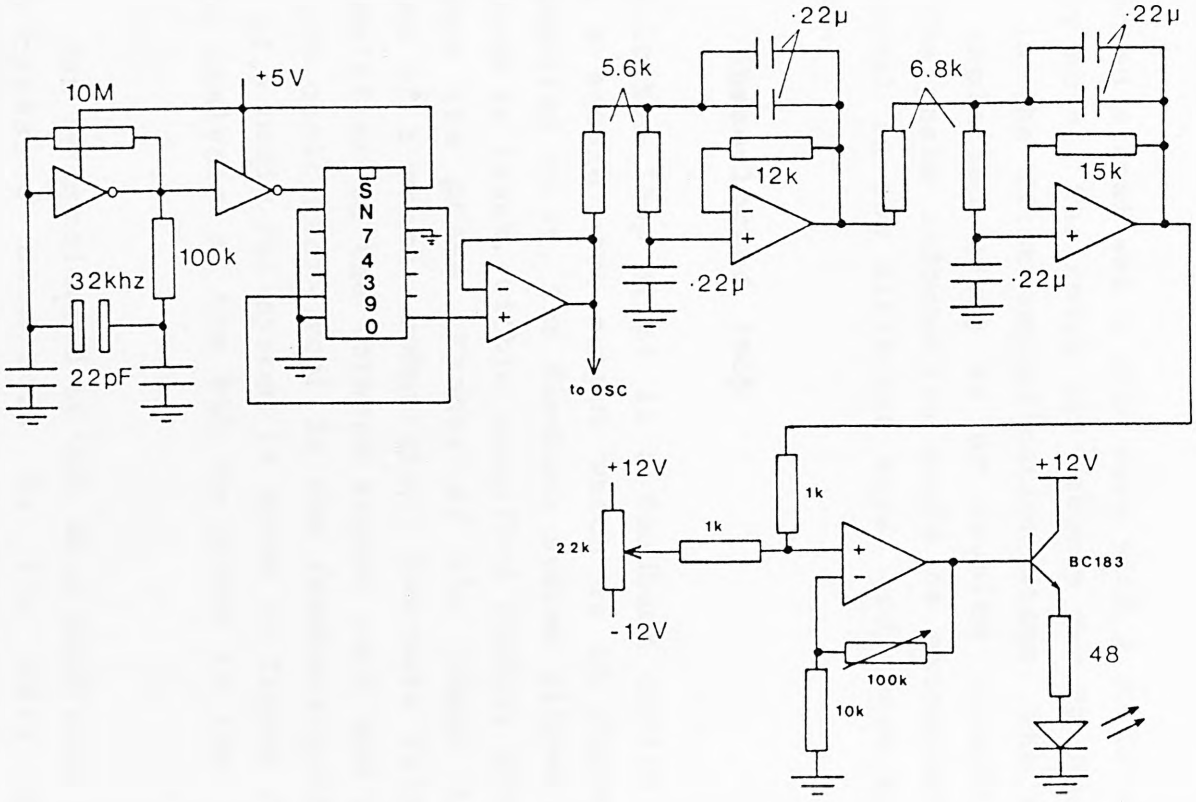

Figure 6.11 - Complete diagram of the sine wave generator and LED drive circuitry. (All op-amps are 071 series) (oscillator feeds into circuit in figure 6.14)

6.4.2 Receiver circuit

A photodiode with an integral amplifier was used to detect the low level of red fluorescent emission. The large surface area of this device ($5mm^2$) gave excellent sensitivity ($600mV/\mu W$) in the visible spectral region at very low cost (approximately twelve pounds).

The detected signal was a sine wave with a dc level and high frequency noise. The noise was largely due to Johnson noise arising in the first amplification stage. The signal was further amplified using an ac coupled inverting op-amp stage. The phase information could be extracted from the noisy signal in two different ways, and these will now be described.

6.4.3 Phase-locked loop

A phase-locked loop (PLL) is a feedback device which can provide a square wave output which is in phase with the input applied to it. The feedback system allows the phase-locked loop to track, within specified limits, the frequency and hence the phase changes of the input signal. It comprises of a phase comparator, low-pass filter and an error amplifier in the forward signal path and a voltage-controlled oscillator (vco) in the feedback path. A block diagram of a basic PLL system is shown in figure 6.12, and a detailed analysis of the PLL is given in the literature (82).

The PLL can be considered to act as a band-pass filter and a zero-crossing detector. By its very design it discriminates against much of the noise on the input signal. The noise in this case was reflected as fluctuations in the transition edge of the output square wave - also referred to to as 'jitter'. The jitter on the output square wave reduced the accuracy of the phase measurements, as will be explained

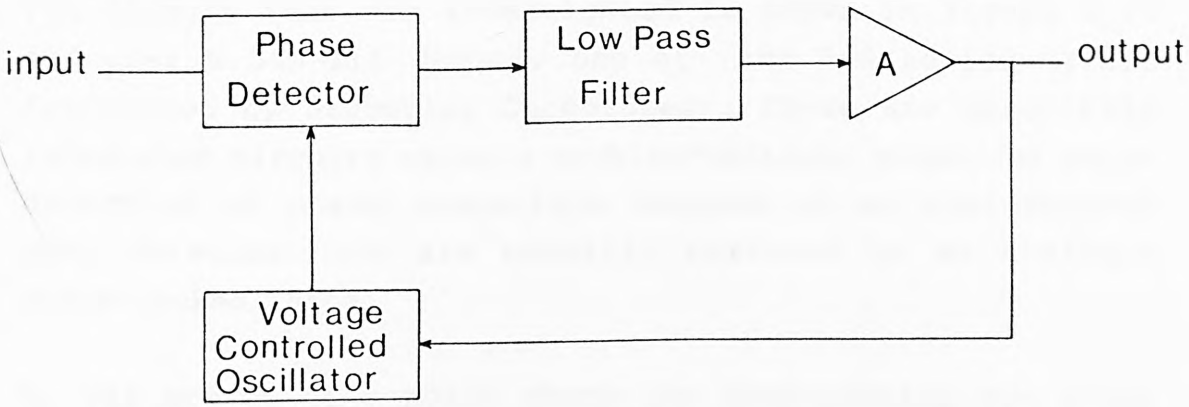

Figure 6.12 - Block diagram of the phase-locked-loop.

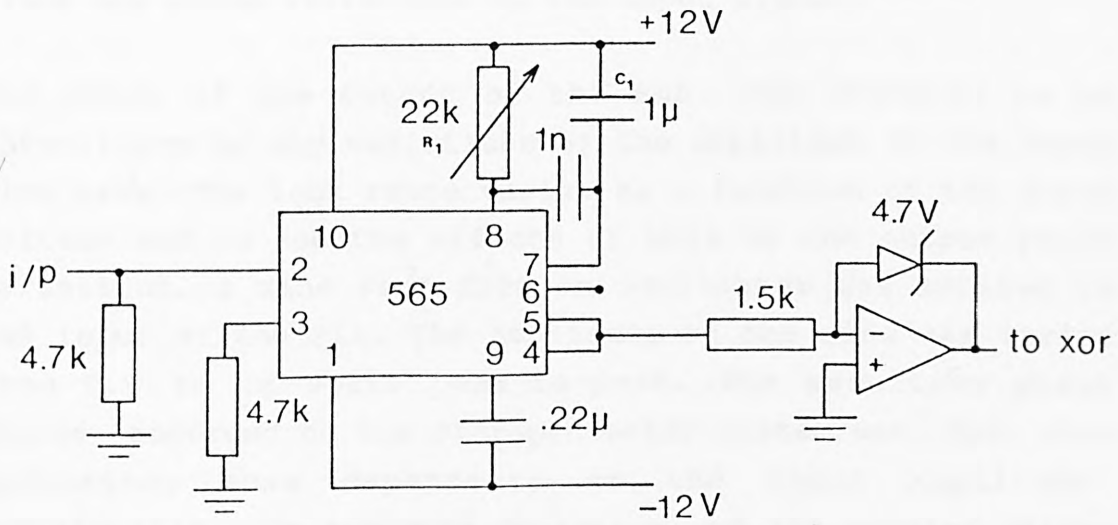

Figure 6.13 - Circuit diagram of the phase-locked-loop.

later. The discrimination of noise and hence prevention of jitter required careful tuning of the PLL to the input signal frequency and amplitude of that signal.

The circuit that was investigated is shown in figure 6.13 and uses a 565 PLL device, one of the 560 series (first introduced by Signetics Corporated). These are monolithic integrated circuits using a doubled-balanced mixer for phase detection or phase comparison instead of an exclusive-OR gate detector, and are normally referred to as analogue phase-locked loops.

R_1 was preset at a point where the free-running vco locks onto the input signal and could be determined by the following formula:

$$f_o = 1.2/\ 4R_1C_1$$

The PLL will track any frequency changes to within specified limits, but for fixed frequency input, it will track any phase variations in the input signal.

The phase of the output of the PLL was required to be insensitive to any variations of the amplitude of the input sine wave. The lock range varies as a function of the input voltage and to see the effects of this on the output phase variations, a sine wave from an oscillator was applied to the input of the PLL. The amplitude of the sine was varied from 0.4 to 12 volts peak-to-peak. The resulting phase change recorded on the microprocessor system was 13µs, thus indicating some dependence on the input amplitude. Additionally, the standard deviation of 256 sampled values representing each output reading was recorded to be 5µs. With the noisy sine wave input signal from the photodiode detector stage, this figure increased to 20µs. Thus, noise rejection of the PLL was adequate to give an accuracy of one degree Celsius in the lower temperature region from 40-45°C, but achieving a higher figure was one of the aims of

this work.

To overcome the variations in phase with amplitude, an automatic-gain-control circuit was connected before the PLL. Thus, any amplitude variations in the output of the photodetector would be compensated by this circuit. The output of this circuit remains unchanged for a 20dB reduction in the applied input and an appropriate circuit diagram can be found in the RS data sheet No. 4585. Although the amplitude of the signal remained steady for a given input, the phase of this signal varied by about 10-20μs over the 20dB input signal reduction. The circuit was thus introducing a phase-error in the system and coupled with the phase-locked loop, this phase error was accentuated. Thus, this circuit and the PLL were found to be an unsuitable means of phase measurement of sufficient accuracy for a system which could use the high sensitivity of the ruby 'decay-time' to measure temperature.

6.4.4 Phase detection

The alternative method of measuring phase requires firstly a 'cleaning up' of the detected sine wave signal and then a reduction of the noise level superimposed upon it. This was easily achieved by a selective band-pass filter centred on the desired frequency, in this case 125Hz, followed by a zero-crossing detector to transform the sine wave into a square wave which was then passed through an exclusive-OR gate with a reference square wave from the output of the divide-by-eight counter. The complete circuit diagram of the system developed is shown in figure 6.14.

To design the band-pass filter the following considerations were made. A band-pass filter may be designed using purely passive components such as resistors, capacitors and inductors or can use active elements such as op-amps to simulate inductors. The latter method is far more convenient since otherwise large (and often bulky) inductors and

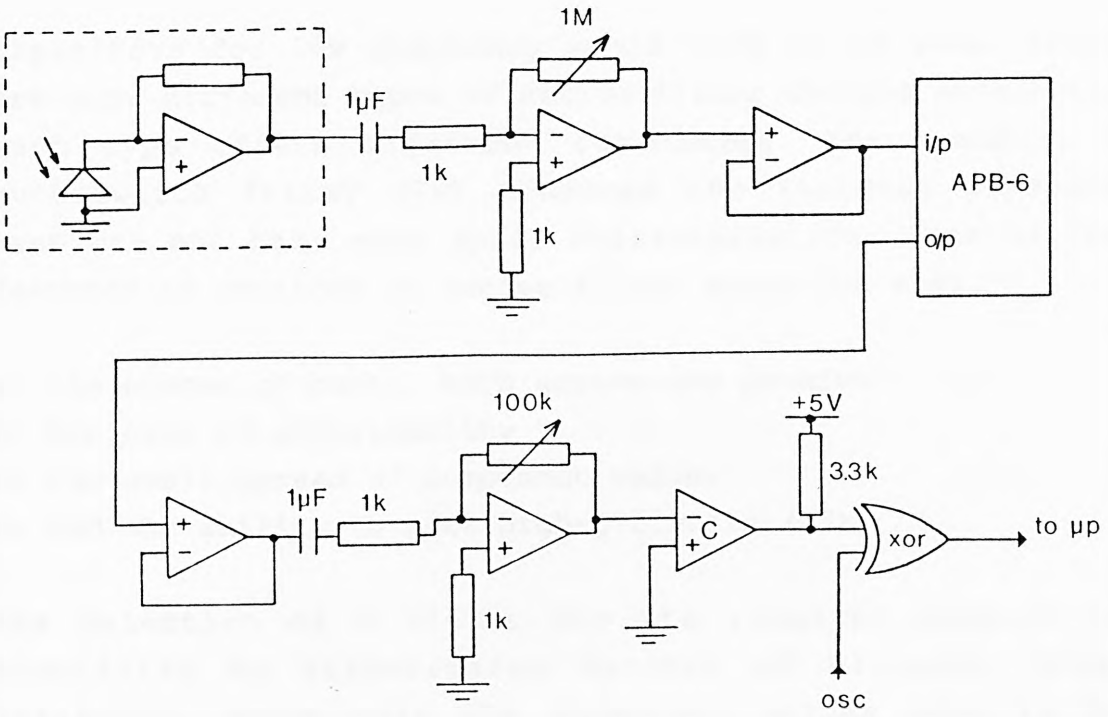

Figure 6.14 - Complete diagram of the analogue phase detection circuit. (All op-amps used were low noise OP37 series with comparator C being CMP01E type).

capacitors for low frequency would have to be used. There are many different types of active filter designs available. Each type offers different advantages. For example, a Butterworth filter (76) produces the flattest passband response but has poor phase characteristics. Some of the features to consider in active filter selection are:

a) the number of parts, both active and passive
b) the ease of adjustability
c) the small spread of component values
d) and the ability to make high-Q filters (76).

The selection of a filter for the required purpose is simplified by standardized designs of circuits being available, where only the capacitor values need to be calculated and the order of the filter needs to be known.

A commercially available band-pass filter with laser trimmed components and designed to give optimal performance at 125Hz was selected (AP Circuit Corporation). The filter was designed to give maximum-peaked response at 125Hz, with a Q-factor of ten. This filter model was APB-6 band-pass filter and has a three pole pair filter. No external adjustments were required and it may be easily interfaced to conventional op-amps. It had a high frequency stability 0.0005%/^{o}C and a very low dc offset ~5mV, which could be ac coupled, if necessary, at the next amplification stage. Owing to its very design and packaging this filter offered extremely good noise rejection and only generated about 70μV of rms noise.

6.4.5 Zero-crossing detector

A zero-crossing detector is simply a comparator (CMP-01EP) with the reference input connected to earth. Any voltage level above zero will cause the output of the comparator to go high and a negative or zero voltage level will produce a zero voltage output. This circuit allows a sine wave to be

transformed to a square wave with the same period. The output from the band-pass filter was amplified to its maximum peak-to-peak level before being fed to the zero-crossing detector. The point at which the comparator switches from a low to a high state depends on the transition threshold or offset voltage of the comparator. The offset voltage is essentially an uncertainty level and the transition to the high or low state can occur anywhere within this level. Hence, this produces 'jitter' on the transition edge of the square wave output. The effect is accentuated with a noisy signal and to minimise this effect, a comparator with a low offset voltage had to be chosen. The following calculations show the typical minimum errors, even with a 'high' quality comparator, for various input voltage levels.

Consider a sine wave input

$$V = V_p \sin\omega t \quad \text{-------(6.17)}$$

where V_p is the peak voltage level

The gradient of the slope at any point on this sine wave can be found by differentiating equation (6.17), which gives the following result:

$$\frac{dV}{dt} = V_p\ \omega \cos\omega t \quad \text{-------(6.18)} \qquad (\text{where } \omega = 2\pi f)$$

The 'jitter' noise occurs at the point where the sine wave goes through its zero value. For $\sin\omega t$ the amplitude is zero when $\omega t = n\pi$ where n = 1, 2, 3, etc. Substituting π for ωt in equation (6.18) gives:

$$\frac{dV}{dt} = -\ V_p\ 2\pi f \quad \text{-------(6.19)}$$ (-ve sign indicates the direction of the slope)

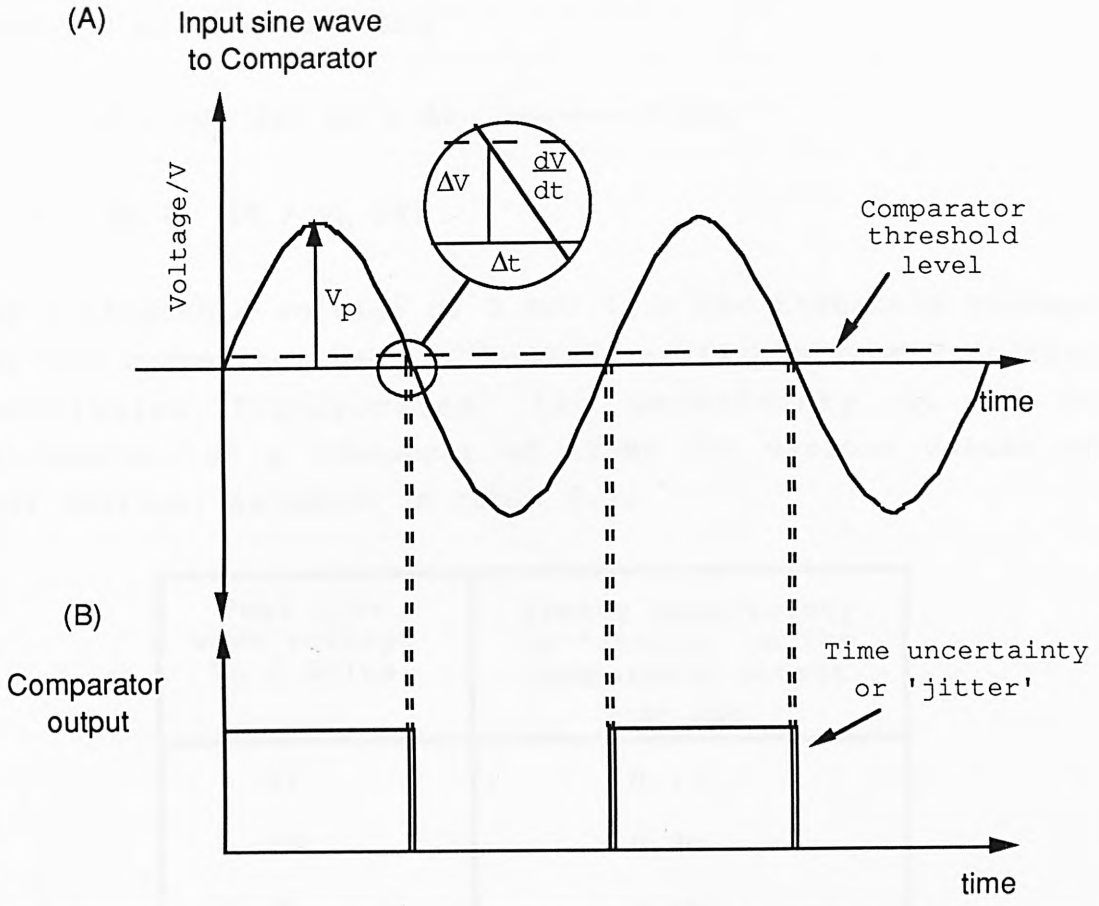

Figure 6.15 - Input and output waveforms of the zero-crossing detector.

The slope of the sine wave near the zero-crossing point can be approximated by a small triangle, as shown in figure 6.15, where voltage ΔV and time Δt represent the threshold voltage and zero-crossing point time uncertainty, respectively. The output square wave of the comparator will thus have a pulse length of $1/2f \pm 2\Delta t$. Where $2\Delta t$ represents the uncertainty with which the resulting square pulse can be measured. From figure 6.15 the following equation can be formulated:

$$V = \frac{dV}{dt} \Delta t + \Delta V \quad \text{-------(6.20)}$$

where ΔV is the threshold voltage and Δt the time uncertainty or jitter.

when V=0 at zero-crossing

$$0 = -V_p \, 2\pi f \, \Delta t + \Delta V \quad \text{-------(6.21)}$$

$$\therefore \quad \Delta t = \Delta V \, / \, V_p \, 2\pi f$$

For a threshold voltage of 0.8mV (i.e the threshold voltage for the comparator used, CMP-01EP, available from Precision Monolithics Incorporated) the uncertainty Δt can be calculated at a frequency of 125Hz for various values of peak voltage, as shown in table 6.1.

Peak sine wave voltage Vp / Volts	Timing uncertainty or 'jitter' on the comparator output $2\,\Delta t$ /μs
12	0.17
10	0.20
8	0.25
6	0.34
4	0.51
2	1.02

Table 6.1 - Shows the effect of varying peak voltage levels on the timing uncertainty.

For the minimum error the amplitude of the sine wave needs to be as large as possible. The uncertainties in the threshold level and the resulting errors in the transition edges are calculated for ambient temperature of 25°C. As the temperature increases the threshold level also increases by 1μV/°C for the CMP-01 comparator. For the working temperature range of the instrument to be up to 70°C, then the uncertainty in the threshold level would increase from 0.8mV to 0.845mV. This would correspond to an increase from

0.17μs to 0.18μs in 2Δt with a signal amplitude of 12Volts. Thus a 45°C rise in temperature corresponds to a very small change in the uncertainty in the transition edge or jitter noise. The comparator is thus, capable of operating over a large temperature range with minimum deleterious effect. It must be noted that in practice the jitter noise will also depend on the noise on the signal. This cannot be easily calculated and it has to be assumed that the threshold level will set the minimum error caused by jitter.

To ensure that the signal from the band-pass filter is as large as possible before being fed to the comparator, an ac coupled inverting operational amplifier, OP-37, was used. The ac coupling ensures that any dc offset introduced by the band-pass filter and buffer amplifier is removed. However, the OP-37 amplifier introduces a small dc offset voltage which shifts the ac sine wave signal from the zero voltage level. This adds to the threshold level error of the comparator. Since the maximum gain of the OP-37 op-amp was set to 100, the addition of this voltage offset error to the threshold error can be calculated. The total dc offset voltage is an addition of the inherent offset voltage and offset voltage due to the bias currents in the op-amp. These depend on the feedback and input resistor values chosen and can be calculated as follows:

Offset Voltage at output = $\pm(R_f/R_1 + 1)\ V_{os}$

where R_f and R_1 are the feedback and input resistors respectively, and V_{os} is the offset voltage for the OP-37.

Thus, the offset voltage as a result of the chosen resistor values is

$$= \pm(100/1 + 1)\ 0.03 \times 10^{-3}$$
$$= \mathbf{\pm 3.03mV}$$

The offset Voltage due to bias currents

$$= \pm I^{+}_{b}\ R_f$$

$$= \pm 100 \times 10^{3} \times 15 \times 10^{-9}$$
$$= \mathbf{\pm 1.5mV}$$

Thus the total offset Voltage = ±4.53mV at ambient temperature of 25°C.

At 70°C this total offset voltage increases to ±6.3mV for the OP-37 op-amp. Now the error in the $2\Delta t$ value at the output of the comparator caused by these offset voltages is 0.96μs and 1.34μs for 25°C and 70°C respectively, with V_p equal to 12Volts. This is a significant addition to the uncertainty introduced by the amplifier compared to that introduced by the comparator. The error introduced by the op-amp was the main reason why the OP-37 was chosen, because it had a very low offset voltage and offset voltage drift compared to other similar low cost amplifiers.

6.4.6 Phase detector

An exclusive-OR gate was used to sense the phase difference between a reference square wave and that generated from the detected sine wave. Since the output of an exclusive-OR gate is a logic 1 only when either one of its two inputs is a logic 1, then this type of phase detector requires both waveforms to be symmetrical i.e 50% duty cycle. Additionally, the maximum phase change that can be sensed without ambiguity is 180°, as shown in figure 6.16. This determines the maximum temperature range for a particular input frequency, although compensation for this effect may be introduced to extend the range. The output pulses were then fed to a microprocessor system to give output reading in terms of microseconds.

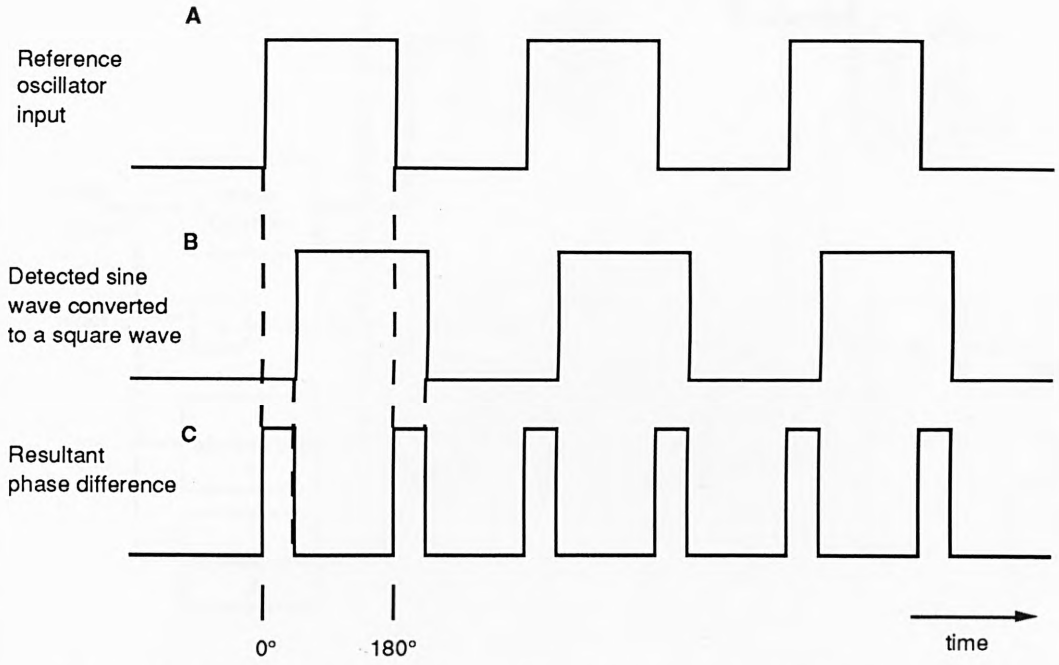

Figure 6.16 - Illustration showing the generation of a series of pulses representing the phase difference between two square waves of the same frequency. The output signal pulses are shown in C.

6.4.7 Microprocessor system for phase measurement

A microprocessor system was designed to measure the duration of the pulses generated by the phase difference between the measurand and reference sine waves. The circuit diagrams of the system, with its support chips, are given in figure 6.17 and, with the associated control logic, in figure 6.18.

Initially the signal pulses, representing the phase difference, were combined with clock pulses from a quartz oscillator, running at 10MHz, in an AND gate. Hence, each signal pulse was divided into very small pulses of 0.1μs duration as shown in figure 6.19; this represented the smallest duration level that was measurable. In principle a 20MHz or a 40MHz oscillator could be used if such timing accuracy was required. These 0.1μs pulses were then fed to two cascaded eight bit binary counters, capable of holding a 16 bit number. The microprocessor accesses the number held

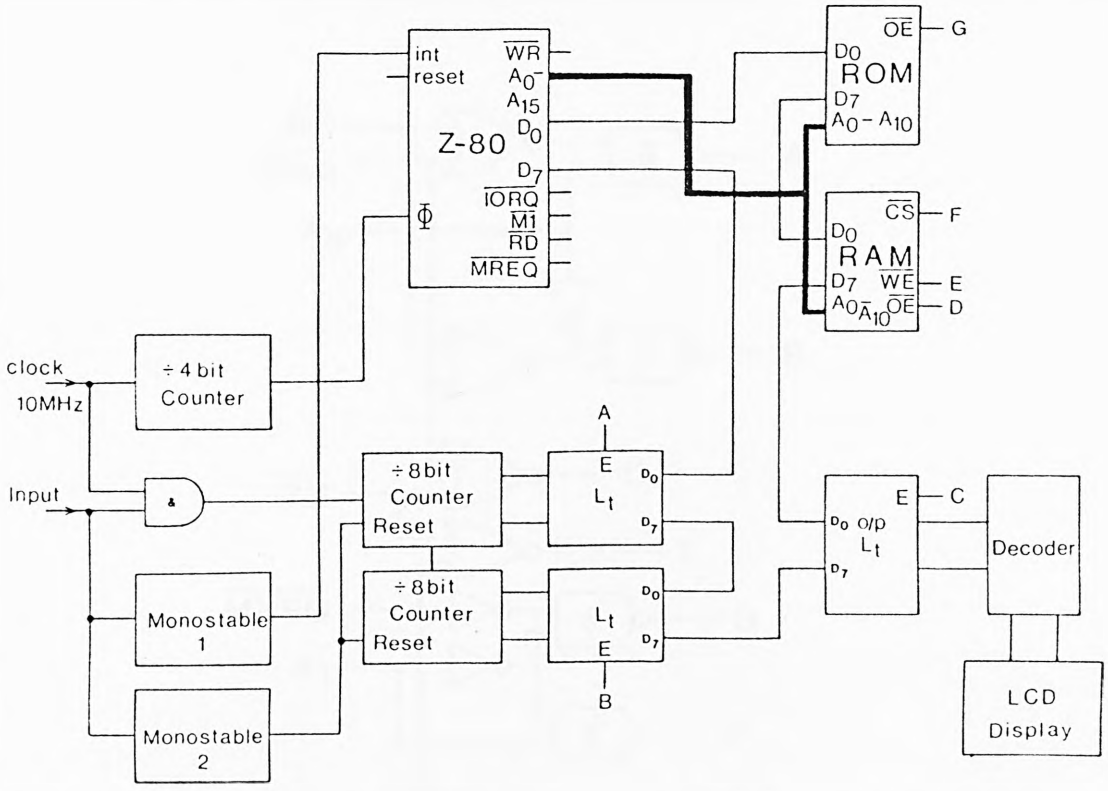

Figure 6.17 - Circuit diagram of the microprocessor system

Z80: Microprocessor

ROM: Electrically programmable read only memory (CMOS 28016 2K).

RAM: Random access memory (CMOS 6116 2K).

L_t: Input latch (74LS373).

O/P L_t: Output latch (74LS373).

÷ 8 counter: 8 bit counter (74LS393).

÷ 4 counter: 4 bit counter (74LS393).

Monostable 1: (74LS123)

Monostable 2: (74LS123).

Decoder: LCD decoder/drive circuit (CMOS 4 digit, 7211Hex)

A_0 - A_{15}: Address bus.

D_0-D_7: Data bus.

WR: Write signal.

RD: Read signal.

IORQ: Input/output request.

M1: Machine cycle.

MREQ: Memory request.

OE: Output enable.

CS: Chip select.

WE: Write enable.

OE: Output enable.

Int: Maskable interrupt.

Φ: Clock.

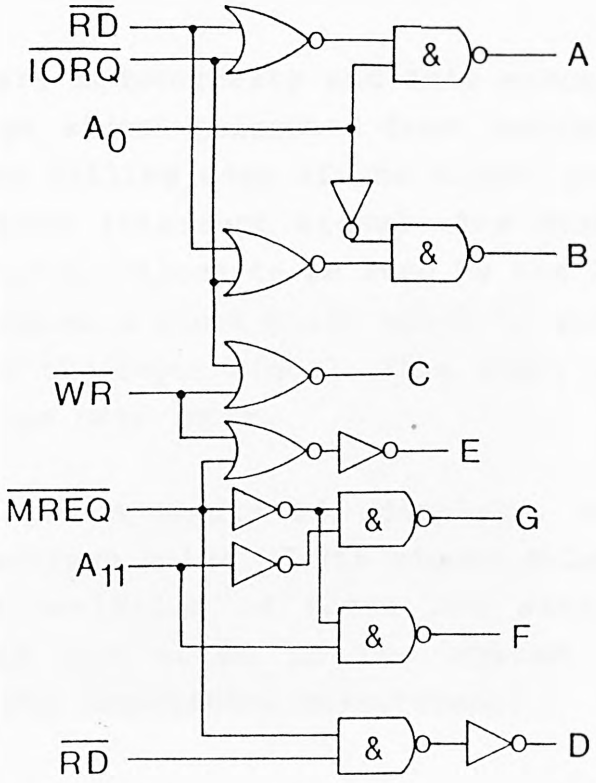

Figure 6.18 - Control logic for circuit in figure 6.17.

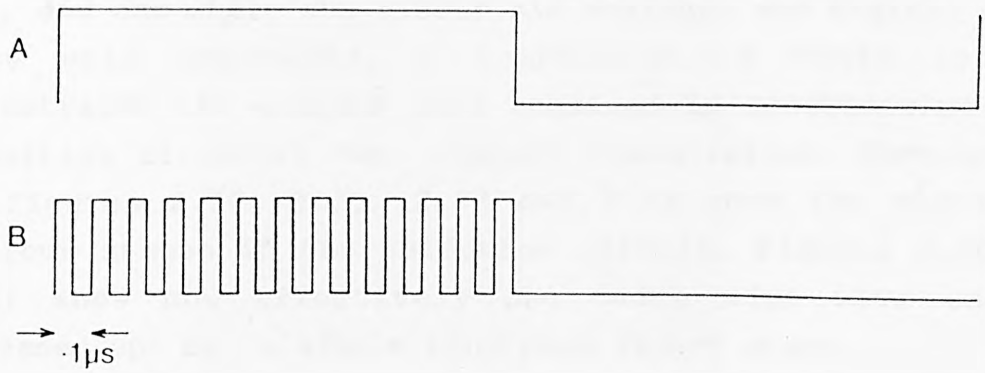

Figure 6.19 - Diagram showing division of signal A into smaller pulses B. (A represents signal 'input' in figure 6.17.

in the counters sequentially and this process is initiated by an interrupt signal generated from monostable circuit 1, which uses the falling edge of the signal pulse to generate a short duration interrupt signal. The maskable interrupt allows the counter values to be read by the Z-80. Monostable circuit 2 produces a short pulse which is generated from the rising edge of the input signal. This short pulse resets the counters for the next input.

The software, in Appendix 14, displays, on a LCD output module, the average value of 256 signal pulse durations and the standard deviation of these 256 samples; giving an indication of the noise in the system, and thus the precision of the temperature measurement.

6.5 RESULTS OF CALIBRATION OF THE DEVICE

Results are given for the use of two different filters, each used to remove the long-tail wavelength in the LED, and a comparison of their performances is made. In addition to this, results are presented for a completely 'housed' version (i.e the components were mounted in an instrument case) of the electronic system shown in photographs (2) and (3), and one where the electronic analogue and digital parts were well separated. A comparison of these results illustrates the extreme care required in constructing such sensitive circuitry for compact installation. Photographs in figures 2.20, 2.21, 2.22 and 2.23 show the signal at various stages in the detection circuit. Figures 2.20 and 2.21 show how effectively the noisy sine wave can be 'cleaned up' by a simple band-pass filter stage.

6.5.1 Calibration with analogue and digital circuitry well separated

This calibration was taken with a short-pass interference filter, centred at 629nm (45% transmission), placed in front

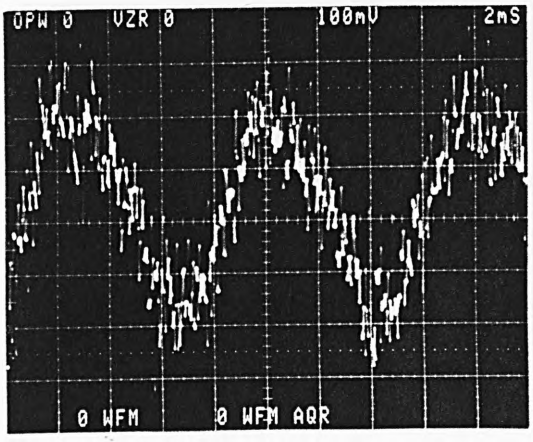

Figure 6.20 - Photograph of fluorescence sine wave at the detector stage in figure 6.14.

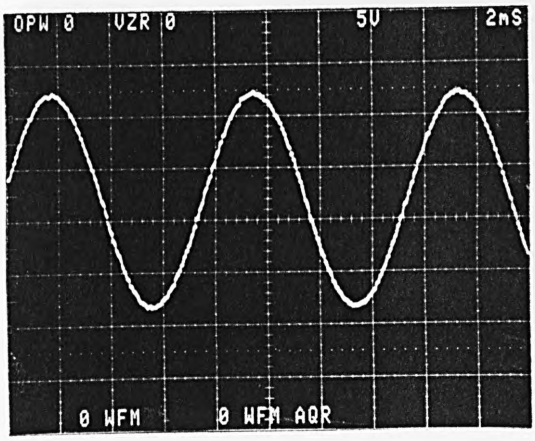

Figure 6.21 - Photograph of sine wave after band-pass filter APB-6 (figure 6.14).

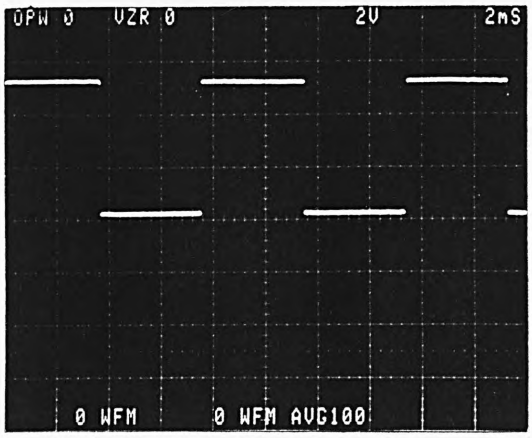

Figure 6.22 - Photograph of sine wave transformed to a square wave by zero-crossing detector (output of comparator C in figure 6.14).

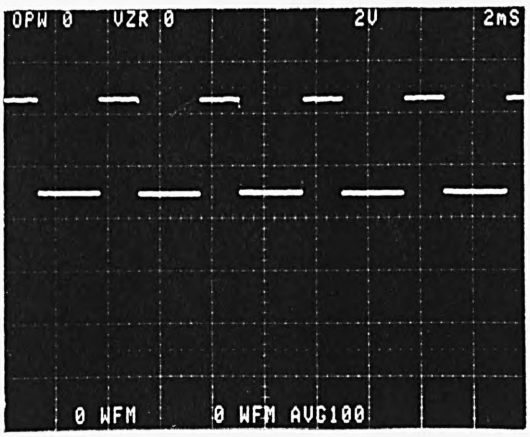

Figure 6.23 - Photograph of pulse duration representing pulse difference (output of XOR gate in figure 6.14).

of the LED and a band-pass interference filter centred at 695.2nm (11nm bandwidth) at the receiver end. Additionally, the analogue and digital sections were completely isolated from each other, hence, minimizing capacitive and inductive interference. During the experiment there was no observable change in the amplitude of the detected signal due to mixing of the green and red light, therefore, indicating that the intensity of green light passing through the band-pass filter was a small fraction i.e ~3% of the total.

The optical probe was placed in an oven and heated to a temperature of ~170°C. The temperature and phase measurements were taken as the probe and oven, slowly cooled to room temperature. The calibration graph thus obtained, of phase change against temperature, is shown in figure 2.24, showing a second-order relationship. The standard deviation on each reading was in the range from 3 to 4μs. Since the calibration curve is non-linear the resolution of the device varies along this curve. At higher temperatures between 155 and 160°C, the precision of the device was calculated to be ±0.04°C, and at lower temperature regions between 40 to 45°C, the precision reduces to ±0.18°C. These precision figures can be enhanced by programming the microprocessor to take the average of more samples, but this would be at the cost of increasing the response time. This will not however, be a limitation in some situations where the temperature varies slowly.

6.5.2 Calibration of sensor with all the electronics housed in an instrument case

In this calibration test the electronic system was housed in an instrument case, as would be necessary for a commercial system. The proximity of the transformer, digital microprocessor and the analogue boards increased the 'noise' on a single pulse by an average of 2μs. Figure 6.25 shows calibration results with the Glen Creston band-pass filter and the Ealing short-pass edge filter. The Glen

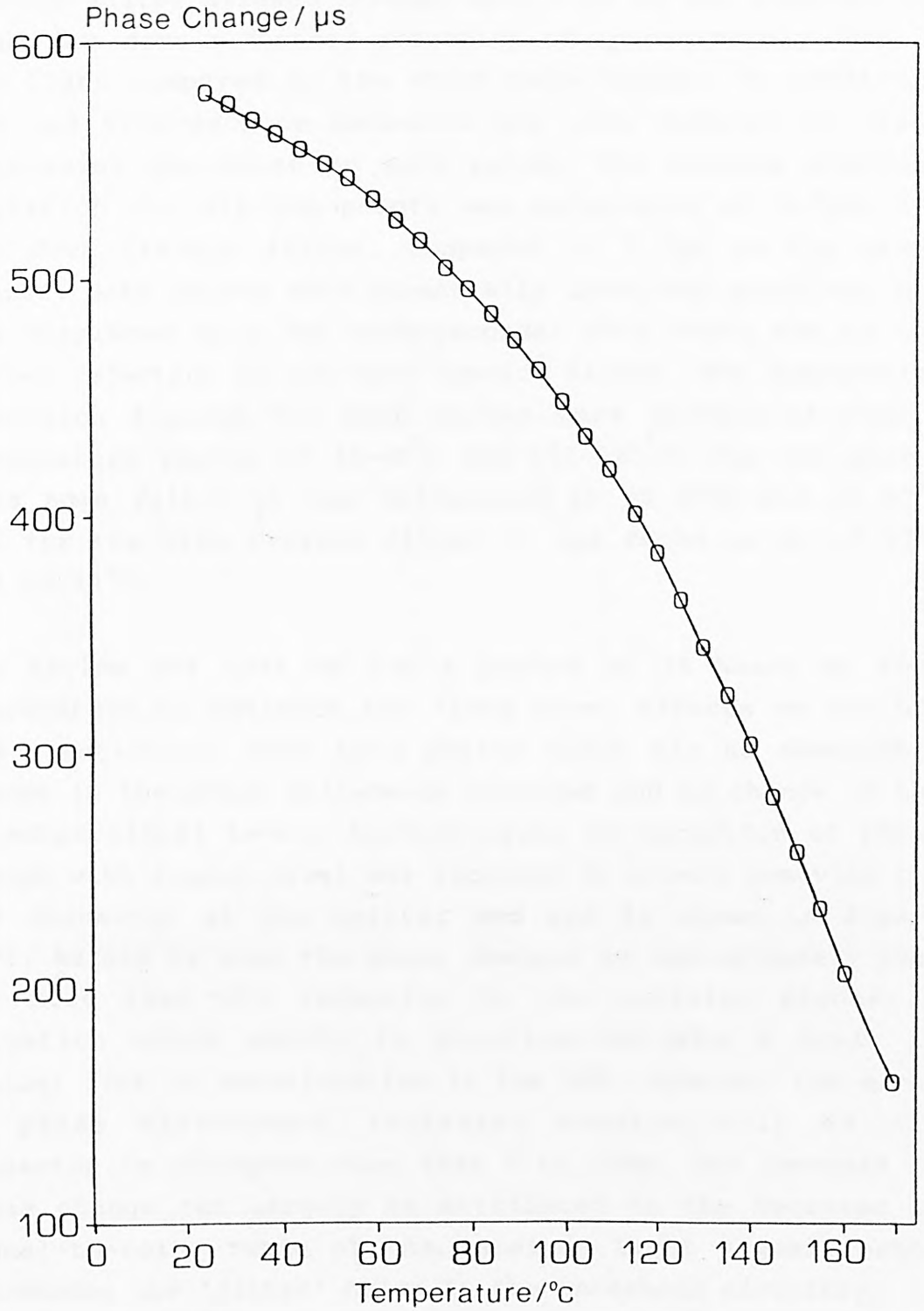

Figure 6.24 - Calibration graph of phase change as a function of temperature taken with the Ealing short-pass filter.

Creston filter allowed through only 1.2% of the unwanted LED light but gave a further reduction of approximately 16dB of red light compared to the short-pass filter. In addition, the red fluorescence emission was also reduced by ~24%, increasing the noise on each pulse. The average standard deviation for all the points was calculated at 9.3µs, for the Glen Creston filter, compared to 5.7µs on the other filter. Both curves show essentially identical profiles, but are displaced by a few microseconds; this being due to the better rejection of the Glen Creston filter. The comparative precision figures for both curves were calculated over a temperature region of 40-45°C and 155-160°C: for the short-pass edge filter it was calculated at ±0.35°C and ±0.07°C and for the Glen Creston filter it was found to be ±0.87°C and ±0.11°C.

The device was left ON for a period of 36 hours at room temperature to estimate the 'long term' effects on the LED and electronics. Over this period there was no observable change in the phase difference recorded and no change in the detected signal level. Another cause of variation of phase change with signal level was recorded by slowly removing the SMA connector at the emitter end and is shown in figure 2.26. As can be seen the phase changes by approximately 18µs for more than 50% reduction in the emission signal; a situation which would, in practice,indicate a fault in optical link or deterioration in the LED. However, the error in phase measurement increases substantially as the connector is withdrawn more than 5 to 10mm. The increase in phase change can largely be attributed to the decrease in signal-to-noise ratio of the received light signal, hence increasing the 'jitter' noise in the threshold circuitry.

The use of the 125Hz modulation frequency yields a 'linear portion' of the calibration curve in the temperature region 120 to 160°C. If greater accuracy is required in another region e.g. the biomedical range 25°C to 50°C, the device

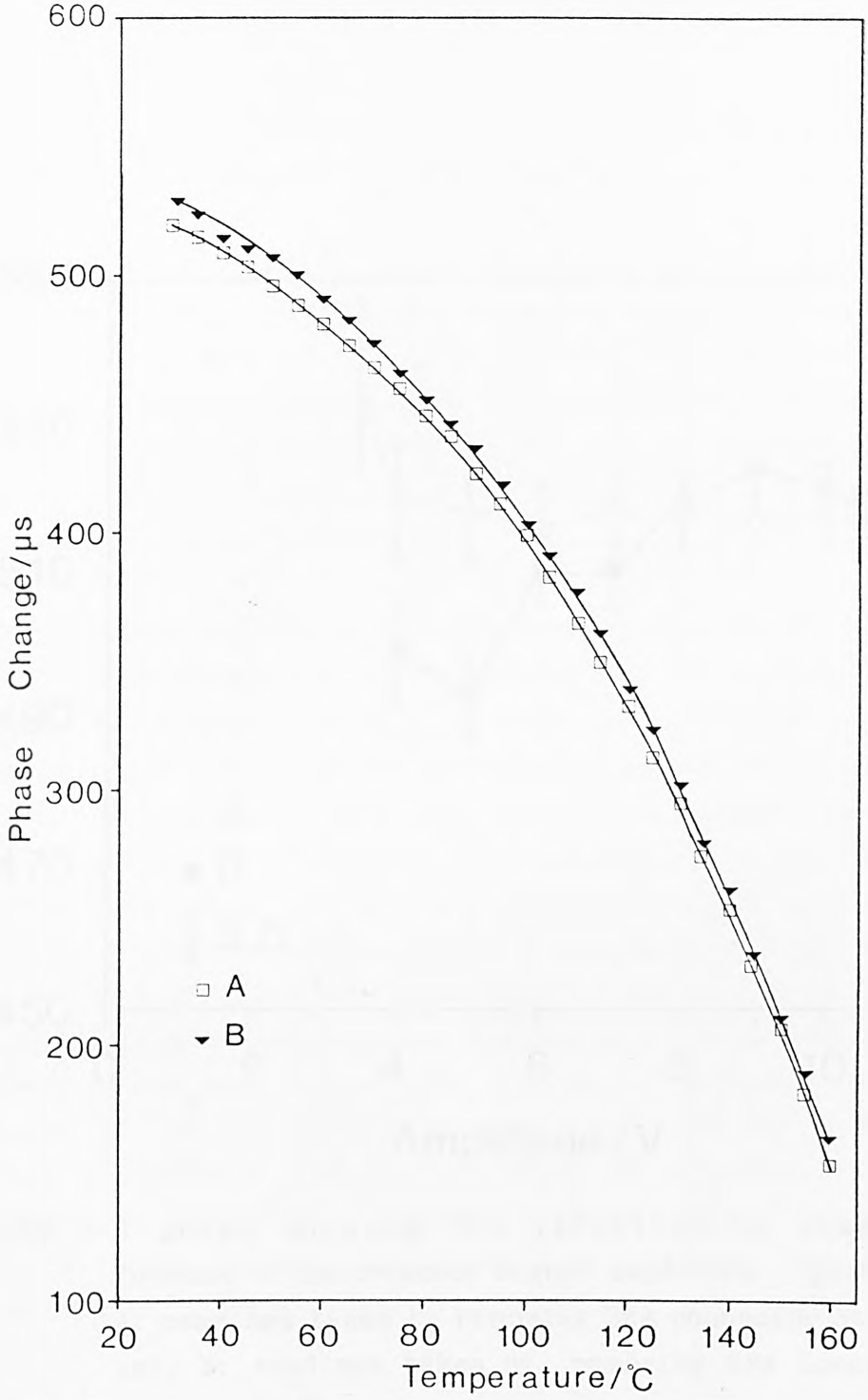

Figure 6.25 - Calibration graph of a phase change as a function of temperature. (Calibration A represents readings taken with Glen Creston filter and calibration B represents readings taken with Ealing short-pass filter).

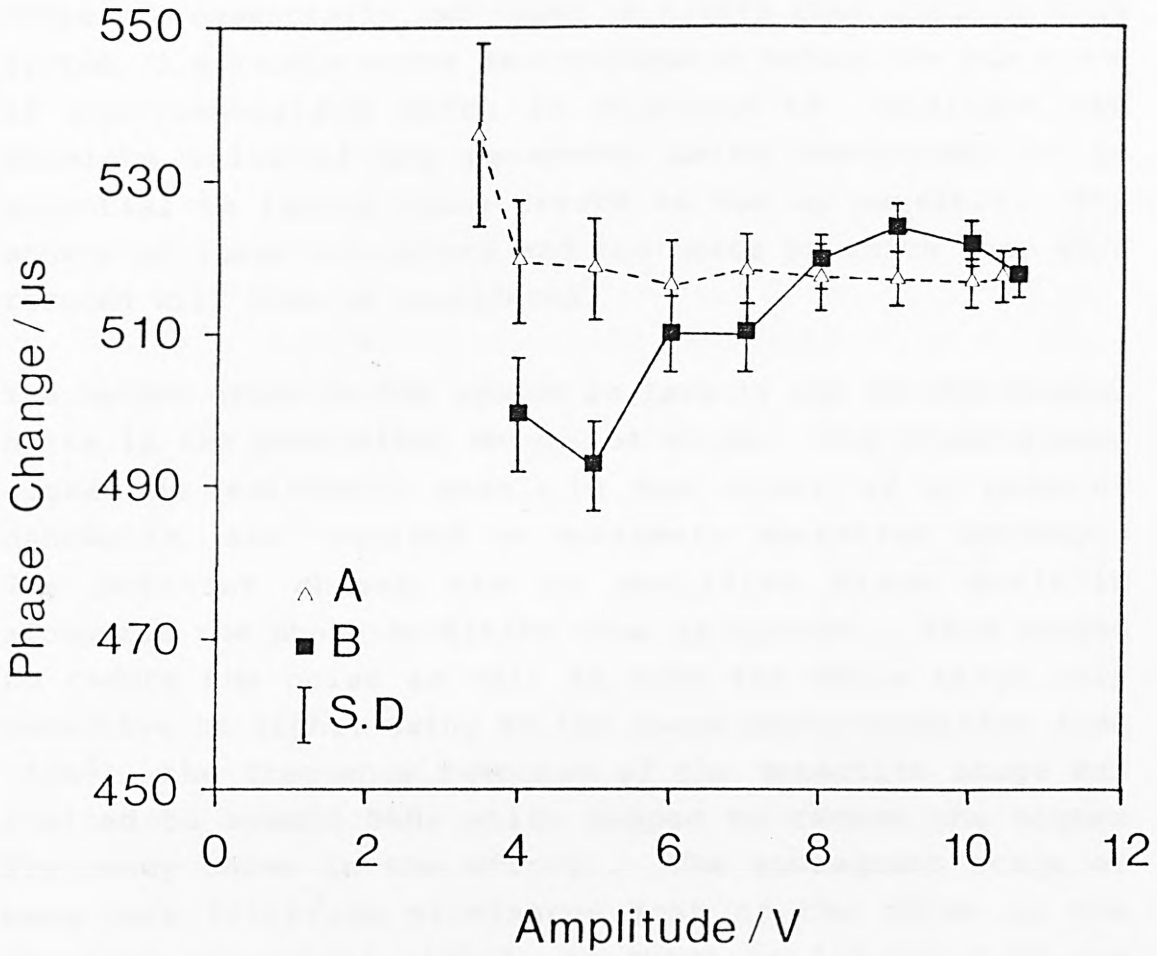

Figure 6.26 - A graph showing the variation in phase as a function of the detected signal amplitude (peak value). A: readings taken by removing SMA connector at emitter end; B: readings taken by removing SMA connector at detector end).
Vertical lines show the standard deviation at each point.

could be designed to operate at an appropriate (lower) frequency to optimize performance in that region.

6.6 ERROR REDUCTION IN THE SYSTEM

There are essentially two types of errors that occur in this system, i.e random error and systematic error. In any piece of instrumentation which is required to indicate the absolute value of the parameter being monitored, it is essential to reduce these errors as far as possible. The source of these two errors and the means by which they were reduced will know be considered.

The random error in the system is largely due to the thermal noise in the photodiode detection stage. The fluorescence signal is extremely weak, in the order of a tens of nanowatts, and required an extremely sensitive detector. The detector chosen had an amplifier stage built-in alongside the photo-sensitive area of Silicon. This helped to reduce the noise as well as make the whole stage very sensitive to light. Owing to the large photo-sensitive area ($5mm^2$), the frequency response of the detection stage was limited to around 5kHz which helped to reduce the higher frequency noise in the circuit. The subsequent stage of band-pass filtering eliminated most of the noise on the received sinusoidal signal, as shown in figures 6.20 and 6.21. However, the major reduction of the effect of random noise on the value mentioned was made using the microprocessor averaging technique.

Averaging a signal over a given time reduces the uncertainty due to random noise in that signal, but by averaging a signal the response time of the system is sacrificed. The larger the number of values taken to determine the mean, the lower is the uncertainty in the measurement. The microprocessor takes a mean of 256 samples over a time of approximately 1s. Over this time, the temperature is

assumed to change by a negligible amount but, however, it can change and it is difficult to predict how much this change has affected the absolute mean value. The more samples taken, the closer the mean value tends towards the 'true' value and the standard deviation of the measurements decreases with increase in the number of samples. It gives a measure of the range of departure of a single measurement from the mean value. The measurement points plotted on the calibration graphs are all mean values and represent accurate measurement points. A further stage in reducing the error of the mean values from the 'true' value is achieved through the least-squares fit routine.

The simplest demonstration of the principle is as follows. Suppose measurements x_1, x_2, ..., x_n are made of a quantity whose true value is X. Then the measurements have errors $\varepsilon_1=x_1-X$, $\varepsilon_2=x_2-X$, ..., $\varepsilon_n=x_n-X$, and the sum of their squares is

$$E=\varepsilon_1^2+\varepsilon_2^2+...+\varepsilon_n^2=(x_1-X)^2+(x_2-X)^2+...+(x_n-X)^2 \quad -----(6.22)$$

X is an unknown quantity which the experiment sets out to find. E, the sum of the squared errors, varies as X varies. The principle of least squares states that *the best choice for X is the one that makes* E *a minimum*. At the minimum, $X=X_o$ say,

$$\delta E/\delta X = -2(x_1-X)-2(x_2-X)-...-2(x_n-X) = 0 \quad -----(6.23)$$

Hence $X_o=(x_1+x_2+....+x_n)/n$ -----(6.24)

This represents the mean value as the best estimate for X, the true value. As mentioned earlier this routine was programmed in FORTRAN on a main-frame computer and the best fit for the calibration graphs was attained, along with the standard deviation of the points from this best fit. The ultimate accuracy of measurement can best be calculated over a small range, i.e 5°C, of temperatures. For example, in the

range of 155 to 160°C in figure 6.24, it can be assumed that the graph is, to a reasonable approximation, linear. The change in the phase measured between these two temperatures is 28.7μs thus the change per degree is 0.17°C/μs (5°C/28.7μs). The average standard deviation for this temperature range was calculated to be 0.23μs (this was calculated by averaging the five standard deviations for each mean value and dividing the answer by the square-root of 256 i.e the number of samples). The precision per degree was thus calculated by the product 0.17x0.23 which gave an answer of 0.04°C. This precision figure represented the best possible theoretical precision achievable over the temperature range studied. The slope of the graph at the higher temperature range is greater and this increases the resolution and alters the accuracy of the measurements.

Hence the precision figures quoted are those attained from highly averaged, random error reduced measurements. The comparative precision figures give an indication of the resolution of this device. The absolute measurement of temperature was, however, limited by the susceptibility of the system to systematic error.

The systematic error in the system could largely be attributed to variations in the optical parameters. Most of these variations have been discussed before at length but it would be useful to highlight them here once again. The first introduction of systematic error comes from the spectral and intensity drifts in the LED and these are discussed in the next section. The coupling of LED light into the optical fibres through the optical filters causes variations in the mixture of green and fluorescence red light. This mixture has to be kept stable otherwise, as was seen through variations of the coupling angle, systematic errors can be introduced into the system. However, since the optical filters were rigidly mounted this effect was minimized. In addition, the properties of the optical filters will change slowly with time and this would warrant

regular re-calibration of the instrument. This, however, is a long-term effect heavily dependent upon the environment and conditions of use of the device.

The electronics used in the instrument was designed to minimize systematic error changes and some of the precautions taken are now discussed. Any drifts in the generated phase of the sine wave are reduced to a minimum by the use of a crystal oscillator. However, slight phase variations could occur in the low-pass filter stages due to temperature changes in the component values. These were minimized by using metal-oxide resistors with low temperature coefficients and mica capacitors which are adequately stable. The existing drive circuit shown in figure 6.11 could be improved to provide a more stable intensity output. It was found over a period of weeks that slight shifts in the intensity of the LED and also of the bias point of the LED occurred. The bias level is provided by a simple potentiometer. This is susceptible to temperature drifts and drifts in the supply voltage. Typical supply voltages can vary by ±5%, and the fact that the op-amp also provides an amplification, accentuates the value of the drift voltage. Thus a slight drift in bias voltage due to temperature is likely to result in a much greater shift in the bias level at the output of the amplifier stage. A second problem arises with the transistor driver circuit. Any variations in the load resistor value and supply voltage will result in fluctuations in the drive current to the LED. Fluctuations are likely to occur more so because the LED is driven above its maximum rating and this causes it to heat up and changes in the current can result. Fortunately, both problems can be remedied quite easily and this would be the necessary step to take towards eliminating long term drifts in the system. Such features should be incorporated in the pre-prototype development stage of a instrument designed for commercial development.
The first problem encountered with the op-amp can be solved

by using a zener diode stabilized dc biasing source instead of a simple variable resistor. These stabilized sources are readily available and would not constitute a great change in the circuit layout.The second problem can be minimized using a constant-current source circuit, as shown in figure 6.27, to control and fix the current in the LED. This would be the next best thing to the actual monitoring of the LED's output with a photodiode and using this signal in a feedback loop to stabilise the LED's output. LEDs, unlike laser diodes, do not have an built-in photodiode and thus it is more difficult to monitor the actual light output which would help to provide the necessary feedback .

Systematic error drifts are introduced into the receiver circuit mainly through two stages, the photodiode and the comparator circuit. The sensitivity of photodiode may drift with time causing amplitude variations in the signal which affects the phase, as discussed in section 6.7. These changes are, however, likely to be small as silicon photodiodes are very stable and this variation is likely to be negligible over the observation period of the calibration measurements. The subsequent stages of amplification and band-pass filtering of the signal can introduce amplitude variations but these are again very small for the observation period. The important point is that all the amplifier stages are ac coupled except the one before the comparator stage. A small systematic error is likely to be introduced due to these two stages, and as discussed in section 6.4.5, efforts were made to minimise this error by careful selection of the comparator circuit and the operational amplifier.

The main points to note about the accuracy of the system and the calibration results is that for the system used, over the limited observation period and under laboratory test conditions, it was capable of very high resolution measurements. The calibration results taken against a secondary standard thermocouple clearly showed the trend in

the measurements, i.e the profile of the calibration curve and the proximity of the individual averaged measurement points to that curve. However, long term stability is extremely important for industrial use, and this instrument would provide a much reduced accuracy of reading (±1 to ±3°C) than those indicated by the calibration results, but taken over a longer period of time. The exact long term accuracy of the system cannot be quoted without actual periodical measurements over a period of several months which was not practicable for the short study undertaken. This should be done after the modifications to the driver circuitry discussed were carried out.

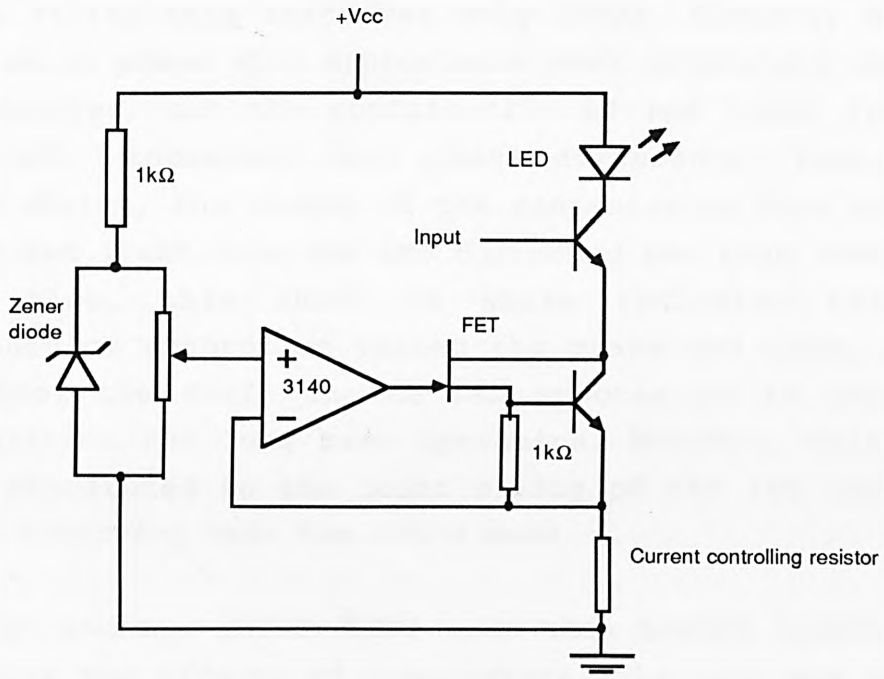

Figure 6.27 - Circuit diagram of constant-current driver circuit.

6.7 SPECTRAL SHIFT IN THE LED

Any optical sensor relying on the changes of absorption of a medium to sense the parameter of interest must ensure that there is no shift in the spectral wavelength of the light

source being used as absorption coefficients are often wavelength dependent. LED emission spectra tend to vary with temperature and with time. To test the effects of spectral shift of the LED on the phase difference, a yellow LED with peak emission at 583nm was used in place of the green emitting device. This indicator type of LED was similar in fabrication and packaging to the green LED, it also emitted a 'long tail' into the red part of the spectrum and was slightly more bright at 140 millicandela. The phase variation caused by changing the exciting LED wavelength was recorded for both Ealing and Glen Creston filters. For the Ealing filter the phase difference from the green to the yellow LED shifted by approximately 200μs and for the Glen Creston filter this shift was only 120μs. Clearly, a large variation in phase with approximate peak wavelength shift of 18nm occurred, but the contribution of red light from the yellow LED increased this phase difference. Thus, to a certain degree, the mixing of the red emission from the ruby and the red light from the LED distorted the true changes in phase. Also, this shift in phase indicated that the wavelength of absorption varied the phase and thus, a need to control the shift in the LED spectra is an important consideration for long term operation. However, this shift may be attributed to the joint mixing of the two red light signals occurring near the 694nm band.

The green and the yellow LEDs were then heated individually to explore the effects of temperature. The heat was applied by bringing the hot tip of a soldering iron in close proximity to the LED without actually touching it. The rise in temperature of the LEDs caused the intensity of output to reduce. Tests on the green LED showed a variation 5μs from room to higher temperature and a reduction in the amplitude of the signal of 25%. Similarly, tests on the yellow LED showed a variation of 14μs with a reduction of 11% in the amplitude from lower to higher temperature. Exactly what temperature change per degree this phase change represents, depends on which point of the calibration curve is

considered. Both tests indicated some dependence on the spectral characteristics of the LED and also the proportion of mixing of the green and red emission signals. The latter effect was reduced by using the Glen Creston filter, however, the effects of shift in the green LED spectrum over a long period are expected to be small, and hence, introduce small errors which can be calibrated out, periodically if necessary.

6.8 DISCUSSION

The system provided a high degree of precision and resolution combined with an overall simplicity of design. This system had demonstrated the capability of measuring to a precision of one twentieth of a degree Celsius and is amenable to much further improvements. The sine wave modulation method allowed a fairly simple means of detecting phase and removal of unwanted superimposed noise. The noise reduction was achieved through a fairly simple means of averaging and obviated the need for much more sophisticated techniques such as cross-correlation. Such a system is potentially of low cost, featuring standardized electronic and optical components. The transmission type probe is easier to fabricate than a reflection type, but the latter design can also be engineered to fit into the system. Owing to the relatively weak red emission signal, the transmission type of probe was favoured over the reflection type because of the higher signal-to-noise ratio that could be achieved. The signal levels detected in a direct optical system are of the order of 40 to 50dB greater than those received from a reflection type of probe. The figure can be improved if the reflection type probe is cut into the shape of a prism as described in chapter 3, so that by means of total internal reflection most of the light addressing the sensor is channelled back through another fibre parallel to the addressing fibre. As a consequence of lower signal level in the reflection probe, the noise level is that much higher

and a comparable performance can only be achieved by averaging more samples or by increasing the level of pump light.

Although the reflection type of probe has an advantage of being able to measure in inaccessible areas without the need for expensive installation, it does require more elaborate means of protection. Whereas the transmission type of probe is easier to adapt to any environment since it can be easily encased in a metal shield.

The simplicity of the probe design and electronic detection scheme used is the principle feature of this system for its commercial exploitation. In comparison with commercialized fluorescence based temperature sensors relying upon intensity-based measurements, the Luxtron 1000/2000 device, described by Wickersheim et al (50) suffers from the use of a conventional lamp source and a complex optical arrangement. Hence, the device is expensive and has now been superseded by model 750, relying upon 'decay-time' measurements (56). The most sophisticated commercial fluorescence based temperature sensor is that reported by workers at ASEA Innovation (51) of Sweden, who used the overall wavelength shift in fluorescence of a semiconductor material. This device is expensive (several thousands dollars per unit) as it requires a number of optical filters and sophisticated electronics. The ruby phase measurement device described has the major advantage of being amenable to providing much greater accuracy levels without additional components or cost. The device has been packaged in a small box shown in photographs (2) and (3), with an overall component cost of around 300 pounds.

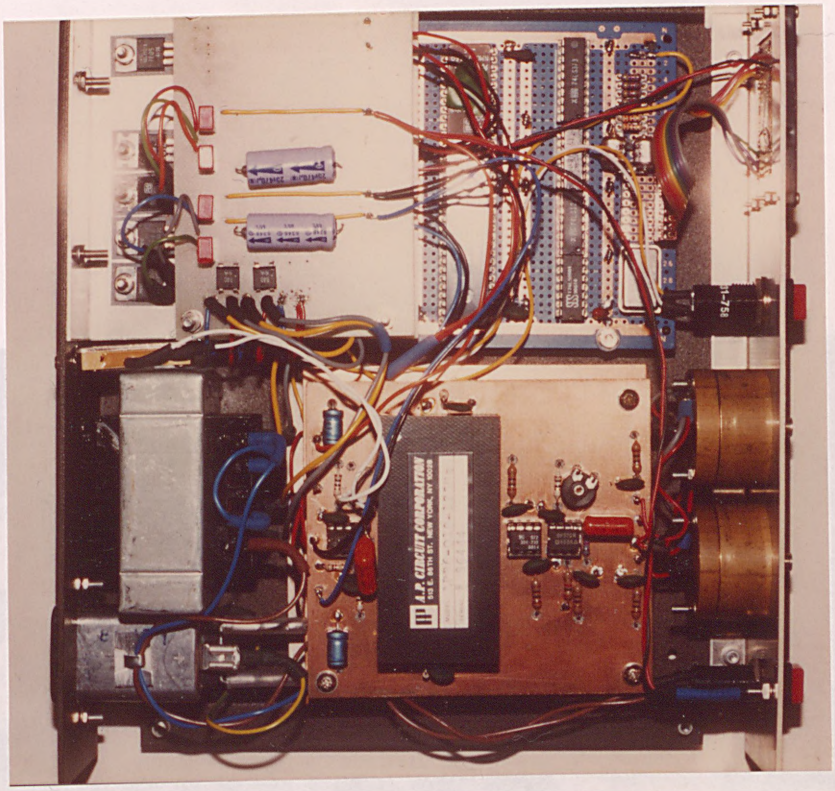

Photograph 2 - Electronic unit for the Ruby phase sensor.

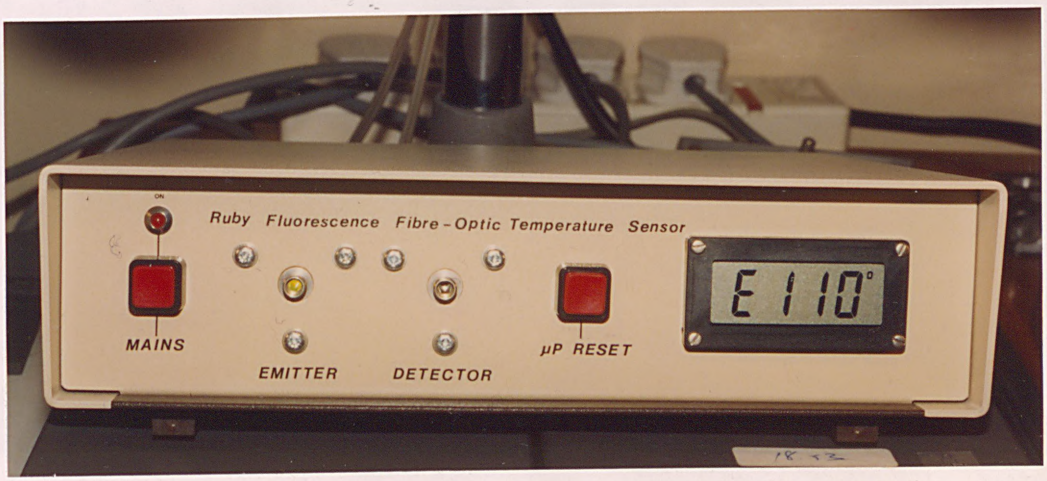

Photograph 3 - Front panel of the electronic unit.

Chapter 7

CONCLUSIONS AND COMPARISONS OF DIFFERENT SYSTEMS DESCRIBED

7.0 CONCLUSIONS AND COMPARISONS OF DIFFERENT SYSTEMS DESCRIBED

This chapter, discussing a comparative evaluation of each system, enables a consideration of the degree of usefulness of each sensor for potential industrial or laboratory use. It is essential to consider how improvements can be made by further development of the sensors and to indicate further work necessary to achieve this end, if possible.

7.1 RESOLUTION AND PRECISION

The self-referenced glass absorption (chapter 2,3 and 4) and ruby wavelength-division (chapter 5) thermometers all show approximately linear variations with temperature, and this makes calculations of resolution, and hence precision, easier than for the non-linear profile of the ruby phase system. The resolution depends on the slope of the response graph and thus the percentage change in the measurand with temperature. The precision of the measurement depends on the deviation of each measured point from the 'best' line that is fitted through all the points. The precision, in terms of temperature, is given by calculating the standard deviation of the points from the line and dividing this by the gradient. For the non-linear curve, the precision and resolution will vary along the curve.

For the direct transmission type of Nd:RG probes, discussed in chapter 2, the change in the ratio over a temperature range of 100°C was 44% for the stainless steel-housed probe, and 22% for the resin-fixed probe. This factor is slightly reduced in the prism probe to 18% over the same temperature range. In the stainless steel housing the glass elements of the probe were in close contact with a very small air-gap between each glass interface, whereas in the

other two probes this air-gap was removed by Epotek resin. Although the resin improves the coupling of light between each element, it also influences the change in the 'probe' and 'reference' signals. The gradient of the line depends on how much the 'probe' and 'reference' signals change relative to each other. If, for example, the 'reference' channel is also affected by changes in the measurand, then the ratio of the 'probe' and 'reference' signals will give a non-linear profile for linear changes in both signals. This is best illustrated in figure 7.1 which shows how the ratio profile changes with increase in the 'reference' signal gradient. Although the referencing scheme is still valid in both cases, it should be noted that in practice the 'reference' signal may be influenced, to some degree, by the measurand as well as by the unwanted light variations. However, in such cases the precision of measurement will vary along the ratio profile.

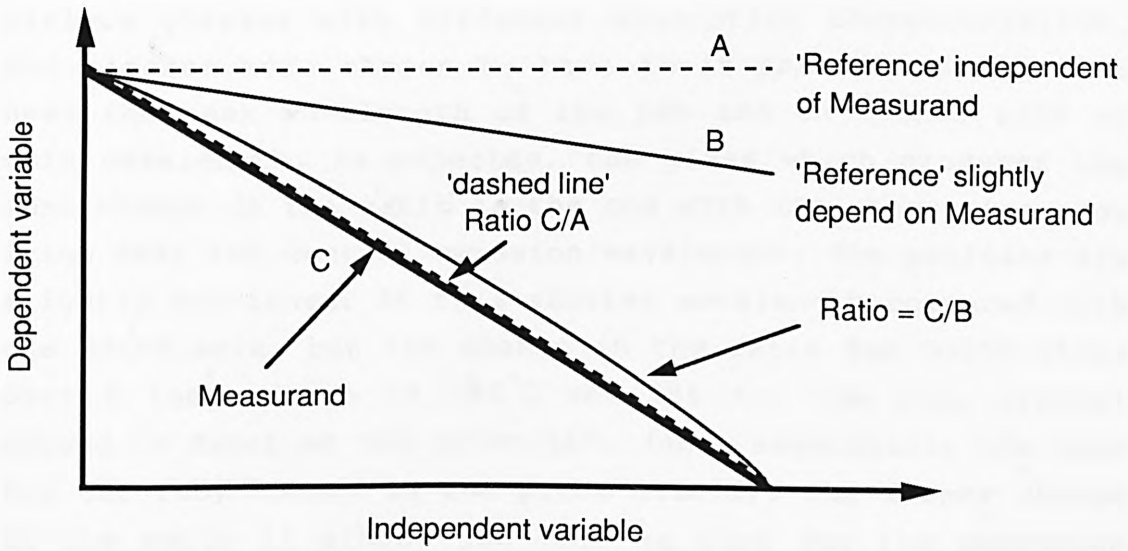

Figure 7.1 - Graph showing how the "ratio" profile is affected by the dependence of the 'reference' signal on the measurand.

In the stainless steel-housed probe the changes in the 'reference' signal are likely only to be influenced, to a significant degree, by the thermal expansion effects of the various glasses and housing, both of which vary the amount

of light coupled from one fibre end to the other. In the resin-fixed sensor the thermal expansion effects will also alter the light path, but the degree to which the resin influences the 'reference' determines how much it changes the ratio and hence, the resolution of the device. Clearly, from the results given, the resin does reduce the resolution and varies the emission signal with temperature. The optical characteristics of the Epotek are unknown at 1.06μm, the dominant emission of neodymium, and could not be determined with available equipment at the University. However, by extrapolation of the manufacturer's data, the transmission at this wavelength would appear to be high under normal conditions of use.

The amount of absorption edge movement with temperature is another factor which contributes to the resolution. In the ruby reference absorption edge thermometer, as described in chapter 4, this is clearly demonstrated by the use of various glasses with different absorption characteristics. The glasses were chosen to have their absorption edge lie near the peak wavelength of the LED and on either side of this wavelength. As expected, the glass which produces the most change in the ratio is the one with its absorption edge lying near the central emission wavelength. The profiles are slightly non-linear at this shorter wavelength compared with the Nd:RG work, but the change in the ratio for OG550 glass over a temperature of 100°C was 45% for the ruby crystal housed in front of the green LED, (and essentially the same for the ruby housed in the probe itself). The former change in the ratio is almost the same as that for the neodymium and RG glass housed in the stainless steel container, thus confirming the adverse influences of the epoxy resin on the resolution. This work also illustrates the usefulness of this much simpler system; one which uses a comparatively cheaper LED source than the one used in the neodymium work.

The uncertainty level in the measurements of the OG550

thermometer is determined by finding the equation of the line that best fits the measured points on the calibration curve. The equation of the curve is used to find the standard deviation of the points from this best fit and by calculating the slope of the curve at the required points, the error in terms of degrees can be found. As described in chapter 4, a second-order polynomial provides an adequately accurate fit and results in an uncertainty in terms of temperature. At a typical value of 75°C it was calculated to be ±0.6°C. Such a curve can easily be programmed into the Z-80 microprocessor to provide readings from the device in terms of temperature.

The ruby wavelength-division fluorescence emission thermometer has similar change in the ratio as the neodymium resin-fixed probe, a 26% change in the ratio over a range of 100°C. The uncertainty level of this system is, however, reduced to ±3°C by the increased noise in the system. The noise level is much greater owing to the relatively weak levels of fluorescence emission detected. As mentioned in chapter 5, the weakest signal detected is the R-line emission at 694nm; this is mainly due to the poor coupling efficiency of the LED light into the 600μm fibre (rather than 1000μm used in the ruby phase work), at approximately 2 to 3% of the total power emitted from the LED. The improvement to the system can be made, as suggested, by further low-pass filtering and averaging the output signals. This has the effect, however, of increasing the response time of the system.

Finally, the ruby phase change temperature measurement system exhibits the best resolution and precision of all the systems developed. This arises from the effectiveness of the noise reduction and averaging technique used combined with a basic simplicity of approach. Filtering a sine wave in the presence of random noise is much easier than filtering the noise on an exponentially decreasing signal where the processed signal has to maintain its original shape, and

hence the noise reduction technique gives more accurate measurements of the phase change and thus temperature.

The calibration of phase change against temperature yields a non-linear approximately quadratic curve, showing a phase change of 418μs over a temperature range from 25°C to 170°C. The average of the standard deviations recorded was 3.56μs, and this represents the uncertainty of each measured pulse length due to noise. The precision of the measured points varies along the curve and at 40°C to 45°C it was recorded at ±0.18°C, but from 155°C to 160°C it improved due to a larger phase change per degree, to ±0.04°C. The measurements recorded with the narrow band Glen Creston band-pass filter yielded a change of 364μs over the temperature range from 31°C to 160°C. Owing to the rejection of the long-tail wavelength in the LED, the light coupled to the ruby crystal and hence the fluorescence emission received was 2.34dB less compared to the signal level detected with the Ealing short-pass filter. This lower level of signal contributed to a higher standard deviation on each pulse. Hence, the uncertainty was reduced to ±0.87°C and ±0.11°C at the temperature range of 40°C to 45°C and 155°C to 160°C respectively. The resolution and precision of this device is far better than the other devices developed in this work. The increase in noise due to the Glen Creston filter, on each measurement is also contributed to by the noise induced by the close proximity of the analogue and digital circuitry in the metal box, as described in chapter 6. Design improvements in this area are possible by good capacitive shielding and better noise filtering in the power supply circuitry.

The precision and resolution of these devices are, however, adequate and in the ruby phase system it is more than adequate in environments where great precision is not required. An example of such an application would be the monitoring of oil temperature in a high-voltage transformers or in electric motors. The oil has a critical operation

temperature and the transformer operates well below this value. In such an application the accuracy of the measurement is not very important since a few degree change is tolerable in such a system. However, what is important is that the sensor output does not drift and produce erroneous results over a long period of operation.

7.2 ERRORS IN THE VARIOUS SYSTEMS

The systems developed during the course of this work have demonstrated the feasibility of the fibre optic methods of temperature measurement. They have shown, under laboratory conditions, that very simple electronic processing may be used with acceptable levels of precision. These electronic processing techniques have been low in cost and thus, have a number of limitations. The precision with which the measurements could be made was limited by the 'quality' of the various processing electronic components used as mentioned in the previous chapters. The 'quality' of these components may be defined as the levels of various specifications such as offset voltages, bias currents, 'Hold' error, droop rate etc. These specifications vary according to the manufacturing techniques employed and, generally, the cost of the component. This increased the susceptibility of the systems to random and systematic errors. Nevertheless, the calibration graphs obtained demonstrate that, for a given short period of time over which the experiments were performed, the random errors in the systems were very small. However, over a longer period of time the errors may be much larger owing to the drifts in the circuitry. The overall error of the systems under such conditions may thus be much larger than is indicated by the relative precision of the calculations. The close proximity of the measured points to the best fitted line through the points gives a good indication of the 'size' of the random error in the system. Nearly all the graphs show a close proximity of the points to the curves and lines drawn.

In the absorption edge filter work, it has been demonstrated that over a certain temperature range 23°C to 120°C, the calibration results indicate a linear relationship against temperature. The work discussed in chapter 4 was the most promising as it demonstrated that with a suitably matched light source and absorption edge filter, the change in the ratio of the detected signals against temperature can be optimized. Correct matching of the source wavelength and edge filter enhances the resolution of the system and hence its accuracy. The system in chapter 4 also demonstrated, along with the work in chapter 6, that an averaging technique greatly improves the performance of the device. These devices proved the feasibility of such a fluorescence based referencing technique which could be widely applicable to intensity-based sensors (9). Further improvements may be necessary in a device intended for commercial production where the higher cost of the components may be offset by the need to have a highly reliable instrument, and where the time for development to a prototype stage is available.

The work in chapter 5, on the ruby wavelength division thermometer, demonstrated the effect of using different parts of the visible spectrum to extract the measured variables and reference signals. This system, partly owing to its poor resolution, showed the worst precision of the systems developed. This precision figure is again a theoretical calculation and does not take into account the long term drifts and temperature effects on the electronic system. As investigation of the wavelength change properties of other fluorescent materials may lead to a more accurate system with the same internal referencing schemes. This work, however, did demonstrate that the 'weak' ruby fluorescence signal can be detected by using a simple low cost photodiode based circuit. This work initiated experimentation on the use of the decay-time properties of ruby, which lead to the development of the instrument described in chapter 6.

The phase measurement work showed how a simple averaging technique can yield, under laboratory conditions initially, high precision levels. These precision figures do not take into account the long term drift problems of this instrument. It was not the aim of this work to produce a fully commercial system out of one "pre-prototype" model, but to look at its limitations and its performance. Under laboratory conditions, where the temperature is fairly stable and the instrument is not subject to rough handling etc, the device has demonstrated that cheap and simple indicator LEDs and photodiodes can be used with appropriate signal processing techniques to yield good results.

7.3 RESPONSE TIME

The 'response time' may be defined as the time taken for the system to reach a steady-state value or normally to reach within a certain percentage of that value. The response time of the system can be divided into the response time of the electronic signal processing and the thermal response time of the probe head.

The precise individual times are difficult to measure since the change in one affects the change in the other i.e. the light changes in the probe are reflected as voltage or phase changes in the electronics. Therefore, only the response time of the whole system may be estimated.

In the self-referenced absorption edge shift thermometers the response time of the electronics used in the signal processing is of the order of a few hundred milliseconds and the thermal response time is limited by the stainless steel housing, to about ten seconds. In order to measure the response time, the probe could be subjected to a transient change in temperature i.e from 100°C to some low arbitrary value such as that of cold water, near zero degrees. This type of measurement gives an approximate value as the probe

has to be physically moved from the hot point to the cold, which under normal circumstances can take a second or two. However, the thermal response of the probe can be approximated using the graphical solutions of the transient heat flow equation for simple shapes such as slabs, cylinders and spheres. The boundaries for the solutions are held at constant temperatures (83) and all that is required to be known is some of the physical properties of the material concerned, which can be found in various references (84).

The resin-fixed probes exhibited much more rapid change and the response time for the prism probe was estimated at 3 seconds; also contributing to the delay was the response of the microprocessor LCD output display which takes a few seconds to change. Further refinements could eliminate this latter source of error. The response time of the phase measurement sensor was estimated at about 10 seconds, and again the microprocessor delayed the output response owing to the slow change in the display. This, however, can be improved by outputting only the phase change rather than outputting the phase change and the standard deviation sequentially as was done. The display of these two quantities has to be delayed as it takes the observer several seconds to record the readings, but for a single quantity the output can be made more rapid. However, it does take the microprocessor up to 5 seconds to take in 256 samples and calculate the mean and standard deviation. It takes the microprocessor just over one second to input 256 samples and a further four seconds to calculate the standard deviation, indicating the slow repetitive nature of the process. The mean value can, however, be displayed within half a second and would greatly increase the response time. The execution time of the Z-80 processor can of course be increased by adding a higher frequency clock. In further developments of the system, the temperature could be displayed continuously with the standard deviation held for display at the touch of a button. Thus the response time can

be greatly improved if a single parameter value is required i.e to approximately 1 second for 256 samples. These parameters can be engineered as appropriate to the user requirements.

7.4 LED VARIATIONS

Light emitting diodes suffer from two major problems when used in these temperature sensing devices, namely those due to intensity fluctuations and spectral drifts. The intensity fluctuations can be compensated for by the self-generated referencing schemes discussed in chapter 2, but for sensors relying on absorption edge movement or absolute absorption by the material, the spectral variations of the LED emission cannot be overcome by dual wavelength referencing.

7.4.1 Spectral drifts

The spectrum of an LED tends to drift due to changes in temperature which causes a greater energy spread in carrier distribution (74) and hence, shifts the peak emission wavelength, typically 0.5nm per degree, towards longer wavelength. The effect of spectral drift in the absorption edge sensors can be illustrated by figure 7.2 - this shows the effect of moving the spectrum towards higher wavelengths. It produces exactly the same effect as if the absorption edge itself has moved with an increase in temperature. The output intensity will thus vary due to this spectral drift, without it being possible to determine whether those changes were due to temperature or spectral drift. This is the severest limiting factor of such devices for long term operation, which will inevitably involve the degradation of the LED with its consequent intensity and spectral variations.

There are, however, two methods to overcome spectral variations. Firstly, by providing a temperature controlled

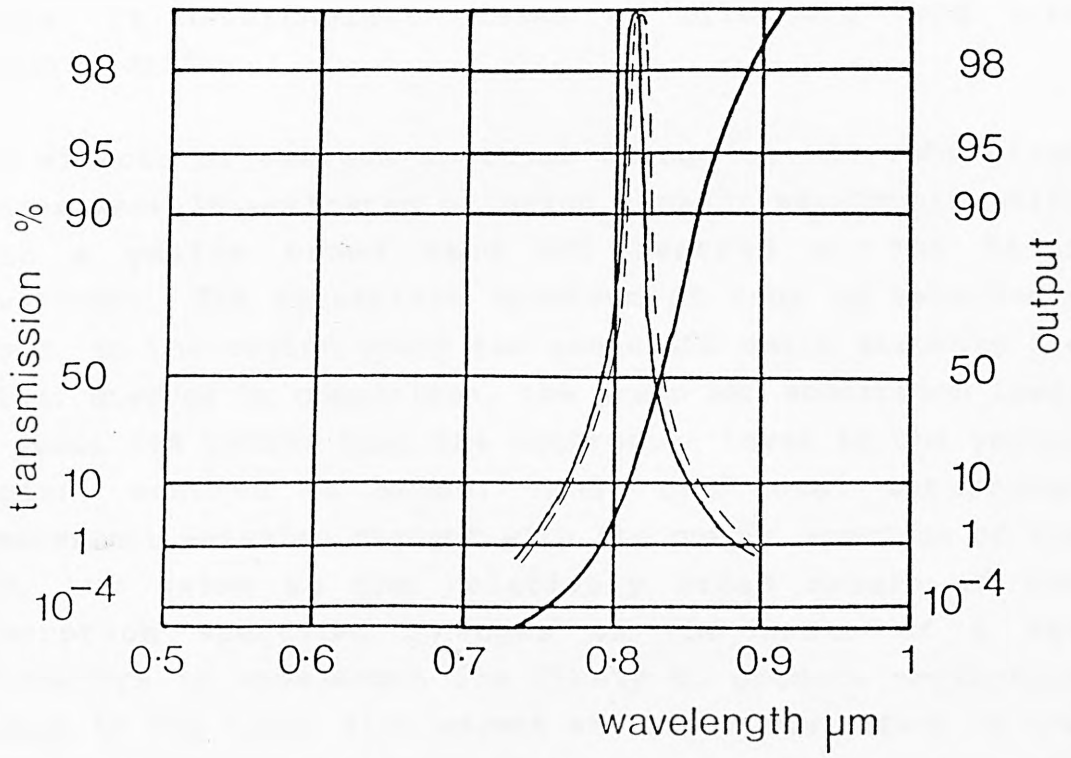

Figure 7.2 - LED spectrum with overlapping absorption edge RG 830 filter. The dotted line shows LED drift.

environment for the LED such spectral shifts may be avoided, but this tends to be expensive. An alternative method proposed by Theocharous (85), uses two identical probes. In a temperature sensor using the absorption edge movement of a semiconductor crystal and dual wavelength referencing, a second reference probe at a fixed temperature is used to monitor changes in the spectrum. Although the technique uses expensive couplers, two photodiodes, two LEDs and a second probe, it nevertheless claims to eliminate long term spectral drifts.

The effects of extreme spectral change on the ruby phase sensor were investigated by using a major wavelength shift with a yellow broad band LED centred at the 583nm wavelength. The absorption spectrum of ruby is relatively broad in the region where the green LED emits strongly i.e 565nm. However by comparison, the green LED absorption level is about 50% better than the absorption level in the yellow region, centred at 583nm. Thus, the total integrated fluorescent emission changes with the output spectrum of the LED, but owing to the relatively broad nature of the absorption spectrum, changes of the order of a few nanometers in wavelength are likely to produce negligible change in the total fluorescent emission. The effect on the measured decay-time from the green to the yellow LED resulted in a change of 200μs, using the short-pass interference and band-pass filters. With the Glen Creston band-pass filter centred at 565nm, this phase change reduced to 120μs. The amplitude of the detected sine wave also reduced by 13dB with a consequent increase in noise, giving a standard deviation of 125μs. Hence, it shows that the rather larger phase change recorded with the short-pass edge filter was, essentially, contributed by the mixing of the red part of the LED light and ruby emission light as was subsequently verified by the use of higher 'quality' Glen Creston filters with rejection at cut-off edges of 10^{-6} (i.e allows through only one millionth of the unwanted light

compared with its maximum transmission). Thus there was nothing to be gained through the use of this LED as the filters were specifically chosen for use with the green one, as the output fluorescence wavelength ranges are essentially independent of the pump wavelength changes over the absorption band.

7.4.2 Temporal stability of photodiodes

In work conducted by Stock (86), several silicon photodiodes were examined for temporal stability. Such work was conducted to investigate the ageing effects of silicon detectors used in radiometric and photometric measurements. It was found that photodiodes studied showed up to 10% change in responsivity over a period of one year in the visible region. However, in the region between 550nm and 1100nm the ageing rate was smaller at $\pm$1.5% per year (the ageing effect at shorter wavelengths increases to 10% and more). It is suggested by the workers that photodiodes with thin SiO_2 coatings tend to give better long term stability.

The variation in photodiode responsivity is an important consideration in fibre optic devices relying on intensity modulation at two wavelengths and which use two photodiodes at the optical receiver stage. Each photodiode is likely to exhibit different degrees of change with time and also its varying change over the spectral region will affect the two wavelength scheme, since the response of the photodiodes will change for each wavelength used. Such spectral and ageing effects may warrant regular calibration of the systems described using two photodiode detectors. It is likely that the change will affect both wavelengths almost equally. However, these effects are of no importance in the ruby phase measurement system. In this system a single photodiode is used which detects light at a particular wavelength region. In addition, any responsivity variations in the photodiodes will only result in the variation of the amplitude of the signal, which, over a limited region, has

negligible effect on the calibration.

7.5 PROBE CONSTRUCTION

The probe developed has to be capable of operating without degradation in severe environments, as required in many industrial applications. The engineering aspect of the probe still remains an area for further development and this is seen even for commercialized fibre optic systems. One such case has been the Luxtron probe relying on the change of phosphorescence with temperature. It was found that the phosphor material used deteriorated with time. Any commercialized sensor system must be capable of long term operation without the need for extensive adjustment, calibration or replacement.

The major problem of temperature probe design is the thermal expansion effects of the individual components of the probe. Temperature variations cause thermal stresses between the bonded components and these stresses can be severe, particularly when there is a mismatch of expansion coefficients between the adherand and the adhesive. The difference in thermal expansion coefficient causes the adherand and adhesive to move by differing amounts, and the resulting stress may be enough to tear the adhesive or the adherand or cause their separation. Stress can also arise during cure and lead to failure of the adhesive because the stress may act to initiate cracks. Additionally, the volume of resin reduces owing to solvent loss causing 'curing shrinkage' stresses. Fortunately, epoxy resins contain very little solvent, so there is not much shrinkage during cure. The Epotek resin chosen was used because of claimed negligible shrinkage up to 200°C and its excellent optical properties. However, some problems did occur in the above mentioned areas.

Fillers are commonly used to adjust the thermal expansion

coefficient of an adhesive to a value close to that of the adherand. Fillers generally lower the expansion coefficient of the resin because they themselves have a low thermal expansion coefficient. Therefore, the heat they soak up does not result in much increase in the volume of the resin. The amount of filler used has to be selected with care because many of the strength properties of the adhesive fall off after a certain filler level has been reached.

Another important consideration for a durable probe construction, is the geometry of the adherand parts. For instance, in the prism probe design, as shown in figure 3.1, the fibres are bonded onto the surface of the glass without any support and the contact area is kept to a minimum. The contact area should be as large as possible to add strength to the bond and configured in such a way as to avoid weak points where stress can act to tear the bond. For good adhesion, it is desirable not to have an extremely smooth surface, but this is unavoidable in this type of work where high quality optical finish is essential for optimal coupling of light. However it may be possible to grind the surface slightly to improve adherence and yet not destroy the optical properties too much. Thus, a combination of matching the thermal coefficients of the probe parts and selecting a suitable probe geometry, which ensures large overall surface contact between the resin and the adherands, is necessary if the probe is to survive in hazardous environments and perform without degradation over a long period of time.

The effects of a mismatch of the expansion coefficient were often encountered; it was found that the fibres moved several millimeters inside the metal sleeving at elevated temperatures. This was primarily caused by the differing expansion of the metal housing, fibres and the resin. In all the metal probes used in this work, after repeated cycling to higher temperature, the fibres became loose inside their sleevings and could easily be pulled out by hand. The resin

used in the neodymium infra-red work was (Epotek-353ND) a heat curing epoxy designed for high temperature applications. It had to be applied in thin layers since the two constituent parts, when added together, formed a very fluid mixture. This epoxy had to be transparent at infra-red wavelengths, but only spectral transmission in the 700 to 900nm range was quoted as >95%. Hence, the performance of the glue at 1.06μm was not explicitly available. The most important characteristic of the epoxy, found through experimentation, was that it become quite fragile and the probe would easily fall apart after repeated temperature excursions. To prolong the working life of the probe, it would be necessary to encase it in a protective sheath which can, itself, withstand the required temperature environment.

The ruby glass filters used in the absorption edge thermometer could easily be cut and polished into any desired shape. The epoxy resin adheres to the surface of the glass very readily and forms a strong bond between the fibre and ruby glass. However, the resin-fixed probe is fragile and has to be handled with care. It needs further protection against mechanical shocks without an overall increase in the thermal response time. A metal housing has proved to be the best form of mechanical protection for this type of probe and a metal encapsulation could be designed for a prism type probe. This would also help to hold the probe together, but the relative thermal expansions would again be the major problem to bear in mind.

The ruby crystal is a sapphire whose hardness and resilience to mechanical shocks make it highly suitable for severe environment applications. It has the disadvantage, however, that it is difficult to polish, but it is amenable to extremely high optical finish. The probe design described in chapter 6, was used for its simplicity; the crystal could be easily removed without the need for solvents and re-glueing. The only drawback is the increase in response time, but in many industrial applications this would not be the case.

Epotek was found to be an ineffective bonding agent between the fibre and the ruby crystal - an alternative (this is left for future work) is to use UV curing glue. This has been used fairly successfully in the ASEA commercialized probe. However, it should be mentioned that no independent data is available on the working life of this probe and its capability to work in severe environments for a long period of time. It is left as future work that an investigation should be conducted into a reflection type ruby phase sensor that uses crushed ruby cemented onto the end of a single or twin fibres with a suitable UV curing glue. Such an approach has the advantage that firstly, the probe would be easier to construct, the thermal response time will decrease, no metal housing would be required, no cutting and polishing will be essential and no thermal expansion problems as far as a metal/glass interface is concerned. However, such a construction of the probe will yield a much lower level of received fluorescence emission signal and this will increase the noise in the system and hence increase the uncertainty level in the measurements.

7.6 COMPARISON OF DEVICES DEVELOPED

A comparison of the devices developed in this work and two commercialized temperature sensors are given in table 7.1 and 7.3. The assessment of performance of commercial sensors was made by Harmer(32), and shows that the fluorescence intensity sensor using the temperature dependent fluorescence intensity of a semiconducting crystal, gives better performance figures than a device that relies on the pulse decay of fluorescence from a phosphor. Errors increase with higher temperatures due to a decrease in the light level in the latter device, whereas the accuracy achieved in the intensity dependent sensor is better than $\pm 0.4^{\circ}C$, if the probe is individually calibrated.

The temperature sensors developed in this work all show reasonably good levels of accuracy and precision, with the ruby phase sensor exhibiting the best performance of all the devices developed.

	Nd:glass (housed)	Nd:glass (Resin-fixed prism)	Ruby:glass (housed)	Ruby wave length Division (housed)	Ruby phase (housed)
Principle	AE	AE	AE	Fluorescence intensity	Decay-time
Fibre (PCS)	600µm	600µm	1000µm	bundle	1000µm
Range	-50 to 130°C	-50 to 130 °C	20 to 200 °C	20 to 160 °C	20 to >160 °C
Precision (best performance)	±0.3°C	±2.5°C	±0.6°C	±3°C	±0.04°C
Response (s)	~13	~3	>10	~10	~10

Table 7.1 - Comparative performance levels of devices developed (AE - Absorption Edge) . The theoretical accuracy were the best figures achieved.

The comparative precision figures given in table 7.1 are all theoretically calculated from the calibration curves which do not take into account any systematic errors in the devices. It is possible to calculate the approximate error of the phase decay-time sensor at the lower and higher temperature ranges given the errors which occur when the optical components are misaligned and those due to the electronics. Table 7.2 shows the results of that exercise having taken into account most of the errors in the fluorescent phase variation sensor.

Temperature range/ °C	Theoretical accuracy from figure 6.24	Optical fibre removed by a few millimetres	Electronic component uncertainty	Calibration accuracy (reference to a thermocouple)	Total practical uncertainty of Instrument
40 - 50	±0.18°C	~±2°C	~±1°C	±1°C	~±4.2°C
155 - 160	±0.04°C	~±0.5°C	~±0.2°C	±1°C	~±1.7°C

Table 7.2 - Phase decay-time sensor accuracy under laboratory test conditions.

The uncertainty is larger at low temperatures than it is at higher temperatures, owing to the increase in resolution with temperature. This uncertainty may be reduced at the expense of increasing the response time of the instrument. This may be useful in applications where higher accuracy is required and where temperature changes occur very slowly, compared to the sampling time of the system. It is important to note that the electronic uncertainty, in table 7.2, is likely to affect the instrument over a much longer period of time compared to the time it takes to make a measurement. It essentially indicates the effects of the offset voltage drifts within the amplifier and comparator stages.

The results of a comparison of commercial instruments carried out by Harmer(32), shown in table 7.3, indicate the high degree of accuracy of the intensity based ASEA system. A full comparative test on the phase decay-time system developed cannot be made as all the conditions of the test conducted by Harmer are unknown. Table 7.2 does indicate, however, that under some similar conditions, the uncertainty of the instrument does increase significantly at low temperatures but is still below $\pm 2^{\circ}C$ uncertainty for higher temperature regions and could be improved by reference to a stable calibration.

	ASEA	LUXTRON
Principle	Fluorescence intensity	Fluorescence decay-time
Fibre type	100μm	305/362μm
Range	200°C	-35°C to 250°C
Accuracy	±0.4°C	3.5°C
Effect of reconnection	0.7°C (max)	1.5°C
Microbending effects error (5dB loss)	0.9°C	2.1°C

Table 7.3 - Commercialized probes (from Harmer(32)).

7.7 PATENTS

Luxtron Corporation was granted a patent (87) in UK in December 1978, shown on pages 193 and 194, for the exclusive commercialization of fluorescence based fibre optic temperature measuring devices. It has also been issued a similar patent (88) in the USA.

This patent limits the possibility of commercial exploitation of any independently developed fluorescent based temperature sensor without the approval of the patent holder due to the apparent breadth of the patent. However legal advice would be required to make a full assessment of the restrictions in that patent on further development. In addition, patents for work using fluorescent techniques are held by GEC in the UK. It is, perhaps, unfortunate as work to develop and improve such devices needs to be continued and the incentive to do so can only arise when the possibility for commercial rewards exists. The involvement

of a major European manufacturer very recently seems to indicate that commercial developments will go ahead inspite of the above.

Patent (87) granted to Luxtron Corporation in UK in December 1978 (pp. 193-194) has been removed for copyright reasons

APPENDICES

A1.0 ABSORPTION OF RADIATION BY DOPED GLASSES

The transmission of light in doped glasses varies, as with most materials, with wavelength. Depending on the wavelength range of light incident, this variation may be determined either by the major constituents of the glass composition itself or by doping constituents present, usually in relatively small proportions. These constituents are deliberately added to control the transmission of light by the material.

Optical absorption by glass in the UV wavelength region is due to photon excitation of the valence electrons. If oxides such as ions of Fe^{3+}, Cr^{3+} and Ti^{3+}, are added to the glass then the absorption in the UV can be increased. The electron transitions responsible for this absorption are called charge transfer transitions, because they involve excitations in which an electron leaves an orbital mainly located on one ion, eg an Fe^{3+} ion to occupy an orbital mainly located on a nearby ion, or for example one of the nearest-neighbour oxygen ions.

Optical absorption in the infra-red is largely determined by interactions between the material and radiation which excites atomic vibrations. These may involve oscillatory changes in interatomic distances (bond stretching) or in bond angles (bond bending). For oxide glasses at least, there are only one or two instances of infra-red absorption bands due to the excitation of electrons. For a simple diatomic molecule, absorption of radiation may occur at the natural vibration frequency of the molecule.

Optical absorption in the visible region of the spectrum is due to absorption by impurity atoms and scattering of light by these particles. This shall now be discussed in more detail, as it is this effect which is utilized in sensor development.

A1.1 'Ruby' Glasses (RG) and temperature effects.

Some metals and semiconductors are slightly soluble in oxide glasses. By suitable heat treatment at temperatures below the melting point they can be made to precipitate out from solution to give a large number of particles of colloidal size. The glass is coloured, the colour depending on the optical properties of the precipitated metal, or semiconductor and on the size and concentration of the particles.

The materials most commonly used in producing colloidal colour in glass are listed in Table A.1.

Material	Colour
Au	Deep Red
Ag	Yellow or amber
Cu	Deep Red
Cu_2O	
Se	Pink
CdS	Yellow
CdSe	Deep Red

Table A.1 - Colours produced in glass by colloidal particles of metals and semiconductors (89).

The absorption of light by these particles, when the size of the particles becomes comparable with the wavelengths of light, depends on diffraction effects and reflection from the surfaces of the particles, as well as refraction and absorption within individual particles. The intensity of

light versus wavelength characteristics depends on the optical properties of individual particles and on their size.

Heating the glass causes the particles to grow and this growth in particle size is responsible for the change in the characteristic, which may be seen as an apparent movement of the absorption edge to the longer wavelength region. However, above a certain temperature the particles coagulate and change the colour of the glass itself permanently. Thus these glasses are only useful over a limited temperature region. The manufacturers specify that the observed absorption edge movement in linear and reversible over a temperature region in the range 23°C to 120°C. Beyond this temperature the structure of glasses is irreversibly altered. In the early experimental stage, in this work the aim was to find the useful working limit of the referencing scheme, and so temperatures above the upper limit were used. Continued cycling to these high temperature would cause the type of irreversible change discussed. In chapter 4, recycling of the probe to high and then to room temperatures shows the reversible nature of the optical properties of the filter glasses within a good working temperature range.

A2.0 PROPERTIES OF Nd^{3+} IN GLASS

The rare earth metal ion neodymium Nd^{3+} is used to dope the host material, glass. The Nd^{3+} ions, which are randomly distributed, provide the energy levels for the familiar lasing transitions and pumping. A typical energy-level diagram for Nd-doped in glass is shown in figure A2.1. At this stage it will be valuable to review the significance of the spectroscopic notation as well as the fundamental nature of absorption and fluorescence.

A2.1 Note on spectroscopic terminology

The letter designation refers to the total orbital angular momentum, L, of the electrons (S=0, P=1, D=2, F=3, G=4, H=5, I=6 etc). For example, the F states have an orbital angular momentum of 3. The superscript refers to the total spin angular momentum. If the total spin angular momentum is S, then the superscipt is 2S+1. Thus, for a ^7F configuration the total spin is also 3 (7= 2x3+1). The spin and the orbital angular momentum coupled together to give the total angular momentum J. The subscripts gives the value of J. Thus, in the $^4F_{3/2}$ level, S=3/2 (there are three unpaired electrons in the ^4F subshell of the Nd^{3+} ion), L=3 and J=3/2.

A2.2 Absorption

Absorption of a photon of light causes the transition of an electron to a higher energy state. In general,the absorption of light in a material occurs when the difference between two energy states is equal to the energy of the radiation required to bring about the transition of an electron. The expression for the wavelength of the radiation required for the transition of an electron from a lower energy state E_1 to higher energy state E_2 is given in equation A2.1. According to the

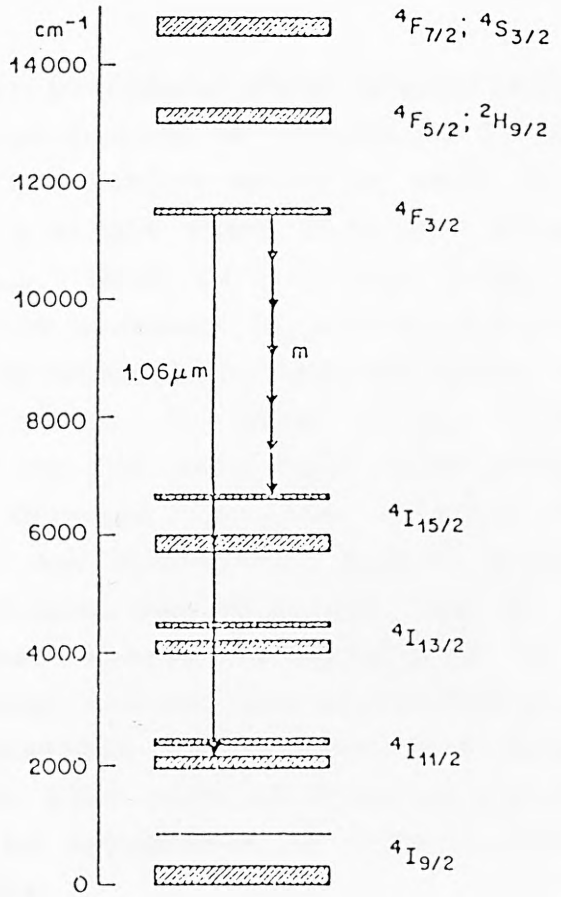

Figure A2.1 - Energy level diagram of Nd doped in glass

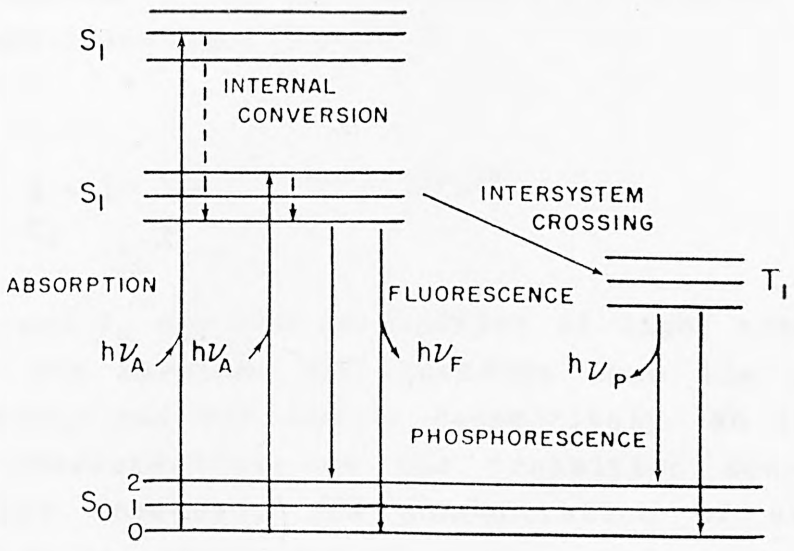

Figure A2.2 - Jablonski diagram

Stark-Einstein principle which states that a molecule can only absorb one quantum of radiation, it might be expected that such a transition would be seen in the absorption spectrum as a single sharp line at a wavelength given by equation A2.1. This is not the case, however, as a transition from a ground to an excited state is normally observed as an absorption band extending over a range of wavelengths with, in some cases, subsidiary peaks superimposed on the main band. The phenomemon of band spectra as opposed to line spectra arises because molecules in any electronic state, ground or excited, possess vibrational and rotational energy. The vibrational and rotational energy is quantized (i.e confined to specific values) and for any electronic state there are a number of possible vibrational and rotational energy levels. These give rise to fluctuating internal fields which give the appearance of forming bands rather than discrete levels.

$$\lambda = \frac{hc}{E_2 - E_1} \qquad \text{-------- (A2.1)}$$

The absorption of radiation occurs in accordance with the Beer-Lambert law equation (A2.2).

$$\frac{I}{I_0} = 10^{-ecl} \qquad \text{-------(A2.2)}$$

Where I and I_o are the intensities of light transmitted through the absorber and incident upon the absorber respectively and e,c and l, respectively, an intensity factor characteristic of the transition ion in the particular molecule, the concentration of absorbing molecule in the sample and the length of the path of light through the sample. I/I_o represents the fraction of light transmitted at a given wavelength required to produce the

electronic transition, on passage through the sample.

A2.3 Fluorescence

The absorption of light is very rapid, typically of the order of 10^{-15} second and leaves the molecule in one of a number of possible vibrational levels of one of its electronically excited states. The absorption process and the sequence of processes which follow can be best described by the Jablonski diagram (90) in figure A2.2. S represents the ground electronic state with its corresponding vibrational levels (0,1,2), S_1, S_2 represent excited electronic states which enable the absorption of light. Several processes follow this once the electrons are excited to the upper energy levels. The electrons rapidly relax down via a process known as Internal Conversion to the lowest vibrational level of S_1, in approximately 10^{-12}s. This is followed by one of two processes depending on the material. Fluorescence emission occurs as a result of the excited electrons in the upper electronic state descending to the ground energy level, S_0. Molecules in the S_1 state can also undergo conversion to the triplet state T_1 via Intersystem Crossing. Emission from T_1 is known as phosphorescence since transitions from T_1 to the ground state are forbidden and as a result the time constant of emission is several orders of magnitude smaller than that of fluorescence.

The fluorescence phenomenon results in the emission of light energy of a longer wavelength than that at which it is excited. The typical absorption and emission characteristics of Nd:glass are illustrated in figures A2.3 and A2.4, showing strong absorption in the infra-red, a region where convenient and inexpensive light emitting diodes sources are available.

In recent years there has been considerable work undertaken to investigate the fluorescence characteristics

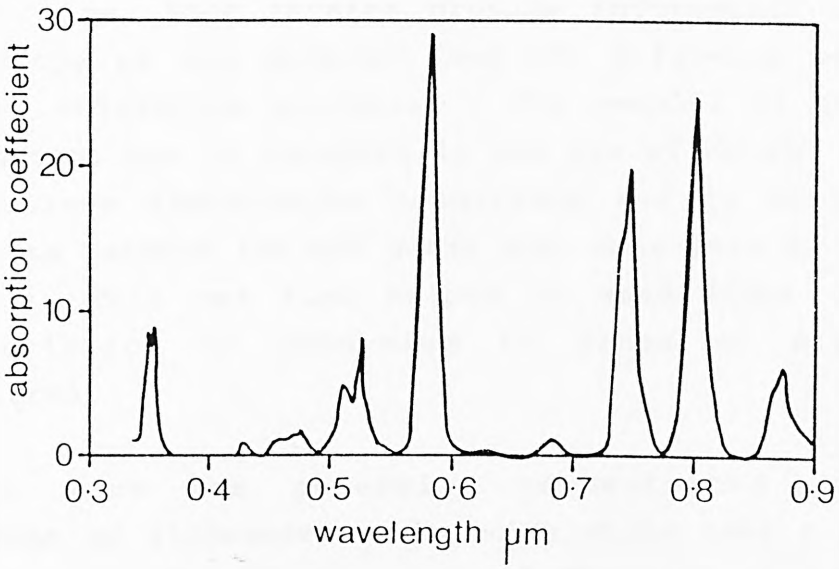

Figure A2.3 - Absorption spectra of Nd^{3+}

Figure A2.4 - Fluorescence emission of Nd^{3+}

of the $^4F_{3/2}$ state of neodymium in various host materials, the upper laser level for the much used 1.06μm emission line. Such studies provide information on the spectroscopy of the material and the influence of non-radiative relaxation processes . The results of such an investigation are of interest in the use of Nd:YAG lasers under extreme temperature conditions and in some work comparisons between YAG and glass host materials have been made (71). This has also helped to shed light on the characteristics of neodymium in glass at elevated temperatures.

Previous work has generally concentrated on the measurement of fluorescence characteristics over a narrow temperature range. In the work of Thornton et al (71) these authors have observed experimentally that the fluorescence decay from the $^4F_{3/2}$ level to the $^4I_{11/2}$ level in Nd:YAG and Nd:Glass is almost independent of temperature, T, in the region $300 < T < 500K$, and the average fluorescence lifetime increases only slightly with such an increase in temperature. The fluorescence emission is normally seen as an exponential decay with time when the fluorescent material is excited with a pulse of light. The degree to which this fluorescence emission follows an exponential profile has received considerable attention(71,78,91). It has been proposed that this exponential decay is the sum of much smaller exponential decays (92,93), but some evidence points to a single exponential for low doped samples (94). In work by Thornton et al deviations from a pure exponential at room temperature of the Nd:YAG were never large enough to allow calculation of a separate decay-time for the final portion of decay. Also, Lupei et al (91), using Nd:YAG at concentrations of dopant beyond 0.4% show that the $^4F_{3/2}$ level decay eventually becomes slightly non- exponential after the first decade at room temperature. But in contrast, in recent work by Grattan et al (61) a single exponential decay curve was fitted over a temperature

range 300 < T < 1100K using Nd:YAG and Nd:Glass.

Much of the work on neodymium doped glasses has concentrated on the determination of the decay-time and the effects of non-radiative transitions. In this work using (Q-100) phosphate glass, the decay-time varies with temperature as reported by Grattan et al (59). However, the significance of this decay-time change on the total emitted fluorescence is negligible for the temperature region of interest, as shown later. The most important requirement in this work, where a reference is generated from the neodymium glass, is for the input energy to this material to be dependent on the pump intensity, so that losses in the optical path and variations in excitation source may be monitored.

Earlier work carried out by Morey et al (95) on a 'Nd doped fibre optic temperature sensor' gives the temperature characteristics of absorption of Nd:Glass. The technique used the absorption variations of Nd doped fibre, over a length of 3.8cm and with doping levels of 5%, with temperature. At most wavelengths the transmission was found to decrease with temperature; however, within a few narrow wavelength regions the transmission increases with temperature. The relative percentage change in transmission from 22°C to 230°C in temperature, corresponds to approximately 10% over this range. Over a shorter distance <1cm this change in transmission with temperature is expected to be lower. These changes in the transmission give an indication of the absorption changes with temperature, which must in addition be reflected as fluorescent emission changes. However, in addition to these changes in the Nd:glass with temperature, non-radiative processes will also increase the dependence of fluorescence on temperature, however, no evidence of this was found. In part, changes in fluorescence, even those due to absorption changes, were found to be within 1% for

the working temperature region of this sensor. It may be of help to say a few words about the nature of the non-radiative processes.

The probability of non-radiative transitions between energy levels is a function of the energy separation, rare earth ion concentration and the host material. Non-radiative transitions occur without the emission of a photon of light, but instead allows the excited electron to relax down to a lower energy state through other processes such as phonon emission, cross-relaxation and intersystem crossing (96). The phonons are quanta of energy with specific modes of vibration. These are used to transfer the vibrational energy in one part of the crystal, associated with an increase in temperature, to another. The concentration of dopant ions influences the behaviour of the de-excitation processes in a complex manner. The distance of Nd-Nd ions is determined by the doping level and the doping process (i.e homogeneity - which is the case in glass (71)). The distance between the active ions determines the strength of interaction and energy level separation, which in turn influences the degree to which the various quenching processes influence the rate of decay of the fluorescence emission.

A2.4 Temperature dependent spectral characteristics

Knowledge of the characteristics of Nd^{3+} in glass is important in this work as the generated reference intensity needs to be constant at elevated temperatures. A recent review on the status and properties of laser glasses was conducted by N.Neuroth (97). Only 20 to 30 glass types are commercially available with a useful range of properties important in applications such as active materials in solid state lasers. A number of these properties have to be optimised and some have to be reduced to minimise their deleterious effects; for

example, absorption and conversion to emission has to be efficient, magnitude of the non-linear refractive index and optical losses at the lasing wavelength need to be small. A list of these and other properties are listed in table A2.1 and A2.2, (97).

As mentioned previously, temperature changes affect the absorption spectrum of Nd:Glass. Work by N.B.Brachkovskaya (98) on silicate GLS-2 and phosphate GLS-22 glasses shows changes in the absorption band contours in the 300 to 700K temperature range. Such changes are likely to affect the pumping conditions of a laser element. The emission bands undergo similar changes to the absorption bands: there is some broadening of the bands and shifts to a longer wavelength. Similar behaviour is likely to be observed in other host phosphate glasses, but the study shows (98) the changes in absorption and emission intensities over a limited region from 295K to ~493K have a relatively small effect (<10%) on the emission light output for a constant light input, over this temperature region. In work by Thornton et al (71) the conversion efficiency (defined as the fraction of fluorescence photons per absorbed photons) of emission at 1.06μm wavelength over a temperature region from 300 to 500K is shown to decrease by 10% at 500K in Nd:Glass. The fluorescent emission, in more recent work by Grattan et al (61), shows that pulse excitation of Nd:YAG in the infra-red region produces fluorescence emission predominantly in the 1.06μm region whose intensity was observed to vary by only ±5%. Similar results were obtained, but not mentioned in the paper, for Nd:Glass (Q-100). Some work, as mentioned, by other authors on Nd:glass has shown that there is some small dependence on the fluorescence emission on temperature. However, this dependence has been shown to exist only over a very large temperature region i.e 1100K in one case. For this work it has been shown that the fluorescence emission over the temperature range from 273 to 423K remains unchanged for a constant excitation light level. Hence,

Table A2.1 - Commercial silicate laser glasses

the neodymium doped glass was shown to provide a constant reference source with negligible dependence on temperature for the region of interest.

A3.0 DERIVATION OF V_{op} and I_{sh}

From the internal characteristics of a photodiode an equivalent circuit can be derived as shown in figure 2.13. The photodiode is modelled as a constant current generator with an ideal diode across it plus a shunt resistor (R_{Sh}), a shunt capacitor (C_j) and a series resistor (R_S). The current generated via photon absorption can be written as

$$i_p = \frac{\eta I_o A e \lambda}{hc} \quad \text{-------A3.1}$$

where I_o- is the irradiance of the light
η - quantum efficiency
A - area of photodiode
e - electronic charge
λ - wavelength
h - Planck's constant
c - velocity of light

Assuming operation is restricted to low optical modulation frequencies, then the effect of shunt capacitance may be neglected (i.e I_C=0). By Kirchoff's law

$$i_p = i_d + i_{SH} + i_L \quad \text{-------A3.2}$$

also $$V_L = V_d - i_L R_S \quad \text{-------A3.3}$$

and $$V_d = i_{SH} R_{sh} \quad \text{-------A3.4}$$

Now the current-voltage behaviour is given by the following equation:

$$i_d = i_o(\exp(e.V_d/kT) - 1) \quad \text{-------A3.5}$$

Where i_o - is the reverse bias leakage current.
In the photovoltaic mode, the external current flow is negligible; hence
$i_L=0$, thus equations A3.2 and A3.3 become

$$i_p = i_d + i_{SH} \text{ -------A3.6}$$

$$V_L = V_d \text{ -------A3.7}$$

Substituting A3.4 and A3.5 into A3.6 we obtain:

$$i_p = i_o(\exp(e.V_d/kT) - 1) + V_d/R_{sh} \text{ -------A3.8}$$

Thus the short-circuit current I_{sh} (note: this is not the same as i_{SH}) is the current when $R_L=0$.

$$I_{sh} = i_p - i_o(\exp(e.V_d/kT) -1) - V_d/R_{sh} \text{ -------A3.9}$$

Similarly, the open-circuit voltage V_{op} is the output voltage when $R_L = \infty$

$$V_d = V_{op} \text{ --------A3.10}$$

from equation A3.8

$$i_p - i_{SH} = i_o(\exp(e.V_{op}/kT) - 1) \text{ -------A3.11}$$

$$V_{op} = (kT/e)\ln((i_p - i_{SH})/i_o) + 1) \text{ -------A3.12}$$

A4.0 TRANSIMPEDANCE FEEDBACK AMPLIFIER

The transimpedance amplifier has a number of advantages, when compared to other types of photodiode voltage amplifier circuits. A voltage amplifer normally requires some form of equalization; this can best be seen from the small-signal equivalent circuit as shown in figure A4.1. This circuit represents a photodiode detector connected to a voltage amplifier.

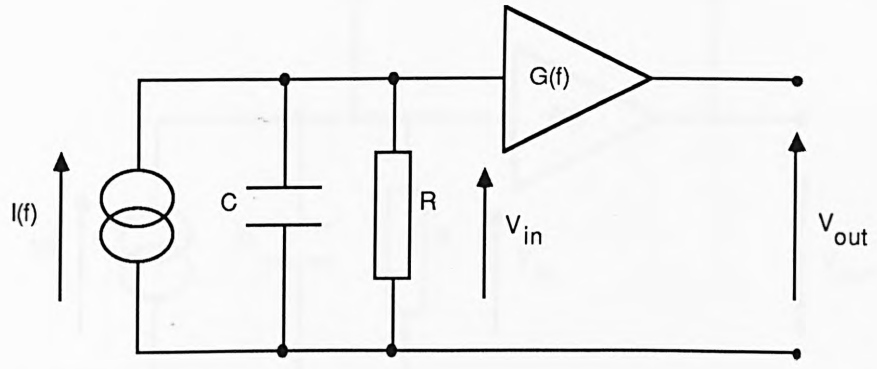

Figure A4.1 - Voltage amplifier

The transfer function is given by

$$V_{in}(f) = RI(f)/(1 + j\omega RC) \quad \text{-------A4.1}$$

$$V_{out} = G(f)\ V_{in}(f) = G(f)\ RI(f)/(1 + j\omega RC) \quad \text{-------A4.2}$$

The input capacitance, C, causes the bandwidth to be limited at frequencies higher than $(1/\omega RC)$. Signals which vary more rapidly than this are effectively integrated at the input. For the overall transfer function to remain frequency independent, it is required that

$$G(f) = G_o\ (1 + j\omega RC) \quad \text{-------A4.3}$$

then

$$V_{out} = G_o RI \quad \text{-------A4.4}$$

Effectively a differentiating circuit is needed for equalization to improve the frequency response of the circuit.

The transimpedance feedback amplifier configuration, shown in figure A4.2, obviates the need for equalization.

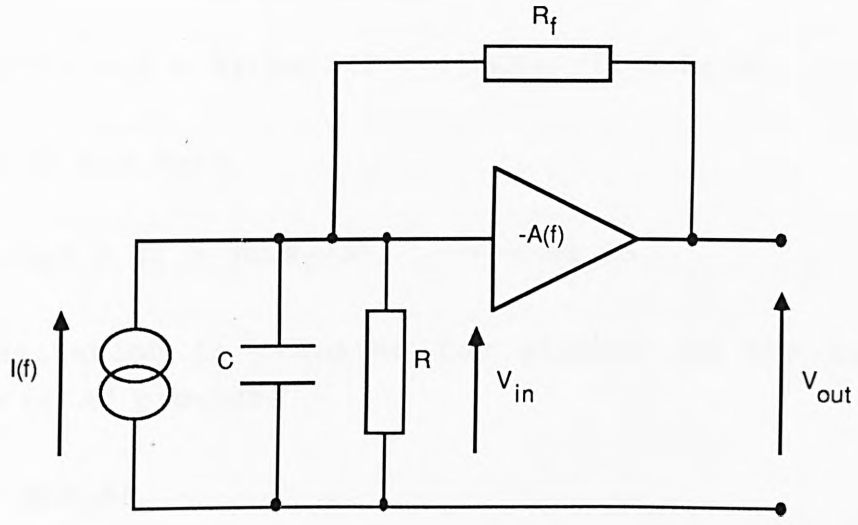

Figure A4.2 - Transimpedance amplifier

R and C represent the total resistance and capacitance of the photodiode and the amplifier. The transfer function can be calculated as follows:

$$V_{in} = -V/A \quad \text{-------A4.5}$$

where A is the open-loop gain

$$I + (V - V_{in})/R_f = V_{in}(R/(1 + j\omega RC)) \quad \text{-------A4.6}$$

$$I + (V - V_{in})/R_f = V_{in}((1 + j\omega RC)/R) \quad \text{-------A4.7}$$

$$I + (V - (-V/A))/R_f = (-V/A)(1/R + j\omega C) \quad \text{-------A4.8}$$

$$I + (V + V/A)/R_f = -V/RA - j\omega VC/A \quad \text{-------A4.9}$$

$$R_f I + V + V/A = -VR_f/RA - j\omega VCR_f/A \text{ --------A4.10}$$

$$R_f I = -V(1 + 1/A + R_f/RA + j\omega CR_f/A) \text{ -------A4.11}$$

$$\therefore \quad V = -R_f I \; / \; (1 + 1/A + R_f/RA + j\omega CR_f/A) \text{ -------A4.12}$$

Dividing top and bottom by $(1 + 1/A + R_f/RA)$

$$V = -R_f I(1+ 1/A+ R_f/RA)/(1 + (j\omega CR_f)/A(1+1/A+R_f/RA)) \text{--A4.13}$$

$$V = -R_f I(1+ 1/A + R_f/RA)/(1 + (j\omega CR_f)/(1+A+R_f/R)) \text{ ----A4.14}$$

Since $A >> 1 + R_f/R$

$$\therefore \quad V = -R_f I \; / \; (1 + j\omega CR_f/A) \quad \text{------A4.15}$$

No equalization is required for signals in the frequency range 0 to Δf provided

$$A >> \omega CR_f \Delta f$$

$$\therefore \quad \mathbf{V \cong -R_f I} \quad \text{-------A4.16}$$

Thus the voltage output of a transimpedance amplifier depends on the value of the feedback resistor and the current from the photodiode.

A5.0 GAIN PEAKING EFFECT

The so called gain peaking effect causes ringing in the output voltage response to a pulsed light input. This occurs by virtue of the fact that the reactance of the input capacitance and that of the feedback capacitance on the operational amplifier circuit may jointly form an unstable amplifier with respect to the noise present in the input operational amplifier. This tends to cause inaccuracies in the measurement of both the 'probe' signal and 'reference' signal. In the output voltage against frequency response curve, the gain peaking effect occurs at the point where the frequency response starts to roll-off near the 3dB point, as shown in figure A5.1, causing the curve to overshoot and this overshoot results in ringing, appearing on the transition edges of the pulse excitation as shown in figure A5.2.

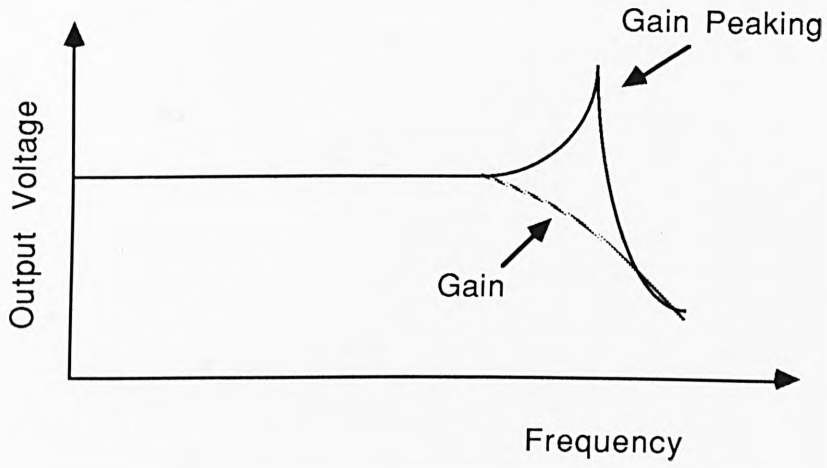

Figure A5.1 - Gain Peaking Effect

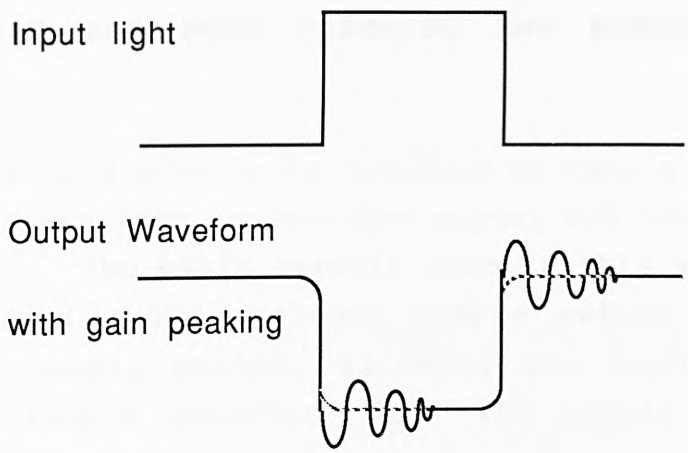

Figure A5.2 - Gain Peaking effect on input light.

The effects of gain peaking are avoided by switching out the transient change with an electronic analogue switch.

A6.0 SAMPLE and HOLD CIRCUITS AND ERRORS IN THEIR USE.

A sample and hold circuit is designed to take a sample, on a short time scale from an analogue signal and hold that value indefinitely. The basic circuit used in this work is shown in figure A6.1. The analogue sample switch (S_1) closes during the sample period, allowing the input signal to charge the sample capacitor C_H. The sample switch then opens up again, leaving the capacitor charged to the value of the analogue input signal.

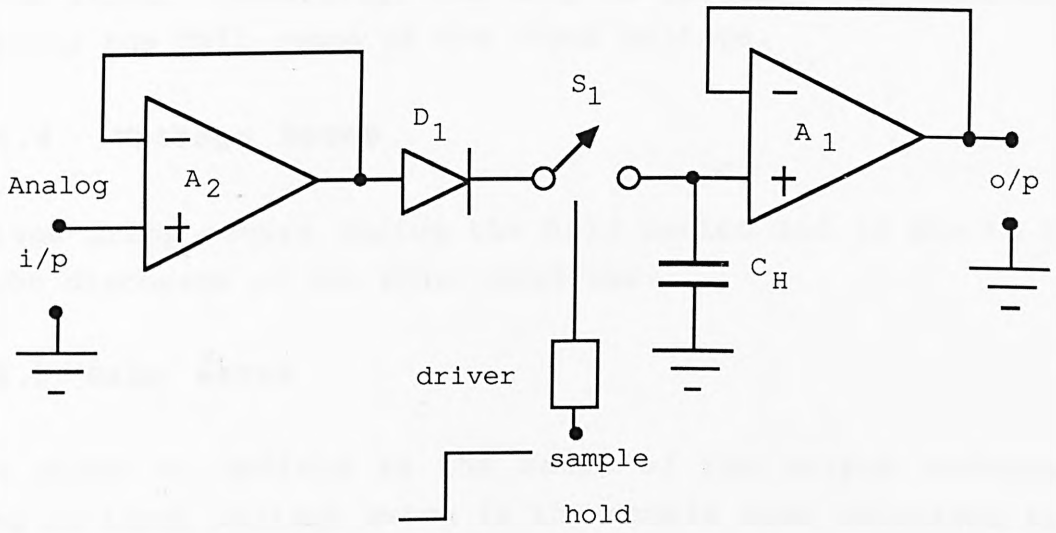

Figure A6.1 - Sample and Hold circuit

A6.1 CONSIDERATIONS IN THE USE OF SAMPLE AND HOLD CIRCUITS

A6.1.1 Acquisition time

This is the maximum time between the application of the sample command and the time when the output begins to track the input within some stated accuracy, regardless of the

previous state of the input. The acquisition time becomes important because it limits the resolution of the circuit for any given input signal slew rate.

A6.1.2 Aperture time

This is the delay between the Hold command to sample and the actual closing of the switch.

A6.1.3 The settling time

This is the maximum time for the output to track the input within a stated accuracy band for a specified step change in the input. Generally, the step is specified as accuracy covering the full range of the input voltage.

A6.1.4 Voltage Droop

Voltage droop occurs during the hold period and is due to a slight discharge of the Hold capacitor.

A6.1.5 Gain error

Gain error is defined as the ratio of the output voltage swing to input voltage swing in the sample mode expressed as a per cent difference.

A6.1.6 Dynamic sampling error

This is the error introduced into the held output due to a charging analogue input at the time the hold command is given. Error is expressed in mV with a given hold capacitor value and input slew rate.

These various error are shown diagrammatically in figure A6.2.

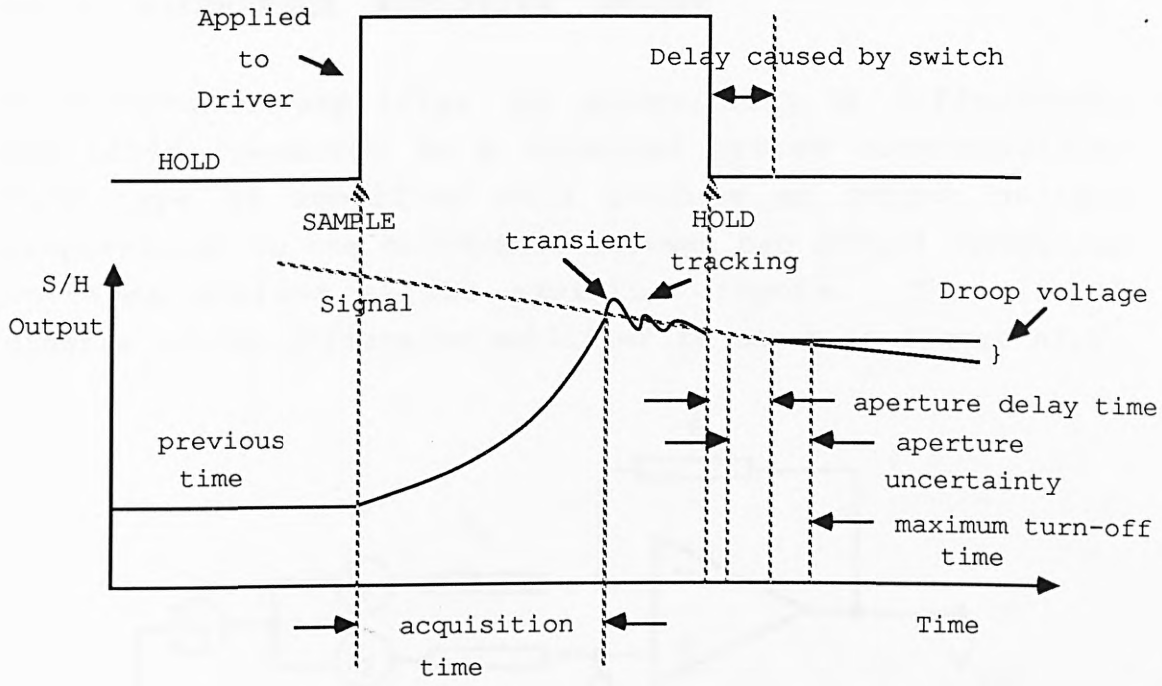

Figure A6.2 - Sample and Hold waveform errors

A7.0 DIFFERENCE AMPLIFIER ERRORS

A difference amplifier is essentially a differential amplifier connected in a balanced system configuration. This type of amplifier will produce an output voltage proportional to the difference between two ground referenced voltages applied to the amplifier inputs. The circuit diagram of the difference amplifier is shown in figure A7.1.

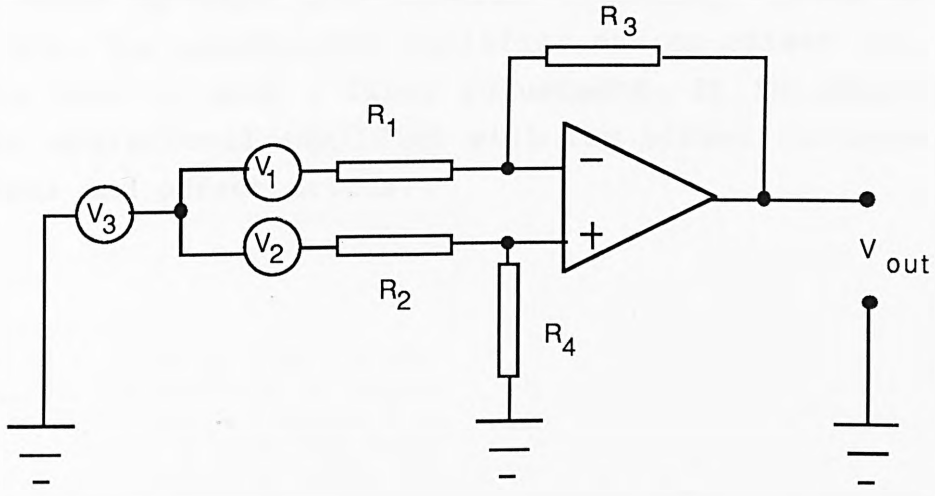

Figure A7.1 - Difference amplifier

Where V_1 and V_2 are the separate voltages applied to amplifier's input, and V_3 is the voltage common to both inputs arising from the earth loop - this is generally ignored as it is very small compared to the input volatges V_1 and V_2. The output voltage is given by the following equation:

$$V_{out} = -\frac{R3}{R1} V_1 + \left(\frac{R3}{R1} + 1\right)\left(\frac{R4}{R2 + R4} V_2\right) \quad \text{----(A7.1)}$$

For the output voltage to be zero, $V_1 = V2$ then $V_{out} = 0$ provided R1=R2 and R3=R4 thus V_{out} becomes:

$$V_{out} = (V_2 - V_1)\frac{R4}{R2} \text{ or } (V_2 - V_1)\frac{R3}{R1} \text{ ----(A7.2)}$$

This circuit will reject common mode voltages reasonably well i.e ~50dB, provided the resistors are well matched. The tolerances on the resistors have to be kept very low i.e < 1% and variable trimmers can be put in series to adjust the values if necessary. By using 1% metal-film resistors, the common-mode rejection ratio (CMRR) is typically 40dB. With good op-amps and careful trimming, 100dB CMRR is possible. The operational amplifier has an offset null which can be used to give a finer adjustment. It is important to select operational amplifier with low offset voltages, bias currents and offset drifts.

Appendix 8.0 RMS-TO-DC CONVERTER DATA SHEET (pp.218-224) has been removed for copyright reasons

A9.0 LAWS OF THERMAL COOLING

The thermal response time of the probes are essentially determined by two simple laws. The first is the five-fourths power law which applies to a body that is cooled by natural convection in still atmosphere. It is defined as follows:

$$(\text{rate of heat loss}) \quad \alpha \quad (\theta - \theta_s)^{5/4}$$

where a body at temperature θ in surroundings at temperature θ_s. For small values of $(\theta - \theta_s)$, the five-fourths law approximates to a linear law.

The second law is Newton's law of cooling which applies under conditions of forced convection, i.e in a steady draught, for all methods by which the body loses heat. It is defined as:

$$(\text{rate of heat loss}) \ \alpha \ (\theta - \theta_s)$$

This is an empirical law which holds for quite large temperature differences. It can be expressed as follows:

$$\Delta\theta = \Delta\theta_o \ e^{-k\Delta t}$$

Where the body cools from a temperature excess $(\theta - \theta_s)$ of $\Delta\theta_o$ to one of $\Delta\theta$ in a time interval Δt. The value of k takes into account: heat capacity, the body's surface area, the nature of its surface (e.g. its roughness), and the shape of the surface and its orientation. The rate of cooling against time graph for a body, shown in figure A9.1., shows rapid initial cooling followed by a much slower decrease in the body temperature as that body approaches the temperature of its surroundings.

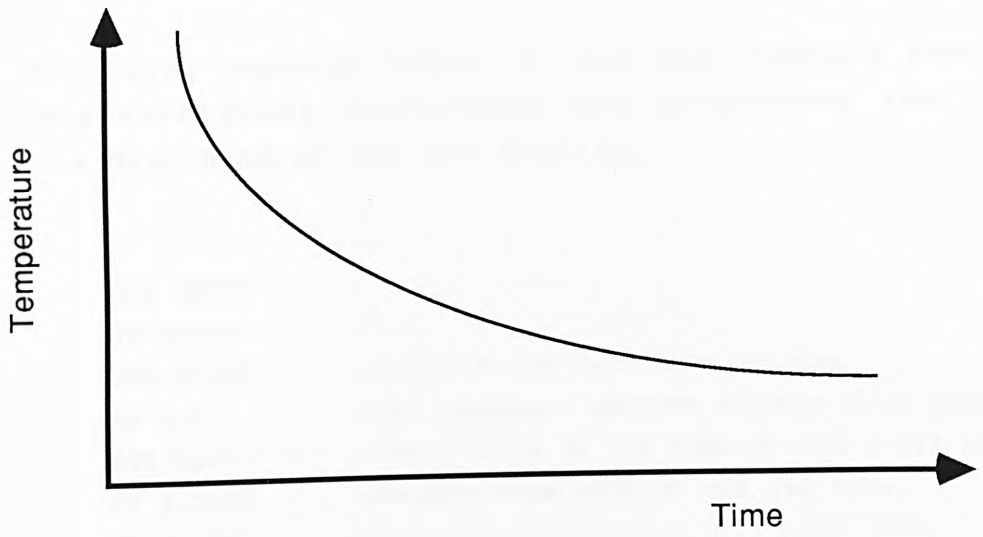

Figure A9.1 - Thermal response of a body with time

Appendix 10.0 - ASSEMBLY LANGUAGE PROGRAM (pp.227-235)
has been removed for copyright reasons

Appendix 11.0 PHYSICAL AND OPTICAL CHARACTERISTICS 236
OF EPO-TEK 353ND (pp.236-237)
has been removed for copyright reasons

A12.0 BEHAVIOUR OF GLASSES AT HIGH TEMPERATURES

Most elements and compounds when molten have a viscosity about the same as that of water. On cooling the molten material, or melt, crystallization occurs very rapidly at, or a little below the freezing point. There are, however, a few materials which form melts which are considerably more viscous. The high viscosity indicates that the atoms or molecules in the melt are not so easily moved relative to one another by applied stresses. The process of crystallization involves structural changes, i.e the re-arrangement of atoms relative to one another.

If the crystallization rate is low enough, it is possible to go on cooling the melt below the freezing point without crystallization taking place. As the melt cools, its viscosity continues to increase. This viscous liquid below the freezing point is a super-cooled liquid. Further cooling results in the viscosity rising to a value where the mechanical properties are closely similar to these of an ideal elastic solid.

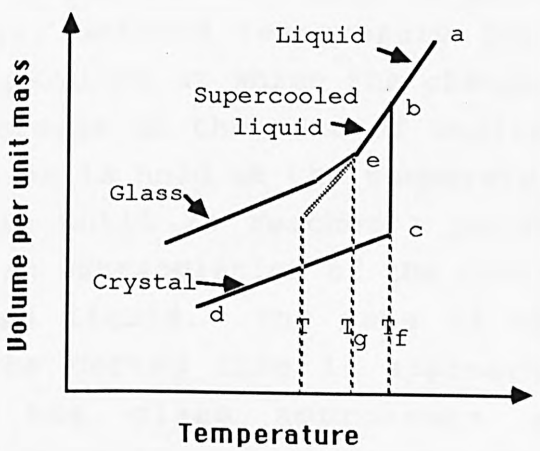

Figure A12.1 - Relation between the glassy, liquid and solid states.

The volume of the melt changes with temperature and is best illustrated by the volume-temperature diagram shown in

figure A12.1 (89). If the melt crystallizes an cooling, this is usually accompanied by a marked increase in density at the melting point, T_f. However, no such change occurs if the melt super-cools. The volume decreases along the line, be. The decrease in volume on cooling is due partly to the decreasing amplitude of atomic vibrations, and partly to changes in the structure of the melt which result in it becoming more compact as the temperature falls. At temperatures near T_f these structural changes can occur very rapidly and will appear to occur instantaneously following any change in the temperature of the material. As the viscosity increases with falling temperature, the structural changes occur increasingly slowly until eventually the viscosity becomes so high that no further such changes are possible. A decrease in slope then occurs in the curve (point e). With a further fall of temperature, the decreasing volume is due almost entirely to the decreasing amplitude of the atomic vibrations. The change in slope at the transformation temperature, T_g. below which the material can accurately be called glass.

The change from super-cooled liquid to glass is not sudden, nor is T_g a well defined temperature for any particular glass. The temperature at which the change in slope occurs is found to decrease as the rate of cooling is decreased. Also, if the glass is held at the temperature T, its volume decreases slowly until it reaches a point on the dotted line, which is an extrapolation of the contraction curve of the super-cooled liquid. The rate of change of volume decreases as the dotted line is approached, i.e as the structure of the glass approaches an equilibrium "configuration" which is characteristic of the super-cooled melt at the temperature T.

A13.0 PROPERTIES OF RUBY

Ruby is a crystalline form of Al_2O_3 (corundum) containing between 0.05% and 0.5% by weight of Cr_2O_3. At the lower concentration it is a pale pink whilst at higher concentrations it becomes a deep red. Geometrically the sapphire Al_2O_3 lattice is rhombohedral with each unit cell containing two Al_2O_3 molecules, as shown in figure A13.1. The crystal has a threefold axis of symmetry which forms the major diagonal of the unit cell (a threefold axis or c-axis is one about which the crystal lattice may be rotated by 120^o and appears unchanged). Owing to this rotational symmetry, the crystal has two indices of refraction; the ordinary ray having the electric field vector perpendicular to the c (optic) axis, and the extraordinary ray having the electric field vector parallel to the c-axis. Since the chromium ion enters the Al_2O_3 lattice substitutionally in place of the Al^{3+} ion, it finds itself surrounded by six nearest- neighbour O^{2-} ions. These O^{2-} ions are arranged nearly octahedrally and therefore subject the Cr^{3+} to a predominantly cubic field. The O^{2-} ions, however, do not form a perfect octahedron. Therefore, there is an additional relatively strong component to the crystal field which is trigonal with its axis along the optic axis of the crystal.

The energy level for ruby is shown in figure A13.2 (80), illustrating two broad absorption bands at $^4F_2$ and $^4F_1$. The ^4F term is separated into three levels designated by the symbols $^4F_1$, $^4F_2$ and $^4A_2$. Optical pumping is used to excite the ions from the ground state $^4A_2$ to the $^4F_1$ at ~400nm region and $^4F_2$ at ~550nm region as shown in figure A13.2. The two latter states are separated by a forbidden region. These levels form bands rather than discrete levels owing to the variation of the internal fields, which move the levels up and down with the field fluctuations thereby creating the appearance of forming bands. These bands allow electrons in the ground state to absorb light over a range of energies.

These induced transitions then undergo rapid relaxation (~$5x10^{-8}$ s) via photon emission into two closely spaced levels $^2E(2A)$ and $^2E(E)$. This transition is almost entirely non-radiative since the quantum efficiency of the red fluorescence, i.e ratio of the number of the emitted red photons to the number of photons absorbed in the green and blue absorption bands, was found to be nearly unity by Maiman (99). The two subsequent transitions from E and 2A to the ground level $^4A_2$ are known as R_1 and R_2 respectively. There is also some absorption near the R-lines owing to transition from $^4A_2$ to ^2E, but the absorption coefficient is quite small; being ~$0.28cm^{-1}$ (for 0.05% Cr^{3+} concentration) for the R_1 line. This is due to the fact that $^4A_2$ - ^2E transition is spin and parity-forbidden, and the small electric-dipole transition probability which does exist results primarily from the trigonal lattice distortions (80). The spectrum of the R-lines shows a fine structure, this has been attributed to the presence of different isotopes of chromium. The absorption spectrum shown in figure 5.1 was taken with an unpolarized light source. It is interesting to note that the absorption spectrum is different when the incident light is parallel to the [111] direction (c-axis) than it is when it is perpendicular to this direction, as shown in figure A13.3.

As has already been mentioned the almost entirely radiative nature of the ^2E to $^4A_2$ transition results in a quantum efficiency of nearly unity, Maimann (99). Subsequently, however, Maimann (100) measured the quantum efficiency and found it to be between 60 and 80% for both the blue and green bands. Measurements of quantum efficiency were conducted by Burns and Nathan (79) over a temperature range of 77 to 513K. They found that the red fluorescence is not confined to the R_1 and R_2 lines but is actually spread over a range of about 80nm, as a result of phonon-assisted transitions. They found the total red fluorescence efficiency to be independent of temperature up to 240°C. However, there was found to be a change in the spectral

distribution of energy near the R-lines. Figure A13.4 shows the emission from pink ruby (0.05% Cr^{3+}) at several temperatures taken form Burns and Nathan (79). As the temperature increases the R-line intensity decreases at a linear rate (the R-line fluorescent efficiency was found to decrease from ~55% to about 10% between 273 and 513K, and below 273K the R-line quantum efficiency was found to be approximately constant at a value of ~55%); this loss of energy in the R-lines is redistributed to higher and lower wavelengths on either side, hence maintaining a constant total fluorescent output, up to 240°C. It should also be mentioned that the fluorescence peaks shift to longer wavelengths as temperature is increased (101). The shift in the R- lines is given by

$$= 6943.25 + 0.068(T-20) \text{ -------(A13.1)}$$

Where T is in degrees Celsius.

This shift is 9.52nm for a temperature of 160°C, indicating that the R-line shift will enhance the intensity variation of the measurand signal and has negligible effect on the total generated fluorescent emission.

It is appropriate at this point to mention the lifetime of the R-lines and how these are affected by temperature, as the next chapter discusses a decay-time ruby thermometer. At room temperature the lifetime for R_1 fluorescence is ~3ms at a wavelength of 694.3nm, and the lifetime for R_2 is slightly less, 2.9ms, at a wavelength of 629.8nm (102) (the lifetime of the samples used in these sensors was of the order of 3.5ms). The E and 2A levels (also known as the metastable state) are approximately 970GHz apart and since chromium ions vibrate in this and higher energy levels (i.e ^4I levels) are broadened to lesser or greater extent by temperature because the vibration amplitudes and lattice spacings change with temperature. This dependence of energy levels to the distance between a Cr^{3+} ion and its nearest

neighbour was theoretically explained by Kubo and Toyazawa, as described in the book by Levine (80). E and 2A are strongly coupled by relaxation of the crystal, a process which is temperature sensitive since it depends on the availability of lattice phonons. Phonons are quanta of energy with specific modes of vibration. These are used to transfer the vibrational energy in one part of the crystal, associated with an increase in temperature, to another. Phonon means of energy transfer is associated in non-metallics, where there are no free electrons and the atoms are closely coupled together. Both E and 2A can decay by phonon-assisted processes, whereby only part of the energy is radiated in the form of a photon of light, the remainder being transferred directly to the lattice as phonons.

The decrease in the decay-time of the ^2E state of ruby at elevated temperatures was shown by Kisliuk et al (103) to be the result of populating the shorter-lived $^4F_2$ level in thermal equilibrium with the metastable state ^2E. In addition they showed that the transition from $^4F_2$ to the ground $^4A_2$ state is mostly radiative. Thus, the emitted radiation was reported to be the result of de-excitation of the $^4F_2$ and the metastable states. The combined decay-time was shown to be dependent on the energy difference of these states and the strength of the radiative transitions to the ground state, where the $^4F_2$ state was expected to decay to the ground state more slowly than ^2E.

Appendix 14.0 - ASSEMBLY LANGUAGE PROGRAM (pp.244-252) has been removed for copyright reasons

REFERENCES

1. McGeehin P., 'Fibre Optics in Perspective - Workshop' Univ. of Strathclyde, Glasgow, 13-14, July 1987.
2. Kao K.C., Hockham G.A., Proc. IEE, 113(7), 1151-1158, 1966.
3. Werts A., L'Onde Electrique, 46, 967-980, 1966.
4. Medlock R.S., Measurement and Control, vol.19, Feb. 1986.
5. Theocharous E., J Phys. E:Sci Instrum. 18, 253-255, 1985.
6. Theocharous E., Digest 3rd Int. Conf. on Optical Fibre Sensors, San Diego, Optical Society of America, 148-149, 1985.
7. Jones B.E., Spooncer R.C., Proc. 2nd Int. Conf. on Optical Fibre Sensors, Stuttgart, SPIE vol.514, 223-226, 1984.
8. Kopera P.M., Melinger J., Tekippe V.J., Proc. SPIE Int. Soc. Opt. Eng., vol.412, 82-89, 1983.
9. Grattan K.T.V., Mouaziz Z., Palmer A.W., Selli R.K., Journal of Optical sensors, vol. 2, no. 5, 1987
10. Culshaw B., Foley J., Giles I.P., Proc. 2nd Int. Conf. Fibre Optic Sensors, Stuttgart, SPIE vol.574, 117-120, 1984.
11. Giles I.P., McNeil S., Culshaw B., J. Phys. E:Sci Instrum, 18, 502-504, 1985.
12. Accufibre Corp. Vancouver, Canada.
13. Peterson J.I., Goldstein S.R., Fitzgerald R.V., Anal.Chem. 52, 864-69,1980.
14. Oximetrix Inc. Mountain View, CA, USA (Abbott Laboratories)
15. Yoshiya I., Shimada Y., Taraka K., Med. & Biol. Eng. & Comput. 18, 27-32, 1980.
16. Criticare Systems Inc., Milwaukee, USA.
17. Smith A.M., Electronics and Power, IEE, 811-813, NOV.-DEC., 1986
18. Grattan K.T.V., Mouaziz Z., Palmer A.W., Biosensors, to be published 1987.
19. Nuwira N., Bbref D., ADV Advances in Exp. Med. Biol., Vol. 169, 913, 1984.
20. Stueflotten S., Christensen T., Iversen S., Hellvik J.O., Almas K., Wien T., Graav A., Proc. 2nd Int. Conf.

on Optical Fibre Sensors, Stuttgart, SPIE vol.514, 87-90, 1984.
21. Jones B.E., Philip G.S., Proc. 1st Conf. Sensors and their Applications (Institute of Physics, London, England).
22. McGlade S.M., Jones G.R., GEC J. Research 2, 315-8, 1984.
23. Grattan K.T.V., Palmer A.W., Saini D.P.S., IEEE/OSA J. Lightwave Tech. LT5, 972-9,1987.
24. Ventakesh S., Culshaw B., Electron. Letts 21, 315-7, 1985.
25. Rogers A.J., J.Phys D:App Phys 19, 2237, 1986.
26. Theocharous E., Proc. 1st Int. Conf. Optical-Fibre Sensors (London), IEE Conf. Publ. No. 221, 10-12, 1983.
27. Jones' Instrument Technology Volume 2, Measurement of Temperature and Chemical Composition, Edited by B E Noltingk, Fourth Edition, Butterworths.
28. C. R. Barber, The Calibration of Thermometers, National Physical Laboratory.
29. R. L. Rusby, The basis of temperature measurement, The Institute of Measurement and Control, Vol.20, No.6, July 1987.
30. Dakin J.P., Kahn D.A. Opt. Quant. Electron. 9,540, 1977.
31. Campbell N.T., Proc. SPIE 197, 295, 1979.
32. Harmer A.L., Technical Digest of 4th Int. Conf. on Optical Fibre Sensors, (OFS), Informal Workshop, Tsukuba Science City, Japan, 1986.
33. Fotonic Sensor - Mechanical Technology Inc., Lathan, N.Y.
34. Bergstrom J., Betibon H., Brogardh T., Persson A. UK Patent Application GB 2010476A, 1979.
35. Croft J.R., Palmer A.W., Valsler R., Proc. SPIE 374,206, 1983.
36. De Rossi D., J.Biomed. Eng. 2, 256, 1980.
37. Blotekjaer K., Sincerbox G.T., IBM Tech. Disclosure Bul. 20, 1929, 1977.
38. Brenci M. Proc. 2nd Opt. Fibre Sensors Conference (OFS), Stuttgart, Germany, p155-60, 1984.
39. Gottlieb M., Brandt G.B., Fiber Optic Conference, Chicago, 236, 1979.
40. British patent 1,390,426.
41. Pinchbeck D, Kitchen C.A. 1985 Proc. Conf. Electronics

in Oil and Gas Industries, London, January 1985.
42. Ramakrishnan S., Kersten R.T., Proc 2nd opt. Fibre Sensors Conference (OFS) Stuttgart, 105-110, 1984.
43. Rogers A.J., App. Opt. 21, 882, 1982.
44. Christiansen C., Ann Phys. Chem. 23, 298, 1984.
45. Knox J.M. Proc. 1st Conf. on Opt Fiber Sensors, (OFS), 1, 1983.
46. Saaski E.W., Skaugoet R.L. 7th IEEE/PES Trans. and Dist Conf., 208, 1979.
47. Kyuma K., Tai S., Sawada T., Nunoshita M., IEEE J. Quant. Electron. QE18, 676, 1982.
48. Schoener G., Bechtel J.H., Salour M.H. Proc. 2nd Optical Fibre Sensors Conference (OFS), Stuttgart, Germany, p203, 1984.
49. Theocharous E., Proc. 1st Opt Fibre Sensors Conference (OFS).p.10, London, 1983.
50. Wickensheim K.A., Alves,R.V., Biomedical Thermology 547-54,Pub:Alan Lirs N.Y. U.S.A., 1982.
51. Ovren C., Adolffson M., Hok B., Proc. Int. Conf. 'Optical Techniques in Process Control' The Hague, Holland, 1983, paper B2 pub:BHRA, Cranfield, Bedford, England.
52. James K.A., Quick W.H. Control Eng. 30 (Feb. 1979)
53. Sholes R.R. Small J.G. Rev. Sci Instrum 51, 882-4, 1980.
54. McCormack J.S. Electron Letts, 17, 630-1, 1981.
55. Bosselmann T. Ruele A. Schroder J. Proc. 2nd Opt Fiber Sensors Conf.(OFS), Stuttgart, 1984.
56. Wickensheim K.A. Heineman S.O., Tran H.N., Sun M.H, 1985. Proc.Digitech '85, Boston U.S.A., Proc. ISA paper 85-0072, p87-94, 1985
57. Hirano M. Technical Digest of 4th Int. Conf. on Optical Fiber Sensors, (OFS) Informal workshop, Tusaba Science City, Japan, 1986.
58. Grattan K.T.V., Palmer A.W., Rev.Sci Instrum 56, 1784, 1985.
59. Grattan K.T.V., Palmer A.W., Proc."Capteurs 86", Paris Pub. CIAME, p173, 1986.
60. Foley G.M., Morse M.S., Cezrairligan A. Temperature Measurement and control in Science and Industry, 5 447-52,(pub. Amer Inst. Phys), 1982.
61. Grattan K.T.V., Manwell J.L., Sim S.M.L., Willson

C.A., Proc. Conf. on Lasers and Electro Optics Baltimore, USA, April 1987. Proc. Pub IEEE/OSA. U.S.A., 1987.
62. Hartog A.H., J. Lightwave Technol. LT1 498-589, 1983.
63. Farries M.C., Fermann M.E., Lamming R.I., Poole S.B., Payne D.N., and Leach A.P., Electron. Lett. 22, 418-9, 1986.
64. Farries M.C., Fermann M.E., Proc. 4th Inst. Symposium on Optical and Optoelectronic Applied Science & Engineering, The Hague, Holland, 798-815, April 1987.
65. Dakin J.P., Pratt D.J., Bibby G.W. and Ross J.N., Proc. 3rd Int. Conf. Optical Fibre Sensors (San Diego, USA) 1985.
66. Dakin J., J.Phys. E.Scientific Instruments August, 1987.
67. Dakin J.P., Pratt D.J., Bibby G.W., Ross J.N., 3rd Int. Conf. on Optical Fibre Sensors, post-deadline paper session, San Diego, USA, February 1985.
68. Hartog A.H., Leach A.P.,Gold M.P., Electron Lett. 19, 14-5, 1985.
69. Saaski, E.W., Hatl, J.C., Mitchell, G.L., Wolthuis, R.A., Afromowitz M.A. Technical Digest of 4th Int. Conf. on Optical Fiber Sensors, (OFS) Informal workshop, Tusaba Science City, Japan, 11, 1986.
70. York Technology, V.S.O.P., York House.
71. Thornton J.R., Fountain W.D., Flint G.W., Crow T.G., Applied Optics 8, 1087-1102, 1969.
72. Kigre Incorporation, USA.
73. National Semiconductor Linear Circuits data handbook.
74. Senior J.M., Optical Fibre Communications Principles and Practice (Prentice and Hall), London, 1985.
75. G.B. Clayton, Operational Amplifiers, second edition, Butterworth Scientific, 1982.
76. Horowitz., Hill., The Art of Electronic, Cambridge university press, 1980.
77. RS data sheet No. 2999, RS Components Ltd.
78. DeShazer L.G., Komai L.G., Journal of the Optical Society of America, vol.55, No.8, August 1965.
79. Burns G., Nathan M., Journal of Applied Physics, 34, No.3, 703-705, 1963.
80. Levine A.K., Lasers, vol.1, 1966, (New York: Marcel Dekker Inc.).
81. Augousti A.T., Grattan K.T.V., Palmer A.W., Journal of

Lightwave Technology, vol.LT-5, No.6, 759-762, 1987.
82. Berlin H.M., Design of Phase-Locked Loop Circuits with Experiments, (Howard W. Sams and Co., Inc.), 1982.
83. Fishenden M., Saunders O.A., The Calculation of Heat Transmission, published by Her Majesty's stationary office, 1932.
84. Brandes E.A., Smithells Metals Reference Book, 6th edition, (Butterworth)
85. Theocharous E., 4th Int. Symposium on Optical and Optoelectronic Applied Science and Engineering, March 1987.
86. Stock K.D., Proc. 12th Int. Symposium, Photon Detectors, IMEKO, Verna, 129-136, 1986.
87. British Patent 1,605,117
88. United States Patent Re. 31,832
89. H. Rawson, Properties and Applications of Glass, Glass Science and Technology 3, Elsevier Scientific Publishing Company, 1980.
90. Lakowicz J.R., Principles of Fluorescence Spectroscopy, Plenum Press, New York, 1983.
91. Lupei N., Lupei A., Georgescu S., Ionescu C., Opt. Commun. 60, 59-63, 1986.
92. Liao P.F., Weber H.P., Journal of Applied Physics vol.45, No.7, July 1974.
93. Deb K.K., Buser R.G., Paul J., Applied Optics, April, 1981.
94. Singh S., Bonner W.A., Grodkiewicz W.H., Groisso M., Van Uitert L.G., Applied Physics Letters, vol.29, No.6, September 1976.
95. Morey W.W., Glenn W.H., Snitzer E., Int. Intsrumentation symposium, 29th Albuquerque, New Mexico, 261-274, 1983.
96. Levine A.K., (ed), 1968, Lasers, vol.2 (New York: Marcel Dekker).
97. Neuroth N., Optical Engineering, vol.26, No.2, February 1987.
98. Brachkovskaya N.B., Przhevuskii A.K., Zhurnal Prikladnol Spektroskopii, vol.36, No.1, 126-133, January 1982.
99. Maiman T.H., Phys. Rev. letters., 4, 564, 1960.
100. Maimann T.H., Hoskins R.H., D`Haenens I.J., Asatra C.K., and Evtuhov V., Phys. Rev., 123, 1151, 1961.

101. Jones K.A., Introduction to Optical Electronics, (Harper and Row, New York, 1987).
102. Eastham D., Atomic Physics of Lasers, (Taylor and Francis: London), 1986.
103. Kislink P., Moore C.A., Physical Review, vol.160, No.2, August 1967.

LIST OF PUBLICATIONS

1) "Doped glass absorption thermometer with fluorescent referencing", Grattan K.T.V., Palmer A.W., Selli R.K., Society of Photo-Optical Instrumentation Engineers Proceedings, vol.566, 333-339, 1985.

2) "Self-referenced fibre-optic glass absorption thermometer", Grattan K.T.V., Selli R.K., Palmer A.W., paper presented at SPIE 2nd International Technical Symposium on Optical and Electro-Optical Applied Science and Engineering, Cannes, France, November 1985. Society of Photo-Optical Instrumentation Engineers Proceedings, vol.586, 142-149, 1985.

3) "Fibre optic absorption temperature sensor using fluorescence reference channel", Grattan K.T.V., Selli R.K., Palmer A.W., Review of Scientific Instruments, 57, 1175-1178, 1986.

4) "A miniaturized fluorescence reference glass absorption thermometer", Grattan K.T.V., Selli R.K., Palmer A.W., paper presented at the 4th International Conference on Optical Fibre Sensors (OFS '86), Tokyo, Japan, October 1986.

5) "pH sensor using a LED source in a fibre optic device", Grattan K.T.V., Mouaziz Z., Selli R.K., Proc. SPIE Fibre Optic Sensors II, vol.798, 230-237, 1987. Paper presented at the Conference held in The Hague, Netherlands.

6) "Fibre-optic temperature sensor using wavelength distribution of fluorescence emission", Grattan K.T.V, Selli R.K., Palmer A.W., paper presented at 5th Int. Conf. on Fibre Optics and Opto-Electronics, April 1987.

7) "A Prism configuration internally referenced temperature sensor", Grattan K.T.V., Selli R.K., Palmer A.W., International Journal of Optical Sensing - accepted for publication, 1987 or 1988.

8) "Ruby fluorescence wavelength division fiber-optic temperature sensor", Grattan K.T.V., Selli R.K., Palmer A.W., Rev. Sci. Instrum. 58(7) July 1987

9) "Ruby Fluorescence-Based Temperature Sensor - Use of Temporal and Wavelength Division", Grattan K.T.V., Selli R.K., Palmer A.W., presented at 13th IMEKO Symposium of Technical Committee TC-2, Braunschweig, West Germany, Sept. 1987.

10) "Development of simple optical pH sensors for use in acid-base titrations", Grattan K.T.V., Mouaziz Z., Palmer A.W., Selli R.K.,Jour. Opt. Sensors, vol. 2, no. 5, 1987

11) "Phase-measurement based ruby fluorescence fibre optic temperature sensor", Grattan K.T.V., Selli R.K., Palmer A.W., accepted for presentation at Optical Fibre Sensors Conference (OFS) '88, New Orleans, USA, Jan. 1988.

12) "Fluorescence Referencing for Fibre Optic Thermometers using Visible Wavelengths", Grattan K.T.V., Selli R.K., Palmer A.W., Review of Scientific Instruments, 59, 256,1988.